The University Of Sheffield.

Department Of
Materials
Science
and Engineering

Brannerite ceramic and glass-ceramic composite materials for immobilisation of damaged and degraded nuclear fuels

Malin Christian John Dixon Wilkins

Thesis

Submitted for the degree of Doctor of Philosophy

September 2021

Immobilisation Science Laboratory

Department of Materials Science and Engineering

The University of Sheffield

Abstract

Future disposal of high actinide content nuclear wastes that are unsuitable for further reprocessing requires robust, durable wasteform materials. Brannerite, nominally UTi_2O_6, is a naturally occurring mineral that can retain the majority of its uranium inventory despite metamictisation and extensive weathering. Due to this, synthetic brannerites have been proposed as candidate materials for immobilisation of high actinide wastes, either as a ceramic or as the ceramic phase in a glass-ceramic composite. This work has investigated the underlying chemistry of a range of brannerite structured materials to examine their suitability for this application.

Initial investigations examined the formation of UTi_2O_6 from the component oxides in a glass-ceramic composite for the first time. A suite of samples with variations in UO_2:TiO_2 molar ratio, and processing time and temperature was produced and characterised by XRD, SEM, and U L_3 edge XANES. Materials with stoichiometric amounts of UO_2 and TiO_2 contained a small fraction of UO_2 in the glass matrix, but additions of hyperstoichiometric amounts of TiO_2 resulted in high quality UTi_2O_6 glass-ceramic composites. It was observed that some grains of UTi_2O_6 were encapsulating small regions of UO_2, suggesting that brannerite formation occurs mainly around particles of UO_2, with diffusion kinetics playing a key role.

After the success of the initial investigation, a further suite of UTi_2O_6 glass-ceramic composites was produced, with varying glass:ceramic ratios. The compatibility of these materials with hot isostatic pressing was also examined. Materials containing up to 90% UTi_2O_6 by weight were successfully synthesised in a one step process at 1200 °C, showing the flexibility of this glass-ceramic system. Compared to formation of a pure ceramic brannerite, the addition of only 10% glass by weight allowed for a reduction in reaction time and temperature compared to pure ceramic brannerites (1200 °C for 6 hours, compared to 1300 °C for 24 hours or more). Hot isostatically pressed UTi_2O_6 glass-ceramic composites were also produced, and the impact of HIP temperature and time examined.

The impact of the glass phase composition (in the system $Na_2Al_{2-x}B_xSi_6O_{16}$) on the formation of UTi_2O_6 was also examined. Unlike the formation of zirconolite, the glass composition did not have a strong effect on the formation of brannerite, with all materials forming glass-ceramic composites with UTi_2O_6 as the major crystalline phase. This difference was ascribed to the lack of easily formed U/Ti silicate phases in these brannerite glass-ceramic composite systems, where analogous zirconolite systems have been reported to form sphere/titanate and zircon ceramic phases when the glass phase has a relatively higher silica activity.

The effect of Ce oxidation state and O vacancy fraction as a function of temperature and atmosphere on $CeTi_2O_6$ stability was also examined, utilising thermogravimetric techniques, XRD, and Ce L_3 edge XANES. It was shown that the temperature dependent Ce^{3+}/Ce^{4+} redox couple is active in $CeTi_2O_6$, and the maximum stable Ce^{3+} content determined to be between 13.1% and 15.7% Ce^{3+}. The thermodynamics of $CeTi_2O_6$ formation were also discussed, and it was proposed that the reduction of a small fraction of Ce^{4+} to Ce^{3+} at temperature must occur for the formation

of $CeTi_2O_6$ to be energetically favourable. The results of this investigation demonstrated that Ce is a poor surrogate for Pu in some systems, particularly in thermal regimes where the Ce^{3+}/Ce^{4+} redox couple is active.

Two investigations into the crystal chemistry of actinide brannerites were performed. The first examined the formation of ATi_2O_6 and $A_{0.5}B_{0.5}Ti_2O_6$ (A and B = U, Th, Ce) ceramic phases in glass-ceramic composites in two different process atmospheres, air and Ar. The key factor controlling the formation of brannerite was identified: the availability of an overall A-site charge of 4+. This was most directly observed in the samples batched as $U_{0.5}Ce_{0.5}Ti_2O_6$: when processed in air a $Ce^{3,4+}/U^{5+}$ brannerite was formed; under Ar, a $Ce^{3+}/U^{4,5+}$ brannerite. Although the addition of glass allows for complete formation of UTi_2O_6, the kinetics of $ThTi_2O_6$ formation were slower, with larger fractions of ThO_2 and TiO_2 observed in the final phase assemblages compared to UO_2 and TiO_2 in UTi_2O_6 glass-ceramic composites produced by the same heat treatment.

The second investigation examined the solid solubility of Al^{3+} in UTi_2O_6, and was the first systematic investigation into the use of a high fraction, lower oxidation state Ti-site dopant to stabilise the formation of U^{5+} brannerite. A near single phase material was produced in the material batched as $UTiAlO_6$, and the structure examined by time-of-flight neutron diffraction. The impact of cation size on the brannerite structure was examined, with changes in average U oxidation state and Al^{3+} content causing shrinkage of the brannerite unit cell. The use of a Ti-site dopant to stabilise the brannerite structure when formed in air was successfully demonstrated, allowing for charge-balancing of U^{5+} whilst retaining the high U content that makes brannerites particularly attractive as wasteforms for high actinide content wastes.

As always, I dedicate this work to my late mother.

Acknowledgments

It is not an overstatement to say that ‘during the production of this thesis’ I have experienced some very difficult times. I am still here due to every single one of my colleagues, friends, and family. Thank you.

That being said, my first thanks must go to my supervisors Martin Stennett and Neil Hyatt. I have yet to find a question that either of you could not answer (despite my best attempts). I have struggled with motivation throughout my PhD, but an impromptu ten-minute conversation with one or both of you has never failed to reignite my interest, both for my project and for science.

To everyone that I have worked with, and everyone who has ever had to accommodate my last minute requests for equipment time/tools/samples, thank you! In particular, I must thank Laura Gardner for managing to keep the HIP running after I have been operating it, including the ‘user induced unplanned depressurisation event’, and Dan Bailey for putting up with my endless questions about technetium, ceramics, and most everything else.

James Shipp and Josh Nicks, I am sorry that you have become ‘The Chem Boys’! Thank you for being there in every sort of situation, from traumatising to amusing, and for putting up with my (usually) drunken antics for eight years. I must also thank my partner in crime Lewis Blackburn, from early afternoon pints in Sheffield to late night pints in Tokyo, we have managed to do it all in these four years. Hao Ding, thank you for putting up with my awful Chinese and stupid questions, I am looking forward to coming to visit soon! Dan Martin, my PhD life would have been very different if you had not also been here, though I cannot believe you have abandoned me for a high paying job down south. Dan Austin, I will never again doubt your dancing credentials for as long as I live.

To everyone in the ISL (and the K Floor office), if I listed you all by name I could probably get another five pages of thesis length, but instead I shall say: thank you all for tolerating my disruptive office (lab, pub, *etc.*) presence, I am not sure how you have managed to live with me for so long. I have thoroughly enjoyed working with you all, and every day I am glad at how friendly our group is!

Publications

The author contributed to the following publications during production of this thesis:

"The formation of stoichiometric uranium brannerite (UTi_2O_6) glass-ceramic composites from the component oxides in a one-pot synthesis", MC Dixon Wilkins, MC Stennett, ER Maddrell, NC Hyatt*, J. Nucl. Mat.*, 2020, 542, 10.1016/j.jnucmat.2020.152516

"Synthesis and characterisation of high ceramic fraction brannerite (UTi_2O_6) glass-ceramic composites", MC Dixon Wilkins, ER Maddrell, NC Hyatt, *IOP Conf. Ser.: Mater. Sci. Eng.*, 2020, 818, 10.1088/1757-899X/818/1/012018

"The effect of temperature on the stability and cerium oxidation state of $CeTi_2O_6$ in inert and oxidizing atmospheres", MC Dixon Wilkins, ER Maddrell, MC Stennett, NC Hyatt, *Inorg. Chem.*, 2020, **59**(23), 10.1021/acs.inorgchem.0c02681

"The effect of A-site cation on the formation of brannerite (ATi_2O_6, A = U, Th, Ce) ceramic phases in a glass-ceramic composite system", MC Dixon Wilkins, MC Stennett, NC Hyatt, *MRS Adv.*, 2019, **5**, 10.1557/adv.2019.470

"A feasibility investigation of laboratory based X-ray absorption spectroscopy in support of nuclear waste management", LM Mottram, MC Dixon Wilkins, LR Blackburn, T Oulton, MC Stennett, SK Sun, CL Corkhill, NC Hyatt, *MRS Adv.*, 2020, **5**, 10.1557/adv.2019.470

"Safely probing the chemistry of Chernobyl nuclear fuel using micro-focus X-ray analysis", H Ding, MC Dixon Wilkins, C Gausse, LM Mottram, SK Sun, MC Stennett, D Grolimund, R Tappero, S Nicholas, NC Hyatt, CL Corkhill, *J. Mat. Chem. A*, 2021, **9**(21), 10.1039/D0TA09131F

"Crystal and Electronic Structures of A_2NaIO_6 Periodate Double Perovskites (A = Sr, Ca, Ba): Candidate Wasteforms for I-129 Immobilization", SE O'Sullivan, E Montoya, SK Sun, J George, C Kirk, MC Dixon Wilkins, PF Weck, E Kim, KS Knight, NC Hyatt, *Inorg. Chem.*, 2020, **59**(24), 10.1021/acs.inorgchem.0c03044

"Chemical state mapping of simulant Chernobyl lava-like fuel containing material using micro-focused synchrotron X-ray spectroscopy", H Ding, MC Dixon Wilkins, LM Mottram, LR Blackburn, D Grolimund, R Tappero, S Nicholas, SK Sun, CL Corkhill, NC Hyatt, *J. Synchrotron. Radiat.*, 2021, **28**(6), 10.1107/S1600577521007748.

"Synthesis, characterisation, and crystal structure of novel uranium (V) dominant brannerites in the $UTi_{2-x}Al_xO_6$ system", MC Dixon Wilkins, LM Mottram, ER Maddrell, MC Stennett, CL Corkhill, KO Kvashnina, NC Hyatt, *Inorg. Chem.*, submitted September 2021, under review.

During the production of this thesis, the author also presented at the following events:

9th NDA PhD Bursary Seminar 2021, 29-30 April 2021, held online (oral presentation)

8th NDA PhD Bursary Seminar, 29 January 2020, Manchester, UK (oral presentation)

THERAMIN 2020, 4-5 February 2020, Manchester, UK (oral presentation)

43rd Annual Symposium on the Scientific Basis for Nuclear Waste Management, 21-24 October 2019, Vienna, Austria (oral presentation)

PACRIM13: The 13th Pacific Rim Conference of Ceramic Societies, 27 October – 1 November 2019, Okinawa, Japan (poster presentation)

THERAMIN Technical Training School, 12-14 June 2019, CEA Marcoule, France (poster presentation)

7th NDA PhD Bursary Seminar, 23 January 2019, Manchester, UK (poster presentation)

Uranium Science Conference, 21-22 January 2019, Bristol, UK (poster presentation)

6th NDA PhD Bursary Seminar, 17 January 2018, Manchester, UK (short oral presentation)

1 Introduction

1.1 Nuclear power

1.1.1 Nuclear fission

By the early 20th century scientific understanding of radioactive decay mechanisms was swiftly advancing, with many researchers around the world examining the decay processes of both naturally occurring isotopes[1,2] and those produced artificially.[3,4] By the late 1930s, a new type of radioactive decay of heavy nuclei was theorised and later proven true: nuclear fission, the division of a heavy nucleus into two (or occasionally more) lighter daughter nuclei (see Figure 1), accompanied with a large release of energy, and, for some nuclei, one or more neutrons.[5,6]

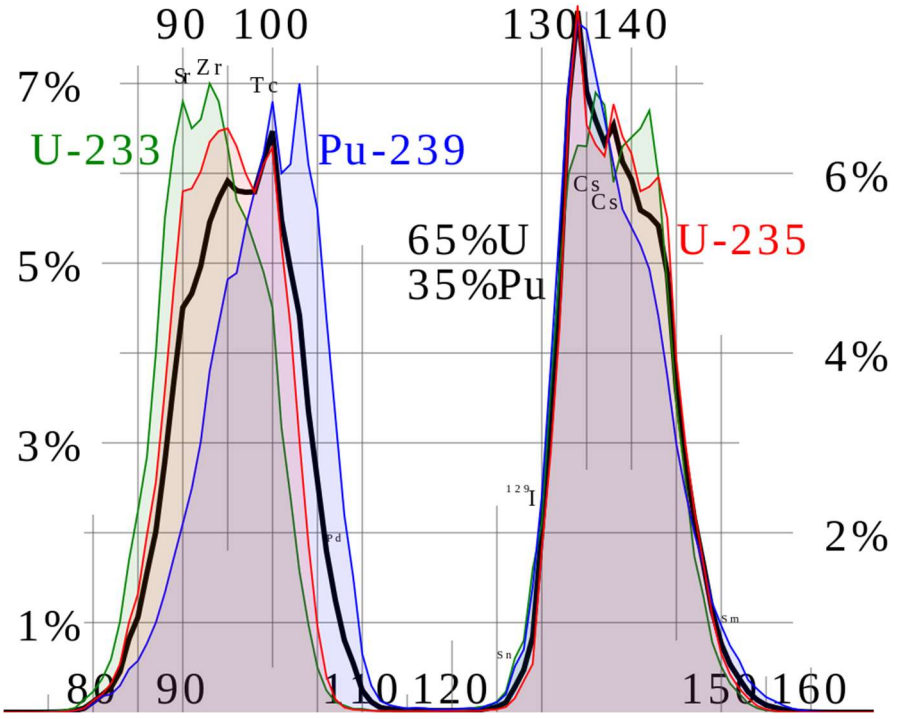

Figure 1: Fission product yields for different fissile nuclei: ^{235}U, ^{233}U, ^{239}Pu, and a mixed $^{235}U/^{239}Pu$ fuel. Image from user JWB at en.wikipedia, used under licence CC BY 3.0.[7]

Fission is only one of many radioactive decay paths available to heavy, unstable isotopes, and spontaneous fission (where no external factors affect nuclear stability) is rarely observed in isotopes occurring naturally compared to other decay paths; particularly alpha and beta emitting processes. The majority of nuclear fission processes that have been observed by scientists require the input of additional species, often, but not always, a neutron. If the species is a neutron, it must also have sufficiently high energy to initiate fission, but sufficiently low energy to be captured by the nucleus under bombardment.[8]

Despite this, the production of neutrons in some fission processes, particularly the fission of heavy nuclei, means that under the right conditions a nuclear chain reaction can occur, where each fission event produces more (or the same amount of) neutrons than were initially input.[8] In these

cases, the system is said to be critical if there is no net gain (or loss) of neutrons in the process, or supercritical if there is a net gain of neutrons.

1.1.2 Nuclear power generation

The first nuclear reactors were designed so as to make use of the excess neutrons for material irradiation or nuclear transmutation, but it was quickly realised that the heat produced by a controlled nuclear chain reaction could be utilised in the generation of electricity. Unsurprisingly, nuclear reactors are extremely complex, requiring careful monitoring and control of the chain reaction to ensure working safety, and only a general introduction will be provided here.

The goal of a power generating nuclear reactor is to generate electricity from the heat released by an ongoing fission chain reaction. For this purpose, there must be control of the energies of produced neutrons (moderation of the neutron energy), and a method of transferring heat from the reactor core to the electricity generating systems. Moderation of the neutron energy is necessary as lower energy neutrons (thermal neutrons) have a much higher probability of fissioning the fissile fuel nucleus, and a lower probability of being captured by non-fissile isotopes (chiefly ^{238}U), allowing for the nuclear chain reaction to continue.

For example, the current UK nuclear fleet consists of 14 advanced gas-cooled reactors (AGR) and a single pressurised water reactor (PWR). AGR systems utilise high purity graphite as the neutron moderator; PWR, high pressure light water (*i.e.* non-deuterated water, H_2O). For transferring heat from the reactor core to boilers, AGR designs utilise gaseous CO_2, whilst PWR reactors use the same light water that acts as a neutron moderator. Modern reactor designs use closed cooling loops with heat exchangers to allow for transfer of heat, but not chemical species, away from the reactor core, where it can then be used to generate electricity (commonly by a system of boilers and turbines).

Nuclear fuels for civilian power generation in use around the world utilise U as their main fuel material, usually in the form of low-enriched U (LEU), with 3-5% ^{235}U present as the fissile species (the remainder, ^{238}U, is only efficiently fissionable by fast neutrons). Alternative nuclear fuels include ^{232}Th species (though not fissile itself, fissile species can be bred by irradiation with neutrons) and mixed oxide fuels (MOX, a blended mix of UO_2 and recycled PuO_2). MOX fuels can be utilised in some modern reactors as a replacement for LEU, and will be discussed further below.

Currently, the majority of operating power plants around the world utilise fuels of U oxides; however, historically in the UK much of the nuclear fleet was made up of Magnox reactors, utilising metallic U fuels clad in Mg alloy, with graphite moderators and pressurised CO_2 coolants. Though the last of the UK's Magnox fleet was shut down in 2015, the wastes generated remain.

1.1.3 Nuclear waste materials and classifications

As the fission chain reaction continues, the starting fissile species (^{235}U in modern civilian nuclear power reactors) is depleted, and the fission products (those daughter nuclei mentioned

above, see Figure 1) begin to form a significant fraction of the fuel material (commonly 3-5% by weight, depending on initial fuel composition and overall fuel burnup). It should be noted that the driving force behind nuclear fuel replacement is not the depletion of fissile species, but the build-up of fission products (and their decay products), some of which act as neutron poisons preventing the nuclear chain reaction by absorbing a significant fraction of the neutrons produced during the reaction (particularly ^{135}Xe and ^{149}Sm).

The fission products present in spent nuclear fuels include elements from much of the periodic table, though much of the yield is concentrated in the two groups seen in Figure 1: lighter elements including Sr, Zr, Tc, Mo, Rh, Ru, Pd; and heavier elements including I, Xe, Ba, Cs, La, Ce, Sm. It should be noted that the majority of daughter nuclei produced are themselves unstable isotopes, and will undergo further radioactive decay(s). Other species present in spent fuels are the result of neutron capture processes, rather than fission, and include various isotopes of Pu as well as many isotopes of the minor actinides (*i.e.* those actinides other than U and Pu). The complex chemistry and heterogeneous nature of spent nuclear fuels means that, depending on the final destination of the fuel material, chemical separations are necessary, see Section 1.2.1.

Considering the whole nuclear fuel cycle, including post-separation fuel materials, an extremely varied range of wastes are produced. These include obvious categories such as the fission products, minor actinides, fuel cladding materials, *etc.*; but also more indirect wastestreams such as ion exchange resins, damaged or otherwise degraded fuel materials unsuitable for reuse, and other contaminated materials (*e.g.* personal protective equipment, building materials, *etc*). These wastes are often categorised into high, intermediate, and low level wastes, though the exact definitions vary between countries and organisations. See Figure 2 for a breakdown of the UK waste volumes and masses of the below categories.

The current UK Nuclear Decommissioning Authority (NDA, part of Her Majesty's Government of the United Kingdom, HMG) definitions are as follows:

- High level wastes (HLW) are those that generate significant heat as a result of their radioactivity (*e.g.* fission products, minor actinides).
- Intermediate level wastes (ILW) are waste that has sufficient radioactivity to not be classed as LLW, but is not significantly heat generating (*e.g.* neutron activated steel and graphite).
- Low level wastes (LLW) are wastes with a total radioactivity of less than 5 GBq alpha activity or 12 GBq beta/gamma activity.
- Very low level waste (VLLW) is a sub-category of LLW that has low enough overall activity to be disposed of in conventional landfill sites (*e.g.* rubble and soil from nuclear sites).

It must be noted that HMG considers both spent fuel materials and the separated (or separable) Pu, U, and transuranics as neither waste materials, nor valued assets; instead they are seen as zero-value assets (though of possible future use). This has led the UK to have the world's largest

stockpile of civil separated Pu (see Table 1). The current NDA strategy is to reuse Pu in MOX fuels (see below, Section 1.2.2), though currently no UK electricity-producing reactors are licensed to use MOX fuels.

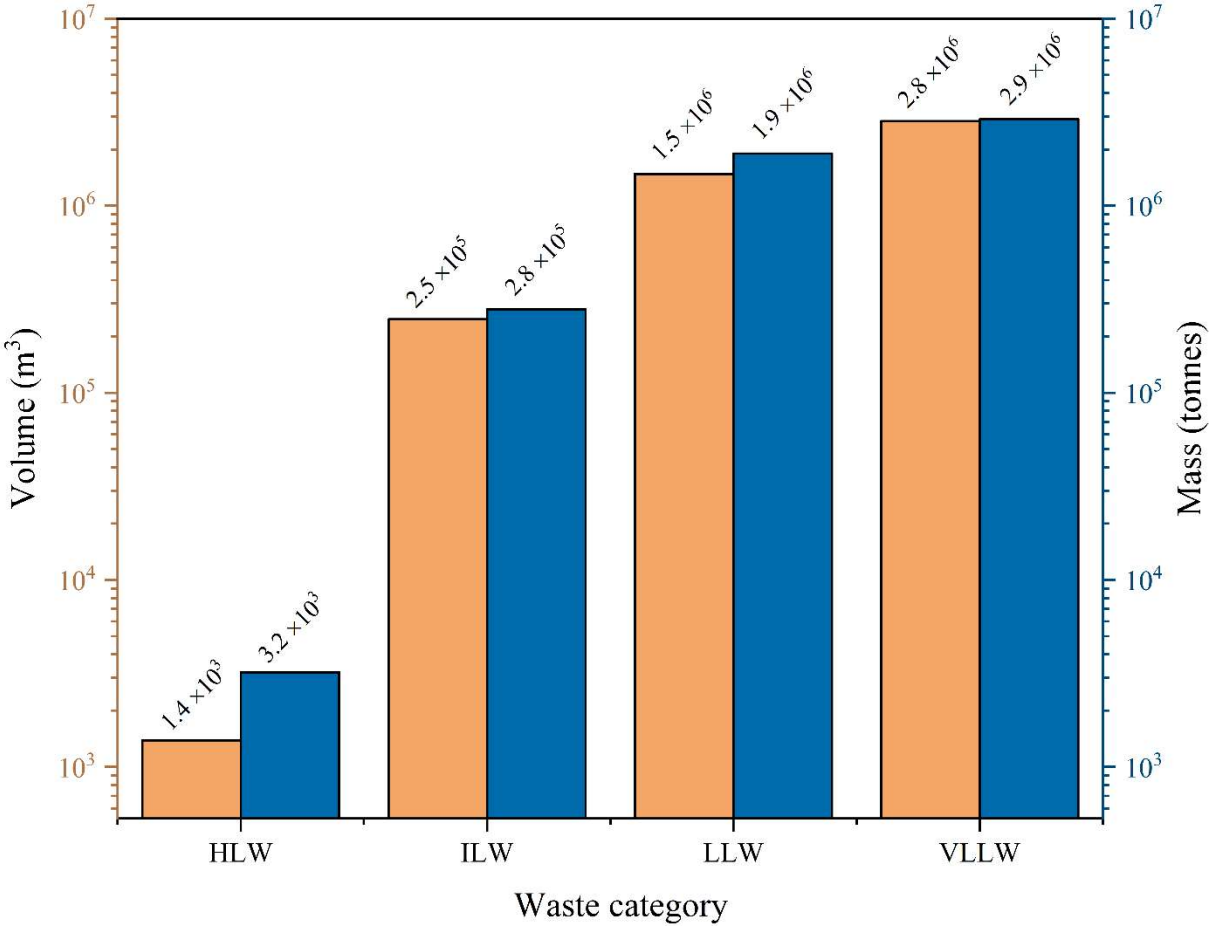

Figure 2: Reported waste volumes (orange) and masses (blue) for the four categories of radioactive waste, note the logarithmic scale. Data from the 2019 United Kingdom Radioactive Waste and Materials Inventory.[9]

1.2 Nuclear waste processing and disposal

1.2.1 Processing of spent fuels

Once fuel rods are no longer suitable for power generation, usually due to accumulation of high neutron cross section fission products, they are removed from the reactor. When first removed, the fuel activity is particularly high due to decay of short-lived fission and neutron activation products. In most power stations the spent fuel is stored in ponds for several months, with circulating (light) water acting as both radiation shielding and coolant.

After the initial period of wet storage, the spent fuel can then be reprocessed. In most countries (including the UK) reprocessing takes place in one or more centralised facilities, often close to large mid- or long-term stores. The fuel is transported in specialised casks to ensure no radionuclides would be released in the case of a road or rail accident. Before chemical separations

take place, the fuel cladding is removed for separate processing, and, in some cases, the fuel itself is mechanically broken up.

Where the spent fuel is not to be directly disposed of, chemical separations are performed to extract the remaining fuel species (the spent fuel still contains over 95% of the original ^{238}U content). The most common industrial extraction method is the PUREX process (Plutonium Uranium Reduction Extraction, occasionally Plutonium Uranium Recovery by Extraction), which will be briefly described here (see Figure 3).[10,11]

First, the de-clad spent fuel is dissolved in concentrated nitric acid (approximately 7 M) and the solution filtered to remove solids to prevent colloid formation. An organic solution of tributyl phosphate (TBP) in kerosene is then added, with U and Pu forming nitrate-TBP complexes in the organic phase. The aqueous phase containing nitrate complexes of the fission products and minor actinides (often called PUREX raffinate or HAL, high-activity liquor) is then removed for further treatment, and eventual disposal. Separation of U and Pu is achieved by the addition of an aqueous reductant solution, reducing Pu^{4+} to Pu^{3+}, which exhibits high aqueous solubility and is partitioned into the aqueous phase. After partitioning of U and Pu, the actinides can then be extracted from the solutions.

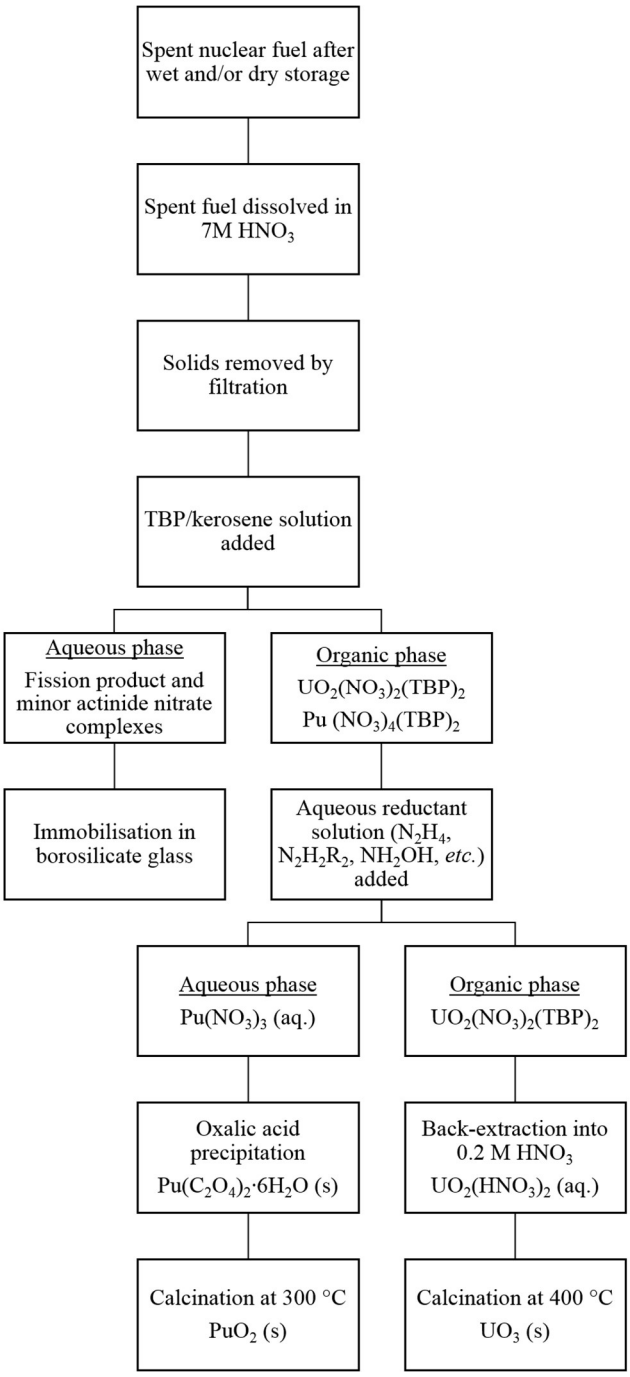

Figure 3: Process flowsheet of a simplified PUREX-type process, showing U and Pu speciation at select stages.

In addition to the established PUREX process there are many other reprocessing strategies. Many of these methods are based on a modified PUREX process,[12] including: UREX, where Pu and Np are not partitioned from U to further prevent Pu proliferation; and TRUEX, where transuranics (particularly Am and Cm) are also extracted from the raffinate. Other processes do not utilise chemical oxidants or reductants, instead relying on electrorefining techniques to separate species. Much of the work on alternative processes has been focussed on extracting both actinides and lanthanides from the spent fuel, lowering both the waste volume and waste activity of the raffinate (or equivalent for non-solution phase processes). Of particular note are pyroprocessing

techniques, where the spent fuel is dissolved in a molten salt eutectic and separation achieved by electrorefining. Pyroprocessing wastes are commonly in the form of chloride salts of fission products/minor actinides, which are not compatible with the majority of common wasteform materials (including standard borosilicate glasses).[13,14]

1.2.2 Recycling and reuse of U and Pu

One of the most important wastestreams is that of spent fuel materials, consisting mainly of the U fuel species (primarily UO_2), but also containing up to 5% by weight of fission products and Pu. As mentioned previously, the strategy currently favoured by HMG is the reprocessing of spent fuels, attempting to maximise the usage of all species in a near-closed fuel cycle.[15] This includes reuse of the separated Pu in MOX fuels.

The blending and use of PuO_2 within a bulk of UO_2 (from natural, reprocessed, or depleted sources) can be done to form a fuel material similar in behaviour to a standard low enrichment UO_2 fuel, called mixed oxide fuel, MOX. The PuO_2 content can vary from 1.5% to 30% by weight, depending on the isotopic composition of the UO_2 and PuO_2 feedstocks, and the design of the reactor within which it will be burnt. MOX fuels can be used in both thermal and fast reactors, but only in fast reactors are they efficiently fissionable past the first or second cycle of reprocessing.[16] Each subsequent cycle of reprocessing and burn-up increases the amount of energy output by the original U ores, making it a valuable process in terms of sustainability and longevity. It should be noted that as MOX fuels are repeatedly used for energy generation and reprocessed the Pu isotopic composition changes, with a decrease in ^{239}Pu content (which is fissionable in both thermal and fast reactors) and a corresponding increase in ^{240}Pu and ^{242}Pu contents (which are only efficiently fissionable in fast reactors).

Although MOX fuels seem to be an attractive use of separated Pu (both civil and military), they are not without drawbacks. Foremost for the British stockpile is that currently no power plant in the UK is licensed to burn MOX fuel, and it would take an extended period of time before new reactors could be commissioned or current reactors licensed for this purpose. Further to this, and as noted above, multiple cycles of reprocessing of MOX fuels are only useful when the fuel is to be used in fast reactors, which the current UK nuclear fleet does not include. A more pragmatic issue comes with the problem that not all MOX fuel will be suitable, whether due to becoming damaged during production or becoming harder to handle over time (caused by production of ^{241}Am from decay of ^{241}Pu), making them unsuitable for further processing or energy production. It is clear that even if the nuclear fuel cycle is close to “closed”, some amount of high-actinide content material must be disposed of, and high performance wasteform materials will be required.

Table 1: Amount of civil separated plutonium held in the UK, as of 31st December 2018.[17]

British civil holdings of separated plutonium	Amount (t)
Unirradiated separated plutonium in stores at reprocessing plants	134.8
Unirradiated separated plutonium in the course of manufacturing	0.7
Plutonium contained in unirradiated MOX fuels	2.0
Unirradiated separated plutonium held elsewhere	1.4
Total held	138.9
Amount of total belonging to foreign bodies	23.1

1.2.3 Long-term disposal of radioactive wastes

Depending on the nature of the radionuclides in the waste, it may be necessary to ensure no significant radioactive release is possible for hundreds, thousands, or even (for particularly long-lived wastes) hundreds of thousands of years, so suitable disposal strategies are an essential part of the overall nuclear power cycle. There have been many different strategies proposed, but the consensus opinion in the international nuclear community is the emplacement of wastes in an end-of-life geological disposal facility (GDF) with no planned retrieval of material. The location and engineering requirements of a (GDF) are complex, and will only be discussed here in brief, in an attempt to provide context for what may be the final resting place of many wasteform materials.

First and foremost is the site selection of a GDF. This includes the natural geology of the proposed site (*e.g.* utilising natural geologies less permeable to water, particularly clays), and is also affected by the proposed depth of the GDF, commonly in the range of 100 to 1000 metres. Present and future hydrogeology (the distribution and movement of groundwater) is also an important factor, even if the GDF and wastes are initially impermeable to water. In addition to site selection, many further challenges are associated with the materials proposed to be utilised. This includes the choice of wasteform materials (or direct disposal of spent or reprocessed fuels), cask materials and design, backfill materials (commonly clays and/or cements), and many more.

Figure 4: KBS-3 HLW GDF cask design, showing the multi-layer structure of the proposed cask. Zircaloy-clad spent fuel bundles are held within cast iron canisters (right), which are in turn encapsulated in copper canisters (right). Image is in the public domain.[18]

Other less developed options for long-term waste disposal have been proposed, but all include obvious safety issues that, with contemporary technologies at least, preclude their use. They include: space disposal of wastes in low Earth orbit, high Earth orbit, or on the surface of the moon (current space launch technologies are unreliable, with a failed launch having the possibility of spreading radioactive material over a significant area); disposal in one of the many ultra-deep ocean floor trenches (though with no control over water ingress/egress); or tectonic subduction zone disposal, where one tectonic plate descends below another.

2 Literature Review

2.1 Introduction to wasteform materials

2.1.1 Desirable material properties

To assist in the review of current and previous wasteform materials, a brief description of desirable material properties for high actinide wasteforms will be given here.

The amount of waste per volume or mass (the waste loading) of the material is of particular importance when considering geodisposal: the higher the final waste volume, the larger or more numerous the GDF(s) must be. Of particular importance to high actinide content wastes is the prevention of criticality, where fissile isotopes must be sufficiently diluted throughout the final wasteform or additional neutron absorbing species introduced. So long as criticality is prevented, waste loading is of lesser importance for HLW materials compared to LLW materials, where the volume of waste is much greater than the volume of radioactive material held within it.

The long-term durability of the wasteform must also be sufficient to reliably immobilise the contained radionuclides over the desired timescale. Wasteform durability for high actinide materials must be considered in three different ways: aqueous durability, radiation tolerance, and proliferation resistance.

Although many of the siting and engineering concerns for a GDF are aimed at preventing water ingress, for the sake of a strong safety case it must be assumed that water will eventually reach not only the GDF, but also the wasteform material itself. This means that the wasteform material must be highly resistant to aqueous leaching, preventing radionuclide release.

Particularly for HLW, the radiation tolerance of the wasteform material must be examined to ensure that the material will be stable over its lifetime, despite containing highly radioactive species. Radiation-induced phase changes (from crystalline to amorphous, or *vice versa*) may result in a material with drastically lowered aqueous durability, or have no significant effect on the material properties, so must be well understood before the material is to be used as a wasteform.

Proliferation resistance is the ability of the wasteform to resist purposeful extraction of fissile species. It is only relevant for wastes containing a high fraction of actinides, particularly Pu, and must be considered in tandem with other factors (*e.g.* geographical location of a GDF may act as more of a deterrent to proliferation than the wasteform material).

2.1.2 Benefits of natural analogues

In the search for candidate ceramic wasteforms, the examination of various mineral systems is often used as a basis to suggest ceramic systems. Generally, modelling a ceramic on a natural analogue has many advantages: they tend to be well-characterised, aged samples are often available, and their continued existence alone suggests a certain level of chemical and thermodynamic stability. In addition, the data relating to the natural analogue of a proposed candidate wasteform can be used alongside the data gathered from anthropogenic samples when examining the material properties of a chosen wasteform.

The past work of geologists, mineralogists and crystallographers mean that there is a wealth of useful information on natural minerals that can be used as a basis for further research, if the synthetic analogue is promising. In a similar vein, many minerals that have been investigated as a source of an in-demand species (for example, U from brannerites) will have had their leaching, dissolution and other behaviour characterised whilst being considered as a possible minable asset. Natural analogues are also a powerful tool when demonstrating wasteforms or other disposal methods to non-technical audiences, as they are an understandable illustration of real-life properties.[19,20]

2.1.3 Natural brannerites

Named for Prof. J. C. Branner, the brannerite family of minerals is widespread, with natural samples of the eponymous U brannerite (ideally UTi_2O_6) found around the world; including Binntal, Switzerland; Ontario, Canada; Idaho & California, USA; Sierra Albarrana, Spain; Crocker's Well, Australia; Western Province, Zambia; Bou Azzer, Morocco; Bourg d'Oisans, France; and many others.[21–27] Brannerite is not the worldwide preferred source of U, but is a minor component of many ores currently being processed, and is the main U mineral in ores mined in the Elliot lake region of Ontario, Canada.[22] Currently the main natural source of U is pitchblende (largely UO_2), but as easily processed ores become scarce, more refractory ores must be used (brannerite is the most abundant of these) and as a result much research has been done on the extraction of U from brannerites.

Like many minerals containing large amounts of radioactive species, natural samples of brannerite tend to have some degree of metamictisation (a geological term used to describe minerals that have undergone extensive radiation induced damage, causing them to become amorphous, see Figure 5). Although it may seem that this amorphisation would lead to loss of large amounts of U, this is not the case, with all but the oldest samples of brannerite retaining the majority of their inventory.[21,25,27–29] This is clearly a desirable behaviour for a long-term wasteform, as the long retention lifetime of the immobilised species is one of the most important properties of a wasteform. Many investigations have been done using recrystallised natural brannerites, especially before reliable syntheses were found (in older literature the product of this recrystallisation is often referred to as "ignited" brannerite).

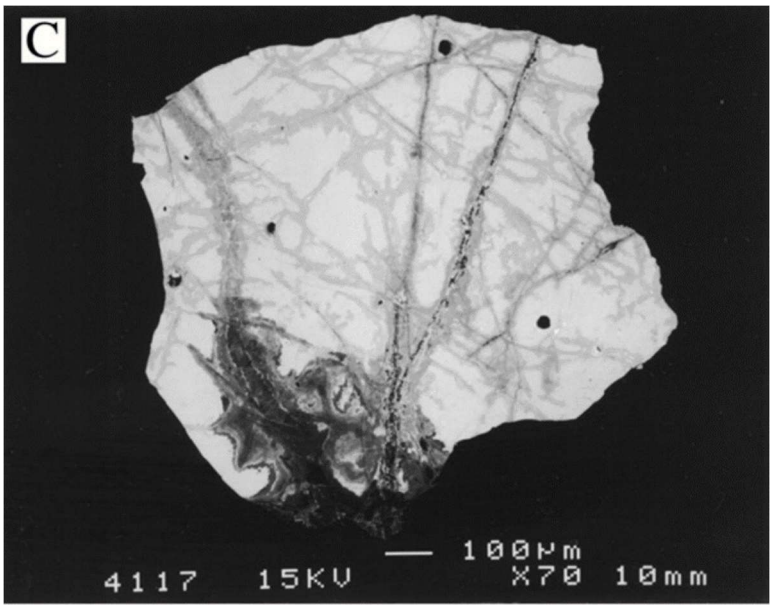

Figure 5: SEM micrograph of a sample of natural brannerite (over 100 million years old) from Sierra Albarrana, Spain, showing partial amorphisation and dissolution (darker colouration) around cracks.[25]

2.2 Current candidate wasteform materials

When investigating a material that is proposed as a possible nuclear wasteform, it is important to understand the other current and proposed wasteform materials, so as to present a fair assessment of the advantages and disadvantages the new material may have. The following sections will outline the most important and well-studied wasteforms for HLW, with a focus on U and Pu immobilisation.

2.3 Vitreous wasteforms

2.3.1 Borosilicate glasses

Currently HLW (mainly consisting of fission products and minor actinides) is disposed of by vitrification in borosilicate glasses, with modern formulations developed and beginning production in the 1980s. They have since been widely-studied, and are currently utilised in several countries (including France, UK, USA, China, Japan, and Russia). There are a few important reasons borosilicate-based glasses continue to be used as wasteforms: relatively low processing temperature, and high waste loading, chemical flexibility and aqueous durability, all of which are necessary for an HLW wasteform. To a lesser extent, the simple processing route using established infrastructure is also important, and must be taken into account when considering the suitability of glassy wasteforms.

Unfortunately, borosilicate glasses are not a fully optimised solution. The solubility of actinides and platinoids tends to be low, resulting in a high waste volume (compared to high actinide content ceramics) and making them poor wasteforms for high U and Pu content wastes.[30–33] The high processing temperature required (although lower than that required for pure vitreous silica) can

result in volatilisation of some wastestream species, including Cs, Ru, and Tc. It must also be noted that glasses are not thermodynamically stable, with crystallisation prevented by kinetic considerations only.

An important benefit of vitreous wasteforms is the simplicity of their processing. There are three main processes currently in use, but all use a similar philosophy: a continuous production process where the waste passes through a rotary calciner, before being combined with glass frit within a melter, whilst portions of molten glass are fed into separate storage containers through a valve. This continuous operation is excellent for largescale production of an HLW wasteform, as it removes the need for unnecessarily complex processes and minimises equipment-waste contact.[34]

The major differences between the three currently used processes are the design and operation of the melter. France and UK use inductively heated Inconel furnaces (this is also known as Atelier de Vitrification Marcoule, or the AVM process), which are significantly corroded over time by the melt (see Figure 6), leading to limited furnace service lives.[35] Joule-heated ceramic melters are used in many countries (including the USA, Germany, Russia, Japan, and China), and, although the process is similar to the AVM process, a highly viscous layer of glass forms on the walls of the melter, protecting it from the melt.[36] Following the philosophy of the JHCM processes, cold crucible induction processes use a water-cooled induction-heated crucible, where the relatively cold walls of the crucible allow formation of a solid layer of glass, protecting the furnace and preventing contamination (cold crucible processes are operational in Russia, with many other countries commissioning future plants).[37]

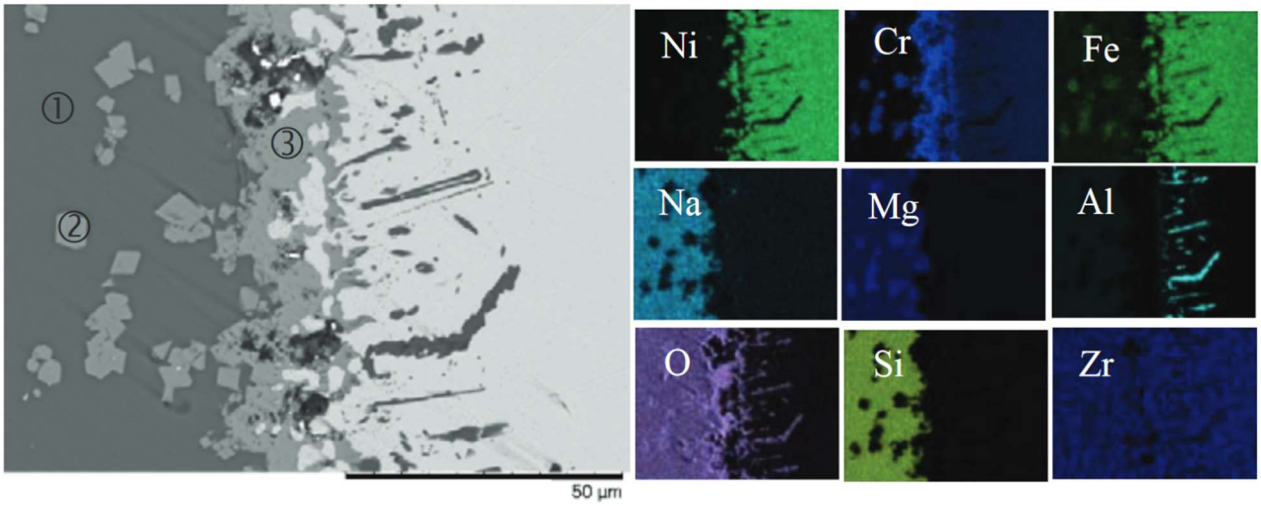

Figure 6: SEM micrograph and matching EDX maps showing elemental distributions at the interface of a simulant Magnox waste borosilicate glass (MW) and Inconel 601 piece after 14 days at 1060 °C. The region labelled 1 is glass, 2 a mixed Cr, Fe, Mg oxide, and 3 a Cr oxide.[38]

Many waste glass formulations have been proposed and utilised for vitrification of radioactive wastes, so to aid in comparisons the International Simple Glass (ISG) has been widely adopted as a common reference material. The ISG is based on the French SON68 glass, but has been simplified

to only contain six components. The physical and optical properties of the ISG are well-studied,[39–43] and reports of the aqueous durability in many different leachants are available in the literature.[41,44–46]

The current baseline UK HLW glass was originally formulated for vitrification of wastes from the UK Magnox fleet of reactors, and so is commonly referred to as the MW25 glass (25 referring to an approximate waste loading of 25% by weight). It is a highly complex glass, with over 20 components, 12 of which comprise greater than 1% by weight of the final glass.[47] The leaching behaviour of simulant MW25 glasses has been heavily investigated in the past,[48,49] with the high Mg content appearing to increase the rate of dissolution in deionised water compared to the French SON68 glass.[50] Like many alkali-borosilicate waste glasses the target waste species to be immobilised are mainly the highly active fission products, and so the actinide solubility within the glass is low, making them poor wasteforms for high actinide content wastes.

2.3.2 Phosphate glasses

Phosphate glasses were originally investigated as a possible wasteform material in the USA alongside borosilicate glasses in the 1950s. Unfortunately, although phosphate glasses have relatively low melt temperatures and high actinide solubility compared to borosilicate glasses, the melts tend to be highly corrosive and the solidified glasses have a high rate of devitrification. The devitrification of glasses can lead to the formation of crystalline phases, which may be more soluble than the bulk glass and/or lead to a less durable glass (*e.g.* the precipitation of refractory species into crystalline phases can result in a more soluble bulk glass). The addition of Pb and Fe oxides to phosphate glasses can help to remedy these problems, by further reducing the melt viscosity and preventing devitrification, but the corrosive nature of the melts makes them incompatible with the Inconel furnaces used in the AVM process (see Figure 7).[51,52]

Although work on different phosphate glasses is ongoing, they are generally not seen as attractive wasteform materials due to difficulties in large-scale processing. Russia is the only modern industrial producer of phosphate-based waste glasses, having been producing Na-Al-phosphate glass wasteforms since 1987.[53] Recent work on the application of Na-Al-(Fe)-phosphate glasses to vitrification of high U content wastes demonstrated very high U solubilities (up to 41.7% by weight UO_3) without crystallisation or any negative impact on the aqueous durability.[54–56]

A further application of phosphate waste glasses is in the immobilisation of future actinide halide wastes, from either molten salt reactors (mainly fluorides) or pyroprocessing wastes (mainly chlorides). The solubility of a mixed fluoride simulant waste (containing Cs, Sr, Zr, Ce, and Sm fluorides) in Na-Al-phosphate and Na-Al-Fe-phosphate glass has been determined, with no crystalline phases observed up to 13.8 mol.% or 8.5 mol.% respectively.[57–59] Similar studies on the addition of actinide chloride surrogates have also been performed, though the glasses produced displayed poor thermal stability.[60,61]

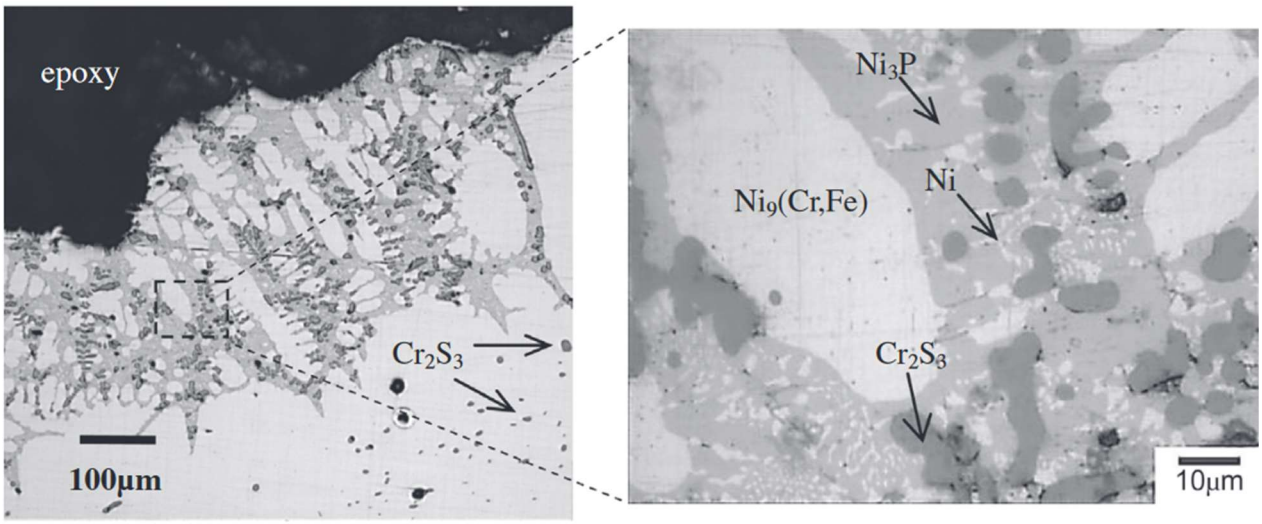

Figure 7: SEM micrographs showing the extent of surface corrosion of a piece of Inconel 693 after 7 days in an iron-phosphate melt at 1190 °C.[51]

2.3.3 Novel glass compositions

Further to the well-studied borosilicate and phosphate glasses, there have been a number of glasses suggested with more novel compositions. Erdogan *et al.* reported a binary Pb-borate glass that could contain high amounts of SrO and Cs_2O (up to 30 mol.% and 25 mol.% respectively), but performed poorly in leaching tests.[62] Investigation into high lanthanide content (up to 55% by weight) borosilicate glasses (called Löffler glasses, developed as an optical glass in the 1930s) have been done, showing them to have higher actinide waste loadings than standard borosilicate waste glasses.[63] Similar glasses have been proposed for wastestreams that contain no volatile species (such as defence PuO_2), where high melt temperatures are less of an issue.[63–65] Due to the low alkali concentrations compared to borosilicate and phosphate glasses, the chemical durability of Löffler glasses is significantly higher, with dissolution rates approximately 20-50 times lower than typical HLW glasses.[66–69]

2.4 Ceramic wasteforms

A huge number of different ceramic materials have been studied in the search for suitable candidate wasteforms, with many showing promise. Ceramics tend to be the most durable wasteform materials and can often achieve higher waste loadings than a vitreous wasteform; however, depending on the compositional flexibility of the material, wastestreams comprising of more than one species may not be fully compatible with the ceramic, forming secondary phases or worse, preferentially forming a different phase. This is not an issue if the secondary species in the wastestream can be contained within the crystal structure of the ceramic, whether as interstitials or as dopant species, but this is not possible for many systems and must be overcome in a different way (such as purifying the wastestream to remove these secondary species, use of a multiphase ceramic, or addition of a glass phase).

2.4.1 Pyrochlores

The pyrochlore structure, commonly represented as $A_2B_2X_6Y$ where A and B are metal cations, and X and Y are anions, is an anion-deficient sub-type of the fluorite structure (AX_2). The A cation is coordinated to 8 anions, and the B cation to 6. The A cation is commonly REE^{3+} or An^{3+}, with common B cations including Ti, Zr, Sn, Hf, and other M^{4+} cations. The structure can be described as two edge-sharing interpenetrating networks: one of (BO_6) octahedra, the other of (AO_8) cubes. The compositional flexibility of pyrochlores, and their high compatibility with actinide ions, has led to much interest as candidate host materials for high U and Pu content wastes.

Titanate pyrochlores are very well-studied, especially with regards to their durability and compositional flexibility. The majority phase of the Synroc-F and Synroc-FA formulations is betafite, $CaUTi_2O_7$, a sub-type of the pyrochlore structural family (derived from full substitution of M^{3+} in the pyrochlore $M_2Ti_2O_7$ for U^{4+} and Ca^{2+}), with other substituted pyrochlores formed by the M^{3+} species present in the wastestream (for example, Sm, Eu, Gd, Am, and Cm would all be expected to form one or more pyrochlore-structured products).[70,71] The leach resistance of a ceramic containing a majority of this pyrochlore has been tested, and found to be extremely high, as expected, with a 'U'-shaped relationship to pH (minimum at a pH of ~8).[72] The same $CaUTi_2O_7$ containing ceramic has also been examined using the PCT method (a static leaching test), and was found to have a very low rate of leaching.[73] As is observed for many titanate ceramics, leaching tends to be incongruent, with higher rates of non-Ti cations (leaving material enriched in Ti, see Figure 8), although this can vary with composition and pH.[74]

The durabilities of many other pyrochlores have also been examined, and generally found to be higher than a representative borosilicate waste glass.[75–78] The waste loadings of pyrochlores are also remarkably high compared to waste glasses, with $CaUTi_2O_7$ having a U loading of 49% by weight if stoichiometric. Extensive research has also been performed on natural U and Th containing pyrochlores, and their longevity and durability supports the suitability of pyrochlore-based wasteforms.[79–87]

The radiation damage of titanate pyrochlores has been extensively studied, with both natural and synthetic samples having been examined. For example, two different synthetic pyrochlores were found to have become amorphous over time when doped with Cm on the A-site: $(Nd_{0.85}Cm_{0.15})_2(Ti_{0.65}Zr_{0.35})_2O_7$ and $(Gd,Cm)_2Ti_2O_7$.[88,89] The aqueous durability of the damaged ceramics was found to have decreased drastically with respect to the amount of Cm leached (20 to 50 times higher leach rates when compared to undamaged samples).[90–92] There are many other reports of the effect of self-irradiation of doped titanate and zirconate-titanate pyrochlore ceramics,[87,93–98] as well as studies that have irradiated pyrochlore substrates with focussed beams of heavy[99–102] and light[97,103,104] ions, computational studies on the effect of radiation damage,[105,106] and qualitative studies examining actinide-containing natural mineral analogues of pyrochlores.[85,86,107]

Figure 8: HRTEM micrograph showing the surface of a sample of the mixed pyrochlore/zirconolite $Ca(U_{0.5}Ce_{0.25}Hf_{0.25})Ti_2O_7$, leached at pH 4 for 835 days, in a single pass flow-through (SPFT) experiment. The lighter region marked A is an amorphous Ti- and Hf-rich alteration layer at the surface.[74]

Zirconate pyrochlores (for example, $Gd_2Zr_2O_7$ and $Nd_2Zr_2O_7$) and mixed titanate/zirconate pyrochlores (for example the series $Gd_2(Ti_{2-x}Zr_x)O_7$) have been shown to be extremely resistant to radiation damage.[108–110] This makes them good candidates for long-term immobilisation of Pu, as the final wasteform must resist a relatively high flux of internal radiation over a long period of time. Some high Zr content pyrochlores have proven to be fully resistant to radiation, with no amorphisation being induced even when irradiated at extremely low temperatures (where damage recovery mechanisms are significantly slowed).[109,110]

It has been suggested that the radiation resistance of zirconate pyrochlores is due to effects stemming from cation disorder within the structure. Despite high processing temperatures, perfect cation homogeneity does not occur for zirconate pyrochlores, even after extended time at temperature. This means that the transition from pyrochlore ($A_2B_2O_7$) to defect fluorite ($(A,B)_4O_7$) occurs relatively easily when the material is heated or irradiated (both of which introduce extra disorder into the structure). This effect has been suggested as the origin of their resistance to radiation induced amorphisation, as the pyrochlore structure preferentially transitions to the defect fluorite structure rather than becoming amorphous (see Figure 9, note the much lower critical temperatures of recovery compared to those of titanate pyrochlores).

Although not as well-studied as the titanate analogues, zirconate pyrochlores have also shown to be highly resistant to aqueous leaching, with leach rates of both Zr and A-site species comparable to analogous titanate compositions.[111–113] Suggested structures with high radiation resistance and the ability to incorporate actinides include $La_2Zr_2O_7$,[111,112] $Er_2Zr_2O_7$,[114] and the mixed titanate/zirconate series $Gd_2(Ti_{2-x}Zr_x)O_7$ with x between 0 and 1.5.[108,115]

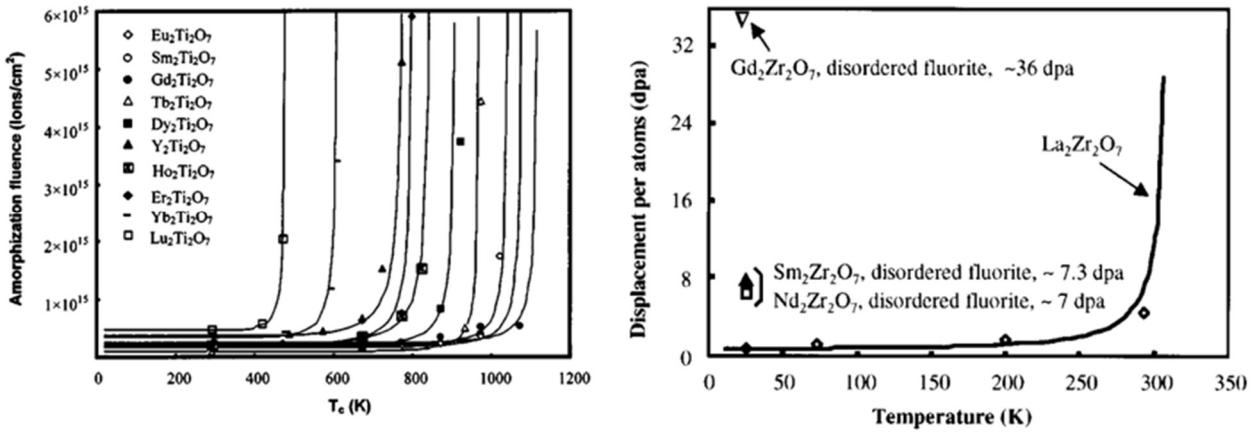

Figure 9: Graphs showing the relationship between temperature and critical amorphisation fluence (left, ions/cm^2), or irradiation (right, dpa) for titanate pyrochlores (left)[116] and zirconate pyrochlores (right),[117] note the different temperature scales.

2.4.2 Zirconolite

The zirconolite ($CaBTi_2O_7$, B is Hf^{4+}, Zr^{4+}, *etc*.) structure is also derived from an anion-deficient fluorite structure, and so is closely related to the pyrochlore structure. In zirconolite the HTB layers are perpendicular to the (001) plane, with ordered layers of mixed Ca (8-coordinate) and B (7-coordinate) site cations interspersed. The zirconolite structure crystallises in various polytypes depending on different cation substitutions. The most important polytypes when considering immobilisation of actinides are the 2M polytype, forming at (near) nominal stoichiometry, 4M forming with high amounts of REE or actinides, and 3T forming near the solid solubility limit of REE or actinides.

In the UK zirconolite has been identified as the most favourable candidate ceramic material (whether single phase, multiphase or as part of a glass-ceramic) for immobilisation of high Pu content residues (and/or Pu stockpile materials), due to its reasonable waste loading, high durability, and reasonable flexibility with regards to cation content (due to the 3 differently sized cation sites available). The fully substituted materials $CaUTi_2O_7$ and $CaPuTi_2O_7$ form as a cubic pyrochlore phase,[70,71,73,118] so work has been focussed on forming materials with high actinide content, but that retain the zirconolite structure. Pu incorporation into zirconolite depends on the oxidation state of Pu (which is controlled by processing atmosphere), and on the mechanisms of charge compensation available, and can occur on both the Ca and B-cation sites.

Materials with Pu^{4+} and/or U^{4+} substituting for Zr^{4+} have been produced, with many studies examining the amount of actinide substitution that can occur before 4M zirconolite is produced. Begg *et al.* found that up to 0.15 formula units of Pu^{4+} can be added with the structure retaining the 2M polytype,[119] which is in good agreement with later studies that found the same limit when substituting U^{4+} for Zr^{4+}.[120]

Zirconolite ceramics have been prepared with Pu^{4+} substitution onto the Ca site (with charge balancing by substitution of two Fe^{3+} onto the Ti site for each Pu^{4+}), with near single phase 2M zirconolite forming up to 0.3 formula units of Pu, and 3T zirconolite forming from 0.3 to 0.4 formula units of Pu.[121] This is in good agreement with previous studies where Ce^{4+} or U^{4+} were used as a simulant for Pu^{4+}, where the 2M polytype was found to be stable up to 0.15 formula units Pu, with Al^{3+} charge balancing,[122] or 0.5 formula units with Fe^{3+} charge balancing.[121]

The radiation resistance (both self- and beam-irradiated) of zirconolites has been extensively tested. They have been found to be highly resistant to self-irradiation, with some needing 1.3×10^{25} αm^{-3} to fully amorphise.[118,123,124] Ion beam irradiation has also been examined, using [Xe^{+}],[125] [Kr^{+}],[125–128] [Ar^{+}],[125] and [He^{+}],[128] with all studies finding them to be highly resistant to radiation damage, comparable to titanate pyrochlores.

2.5 Synthetic brannerites

An overview of brannerites, both natural and synthetic, will be given next. Much of the literature discussion for U brannerite is in the context of mining and mineralogy, but as explained above, information pertinent to the use of brannerite as a wasteform can be extracted. Although the focus will be on UTi_2O_6, the Ce and Th analogues ($CeTi_2O_6$ and $ThTi_2O_6$ respectively) share much of the same chemistry.

2.5.1 The brannerite structure

The brannerite structure (ATi_2O_6, space group *C2/m*(12), see Figure 10) is formed of corrugated sheets of edge-sharing (TiO_6) distorted octahedra connected by chains of (AO_6) octahedra parallel to the *b*-axis. The structure of the (TiO_6) sheets is complex, and they are often simply referred to as ‘anatase-type’ sheets. The sheets are formed of edge-sharing two-wide ‘zig-zag’ chains of (TiO_6) octahedra parallel to the *b*-axis, which are then connected to neighbouring chains by further edge-sharing parallel to the *a*-axis; with individual sheets connected to their neighbours by the (AO_6) octahedra.

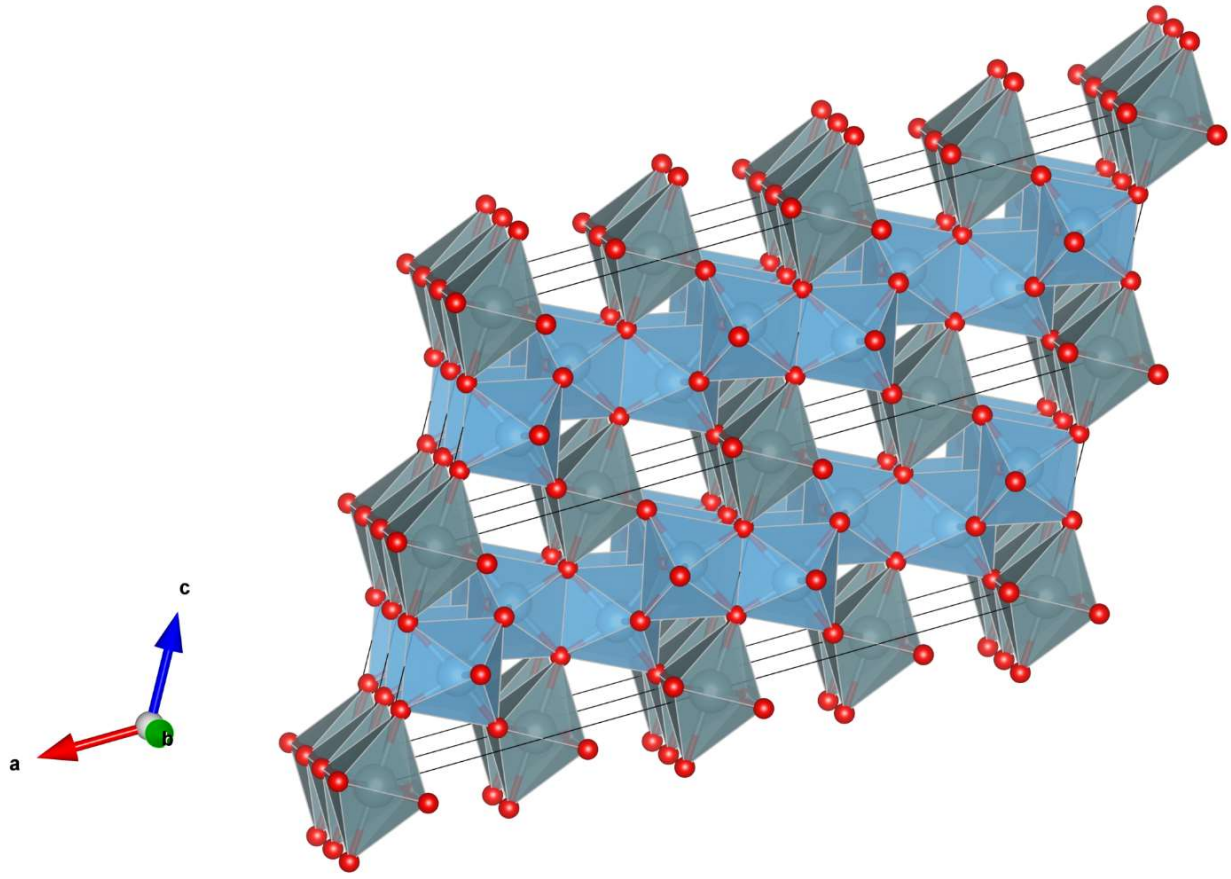

Figure 10: A polyhedral representation of UTi_2O_6, using the crystallographic information from Szymanski and Scott.[129] Blue represents the (TiO_6) octahedra, grey the (UO_6) octahedra, and red the locations of O atoms. The diagram shows a 2×2×2 unit cell ensemble. Produced in the VESTA software package.[130]

2.5.2 Preparation of synthetic UTi_2O_6

The first laboratory preparation of UTi_2O_6 was in 1959 by Kaiman[131] (a concurrent investigation by Patchett and Nuffield yielded similar results[26]). At that time brannerite was not well understood, with many researchers supposing it was a product of some reaction occurring when the amorphous mineral was heated to recrystallise. Both of these early investigations found that UTi_2O_6 was not formed when stoichiometric proportions of TiO_2 and various U oxides were heated in air to 1000 °C, with the only products being the component oxides. When stoichiometric amounts of the oxides were heated in Ar to 1400 °C, brannerite was formed as the major product.

The failure of the air atmosphere syntheses is now understood to be because of the oxidation of U past the U^{4+} that is required for stoichiometric UTi_2O_6. Since these first syntheses, much more research has been done to investigate the stability and solid state syntheses of brannerites, both in inert atmospheres and in O_2-containing atmospheres, as well as various solution-based syntheses.

The general outcome of this research is that the ceramic synthesis of brannerite in air requires a lower oxidation state dopant substituting onto the U site, to stabilise the higher U oxidation states, whilst still allowing formation of the brannerite structure. These commonly take the form of Ca^{2+}, Y^{3+} or REE^{3+}. Synthesis of undoped brannerites involve either an inert atmosphere as mentioned

above, a mildly reducing atmosphere (for example 5% H_2 in 95% N_2 or 5% CO in 95% CO_2),[132] or reacting in a sealed or semi-sealed vessel (hot-pressing in a graphite die[133,134] or sealed stainless steel bellows[135]). It is also common for a small amount of Ti metal (often 2% by weight), to act as a sacrificial material, optimising the redox conditions for retention of U^{4+} during sintering.

Various solution-based methods are commonly used in the synthesis of both pure and doped UTi_2O_6, and confer all the usual benefits of wet chemistry ceramic syntheses (true homogeneous mixing, better control over redox behaviour, quicker synthesis, finer powders, *etc*.). There have been many different syntheses, utilising many different precursors for both U and Ti, including Ti hydroxide, alkoxides and sulphates, and U hydroxide, nitrates and acetates.[135–138]

The most common solution-based method of producing UTi_2O_6 is the alkoxide/nitrate route, starting from Ti isopropoxide ($Ti(OPr^i)_4$) and uranyl nitrate ($UO_2(NO_3)_2{\cdot}nH_2O$). An example synthetic route is as follows: an aqueous solution of uranyl nitrate is mixed with stoichiometric amounts of Ti isopropoxide until homogeneous, before drying (variously around 110 °C) and calcining (under a reducing atmosphere if a U^{4+} phase is desired, commonly at 700-750 °C) to form a mixed U/Ti precursor. This precursor must then be heated to form brannerite proper, with the lower temperature limit of formation often quoted as 1200 °C. If dopants are desired within the product brannerite, they may be easily added into the solution as a nitrate (such as Y, Fe, Gd, Pu, Th, Ca[139–142]), or other water soluble salt. To form a dense ceramic body, the produced powder must then be milled, pelletised, and sintered.

2.5.3 Preparation of $CeTi_2O_6$

Ce and U chemistry are often similar, however, in the case of brannerites, the lack of higher oxidation states of Ce means that it does not experience the same issue of oxidation during ceramic synthesis, but rather the opposite, as a result of the availability of the Ce^{3+} oxidation state.

The common solid state ceramic synthesis of $CeTi_2O_6$ is simple: stoichiometric mixtures of TiO_2 and CeO_2 are pelletised and reacted at high temperature (generally around 1350 °C) for an extended period of time (up to 96 hours). Due to the predisposition of the brannerite structure towards Ti-rich compositions, the stoichiometry of the product does not perfectly match the ideal formula $CeTi_2O_6$, this will be discussed later in further detail.[143]

Various sol-gel and solution-based methods have been reported for the synthesis of $CeTi_2O_6$. Sol-gel methods starting from metal chlorides[144,145] or Ce chloride with Ti isopropoxide[146,147] have been reported, mainly in the context of producing a thin film of $CeTi_2O_6$ on a Si substrate. The alkoxide/nitrate route described above can also be used, starting from a Ce nitrate and Ti isopropoxide.[148] Another similar method, a Pechini polymerisation, has been reported, where Ce nitrate and Ti isopropoxide are polymerised by citric acid and ethylene glycol, before heating to form a polymer.[149] A reverse-micelle sol-gel method has also been reported, using Triton X-114 ((1,1,3,3-tetramethylbutyl)phenyl-polyethylene glycol) as a non-ionic surfactant in cyclohexane, starting from Ce^{3+} nitrate and Ti isopropoxide.[150]

A novel aqueous synthesis has also been reported, starting from Ce^{3+} nitrate or Ce^{4+} ammonium nitrate and an aqueous solution of the water stable Ti complex Ti^{4+} bis(ammonium lactato)dihydroxide (a commercially available catalyst called Tyzor LA). The nitrate is dissolved in the Tyzor LA solution under stirring, and the mixture dried, before calcining and sintering at high temperature ($CeTi_2O_6$ formed as a major product when calcined at 800 °C or higher).[151,152]

2.5.4 Non-stoichiometry of the brannerite structure

It is common for natural and synthetic brannerites to have some A-site deficiency, whether U, Ce or Th. The U deficiency of natural brannerites is often due to partial leaching of the U content over time, producing an altered material that is enriched in Ti.

Synthetic U brannerites are sometimes reported to be non-stoichiometric, with both doped and non-doped compositions showing some degree of A-site deficiency.[132,153] The U brannerite behaves differently (compared to $CeTi_2O_6$ and $ThTi_2O_6$) with respect to these vacancies, as the U^{4+} cations can be oxidised to U^{5+} or U^{6+} for charge balance (neither Ce nor Th have available oxidation states above 4+). These two effects may well be complementary, with the variable U oxidation state stabilising the A-site deficiency and *vice versa*. The presence of U^{5+} and U^{6+} in natural and synthetic brannerites is discussed below.

Synthetic Ce brannerites also show A-site deficiency, and the exact stoichiometry of the structure has been investigated. A neutron diffraction study examining the crystal structure of $CeTi_2O_6$ (prepared by a solid state synthesis) found that the stoichiometry is more correctly described as $Ce_{1-x}Ti_2O_{6-2x}$ where x is approximately 0.025, with O vacancies occurring on the O1 site, as determined computationally.[143] The reaction mixture expected to form stoichiometric $CeTi_2O_6$ had some amount of excess CeO_2 remaining in the final product, in agreement with previous studies.[132] A later study that used a water stable Ti-complex as a starting material (Tyzor LA) also found a certain amount of Ce deficiency and excess CeO_2 in the stoichiometric reaction mixture (trace amounts of TiO_2 were found in the product of reaction stoichiometry of $CeTi_{2.1}$, approximately equivalent to $Ce_{0.952}Ti_2$).[151]

The temperature dependence of this stoichiometric relationship, as well as the effect it has on the Ce^{3+}/Ce^{4+} ratio within the brannerite product has also been investigated.[154,155] It was found that quenching the reaction material from the reaction temperature (1350 °C) led to a more O-deficient brannerite, with a higher proportion of Ce^{3+}. Samples were then annealed at different temperatures, and the O-deficiency was found to be lower, along with a reduction in the Ce^{3+}:Ce^{4+} ratio. It was proposed that this results from the temperature dependant nature of the Ce^{3+}/Ce^{4+} redox couple, with Ce^{3+} more stable at high temperature, being converted to (along with the uptake of O_2) Ce^{4+} on slow cooling or annealing at a lower temperature.[154]

This investigation shows that Ce may be a poor actinide simulant in brannerites, as oxidation states below 4+ have not been observed for U in solid oxides. Although Pu can commonly occur

as both Pu^{3+} and Pu^{4+}, the difference in redox behaviour between the Pu^{3+}/Pu^{4+} and Ce^{3+}/Ce^{4+} pairs may also affect the use of Ce as a simulant for Pu.

In brannerites consisting of only two isovalent cations (*i.e.* UTi_2O_6, $CeTi_2O_6$, *etc.*), there are two different possible mechanisms for compensation of this A-site deficiency: O deficiency (most likely on the O1 site[143]) or partial cation reduction (most likely of the Ce).[154,155] From the evidence presented in the literature it is reasonable to assume that both of these mechanisms occur in real $CeTi_2O_6$ systems, with their relative magnitude decided by cooling rate or annealing steps.

2.5.5 Uranium oxidation state in brannerites

As discussed above, the variable oxidation states of U play an important role in the stability of the structure, with natural samples exhibiting both U^{5+} and U^{6+}.

In natural brannerites, the A-site deficiency is balanced by the existence of U in higher oxidation states than U^{4+}. For example, Lumpkin *et al.* studied 12 different samples of natural brannerites, and used SEM-EDX to find estimated $U^{4+}/(U^{5+}+U^{6+})$ ratios from 0.14 to 0.95, often in combination with naturally occurring lower oxidation state substituents (Ca^{2+}, Y^{3+}, Fe^{3+}, Pb^{2+}) that may play a role in stabilising these higher U oxidation states.[25] Another study investigated different methods (SEM-EDX, EELS, XPS) for determining the U oxidation state in brannerites, and detected both U^{5+} and U^{6+} by XPS (a surface sensitive technique) in synthetic brannerites (see Table 2[153]). Finnie *et al.* demonstrated that the oxidation states of U in brannerites could be examined using near-infrared diffuse reflectance spectroscopy, using XPS as a comparison. An interesting observation was found in the composition where sufficient Ca^{2+} was introduced to charge compensate 1 formula unit of U^{6+}: Ca^{2+} had partially segregated into the grain boundaries, resulting in U^{4+} species still being present in the sample within the bulk of the grains.[142]

Table 2: Average U oxidation states of a range of brannerites, as determined by stoichiometric charge balancing from compositional data (EDX), EELS, and XPS.[153]

Source	Sample	EDX	EELS	XPS
Synthetic	$Ca_{0.2}U_{0.8}Ti_2O_6$	4.58	-	4.7
Synthetic	$Th_{0.55}U_{0.3}Ca_{0.15}Ti_2O_6$	5.00	-	4.8
Synthetic	$Th_{0.7}U_{0.3}Ti_2O_6$	4.00	-	4.2
Natural	B4	5.15	4.4(3)	-
Natural	B10	5.03	4.8(3)	-
Natural	B12	4.10	4.7(1)	-

As mentioned above, the U oxidation state in synthetic brannerites can be controlled by the inclusion of various other species, to the point of stabilising air-fired samples.

Although it has long been known pure UTi_2O_6 can only be synthesised when reacted in an O_2-free atmosphere, during investigations into Synroc, a brannerite phase (which included Gd, Hf, Ca and Pu) both formed when the Synroc was fired in air and had no significant compositional

differences to the brannerite phase produced in Ar-fired Synroc.[156,157] This encouraged investigation into stabilisation of brannerite by addition of lower oxidation state cations.

In 2001 Vance *et al.* found that U brannerite can be sintered in air on inclusion of 0.2 formula units of Ca (forming $U_{0.8}Ca_{0.2}Ti_2O_6$) or 0.3 formula units of Gd (forming $U_{0.7}Gd_{0.3}Ti_2O_6$) on the A-site. The solid solution limits of other cations were also examined (Fe^{3+}, Hf^{4+}, Pu^{4+} substituting for U^{4+}, and Gd^{3+} & Nb^{5+} substituting for U^{4+} & Ti^{4+}) and the average U oxidation states in these samples were increased as a result of the addition of lower oxidation state cations.[135]

Following from this, other studies into air-stabilisation by aliovalent substitution reported similar results. James and Watson (2001) reported on Gd, Ca & La substituted U brannerites that, although sintering in Ar allows for a wider range of solid solubility, it is possible to synthesise substituted compositions in air as expected.[158] The same behaviour has also been shown by Y-doped U brannerites.[148] Studies on U brannerites doped with Gd (to charge balance and act as a neutron absorber) and Ce (as a Pu simulant) have also been reported, with the produced phase assemblages following the trend expected, depending on the processing atmosphere.[159,160]

2.5.6 Brannerite glass-ceramics

Glass-ceramics with a brannerite as the major crystalline phase were reported for both Ce and U brannerite. These materials were synthesised from two different precursor systems: pre-reacted Ce brannerite and glass, and calcined alkoxide/nitrate and glass precursors. Although both methods were reported to produce brannerite glass-ceramics, the extra processing steps necessary to produce the pre-reacted ceramic or ceramic precursors make these less than ideal syntheses for wasteform materials. It should be noted that the formation of UTi_2O_6 in a glass-ceramic composite has not previously been reported, with only U^{5+} brannerite glass-ceramic composites having been examined.

Glass-ceramics with U and mixed U/Pu (see Table 3) brannerites were investigated by Zhang *et al.*[140] The ceramic precursors were synthesised by the alkoxide/nitrate route, before calcining at 700 °C to remove volatile species. A glass precursor was produced by calcining Na_2CO_3, Al_2O_3, H_3BO_3, and SiO_2 at 550 °C. The precursors were mixed, pelletised and sintered at 1200 °C to form glass-ceramics. EDX was used to determine in which phase the actinides and lanthanides were held, and it was found that they were fully partitioned into the ceramic phases. However, some UO_2 and PuO_2 were also present in some samples, an issue that must be dealt with before these glass-ceramics are seen as suitable wasteform materials. The oxidation state of U was probed using diffuse reflectance spectroscopy (DRS), with U^{5+} determined to be the major oxidation state (as expected from the relatively high fractions of the lower oxidation state cations Y^{3+} and Gd^{3+}).

The effect of A-site substitution with charge balancing species (Y^{3+}, Ce^{3+}, and Eu^{3+}) on the structure of the brannerite ceramic phase has also been investigated (see Table 3).[161] Glass-ceramics targeting $M_{0.5}U_{0.5}Ti_2O_6$ ceramic phases were prepared using the same alkoxide/nitrate route as detailed above. Both Y and Eu samples formed ceramic phases close to the nominal

stoichiometry. Due to oxidation of Ce (from 3+ to 4+), the produced stoichiometry was identified to be $Ce_{0.65}U_{0.35}Ti_2O_6$, with Ce present in both 3+ and 4+ oxidation states. The U oxidation state was probed using both DRS and XANES, with U^{5+} dominating in all three samples.

The analogous brannerites $U_{0.5}Tb_{0.5}Ti_2O_6$ and $U_{0.5}Er_{0.5}Ti_2O_6$ has also been produced as ceramic phases within an air-fired glass-ceramic composite. As expected, DRS measurements showed U was present as U^{5+}, with no brannerite phase produced when materials of the same composition were heated under Ar.[162]

Table 3: Compositional information on the ceramic phases observed by Zhang *et al.* in U- and Pu-containing brannerite glass-ceramics[140] and charge balanced U brannerite glass-ceramics.[161]

Targeted ceramic phase	Atmosphere	Resulting ceramic phases	U oxidation state(s) inferred to be present
$Y_{0.5}U_{0.5}Ti_2O_6$	Air	$Y_{0.5}U_{0.5}Ti_2O_6$	5+
$Y_{0.25}U_{0.75}Ti_2O_6$	Air	$Y_{0.5}U_{0.5}Ti_2O_6$, UO_2 (minor)	4+/5+
$Gd_{0.2}Hf_{0.2}U_{0.4}Pu_{0.2}Ti_2O_6$	Argon	$Gd_{0.2}Pu_{0.3}U_{0.5}Ti_2O_6$ & U/PuO_2 (minor)	4+/5+
$Gd_{0.2}Hf_{0.2}U_{0.4}Pu_{0.2}Ti_2O_6$	Argon	$Gd_{0.1}Hf_{0.1}Pu_{0.2}U_{0.6}Ti_2O_6$, $CaTiSiO_5$, U/PuO_2 (minor)	Not reported
$Y_{0.5}U_{0.5}Ti_2O_6$	Air	$Y_{0.51}U_{0.49}Ti_2O_6$	5+
$Ce_{0.5}U_{0.5}Ti_2O_6$	Air	$Ce_{0.65}U_{0.35}Ti_2O_6$, TiO_2, UO_2 (trace)	5+
$Eu_{0.5}U_{0.5}Ti_2O_6$	Air	$Eu_{0.53}U_{0.47}Ti_2O_6$, TiO_2, UO_2 (trace)	5+

The changing phase assemblage of a pyrochlore glass-ceramic system has also been examined by Zhang *et al.*, with brannerite phases dominating as the U loading of the system increased (from the end members $Ln_2Ti_2O_7$ to $Ln_{0.5}U_{0.5}Ti_2O_6$, where Ln is Gd, Y).[163] The U was introduced into the system by double-substitution onto the Ln site ($2Ln^{3+}$ for U^{4+} and Ca^{2+}). In both the $Gd_2Ti_2O_7$ and $Y_2Ti_2O_7$ systems, the charge balanced brannerite $Ln_{0.5}U_{0.5}Ti_2O_6$ began to dominate at approximately 0.5 formula units of substitution, with the excess Ca being held within the glass.

It is important to note that although many of these brannerite phases have only been produced as ceramic phases within glass-ceramic composites, it is expected that the synthesis of pure ceramic brannerites with the same compositions would be facile, though with the caveat requiring higher process temperatures to form.

2.6 Leaching and dissolution of UTi_2O_6

As mentioned above, the extraction of U from natural brannerites is relatively well studied and holds some importance to the long-term behaviour of brannerite wasteforms. There have also been some reports of the leaching behaviour of synthetic brannerite ceramics and glass-ceramics, as well as multiphase ceramics containing brannerite as a constituent phase.

2.6.1 Extraction of uranium from brannerites

As noted above, brannerite has a significant role as a U-containing mineral, and as a result there has been considerable investigation into U extraction from natural brannerites.

Because of the low aqueous solubility of the U^{4+} cation, U ores are mainly leached under oxidising conditions to convert the U content to the significantly more soluble U^{6+}, and both acidic and alkaline leachant systems are common. More refractory ores (including brannerites) are generally leached using the same leachants as less durable ores, but require higher temperatures and reagent concentrations to achieve acceptable extractions.[22] This has led to investigations into more specific leaching systems for high brannerite-fraction ores, which are unfortunately less applicable to leaching of nuclear wasteforms. It is also important to note that extraction of U from natural samples will be from metamict (amorphous) brannerites, which will again make them less applicable to wasteform leaching. Because of these reasons, only the trends important to wasteform leaching will be discussed, and comparisons made between studies on natural and synthetic samples if possible.

Important comparative studies between amorphous and recrystallised samples of natural brannerite have also been done, with the recrystallised brannerites being much more resistant to a standard acidic ferric sulphate leachant than amorphous samples.[28] Zhang *et al.* studied a different natural brannerite before and after annealing and found anomalous behaviour, where the chemical durability of the recrystallised samples did not have a simple relationship with the temperature of recrystallisation.[27] It seems that during annealing some of the brannerite samples exhibited formation of other less durable phases: at higher temperatures some of the larger grains had formed an assemblage of UO_2 and glass, with only some brannerite being recrystallised.

Leaching of mineralogical brannerite is strongly temperature dependant, with some extractions being four times faster at 70 °C than at 50 °C.[164] There are many reports of large increases of U extraction over the same timeframe when temperature is increased,[164–167] although there are suggestions that this may well be due to the higher temperature and acidic conditions allowing for dissolution of the TiO_2 alteration layer.[167]

Kinetic studies on the dissolution of synthetic brannerites have also been reported, with similar findings. Charalambous *et al.* found an eight-fold increase in the amount of material leached between 50 °C and 90 °C,[138] and it has previously been found that the leaching of many U titanate wasteform materials (including brannerite) has a strong dependence on temperature.[72]

The pH dependence of U leaching from natural brannerite is also well examined, but unfortunately many of the previous findings are not widely applicable to wasteform leaching, as they deal with standard mining industry leachants, such as sulphuric acid/ferric sulphate and alkaline sodium carbonate/bicarbonate solutions, which are far more aggressive leaching solutions than would be present if groundwater penetrated a GDF. Two broad observations can be made from previous studies on natural samples of brannerite: it generally requires more acidic/basic leaching

conditions than many U-containing minerals, and leaches more rapidly under acidic conditions than basic.

These observations are backed up by the results of investigations on synthetic brannerites. Zhang *et al.* found that the rate of dissolution at pH 2.1 was higher than that at pH 11.9, with a minimum at pH ~8 forming a 'U'-shaped relationship.[72] Further investigation yielded information on the nature and mechanism of dissolution; this will be discussed later. Charalambous *et al.* found similar results, with a strong relationship between concentration of H_2SO_4 and fractional dissolution of U from a synthetic brannerite: 50 gL^{-1} H_2SO_4 dissolved ~2% of U, whilst 200 gL^{-1} H_2SO_4 dissolved ~9% of U under the same conditions.[138]

2.6.2 Mechanism of dissolution

There is a general consensus in the mechanisms of dissolution of natural brannerites. At low pH, the dissolution rate of U is much higher than that of Ti, leading to incongruent dissolution. The alteration product is a crystalline polymorph of TiO_2 (see Figure 11), with the structure depending on the other species in the leachant solution,[168] with varying reports of anatase[21,169] and rutile[167] structures, with some mentioning a secondary precipitated amorphous (or partially amorphous) polymorph as well.[21,167] The main mechanism of dissolution has been proposed as a two-step reaction: first, the U is oxidised from U^{4+} to U^{6+}, which is then complexed and diffuses into solution as the highly soluble uranyl (UO_2^{2+}) cation.[170]

At high pH, the dissolution rates of U and Ti are approximately the same over the course of leaching, although the dissolution is not fully congruent. The alteration product seems to be made up of an amorphous, fibrous phase, that is enriched in Ti, but also containing a smaller amount of U (see Figure 11).[169]

A recent study on the impact of H_2SO_4 concentration and presence of Fe^{3+} on the dissolution of synthetic brannerite did not observe formation of Ti-rich secondary phases, and reported that dissolution was congruent across the domain of leaching conditions examined.[171]

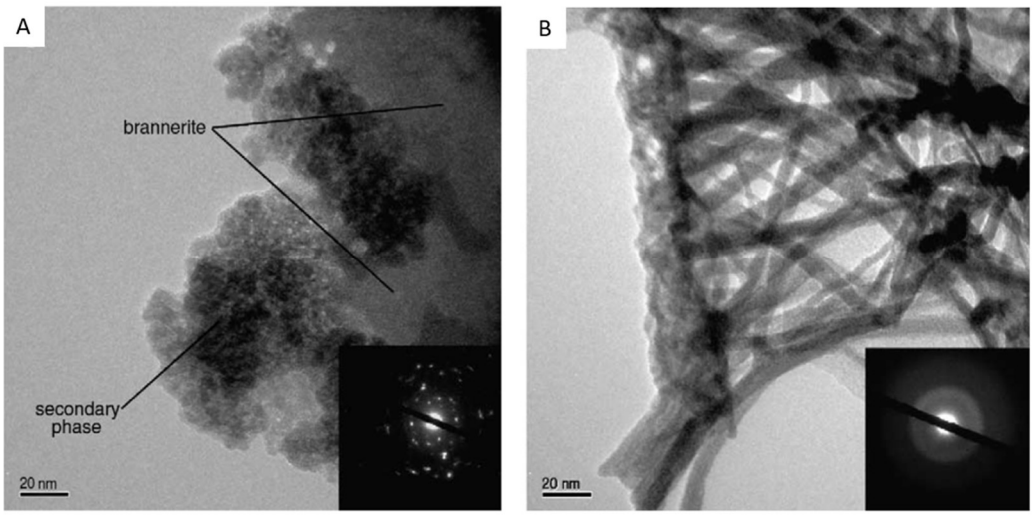

Figure 11: TEM images of Ti-rich secondary phases formed on the surface of samples of brannerite after leaching for 2 weeks at 90 °C, in pH 2 (A, left) and pH 11 (B, right) solutions. SAED patterns are inset.[169]

3 Experimental techniques and theory

3.1 Solid state reactions

3.1.1 Overview and theory

For any chemical reaction to take place, the reactants must be mixed and in contact at the atomic level. For solution phase reactions, this can be simply achieved by stirring the solution, but solid state reactants cannot be intimately mixed so easily. The reactant particles in the reaction mixture may be well mixed, but their size (from microns to millimetres) means that only a small fraction of the material is in contact with a particle of the other reactant(s). This means that reactions depend on the interdiffusion of ions, which is slow in the solid state, especially when compared to liquid- and gas-phase diffusion.

So long as the temperature is sufficient for the reaction to be thermodynamically favourable, interfacial regions of the reaction product will begin form at the points of contact between reactant particles. For reaction to proceed, the product nuclei present at these interfacial regions must reach the critical size of nucleation. The critical size of nucleation is controlled by the balance between the free energy change of product formation and the excess surface energy of such small particles (*i.e.* those with large surface area to volume ratios). Once nuclei have reached the critical size of nucleation it is then thermodynamically favourable for further product to form, growing the nuclei into crystals. Homogeneous nucleation of this type tends to be slow, limited by the low probability for the large number of ions needed to assemble in the right arrangement.

If the product can form on the surface of one (or more) of the reactants, nucleation is much easier, as the reactant surface can stabilise the initial nuclei. This is heterogeneous nucleation, and can occur in many different ways. If the substrate and the product have the same or similar crystal structures heterogeneous nucleation can proceed rapidly, with the substrate-product interface forming an essentially continuous structure, varying in composition from one to the other. This is epitaxial growth, where the structures of substrate and product have similarities in three dimensions. The related phenomenon of topotaxial growth is essentially the same, except the structural similarities are only present at the surface, that is, in two dimensions. Topotaxial growth tends to be more flexible, as many materials share common structural features (*e.g.* a close-packed array of O^{2-} anions), and a close match between the two structures is not required.

Theoretically, given near-infinite time, the reaction would then continue to completion, with the reactants diffusing through the interfacial regions of product and reacting; however, in reality, the kinetics of diffusion prevent this from occurring, as diffusion is extremely slow in the solid state (see Figure 12(a)). There are many ways to modify the reactions kinetics, from choice of starting materials to heating cycle (these will be discussed in further detail below in 3.1.2). The foremost methods of encouraging reaction in the solid state are increasing the temperature of the reaction and reducing reactant particle size (see Figure 12 (b)).

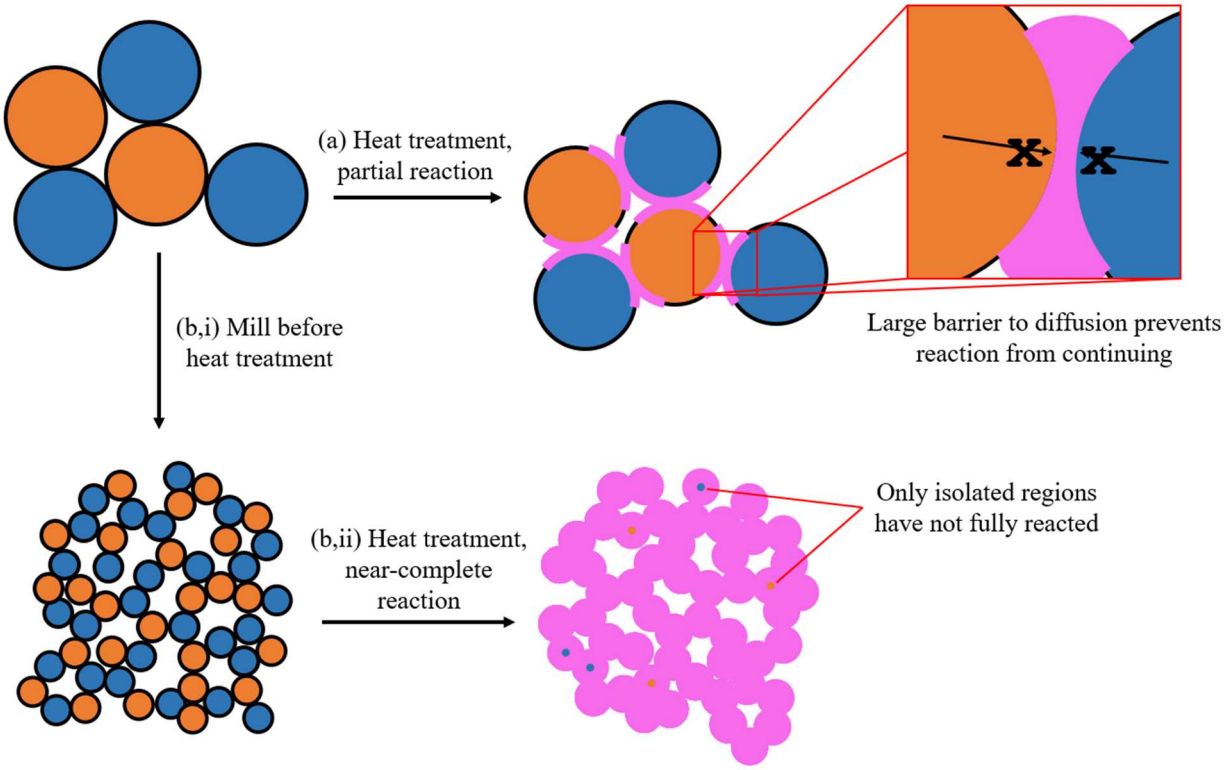

Figure 12: Diagrammatic representation of a solid state reaction between A (orange) and B (blue), forming C (pink), showing how a decrease in particle size increases reactant-reactant contact and encourages full reaction.

Higher temperatures mean that individual ions have greater kinetic energy and have a greater chance to move within the crystal structure. This has two related effects on a solid state reaction. Firstly, as temperature increases, the relative amount of intrinsic defects (those defects formed by the ions comprising the material only) increases. The presence of intrinsic defects (both vacancies and interstitials) reduces the kinetic barrier to diffusion by providing extra sites for movement of ions, both into and out of their usual crystallographic sites. The second effect is more directly related to the increase in kinetic energy of individual ions, where the increase in thermal vibration allows for a greater overall chance that an ion will hop to another site.

A further method to increase the rate of diffusion in an otherwise solid state reaction is the addition of a transport agent into the reaction mixture that in some way allows for a reduction in the kinetic barrier to diffusion. This could be through the addition of a small volume of a liquid or gas phase that dissolves one or more of the reactants, that can then diffuse in solution and react at the surface of another reactant (*e.g.* chemical vapour transport reactions and some methods of flux-growth of single crystals), or a liquid phase that simply allows for faster diffusion of reactant particles (*e.g.* the addition of a small amount of glass or salt that will become molten at the temperature of reaction). Suitable transport agents vary according to compatibility with the reactants, reaction temperature, crucible material, desired end-geometry of the final product, *etc.* A particularly relevant example of a transport agent working to increase diffusion is the case of glass-ceramic composites, where at the temperature of reaction the glass phase is liquid, but highly viscous. This viscosity of the glass allows for rapid diffusion of the reactant material(s) and/or

whole particles of the reactant(s), but, if the glass composition is well-suited for the temperature of reaction, does not allow for changes in the end-geometry (*i.e.* a cylindrical pellet will not slump if the glass remains sufficiently viscous over the heating cycle).

3.1.2 Experimental considerations

As outlined above, the kinetics of a solid state reaction are extremely slow at low temperatures, and limited mainly by the slow diffusion of the reactants towards each other. The rate of diffusion (and so rate of reaction) can be increased using different experimental techniques.

Firstly, is the choice of starting materials for the synthetic route. Although high-purity oxides are commercially available for many elements, some are unreactive due to their refractory nature, and others are unstable, reacting with the air or moisture to form undesirable products. More reactive precursors can be used in a synthesis to encourage the reaction to proceed over a reasonable timescale. A common example of this is the use of a metal carbonate or acetate that will decompose upon heating to form extremely small particles of the metal oxide, increasing the surface energy of the reactant and the amount of reactant-reactant contact, as well as reducing the distance necessary for diffusion to occur. For some materials, the choice is starting material is more complex: for example, the use of alkaline-earth hydroxides in place of the alkaline-earth oxide, in this case the hydroxide decomposes during heating, forming particles of the oxide already in close proximity to the other reactants, but more importantly preventing formation of the thermally stable alkaline-earth carbonate.

A simple method of increasing the rate of diffusion and decreasing the overall amount of mass transport necessary for full reaction is to increase the atomic-scale homogeneity of the reaction mixture. In a pure solid state synthetic route, this often takes the form of milling (see Figure 12). This may be done by manual grinding (*e.g.* in an agate mortar and pestle), low energy ball milling (*e.g.* placing the reagents into a rotating container containing milling media), or high energy ball milling (*e.g.* use of a planetary mill and milling media). The effect of milling is two-fold. Firstly, the more intensive the milling, the better the mixing of the different components, giving more regions of reactant-reactant contact. Secondly, more intense milling operations (especially high energy milling) reduce the average particle size of the reaction mixture through collisions of milling media coated in the materials being milled (this is often assisted by forming a slurry of the material in a carrier fluid). As previously explained, smaller particle sizes increase reactant-reactant contact and reduce the distance that diffusion must occur over. In some cases of high energy milling, the high energy collisions can induce structural defects in the materials being milled, increasing the overall free energy of the material and making the formation of the product material even more thermodynamically favourable.

At the temperatures necessary for solid state reactions to occur over a reasonable timescale, the choice of reaction vessel material is important. For example, borosilicate laboratory glassware is used for many wet chemical syntheses, but has a maximum operating temperature of approximately

500 °C, too low for many solid state reactions to occur. For this reason, crucibles are formed from materials sufficiently refractory and inert at the desired reaction temperature. Some common crucible materials are: precious metals (particularly Au and Pt), Al_2O_3, stabilised cubic ZrO_2 (often Y- or Ca-stabilised) , mullite, graphite, and BN (see Table 4). Many other exotic crucible materials are available, but are often extremely costly to produce, and so are only used where more economical crucible materials would fail (*e.g.* use of W or Mo crucibles for melting of rare earth metals).

Table 4: Maximum service temperature and other experimental information for different crucible materials commonly used in solid state syntheses.

Material	Max. service temp.	Additional information
Pt	1200 °C, up to 1600 °C with alloying Rh	Reacts with Li_2O, BaO, and some transition metal oxides, expensive
Au	900 °C	Generally more inert than Pt, melts at 1063 °C, expensive
Al_2O_3	1750 °C	Porous (can be coated), can introduce contaminants
Stabilised c-ZrO_2	2000 °C, depending on stabilising dopant	Porous (can be coated), can introduce contaminants, costly manufacturing process
Mullite	1500 °C	Porous, introduces contaminants above ~1000 °C, very cheap
BN/graphite	>2500 °C in inert atmospheres	Non-porous, costly manufacturing processes, require inert atmosphere during heating

As discussed above, increasing the temperature of reaction reduces the barrier to diffusion, allowing for a greater amount of reactant-reactant contact, even through the interfacial region of already-formed product. However, more consideration must be given to the heating cycle, as many different chemical processes occur at elevated temperatures. The reaction temperature must be sufficient to allow the reaction to proceed, but not so high as to cause any of the reactants or products to melt. If non-oxide precursors are used in the formation of an oxide product, the temperature of reaction must also be high enough to decompose them to the oxide equivalent. Many materials are metastable at room temperature, and only thermodynamically favoured at high temperatures, necessitating a high reaction temperature for any reaction to occur (rather than low temperature only preventing reaction due to limited diffusion).

Overall, a common solid state only synthetic route can be simple, consisting only of batching and milling of the precursors, and a heat treatment. On the other hand, a large amount of trial-and-error may be necessary to find suitable reaction conditions (*e.g.* finding a heating cycle that forms the target material without melting, contamination, *etc.*). For the individual researcher, careful

consideration of the literature reports on similar or related materials can often give a suitable synthetic route, reducing the time and work necessary for the experiment to proceed.

3.2 Hot isostatic pressing

3.2.1 Overview

Hot isostatic pressing (HIP, HIPed, HIPing) is a high temperature, high pressure processing technique that can be used for many different applications, including, but not limited to, consolidation of powders, densification of pre-sintered pieces, reactive sintering of materials, and interfacial bonding of certain materials. In this work HIP has been used as a method for reactive sintering of actinide and actinide surrogate containing materials, to investigate the viability of this technique for processing of wasteforms for high actinide content wastestreams.

$$p = \frac{2\gamma}{r} \qquad [1]$$

During sintering and consolidation of materials at room pressure, the driving force behind sintering is the reduction in surface energy caused by closure of pores (for the case of an isolated spherical pore, where p is pressure, γ is specific energy in Jm^{-2} and r is the radius of the pore, see Equation 1). For a small pore of 0.1 mm diameter (with a reasonable value of $\gamma = 1$ Jm^{-2}), this driving force is only 40 kPa. When a comparison is made to the additional pressure exerted during a standard HIPing cycle (on the scale of hundreds of MPa), it becomes clear why the technique of HIP can form highly dense work pieces, even at relatively low temperatures.

One of the most important considerations for the consolidation of a work piece is the even application of pressure. In order for the pressure applied to the work piece to be isostatic and the overall pressure gradient that forms the driving force to densification to be maximised, the work piece must not have any open porosity. This can be as simple as HIPing an already near-theoretical density work piece, but in practice this is most commonly achieved by sealing the materials to be consolidated in some kind of deformable but gas-impermeable container (usually consisting of metal or glass), to which the process gas can then apply pressure.

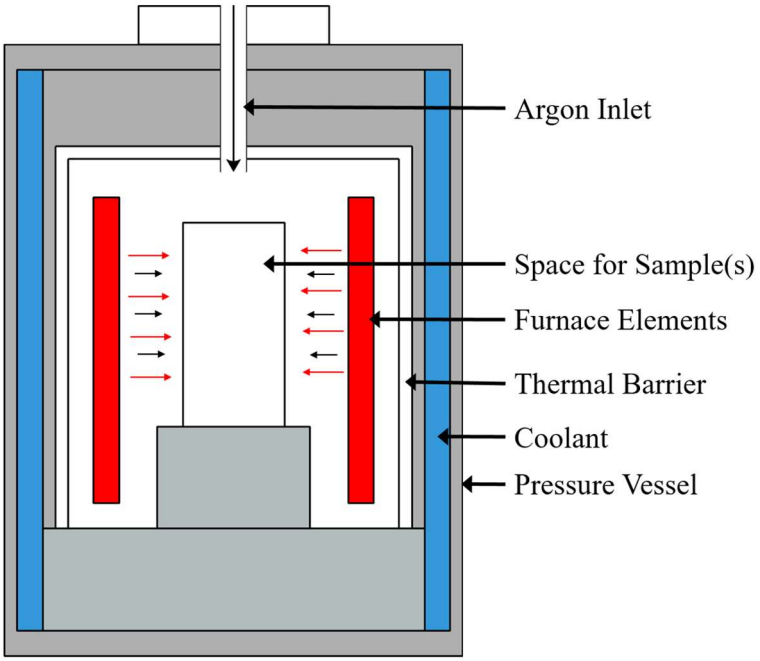

Figure 13: Simplified schematic of the internals of a HIP pressure vessel during heat treatment (sample not shown).

The equipment and overall HIP process is relatively simple: once the sample is sealed into the HIP canister it is placed inside the HIP itself within the thermal barrier (both top-loading and bottom-loading HIP geometries are common). The pressure vessel is then sealed and the HIP cycle proper can be started. The first step of the HIP cycle is the purging of the pressure vessel with Ar to ensure no O_2 is present once the heating cycle has begun (this is to prevent damage to the furnace elements, especially the Mo metal heating elements, as they rapidly oxidise at high temperatures). Once the pressure vessel is free of air, the HIP cycle proper can begin, with heating and pressurisation dictated by the needs of the sample. Ceramic materials can tolerate the simplest heat-pressure cycles, usually consisting of a ramp from ambient conditions to the target temperature and pressure, where the conditions are then held constant over the prescribed dwell time. Once the dwell is complete, the HIP then begins a ramp step from the dwell conditions back to ambient temperature and pressure.

Some materials (chiefly metals, but also some glasses and glass-ceramics) require more complex HIP cycles to obtain the desired product. This can include dwells at lower temperatures to allow for desirable processes to occur. Some examples of this include: grain growth in metals, crystallisation of a glass to form a glass-ceramic, or to relieve the strain formed as a glass cools. Other materials may require uncommon ramp rates or additional ramp steps. These may use the behaviour of the gaseous pressurisation medium to accomplish rapid cooling of the sample by allowing controlled rapid depressurisations, which cause a corresponding drop in gas temperature. Some examples of this include: preventing excess grain growth in metals, and preventing unwanted crystallisation of a glass.

3.2.2 HIP processing of nuclear wasteform materials

Hot isostatic pressing has many advantages when being considered for use as a consolidation method for radioactive waste materials. Firstly, the ability of HIP to achieve near-theoretical densities at relatively low temperatures means that the engineering and material concerns of the waste treatment plant are less demanding, resulting in a higher margin of safety compared to higher temperature processes (this is especially important for ceramic wasteform materials, that often require sintering at temperatures in excess of 1500 °C when consolidated by pressureless techniques).

Although the necessity of sealing the material to be immobilised into a HIP canister does add an additional step to the processing of the wastes (when compared to the current standard immobilisation methods of vitrification), this also confers many benefits. Because the canister must be gas-impermeable, if any gas is evolved from the sample during heat treatment it is contained within the canister, removing the need for complex and costly off-gas capture systems. This, combined with the fact that the canister prevents any direct material-equipment contact, means that the generation of secondary wastes is minimal in comparison to other methods of thermal treatment. The batch nature of the HIP process is also important from a material accountability point of view, where all material at risk of proliferation can be tracked through the entirety of the process (as opposed to the difficulties imposed by continuously operating processes). In addition to this, the use of sealed containers means that one HIP facility can process a diverse range of wastes, so long as each wastestream has the necessary facilities for preparation and filling of suitable HIP canisters.

Current HIP technology allows the production and consolidation of canister geometries that form a regular or near-regular cylinder after processing, and this, combined with the fact that the HIP canister material of choice is a corrosion resistant stainless steel, means that it may be possible for ILW HIP canisters to be directly disposed of. In theory, HLW canisters could also be directly disposed of (the steel is of the same type as that proposed for use as containers for non-HIPed glass and ceramic wasteforms), but it most likely that significant overpacking will need to be utilised for reasons of long-term safety and regulation.

3.2.3 Experimental details

HIPed samples were pressed in an AIP-630H HIP, in stainless steel cans. The powder to be HIPed was packed into the can under a weight of approximately 2 tons using a hydraulic press. The lid, with evacuation tube and filter (steel wool for inactive materials, sintered steel filters for active materials), was then welded on. To increase the densification of the final products and minimise the necessary bake-out time, the powders were precalcined at 600 °C for 5 hours prior to packing into the HIP cans. All HIP cans were baked-out under vacuum at 600 °C, with the bake-out considered complete when the vacuum reached below 50 mTorr, before final sealing and HIPing.

The HIP parameters for most samples were as follows: HIP pressure, 15000 psi (103.4 MPa); process gas, argon; cycle dwell time, 4 hours; heating and cooling rate, 10 °C min^{-1}. The temperature was varied according to the needs of the sample being pressed.

For active samples the heating and cooling rates were set to 5 °C min^{-1}, with extra dwells at low temperature during the ramp up to encourage even deformation of the can. This was especially important for samples of glass-ceramics, as the flow of the vitreous phase would otherwise cause the can to not deform evenly, possibly causing damage to the internals of the HIP system.

To observe the effect of the HIP process on the samples, the cans were removed using either an abrasive cutter or diamond saw to retrieve the sample material. Portions of the bulk were removed and prepared for analysis by standard techniques.

3.2.4 Active furnace isolation chamber

Although each HIP canister is fully sealed, the process of sealing at the laboratory scale includes hand-welding of the canisters and their lids. Unfortunately, this can lead to canisters failing over the course of the HIP cycle due to imperfections in the welds not visible to the naked eye. If canister failure occurs, the most likely outcome is simply the canister does not densify (there is no impermeable surface for the process gas to apply pressure to), but, depending on the size of the hole, some material may be lost. If the material being HIPed is radioactive, this escape of material must be avoided for two reasons.

Firstly, the escape of some material will contaminate the inside of the HIP unit, leading to costly and time-consuming decontamination procedures. Secondly, if material escapes from the HIP (for example during an emergency depressurisation of the vessel), it will contaminate a wide area, at best necessitating decontamination, at worst exposing workers to contamination and/or high doses of radiation.

In order to protect against canister failure from causing larger issues, canisters containing radioactive materials are HIPed within an Active Furnace Isolation Chamber (AFIC), designed to hold the canister and sit within the HIP vessel, preventing material egress using a series of filters.[172] The AFIC and the filters within are designed to allow Ar (the process gas of choice for most HIP applications) to easily flow into and out of the chamber, but will not allow any particulate material through.

The use of the AFIC has allowed for laboratory-scale HIP of radioactive materials, even within a laboratory not specifically designated for radioactive work. The HIP canister can be loaded into the AFIC in a designated radiochemistry laboratory, and is then considered a sealed source. It can then be transported to the HIP unit, processed, and returned to the radiochemistry laboratory for safe opening.

3.3 X-ray diffraction

3.3.1 Theory

The field of diffraction is very broad, and is made up of many different disciplines, including single crystal diffraction, powder diffraction, resonant X-ray diffraction, neutron diffraction, total scattering, micron-scale particle size distribution analysis, *etc.* In this work the main method of diffraction used is laboratory-scale X-ray powder diffraction (also called PXRD or powder XRD), with diffraction patterns being used for phase analysis and crystal structure refinement. For this reason, the following section will outline only the theory and application of diffraction as-applicable to laboratory-scale PXRD.

The nature of X-rays as electromagnetic waves is well-established, and their physics well-understood. Like all electromagnetic waves, X-rays can be described as a sine wave with wavelength λ, phase ϕ, and amplitude A. Where two or more waves are present the intensity does not increase linearly, but rather depends on the relative phase change (δϕ) of the waves. With $\delta\phi = 0$ the waves interfere constructively, resulting in the maximum intensity I_{max} (see Equation 2). With $\delta\phi = \pi$ the waves interfere destructively, resulting in the minimum intensity I_{min}, if the two waves are equivalent, with the same amplitudes, this minimum intensity is zero (see Equation 3). This approximation relies on the system being examined following the Fraunhofer approximation closely. The Fraunhofer approximation is a far-field approximation where the distance between the source and sample (L_1), and the sample and detector (L_2) are assumed to be much larger than the distance between scatterers (D). For X-rays diffracting at the atomic scale this is an excellent approximation (see Equation 4) and the resulting intensity for multiple waves *j*, can then be expressed using Equation 5.

$$I_{max} = (A_1 + A_2)^2 \quad [2]$$

$$I_{min} = (A_1 - A_2)^2, and\ when\ A_1 = A_2, = 0 \quad [3]$$

$$D/L_1 \approx D/L_2 \approx 10^{-10} \quad [4]$$

$$I_{total} = \left[\sum_j A_j exp(i\varphi_j)\right]^2 \quad [5]$$

In the case of X-rays diffracted by a crystalline material, the relationship between the diffracted X-rays and the structure of the material is most easily described by the eponymous Bragg equation (see Equation 6), where the reflections of X-rays are described as different planes within the lattice. These lattice planes are described by indices of the form *hkl*, called Miller indices, with parallel planes having the same index separated by the d-spacing of d_{hkl}. Due to the penetrating nature of X-rays, compared to visible light, lattice planes deep below the sample surface are involved in the overall diffraction process. If these lattice planes are parallel (and so of the same Miller index) with

spacing such that the additional distance travelled by the X-rays reflecting off deeper planes (Δ) is equal to an integer multiple of the wavelength, then the Bragg condition is fulfilled (see Equation 6 and Figure 14), and all X-rays reflected by these planes will constructively interfere. In all other cases, including spacing of non-integer multiples of the wavelength or non-parallelism of the planes, it is easily shown that complete destructive interference will occur: for each reflecting plane in an ideal crystalline solid, there will always be a deeper reflecting plane with Δ of the series ±1/2, ±3/2, …, which will result in complete destructive interference. The combined result of this constructive and destructive interference is that for each d-spacing *d*, complete constructive inference occurs at the angle θ (as calculated from the Bragg equation, see Equation 7), and there will be a sharp intensity maximum, with no intensity seen between these maxima.

$$\Delta = PN + NQ \quad [6]$$

$$n\lambda = 2dsin(\theta) \quad [7]$$

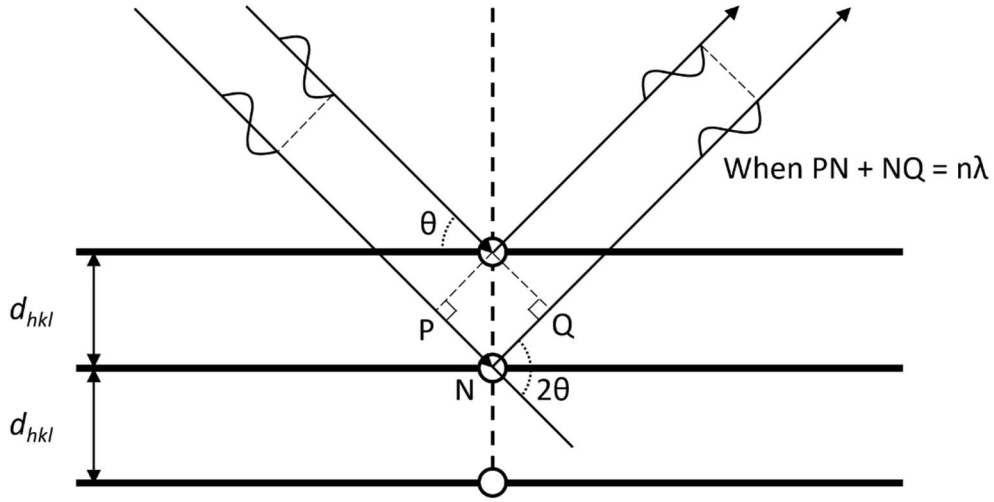

Figure 14: Illustration of the geometry of X-rays constructively interfering from two planes with separation d_{hkl} at the angle 2θ, according to the Bragg equation (see Equation 7)

In real (*i.e.* non-ideal) crystalline solids, both single crystals and polycrystalline, the sharp diffraction maxima are broadened by a combination of instrumental and sample contributions. The most common cause of sample-based broadening is caused by the deviation of crystallite size from the idealised infinite lattice discussed above. This means that the Bragg condition is not completely fulfilled, as close to the angle of reflection the planes necessary for complete destructive interference would be at such a depth as to be not present in the (finitely sized) diffracting crystallite. This leads to broadening of the observed reflection, and is observed most strongly when examining nano-scale materials due to their extremely small crystallite size.

Crystallite strain can also contribute to sample-based broadening. This broadening appears when the diffracting planes of each reflection are not perfectly parallel, resulting in the intensity relating to the reflection with d_{hkl} being spread over a continuous distribution of d-spacings, depending on

the strain present in the crystallite (*e.g.* if the crystallite is subject to uniaxial pressure, the d-spacings of planes normal or perpendicular to the axis of compression will be evenly compressed, but those off-axis will be unevenly compressed, resulting in broadening of the observed reflections). Another similar source of sample-based broadening is that caused by crystallites not being perfectly crystalline, with the planes of reflection being uneven due to the high proportion of crystal structure defects. This results in a continuous range of d-spacings observed for each reflection d_{hkl}, with the corresponding observed reflections broadened as a result. For an example of a diffraction pattern containing phases with and without crystallite size-based broadening, see Figure 15.

The vast majority of samples examined in this work have highly-ordered, unstrained crystallites of sufficient size that size-based broadening and strain-based broadening are negligible compared to the instrumental contributions (which will be discussed further in the section on Rietveld method-based refinements below).

Finally, if the diffracting material does not exhibit significant long-range ordering (*e.g.* the glass phase in a glass-ceramic composite), then there are no definable planes of reflections with specific spacing d_{hkl} to satisfy the Bragg condition, and no distinct reflections can be observed in the final diffraction pattern. Instead, incident X-rays are scattered diffusely, and the diffraction pattern of these materials consists of a single, broad peak, with much lower intensity than an equivalent crystalline material.

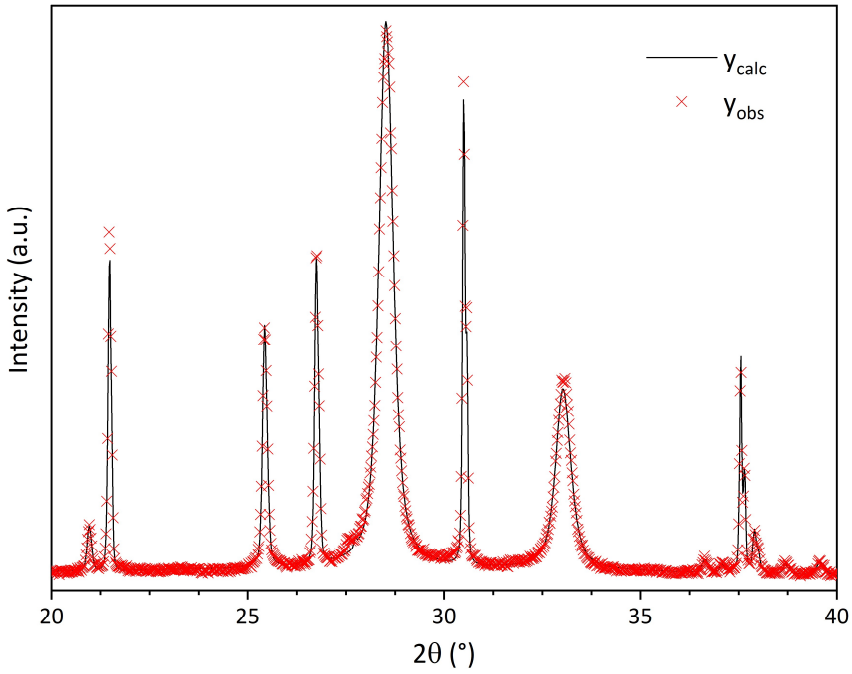

Figure 15: PXRD pattern and Rietveld method refinement of a multiphase polycrystalline material, showing a wide range of peak shapes due to the sample-based effects of crystallite size and strain broadening.

3.3.2 Neutron diffraction techniques

As mentioned above, diffraction-based techniques are also routinely performed with other scattered species, including neutrons. Due to the difficulty of generating a suitable neutron beam, there are two main types of neutron diffraction, relating to the two main methods of neutron generation: constant wavelength (CW) and time-of-flight (TOF).

Following the brief description of nuclear fission reactors above, it is simple to see how a beam of neutrons could be generated from an ongoing fission reaction. This is the basis of CW neutron diffraction techniques. As with polychromatic X-ray sources, the neutron beam must be monochromated to be useful for CW neutron diffraction techniques. In practice, fluxes of monochromatic neutrons suitable for diffraction techniques are generally only obtained from purpose built research reactors (*e.g.* the Institut Laue-Langevin High-Flux Reactor, France and the High Flux Isotope Reactor at Oakridge National Laboratory, USA).

Where constant wavelength neutron diffraction is similar to XRD, time-of-flight neutron diffraction is rather different, utilising a pulsed polychromatic beam of neutrons. As described by the De Broglie relation, the neutron wavelengths, λ, are directly proportional (through the Planck constant, h) to their velocity, ν, and mass, m_n; through a simple derivation, λ can also be derived as a function of the neutron TOF, t, and total flight path, L (see Equation 8). The TOF and position (*i.e.* diffracted angle 2θ) of the diffracted neutrons are both measured, with the TOF known due to the pulsed nature of the neutron beam. In this manner, the TOF (t, in milliseconds) can be related to d-spacing (in Å) using the total flight path L (in metres) (see Equation 9).

$$\lambda = \frac{h}{m_n v} = \frac{ht}{m_n L} \quad [8]$$

$$t = 505.56\, L\ d\ \sin\theta \quad [9]$$

The TOF neutron diffraction patterns in this work were collected at the High Resolution Powder Diffraction (HRPD) beamline at the ISIS Neutron and Muon Source, UK; only a brief description of the working principles will be given here. The process begins with an ion source producing H^- ions, which are then accelerated to approximately 37% of the speed of light by a linear accelerator. The ion beam is then injected into a 163 m synchrotron through an alumina filter, with the filter stripping away the two electrons and leaving only a beam of protons. The synchrotron further accelerates the proton bunches to approximately 84% of the speed of light, before each bunch is extracted from the ring and directed at the spallation target. As the proton bunches collide with the target (at ISIS the targets are made of W metal), neutrons are removed from the target atoms in intense pulses. The neutrons are then slowed to useful energies by passage through one or more moderators, and finally directed to the individual beamline instruments.[173,174]

3.3.3 Application

The first step in collecting the X-ray diffraction pattern of a sample is to generate a suitable beam of X-rays. The ideal X-ray beam is monochromatic (so that each reflection d_{hkl} can only be observed at a single angle 2θ, without the need for an energy discriminating detector) and highly collimated in both the axial and equatorial directions (to prevent beam overspill caused by an excessively long or wide beam). Modern laboratory X-ray tubes work by striking an anode target with an electron beam, usually produced from a highly charged W filament, generating both Bremsstrahlung radiation and X-rays characteristic to the target material (through the photoelectric effect). The most common target material for laboratory XRD is Cu, because it has excellent thermal conductivity (rapid heat dissipation allows the tube to be operated at higher power without simply melting the target anode), and intense K emission lines at a wavelength useful to probe atomic or molecular structures, with the K_β emission easily filtered using Ni metal foils. Other common target materials are Co, Fe, and Mo, depending on the desired application (*e.g.* iron-containing materials fluoresce under Cu K_α radiation, so, for example, researchers examining samples of steel often use Co or Mo target X-ray tubes).

The path of the beam depends on the geometry of the diffractometer. By far the most common type of diffractometer is the coupled θ-θ Bragg-Brentano geometry, where both X-ray source and detector move around the goniometer radius to collect data over the desired angular range in 2θ (see Figure 16). The beam-path optics can be divided into primary (or incident) beam, which are located between the source and the sample, and secondary (or diffracted) beam, which are located between the sample and the detector. The optics can then be further divided based on purpose:

whether they are present to control the shape or size of the beam, or to control the energy range of X-rays used, by filtering or monochromation.

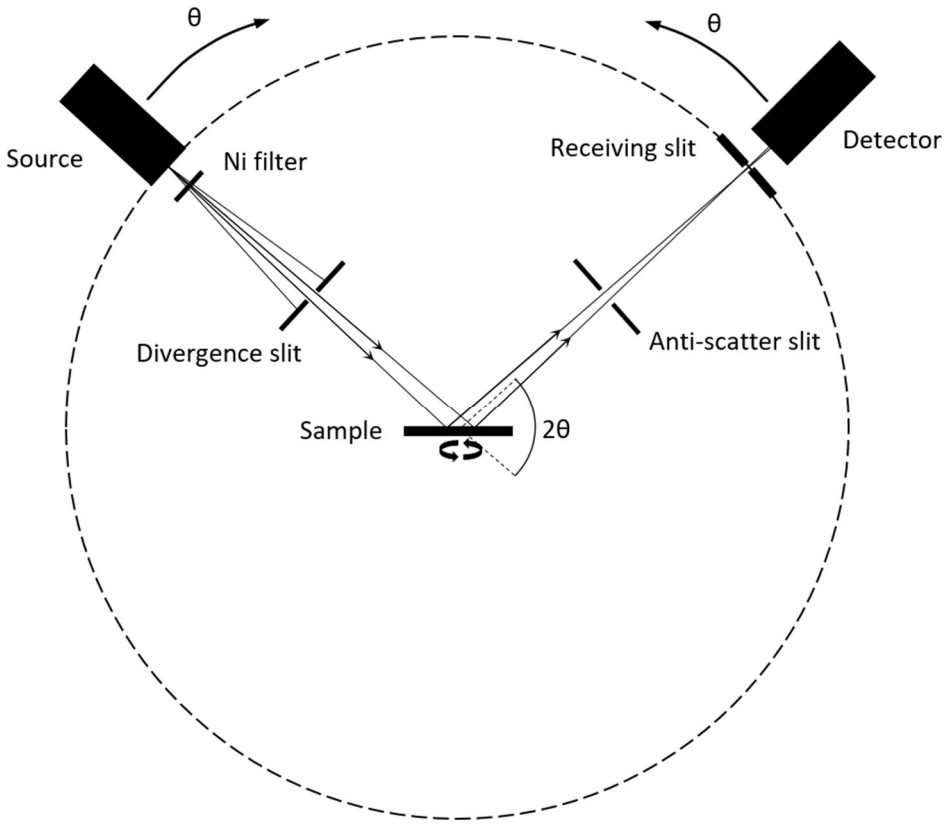

Figure 16: Schematic of a simple Bragg-Brentano geometry diffractometer operating in coupled θ-θ mode with Ni-filtered Cu Kα radiation, where the sample rotates normal to its axis, and the source and detector each move around the diffractometer circle across the desired range 2θ.

The beam-path of a typical laboratory Cu K_α Bragg-Brentano diffractometer can contain many different optical elements from source to detector. Primary beam optics include the X-ray source, a method to remove unwanted X-ray energies (usually a filter or monochromator; for Cu K_α instruments, this usually takes the form of a Ni foil, which strongly absorbs Cu K_β but does not significantly attenuate Cu $K_{\alpha1}$ or $K_{\alpha2}$), one or more divergence slits to control beam length and prevent overspill (these can be fixed or variable slits), Soller slits to control axial divergence, and sometimes anti-scatter slits to further prevent X-rays being scattered by air. The beam then reaches the sample, which is usually either a flat plate or cylindrical capillary, and often rotates about the normal axis to minimise the effects of preferred crystallite orientation. Secondary beam optics can include further anti-scatter slits, Soller slits, one or more receiving slits, a monochromator (if necessary and not present in the primary beam path), and the detector. In transmission geometry diffractometers a final beamstop or contact switch is necessary to safely prevent the high intensity beam of un-scattered X-rays from escaping the diffractometer. The effects of some of these optical elements on the final diffraction pattern and its analysis will be discussed below.

The ideal diffractometer allows for collection of all X-rays diffracted by the sample by utilising a near-spherical area detector, allowing for rapid data collection over nearly all angles 2θ. Unfortunately, detectors of this type are not currently commercially available, but a range of other detector geometries have been developed over the past decades that have allowed for larger jumps in diffractometer efficiency and resolution compared to other diffractometer elements (*e.g.* X-ray tubes have remained much the same over the same timescale, with only small gains in power and focus). The first detectors took the form of photographic films, where the diffracted X-rays cause a chemical reaction to occur at the points of contact, rendering it opaque in those areas. These were technically a 2D detector, allowing for observations of many (or all) reflections at once, but have many drawbacks, including difficulty of handling (darkroom techniques were important to prevent exposure of the film to visible light), non-reusability, and difficulty of digitisation of the collected diffraction pattern (which has become increasingly important over the past two decades).

The first widely available digital X-ray detectors (still in common use today) were scintillation point detectors. Diffracted X-rays collide with a scintillator (or Si/Ge-based solid state detectors in more modern systems), generating visible light, which in turn collides with a photomultiplier, generating pulses of electrons proportional to the intensity and energy of the diffracted X-rays. Some detectors use an ionisation chamber (often Ar gas mixed with methane to act as a quenching agent) to directly count the number of photons incident upon the detector, as each photon will generate a set number of electrons (dependant on the incident X-ray energy) during the process of ionisation of the gas, with a highly charged wire within the chamber attracting the electrons and generating an electrical signal proportional to the incident X-ray intensity. The detector is then moved around a circle to collect the diffraction pattern as a plot of X-ray intensity against diffracting angle 2θ (these detectors can be described as 0D). Early on, it was realised that a linear array of point detectors could be used to collect the diffraction pattern more efficiently by increasing the collecting area. The linear array could either be stationary, measuring only a single range in 2θ, or could also be moved to collect over a large range in 2θ with higher efficiency than a single point detector.

These linear arrays were the first examples of 1D Position Sensitive Detectors (PSD), with the main benefit being a decrease in the time necessary to collect a useful powder diffraction pattern. Other types of 1D PSD include some of the more common types of the aforementioned gas ionisation detectors, where the internal wire is given a large voltage bias at both ends, generating two electrical pulses for each incident photon-ionisation event. The time between the two pulses reaching each end of the wire can be used to calculate where along the wire the event occurred, giving position sensitive X-ray detection. Solid state PSDs work in an analogous way, where the incident photon generates a number of electron-hole pairs equal to the incident photon energy. The electrons and holes then travel to either end of the semiconductor (caused by a potential bias being applied over the length of the semiconductor), with the position of the incident photon calculated

from the relative travel times of the electrons and holes (0D solid state point detectors are also available, working in much the same way).

2D detectors are currently the highest efficiency detector geometry in terms of the fraction of space over which the diffracted X-rays can be collected. Although photographic films are a type of 2D detector, the aforementioned issues have caused other 2D detectors to become more widely used. These include 2D arrays of point detectors (CCD detectors are one type of 2D point detector), arrays of linear detectors, or highly complex 2D solid state detectors that measure the position of the incident photon using directional pulses of electrical charge to locate the photon-ionisation event in two dimensions. More recently, curved 1D and 2D detectors have become commercially available (sometimes called 1.5D and 2.5D detectors), allowing for a larger detector area, but without the additional uncertainties brought on by using a flat detector (which only approximates the curvature of the circle of diffraction as a flat tangent to it). Many other detector types and geometries are currently available and more are being developed, with a focus on higher counting efficiency and greater resolution (in both 2θ and in energy).

3.3.4 Structural refinements from diffraction data

Many procedures for extraction of crystallographic information from single-crystal diffraction patterns are available, which usually consists of extracting the individual structure factors from each reflection, with further analysis then yielding atomic positions. Although this method can be used for PXRD patterns of simple cubic crystalline phases with relatively small and simple unit cells (*e.g.* the defect structures of the system CaF_2-YF_3[175]), the PXRD patterns of more complex structures often contain many overlapping reflections (preventing direct extraction of the structure factors), with peak broadening further contributing to peak overlap. For this reason, different methods of PXRD pattern analysis have been developed.

The first noteworthy method of analysis was developed and reported by H. M. Rietveld for refinement of nuclear and magnetic structures from diffraction measurements using monochromatic neutrons.[176,177] It has since been generalised for use with PXRD, time-of-flight (TOF) neutron diffraction, and energy-dispersive XRD, with the ability to extract many different kinds of physical and crystallographic information, and has been implemented in many different modern software packages, both freely available and commercial (including GSAS,[178,179] TOPAS,[180,181] HighScore,[182] BGMN,[183,184] Fullprof,[185] and many more). The full theory behind the Rietveld method and its derivatives is available in many standard references, and will not be fully explored here, with this section giving an overview of the method sufficient for the reader to understand the Rietveld refinements in this work.

The basis of the Rietveld method is the application of a least squares minimisation, with the residual minimised being based on the difference between the observed and computed intensity (y_{obs} and y_{calc} respectively) at each point in the diffraction pattern (this can be at each point 2θ, *d*, TOF, X-ray energy, *etc.*), see Equation 10. The calculated intensity at each point *i* is shown in

Equation 11, as the sum of all phases p, with each phase weighted by a scaling factor S_p (proportional to the weight fraction of that phase). The contribution of each phase is equal to the sum of all Bragg reflections $\underline{s}$ of that phase (where each $\underline{s}$ is one reflection *hkl* of that phase), with intensity of $|F_{calc,\underline{s},p}|^2$, profile function ($\Phi_{\underline{s},p,i}$) of each point *i* relative to the peak position $|\underline{s}|$, and a corrections term $Corr_{\underline{s},p,i}$. The background is modelled as a separate term for the whole diffraction pattern, Bkg_i.

$$M = \sum_i (y_{obs,i} - y_{calc,i})^2 \quad [10]$$

$$y_{calc,i} = \sum_p \left(S_p \sum_{\underline{s}(p)} \left(\left| F_{calc,\underline{s},p} \right|^2 \Phi_{\underline{s},p,i} Corr_{\underline{s},p,i} \right) \right) + Bkg_i \quad [11]$$

As the least squares minimisation is not linear, each parameter affecting the calculated profile must have an initial value. These can be taken from, for example, literature data of the material or structure (most useful for lattice parameters, atomic positions, *etc.*), estimates based on similar systems, or from the results of a previous refinement. In this way, once a starting model has been established, the least squares minimisation can iterate until it reaches a minimum (which may or may not be the true minimum of the system).

For the minimisation to take place all variables must be parameterised. For accessibility, in modern Rietveld software packages the variables in Equation 11 are already divided into parameters, with many divided such that the individual parameters are directly related to physical properties of the sample and/or instrument (*e.g.* one of the parameters making up the variable $Corr_{\underline{s},p,i}$ is the zero point error, a measure of the diffractometers deviation from the true angle 2θ, at each angle). The relevant parameters and their meaning are briefly described next.

Parameters relating to the background are the most simple, with the observed background fit using simple arithmetic functions (for relatively flat backgrounds, a shifted Chebyshev polynomial of order six to ten is usually sufficient). On occasion more than one function is necessary to describe the observed background, most where often a function of the form $c/2\theta_i$ (where c is the refinable parameter) is added to account for the steep background at low 2θ caused by air scattering of X-rays.

The parameters affecting peak position in the calculated pattern that are most relevant to the simple applications utilising Bragg-Brentano coupled θ-θ diffractometer geometry used in this work include: the previously mentioned zero point error, displacement of the sample away from the focussing circle of the diffractometer (common in Bragg-Brentano geometries and often a symptom of poor XRD sample preparation), axial divergence of the X-ray beam, and occasionally sample transparency/absorption. Of these, axial divergence and sample absorption are often accounted for in the peak shape terms as they also contribute to overall peak shape.

The relevant parameters affecting peak intensity include: the overall phase scale factor (a linear factor accounting for all linear constants affecting intensity, including intensity of the incident beam and time spent measuring at each step in x, *e.g.* 2θ, *d*-spacing, *etc.*), atomic form factors (in most cases these are automatically taken from standard tables for X-ray or neutron scattering), the thermal displacement parameters (a measure of the mean square displacement of atoms/ions due to thermal vibrations), reflection multiplicity (automatically calculated in modern software packages), Lorentz polarisation factor (accounting for both the Lorentz and polarisation factors, and dependent on the presence and material of a monochromator, if any), and occasionally sample transparency/absorption, surface roughness (various different models describing surface roughness are used), and preferred orientation (parameterised using a March-Dollase function or spherical harmonics model).

The peak shape of the observed diffraction pattern can be modelled in two different ways, either the fundamental parameters approach (FPA), where all known factors affecting the peak shape are set and the unknown factors allowed to refine to obtain physically relevant information (most often crystallite size and/or strain); or a more empirical method, fitting the observed peak shapes with mathematical functions (usually a Voigt function, or variant thereof, see Figure 17). A combination of both may be used, and physically relevant information can be extracted from the non-FPA peak shape terms, if certain assumptions are made (*e.g.* extracted crystallite sizes are only relevant if all other factors affecting the peak shape are set to known physical values of the system or do not significantly contribute). In the fundamental parameters approach the parameters include: equatorial source size, receiving slit equatorial length, detector strip length, crystallite size, crystallite microstrain, X-ray tube emission profile, X-ray tube tails (if present), *etc.*, where some or all must be set to known values to accurately and reliably obtain physically relevant information. The most common crystalline materials examined are typically highly-ordered and strain-free, with crystallite sizes large enough that size-based broadening is not observed. In these systems the peak shape is almost entirely derived from instrumental contributions and it is not necessary to use the fundamental parameters approach, as little reliable information on the sample can be extracted from the peak shapes.

An important effect impacting refinement of both peak shape and position is asymmetry of the observed reflections. Although this can be caused by contributions from the sample, *e.g.* anisotropically strained crystallites or compositional gradients within the crystallite, it is far more commonly caused by instrumental contributions, especially axial divergence of the incident X-rays. As with other corrections peak asymmetry can either be parameterised by a fundamental parameters approach (often five distinct parameters are used: tube filament length, sample length in the axial direction, length of the detector/receiving slit, and apertures of the primary and secondary Soller slits, if present[186]), or its effect modelled mathematically.[187]

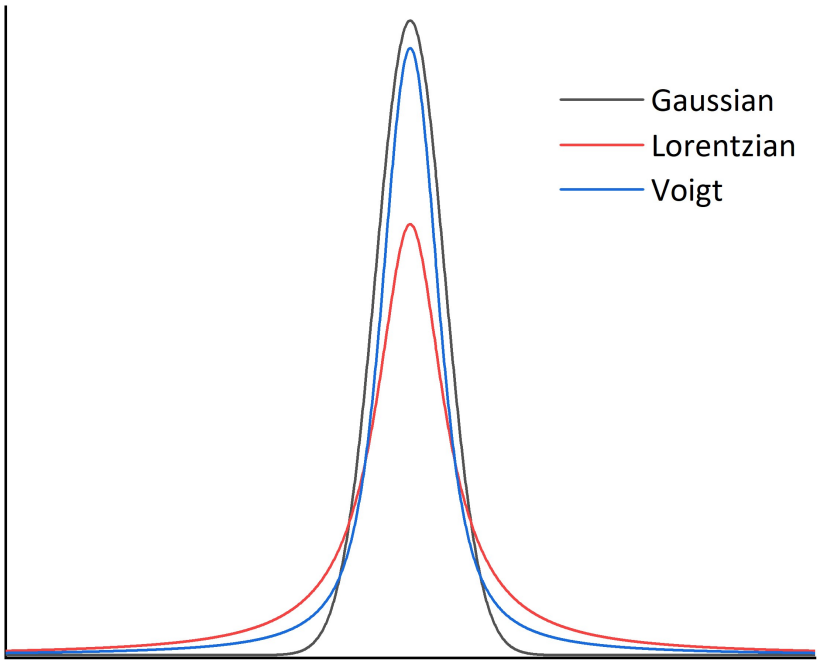

Figure 17: Comparison of three common peak shapes used to model the observed peak shapes in a diffraction pattern, Gaussian, Lorentzian, and Voigt (50:50 weighting of Gaussian and Lorenztian components). Each peak has the same overall area.

During each minimisation cycle many different statistical agreement factors (often referred to as simply R-factors) are calculated to assist in quantification of the quality of fit between the observed and calculated patterns. The derivations of these R-factors are reported in many literature sources, and a useful discussion of their relevance has been published by Toby.[188] The most relevant of these for the end user are R_{wp} (the weighted sum of differences of step scan intensities at all points *i*), R_{bragg} (the sum of differences of integrated intensities at all points *i* specific to that phase), and χ^2 (the ratio between R_{wp}, and the expected best fit R_{exp}). As a general rule, an $R_{wp} <$ 10% and a $\chi^2 > 2$ indicates a good statistical fit between the observed and calculated patterns, but is no guarantee of the refined model having physical relevance if the refinement was carried out improperly or the data are otherwise compromised. For example, a fit of a diffraction pattern with a high background relative to the observed reflections (*e.g.* that caused by sample fluorescence) would result in a low χ^2 but not necessarily a satisfactory fit, as a significant fraction of the overall observed intensities are caused by the elevated background.

Aided by the trends of increasing computing power and increasing diffractometer resolution, Rietveld method refinements are now commonplace in the analysis of laboratory XRD patterns. However, not all data is of high enough quality to be use in Rietveld method refinements (*e.g.* diffraction patterns with particularly low signal-to-noise ratios). In these cases, simpler refinement methods (Pawley refinements and Le Bail refinements are the two foremost examples) can still be used to extract useful (and accurate) information. The basis of both Pawley and Le Bail refinements is the removal of crystal structure refinement (the space group and starting estimates of the lattice parameters are still necessary) and addition of individual reflection intensity refinements.

As direct extraction of all peak intensities and their corresponding structure factor amplitudes is usually difficult for powder diffraction patterns (due to peak overlap of neighbouring reflections), Pawley and Le Bail refinements (together called whole powder pattern decomposition methods) instead use methods to estimate the peak intensity of overlapping reflections. In Pawley refinements the issue of strong correlations in the calculated intensities of overlapping reflections (which can cause negative calculated reflection intensities with no physical meaning) is remedied by introducing constraints on their relative intensities (*e.g.* the 'hard' constraint where the difference in peak position is less than the step size in 2θ is that each intensity is constrained to be equal to the other).[189] In Le Bail refinements the individual peak intensities are first set to an arbitrary value (these can be truly arbitrary or estimates informed by other measurements), and a single minimisation cycle using Rietveld's procedure for partitioning of overlapping peaks is performed, resulting in a set of "observed" intensities I_{obs} (these are not true observed intensities, but on average will be more accurate than arbitrarily chosen values). These "observed" intensities are then used as fixed values in a second minimisation cycle, and the process repeated until a minimum is reached.[190,191] In the past there was much debate in the crystallographic community as to which of these methods was better, with many focussing on the perceived more effective use of prior information and reduced computational needs of Le Bail refinements. With modern computing power the difference between the two is negligible, and both are regularly used as part of procedures for structure solution from powder diffraction patterns and accurate extraction of lattice parameters (even for data of a relatively low quality).

3.4 Electron microscopy

3.4.1 Theory

Microscopy has long been commonplace in materials research, with each different microscopy technique having the same underlying purpose: to make microscopically small features visible to the human eye using one or more lenses. This could be direct imaging, where the image is focussed on the retina (*e.g.* using a loupe to examine features on a cut jewel), indirect imaging, where the image is focussed onto another surface, which can then be examined by eye (*e.g.* using a zoom lens to photograph distant objects using photographic film), direct digital imaging, where the image is focussed directly into a digitisation device with the magnified image stored and displayed digitally (*e.g.* using a zoom lens to photograph distant objects using a digital camera), indirect digital imaging, where an indirect image is digitised (*e.g.* digitisation of photographic films for archiving), or raster imaging, where a digital image is formed pixel-by-pixel, with each pixel presentative of a single point in space (*e.g.* some types of high magnification astronomical imaging).

The practice and theory of light microscopy has a long history, and has been well-studied from many different perspectives since ancient times, with the physics of optics well-established. Although electron microscopy is a much younger discipline, much of the theories of electron microscope optics are shared with light microscopy. Both are characterised by the use of lenses to

produce converging or diverging beams of the imaging species (*i.e.* electrons for electron microscopy), and, with some exceptions, the lenses can be described mathematically in the same way. In this work the only major microscopic technique used is scanning electron microscopy (SEM), so only a brief introduction to the relevant physics will be presented.

The most important characteristic of a microscope is the resolution, defined as the smallest objects that the microscope can resolve. The resolution of an instrument can be either diffraction limited or aberration limited. Rayleigh was the first to describe the phenomenon of diffraction limited resolution as a function of the size of the Airy discs produced by diffraction through an aperture of numerical aperture N_a. Rayleigh proposed that the two neighbouring features could be just resolved if the diffraction maximum of one coincides with the first diffraction minimum of the other. If the distance, r, is larger, then the features will be well-resolved, if it is smaller, then the features are not able to be resolved. This relationship is described by the Rayleigh criterion in terms of wavelength (λ) and the numerical aperture (which can be described by the refractive index (μ) and the lens half-angle (α)), see Equation 12.

$$r = \frac{0.61\lambda}{N_a} = \frac{0.61\lambda}{\mu \sin \alpha} \approx \frac{0.61\lambda}{\alpha} \qquad [12]$$

By examination of the Rayleigh criterion, the effects of the variables λ, μ, and α on overall resolution become obvious; with the optimisation of the magnitudes of these variables forming the basis of the high resolutions achieved by electron microscopy. In comparison to the shorter wavelengths of visible light (approximately 400 nm), the De Broglie wavelengths of electrons of use in microscopy are of the order 0.001 nm to 0.01 nm, making the difference in achievable resolution due to wavelength obvious. However, the increase in resolution due to use of electrons is not only due to their wavelengths, but also the refractive index and aperture half-angle of the lenses. The changes in refractive index as an electron passes through an electron microscope lens are negligible (in most cases μ can be assumed to be unity), further increasing the resolution. If the optics of a 100 kV (approximate wavelength of 0.0037 nm) electron microscope are assumed to be perfect and free from aberration, and the half-angle is set at a reasonable angle of 0.1 rad (approximately 5°), then the theoretical limit of resolution is approximately 0.02 nm, which would allow for imaging of features down to sub-atomic scales. However, the presence of aberrations lowers the attainable resolution of even the highest quality microscopes.

As first described from observations of visible light microscopes, there are three main types of aberration: chromatic aberration, spherical aberration, and astigmatism. Chromatic aberration is caused by waves of differing wavelength being focussed at different lengths (*e.g.* blue light will focus at a shorter distance from the lens, red light at a longer distance). In visible light microscopy this can be avoided using a series of lenses of different refractive indices and shapes, or by using a monochromatic light source. Due to the complexities of electron lenses in electron microscopy chromatic aberration can only be avoided by using beams of electrons with particularly small

ranges of wavelengths, though this is reasonably simple to implement. Spherical aberration is present even for monochromatic rays, and is caused by the outer regions of the lens having a focal length slightly shorter than the centre of the lens. The effect of spherical aberration can be minimised by reducing the size of the lens aperture (in opposition to increasing the aperture size, and so half-angle, in attempts to increase the diffraction-limited resolution). Astigmatism is caused by imperfections in the lenses, for example, if a lens has different properties in the vertical and horizontal planes, then the focal lengths of waves passing through horizontally or vertically will be different. As with spherical aberration, astigmatism can be reduced by reducing the aperture size, in effect bringing the outer regions of the lens closer to the centre of the lens, and so bringing their focusses into closer agreement. Corrections for the different kinds of aberration are possible, with some electron microscopes having such fine control over the lens geometries that they can remove, or at least reduce, the aberrations, whilst others attempt to digitally remove the aberration from the images collected.

3.4.2 Electron-sample interactions

The actual mechanisms of imaging in electron microscopes are relatively simple. The beam of electrons is generated and focussed onto the sample, and then the interactions detected in some way. In transmission electron microscopes (TEM), the electron beam passes through an extremely thin region of the sample, and the transmitted beam projected with further lenses onto an imaging device (a more detailed discussion is below). In scanning electron microscopes (SEM), after the beam is focussed it passes through the scanning coils, which sequentially deflect it towards different regions of the sample in a raster pattern, the interactions at each point are then detected in some way.

Interactions between the electron beam and the sample are complex, consisting of many different possible mechanisms. They can be divided into primary effects and secondary effects, depending on whether the detected species has an energy close to the initial electron energy (primary), or has an energy that is much less than the initial beam (secondary). The most important types of primary effects for electron microscopy are elastic scattering, where the electron does not lose energy relative to the starting energy (this includes TEM electron diffraction, and the back-scattered imaging of SEM), and some of the sub-types of inelastic scattering, most notably inner shell electron excitation, which form the basis of electron energy loss spectroscopy (EELS). The most important types of secondary effects are the emission of secondary electrons, which is a blanket term for any electron that escapes the surface of the sample with energies below approximately 50 eV (used for topographic imaging by SEM), backscattered electrons, which are primary electrons that escape the surface after fewer interactions than secondary electrons, and have correspondingly higher energies (particularly useful for imaging based on atomic composition), and excitation-relaxation effects, where the primary electron scatters by ejecting a localised electron from an atom, generating a high energy state that then decays on emission of a

photon or electron (this can be cathodoluminescence, emission of an Auger electron, or emission of an X-ray of energy characteristic of the emitting element). Due to the thickness of many SEM samples being essentially infinite compared to the mean free path of the species detected, it must be noted that the different species are able to escape from the sample at different depths (*e.g.* backscattered electrons have much higher energy than secondary electrons, so can escape from deeper within the sample, see Figure 18). The detection and applicability of these interactions for the examination of materials will be discussed below.

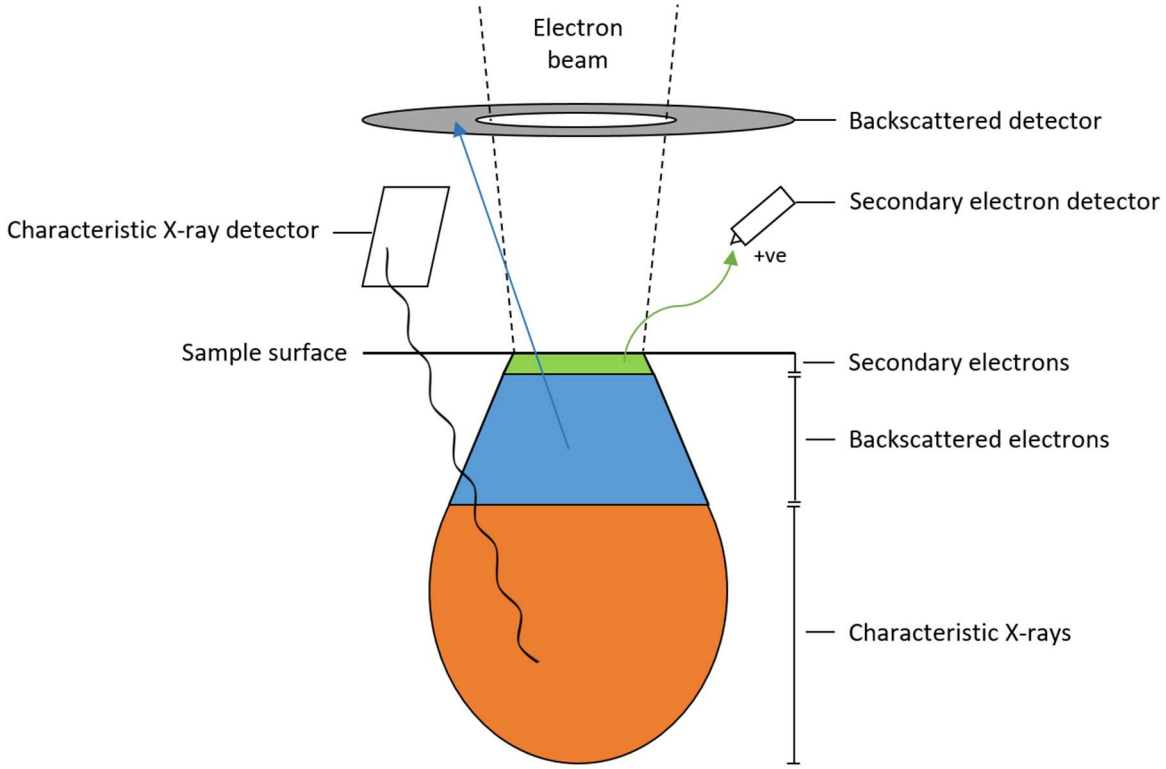

Figure 18: Diagrammatic illustration (not to scale) of the interaction depth and escape depth of the incident electron beam and the species detected in a standard SEM.

3.4.3 Application

It is obvious that the operation and application of electron microscopes is vastly different to that of visible light microscopes. The components of an electron microscope can be divided according to the path of an electron as it passes from source to detector. The most important component of any microscope is the lens(es). Electron lenses take advantage of the elementary charge of the electron by applying a magnetic field parallel to the optical axis, which causes off-centre electrons to spiral towards the centre of the optical axis as they pass through the lens.

The components common to all electron microscopes are the electron gun (where the electron beam is initially produced, by either the thermionic effect or the field effect), some number of condenser lenses (to focus the electron beam), the sample stage, and the detector(s), but both TEM and SEM systems have additional features not often seen in the other.

The path travelled by an electron beam through a standard TEM column is as follows: the electron beam is produced at the electron gun, and is focussed by one or more condenser lenses onto the region of interest on the sample, where it then passes through (TEM sample holders often have multiple axes of tilt to allow for collection of the diffraction patterns of different diffraction planes). The transmitted beam than passes through one or more projector lenses (the projector lens(es) are focussed at the sample for imaging, or at the back focal plane for diffraction), and finally arrives at the detector (either a phosphor screen for viewing the image by eye, or a CCD for digitisation). Additional detectors commonly found in TEM systems are electron energy loss spectroscopy (EELS) detectors and energy-dispersive X-ray (EDX) detectors, which are both usually mounted in backscattered configuration (*i.e.* above the plane of the sample, due to the common angles of scattering of the species of interest).

The path travelled by an electron beam through a standard SEM is as follows: the electron beam is produced and focussed, then passes through the scanning coils, which deflect the beam in a raster pattern onto the surface of the sample. Unlike TEM, the sample is essentially infinitely thick with respect to the mean free path of the incident electrons, and the mode of imaging depends on the species being imaged (no electrons are transmitted through the sample). When using backscattered electron imaging, the contrast of each point depends on the average Z of the atoms at each point, giving compositional imaging. When using secondary effects, the contrast of each point depends on the overall number of secondary electrons escaping the sample surface, giving topographic mapping due to electrons escaping from different regions of the sample (*e.g.* a surface ridge easily allows a large number of electrons to escape compared to a trench of equivalent dimensions). As with TEM, if EDX detectors are present they are positioned above the sample in a backscattered geometry.

The major techniques used in this work are backscattered electron (BSE) imaging, where the compositional contrast is used to identify different regions of the sample (*e.g.* the glass and ceramic phases of a typical glass-ceramic), and EDX spectroscopy and spectroscopic mapping, where the energies of the X-rays emitted are characteristic to the emitting element and their relative intensity can then be used to either examine the composition in a single region or form maps of elemental distribution over a larger area. It must be noted that for elemental composition to be accurately and quantitatively determined by EDX the instrument and detectors must be calibrated with a range of standards of known composition, and where EDX is used in this work it is only semi-quantitative.

3.5 Raman spectroscopy

3.5.1 Theory

Raman scattering is a specific type of inelastic scattering of electromagnetic radiation, first observed experimentally in small organic molecules by, and subsequently named after, Indian physicist V. S. Raman.[192] Raman observed that when a material was irradiated with monochromatic light, small fractions of the scattered light had energies higher or lower than the incident radiation.

It is now known that this is caused by inelastic scattering of some incident photons as they interact with matter. If the scattered photons have energy lower than the incident photons, the energy difference is known as the Stoke shift; if their energy is higher, the energy difference is known as the anti-Stokes shift. Stokes and anti-Stokes Raman scattering are caused by the same theoretical mechanism, but with different starting and energy levels within the material (see Figure 19).

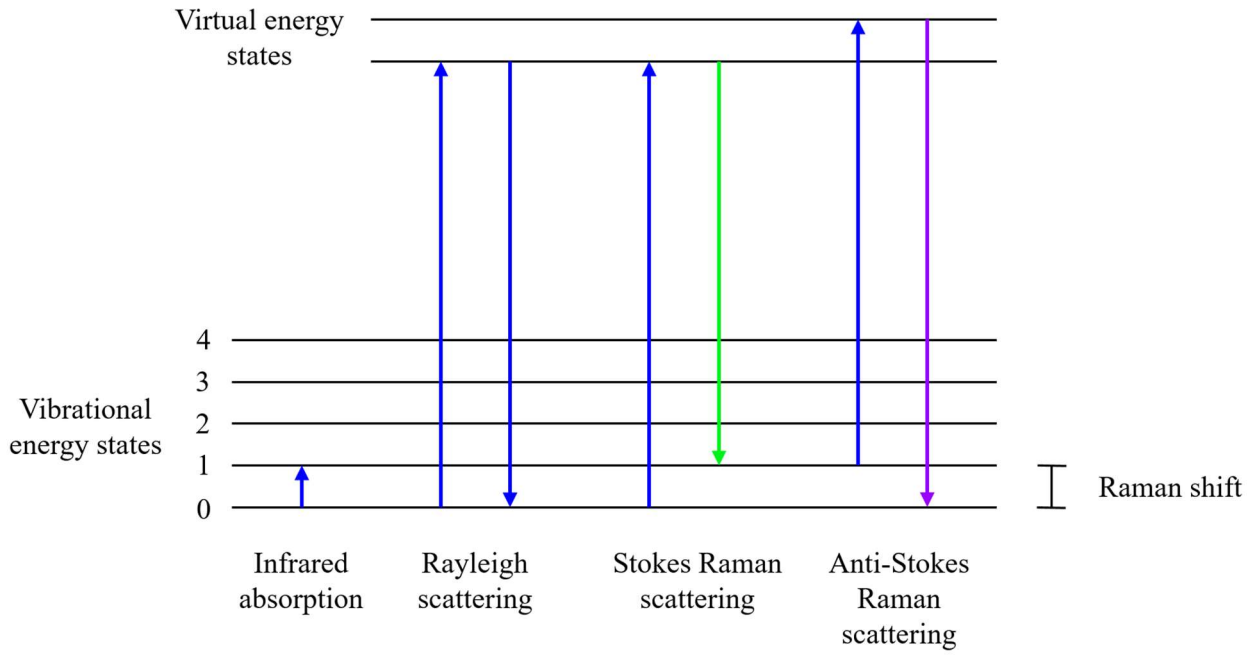

Figure 19: Diagrammatic representations of different types of scattering of light by molecular vibrations. Note the change in photon energy (shown here as a change in colour) before and after the Stokes and anti-Stokes scattering.

The loss (or gain) of energy relative to the incident beam is caused by the final vibrational energy state being different to the initial state. In Raman scattering, the molecule is excited from an initial vibrational energy state to a short-lived virtual energy state. When the virtual energy state decays, it may return to the initial vibrational energy state (the emitted photon having the same energy as the incident photon) or to a different vibrational energy state. If the final state is of higher energy than the initial state, the emitted photon must be shifted to a lower energy to conserve the total energy of the system (this is the origin of the Stokes shift). If the final state is of lower energy than the initial state, the emitted photon must be shifted to a higher energy (this is the origin of the anti-Stokes shift). The vast majority of photons scattered by the sample will not exhibit Stokes or anti-Stokes shifts, and will have been elastically scattered (Rayleigh scattering). For the Raman scattered photons to be detected, the photons scattered by the sample must be separated according to their energy, to remove any that have the same energy as the incident beam.

Although on the surface it may appear that Raman spectroscopy and infrared (IR) spectroscopy examine the same phenomena of available vibrational energy states, the selection rules of each are very different. For a vibration to be IR-active, there must be a change in dipole moment of the molecule being probed. For a vibration to be Raman-active, there must be a change in the dipole-

dipole polarisability of the molecule. As an example, CO_2 is a linear molecule with two different stretching vibrational modes. The asymmetric O-C-O stretch has a change in dipole moment, and is IR-active, whereas the symmetric O-C-O stretch has no change in dipole moment, but does have a change in polarisability, and so is Raman active (see Figure 20). The rule of mutual exclusion states that, for a centrosymmetric molecule (or, to a reasonable approximation in a solid, a centrosymmetric moiety) no vibration mode is both IR- and Raman-active.

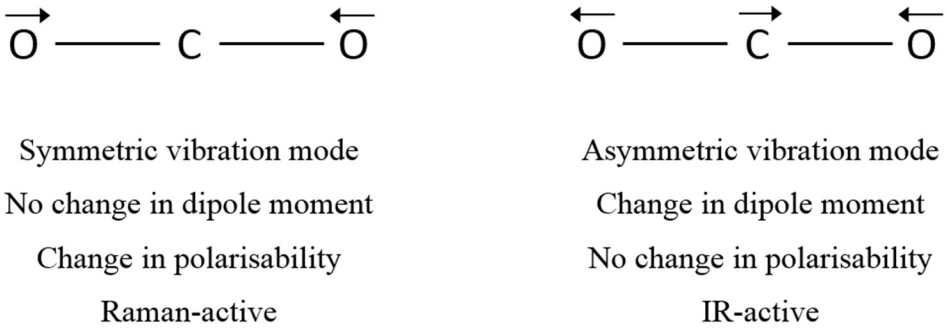

Figure 20: Comparison of the two stretching modes of CO_2. The symmetric vibration mode is Raman active; the asymmetric vibration mode is IR-active. Bending modes are not shown.

The Raman spectroscopy of crystalline solids follows much of the same theory as that of molecular Raman spectroscopy, with a few differences. Most of the vibrational modes within a crystalline solid are similar to the analogous molecular vibrations, for example, the A_g vibration modes of the brannerite structure are caused by symmetric stretching of O-B-O moieties.[141] However, the continuous nature of crystalline solids leads to vibrational modes not observed in isolated molecular systems (*i.e.* gas or solution phase molecular Raman spectroscopy), the most commonly observed of these are phonon vibration modes, where the vibration is moving through the crystal, rather than being isolated or centred around a specific moiety.

3.5.2 Application

Basic modern Raman spectrometers are simple, and, though the method of collection of Raman spectra depends on the material being examined, use the same fundamental setup. The light used to excite the sample is most usually in the form of a monochromatic laser, with wavelengths in the visible or near-IR regions. Optics focus and direct the laser onto the sample, and the output light passes through a filter to remove photons of unchanged energy (relative to the incident laser) before reaching a detector.

For solid samples (usually a monolith or compacted powder) the most common technique is Raman microspectroscopy, based on an optical microscope. The light from standard microscope lamps is used to locate the sample region of interest, and the same optics can be used with low laser power to properly focus the probe. Once spectrum collection is started, the laser light then travels from the sample through the microscope. Photons with the same energy as the excitation laser are removed as the beam passes through one or more filters, and the remainder pass through a

spectrometer, dispersing the beam by wavelength. This can be a crystal monochromator, but is more commonly a simple diffraction grating. The relative intensities of each energy range are collected by a detector, usually a CCD.

Liquid phase, solution phase, and gas phase samples can be analysed in a Raman microscope, but a transmission geometry spectrometer is more usually used when the sample does not strongly absorb the excitation laser wavelength. Transmission Raman spectrometers are essentially the same as Raman microscopes, with the major difference that the beam passes through the sample before reaching the spectrometer, rather than returning through the microscope column. Often transmission Raman spectrometers do not contain any optics for observation of the sample by the operator, as the samples tend to be homogeneous (*i.e.* in a solution or gas).

3.6 Thermal analysis techniques

3.6.1 Background and theory

When examining the behaviour of materials, it is important to understand their stability with respect to temperature. This is particularly applicable to systems that could undergo decomposition, crystallisation, melting, or any other changes that may have a deleterious effect on the final material.

The most commonly used thermal analysis technique is thermogravimetric analysis (TGA), where a sample of the material of interest is heated to a temperature of interest, whilst the mass of the sample is monitored. TGA can be used to examine changes in sample mass as the material changes as a function of temperature. Examples of commonly investigated processes include dehydration (mass loss as water is removed) and oxidation (mass gain as material takes up O_2). In the modern laboratory it is common for gravimetric data to be gathered simultaneously with one or more secondary techniques, including mass spectrometry (MS), differential thermal analysis (DTA), and differential scanning calorimetry (DSC).

Mass spectrometry is a broad field, commonly used in many scientific disciplines, that is concerned with identifying the species present in a sample. In practice, most MS techniques do this by measuring the masses of charged species as a function of their charge ratio m/z (where m is the molecular mass of the ion, and z is the ion charge). When applied to thermal analysis techniques, MS is most commonly used to identify the species present in the off-gas. This is most useful when examining the thermal decomposition of materials, an excellent example of this is the TGA/MS of cements, where the cause of each mass loss (dehydration, decarbonation, *etc.*) observed by the TGA can be assigned to the loss of certain species, as identified by MS.

Although gravimetric measurements are useful in many situations, materials often undergo changes on heating that do not cause a mass change (*e.g.* phase transitions, crystallisation). The two most common techniques used to examine these phenomena are DTA and DSC. Both DTA and DSC use the same underlying principle (but with slightly different implementations), where

these changes are detected by a difference in heat flow to or from the sample caused by the process under examination.

DTA compares the temperatures of the sample and a reference (usually an empty crucible of the same material as the sample crucible) to identify the temperatures that endothermic or exothermic events occur. For example, if the sample melts (an endothermic process), the temperature of the sample will decrease relative to the reference as the phase transition occurs, causing a peak in the DTA curve at that temperature. In an analogous way, DSC compares the energy necessary to heat the sample and the reference at each temperature, allowing for identification of both the temperature and energy of the process under examination.

3.6.2 Application

In-line with the simple nature of thermal analysis techniques, the earliest examples of TGA-specific instruments were essentially a method of weighing and a method of heating coupled together, for example by using a balance with a long sample holder, the sample can be held within a furnace, while the balance is kept at room temperature. Modern TGA instruments are more specialised versions of these original instruments, consisting of a high accuracy balance and a furnace specially shaped to ensure no thermal gradients are formed over the region where the sample is held. Samples can be heated in air or under different atmospheres (*e.g.* N_2 or Ar to prevent oxidation of the sample during heating), depending on the experimental needs of the study.

DTA and DSC instruments have followed the same path: the first instruments were essentially a device for measuring crucible temperatures (for DTA) or energy flow (for DSC), coupled with a heating device. Modern DTA and DSC instruments follow the same theory, but, like thermogravimetric methods, have become more specialised in recent times, allowing for higher accuracy, precision, and repeatability in all aspects of these measurements.

The most important step forward in thermal analysis instrumentation was the combining of multiple techniques in parallel. Now instruments are available that can measure the sample mass change, collect DTA or DSC data, and analyse the off-gas composition using MS, in a single heating cycle.

3.7 X-ray absorption spectroscopy

3.7.1 Theory

As with other spectroscopies, X-ray absorption spectroscopy (XAS) utilises interactions between photons and matter to investigate the system of interest. In XAS, the incident photon energy is of the magnitude necessary to promote a core shell electron, either to unoccupied orbitals or to the continuum of free states (*i.e.* emission of a photoelectron). Consider a system of generic matter that contains no specific atoms: the probability of absorption of an X-ray photon has a near linear dependence with the X-ray energy, that is, lower energy X-rays are more likely to be absorbed than higher energy X-rays, resulting in a steady downward slope. When specific atoms are present, a

sharp increase in absorption is observed once the X-rays have sufficient energy to promote the core shell electrons (the Fermi energy, E_f) of these atoms; these increases in absorption are called absorption edges.

The energy position of an X-ray absorption edge is in the first case influenced by the electrostatic attraction that must be overcome between a core shell electron and the atomic nucleus. This leads to unique edge positions for each element, allowing for examination of the absorption spectra of specific elements of interest within a sample. However, the majority of X-ray absorption spectra contain more features than just the edge itself (see Figure 21). These may include: the whiteline (A), the point of greatest absorption caused by promotion of a core shell electron to the continuum; E_0 (B), a measure of the energy position of the absorption edge (different methods of determination of E_0 will be discussed below); and pre-whiteline features (C), appearing when additional empty electronic states are available (commonly referred to as pre-edge features).

After an electron has been excited to a higher energy level, a core level hole remains and must be filled during relaxation of the nucleus. In XAS measurements the core hole is usually filled by an outer shell electron. As the outer shell electron moves to the lower energy core orbital, it must lose a significant amount of energy, usually by either emission of a lower energy photon (X-ray fluorescence) or emission of an electron (an Auger electron). In the soft (low energy) X-ray regime, emission of Auger electrons is the dominant mechanism; whereas X-ray fluorescence dominates in the hard (high energy) X-ray regime.

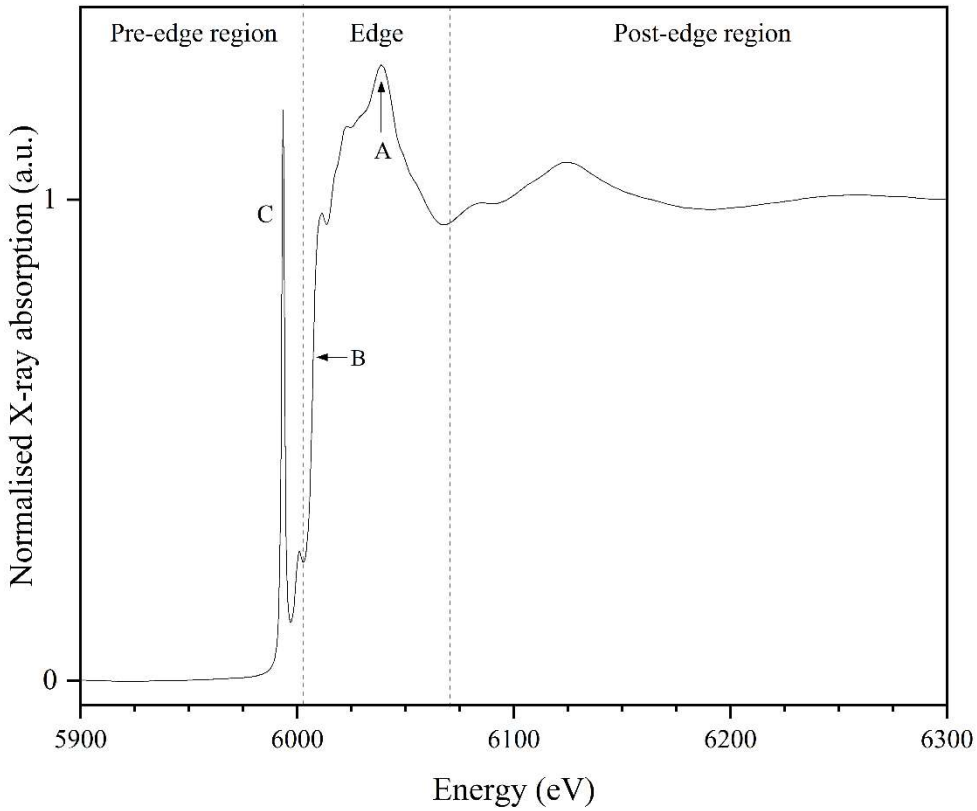

Figure 21: Normalised X-ray absorption spectrum of K_2CrO_4, divided into three regions. The whiteline, E_0, and pre-edge features are marked with A, B, and C respectively.

XAS measurements are commonly divided into two different categories, depending on the region of interest: X-ray absorption near-edge spectroscopy (XANES) examines the pre-edge and edge regions (in the energy range -50 to +150 eV relative to E_0); and extended X-ray absorption fine structure spectroscopy (EXAFS) examines the edge and post-edge regions (+1000 eV or more relative to E_0).

The shapes of the pre-edge and edge regions (those most important in XANES analysis) are dependent on the density of states available to the excited photoelectron, which is chiefly determined by the oxidation state and coordination environment of the central scattering atom. The post-edge region consists of complex oscillations related to scattering of the ejected photoelectron by neighbouring atoms. This means that analysis of EXAFS spectra can yield information on the local structure around the central scattering atom, including the types, numbers, and distances of neighbouring atoms, as well as information on any local (dis)ordering.

In this work U and Ce L_3 edge XANES has been widely applied to assist in the determination of the average U and/or Ce oxidation states present in materials. The analysis of XANES data will be described below.

3.7.2 Application

Fundamentally, XAS experiments only require a method to examine the change in X-ray absorption as it varies over the energy range of interest. The collection of XAS spectra is most often performed

at synchrotron photon sources, utilising a monochromatic beam of X-rays that is scanned over the energy range of interest. In modern practice, there are three main methods of XAS spectrum collection: transmission, fluorescence, and electron yield.

In transmission mode measurements, the intensities of the incident and transmitted beams are simply directly measured before and after interaction with the sample, commonly with gas ionisation chambers (for a brief description, see Section 3.3 X-ray diffraction, *Application*). However, in practice the sample thickness (usually in terms of material concentration and absorption length) must be optimised to actually allow for transmission of an appreciable fraction of the incident beam, whilst sufficient (*i.e.* detectable) absorption can still occur. This can be achieved by the use of thin sections (for bulk solids) or suspension of a small amount of powder in an inert, low absorbance matrix (*e.g.* in this work, XAS samples were prepared as a small amount of sample in a pellet of polyethylene glycol, PEG). The use of tabulated reference data (or tools that utilise the relevant data, *e.g.* Hephaestus, part of the Demeter software suite[193]) means that the ideal amount of sample can be easily calculated and appropriate samples prepared prior to visiting a synchrotron X-ray beamline.

If the nature of the sample is such that transmission measurements would be expected to fail (*e.g.* if a thin section or powder is not available, or materials with very high or low absorber concentrations), fluorescence mode measurements can be performed. Rather than directly measuring the transmitted beam intensity, sample absorbance is inferred by the number of fluorescent X-rays emitted by the sample (often reported as total fluorescence yield, TFY). Though not a true measure of absorbance, in most systems the TFY is highly correlated with the absorbance, giving an excellent approximation, particularly in the hard X-ray regime. Fluorescence mode detectors are placed perpendicular to the direction of the incident beam (in order to avoid detecting the incident or transmitted beam of X-ray that may have been scattered), and are often active even during transmission mode measurements to provide an extra measurement in case the transmission mode measurements are not viable (*e.g.* if a thin section prepared for a transmission experiment has not been adequately thinned).

Analogous to measurement of the TFY, examination of the yield of Auger electrons can give a similar measure of absorption at the sample for comparison with the incident beam intensity. As discussed above in Section 3.4 *Electron-sample interactions*, X-rays can travel much further through condensed matter than electrons, particularly since an electron can experience many different secondary scattering events during travel. This leads to two different methods of detection: total Auger electron yield (AEY) and total electron yield (TEY). AEY measures the yield of Auger electrons only, and is highly surface sensitive (often probing only the top nanometre of the sample). In comparison, TEY is dominated by secondary electrons produced during scattering of the Auger electrons, and is less surface sensitive than AEY (though typically still probing less than 10 nm deep).

3.7.3 XANES data analysis

In this work XANES has been utilised as an element-specific probe of oxidation state for U and Ce. The two methods of XANES analysis used in this work are linear combination fitting (LCF) and linear analysis of the observed E_0 values, and both will be briefly outlined here.

Examination of the values of E_0 is perhaps the simplest method of comparison of XANES spectra. If there is no significant change in spectral shape in the system of interest (*e.g.* U L_3 edge XANES of U^{4+} and U^{5+} species) and in the absence of other factors, E_0 has a near-linear relation to oxidation state. This means that the oxidation state of the element of interest can be interpolated between two carefully selected reference compounds of known oxidation state (*e.g.* utilising $U^{4+}Ti_2O_6$ and $U^{5+}_{0.5}Yb_{0.5}Ti_2O_6$ when examining a brannerite-structured material of unknown U oxidation state). However, this method is not suitable for all measurements or all materials, particularly in systems where more than one variable affecting E_0 is present. For example, where there is significant variation in both oxidation state and coordination number (as both affect the effective nuclear charge of the absorbing atom), or where multiple scattering has a strong impact on the spectral shape in the XANES region.

A further complicating factor, especially in the comparison of data to literature values, is the number of different ways E_0 is commonly derived from spectra. E_0 is most often set to the energy at which there exists a maximum in the first derivative of absorption (with further complication caused by spectra with complex shapes, which may exhibit multiple maxima in their first derivative). Other methods of determining E_0 include: the energy position at a normalised absorption of 0.5 (commonly referred to as E_0 at half the edge step), the first point of inflection of the normalised spectrum, whiteline peak position, and the zero crossing point of the second derivative (for high quality data this is equal to the energy position of the maximum in the first derivative).

Linear combination fitting uses statistical fitting of the spectrum of interest with two or more standard spectra, with the aim of minimising the difference between the observed spectrum and the spectrum calculated from a weighted average of standard spectra. The standards may be spectra of reference compounds of known oxidation state and coordination environment (*e.g.* $U^{4+}O_2$, $U^{6+}O_3$, $U^{4+}Ti_2O_6$, $U^{5+}_{0.5}Yb_{0.5}Ti_2O_6$ and $CaU^{6+}O_4$ are all common U reference compounds), or spectra of notable or otherwise well-characterised samples within the system (*e.g.* using the spectra of materials with batched compositions of UTi_2O_6 and $U_{0.5}Yb_{0.5}Ti_2O_6$ when examining materials within the system $U_{1-x}Yb_xTi_2O_6$).

A successful fit will report the contributions from each standard spectrum, the overall calculated spectrum, a plot of the observed/calculated difference, and one or more statistical measures of the goodness of fit. The use of modern computers and software when performing LCF makes it possible to very rapidly examine many different combinations of standards, and which combinations will best fit the data. However, LCF struggles to fit some systems, particularly those that exhibit a large change in spectral shape over the range of oxidation states of interest (*e.g.* Ce^{3+}

and Ce^{4+} L_3 edge XANES spectra display significantly different spectral envelopes). This can be partially addressed by utilising spectra from within the system of interest, but this can introduce further assumptions that may be a source of additional, non-statistical error (*e.g.* assuming that one sample is fully oxidised and so is suitable for use as a standard).

3.7.4 High energy resolution fluorescence detected XAS

A recent specialised technique of XAS is high energy resolution fluorescence detected (HERFD) XAS. Rather than measuring the total fluorescence yield as discussed above, the intensity of a specific emission is measured as a function of the incident energy (for HERFD U M_4 XAS this is the U M_β emission at approximately 3337 eV). In order to isolate the emission line of interest, the fluorescent X-rays are monochromated, usually by employing one or more spherically bent crystal analysers (SBCA) in a focussing geometry. It should be noted here that, in the same manner as total fluorescence yield measurements, this is not a true measure of absorbance but is an excellent approximation for many systems.

An important advantage of HERFD XAS is the increase in spectral resolution compared to conventional transmission or fluorescence measurements. Conventional XAS resolution is limited by the short lifetimes (for the majority of edges of interest) of the excited state generated on emission of a photoelectron, with shorter lifetimes giving broader spectral profiles due to the uncertainty principle. HERFD XAS line broadening is of the magnitude of the emission core-hole lifetime broadening only, and in some cases is actually smaller (this must be understood in the context of resonant inelastic X-ray scatterings, RIXS, which is outside the scope of this work).

The benefit of this high spectral resolution becomes apparent when the possible chemical shifts of the species of interest are of a similar or lower magnitude. For example, in the U M_4 edge HERFD XANES shown in Figure 22 the contributions of U^{4+} and U^{5+} to the spectrum of the unknown material can be easily differentiated (the features at approximately 3725.15 eV and 3726.35 eV respectively). This differentiation of chemical environments makes linear combination fitting particularly useful in the analysis of HERFD XAS spectra.

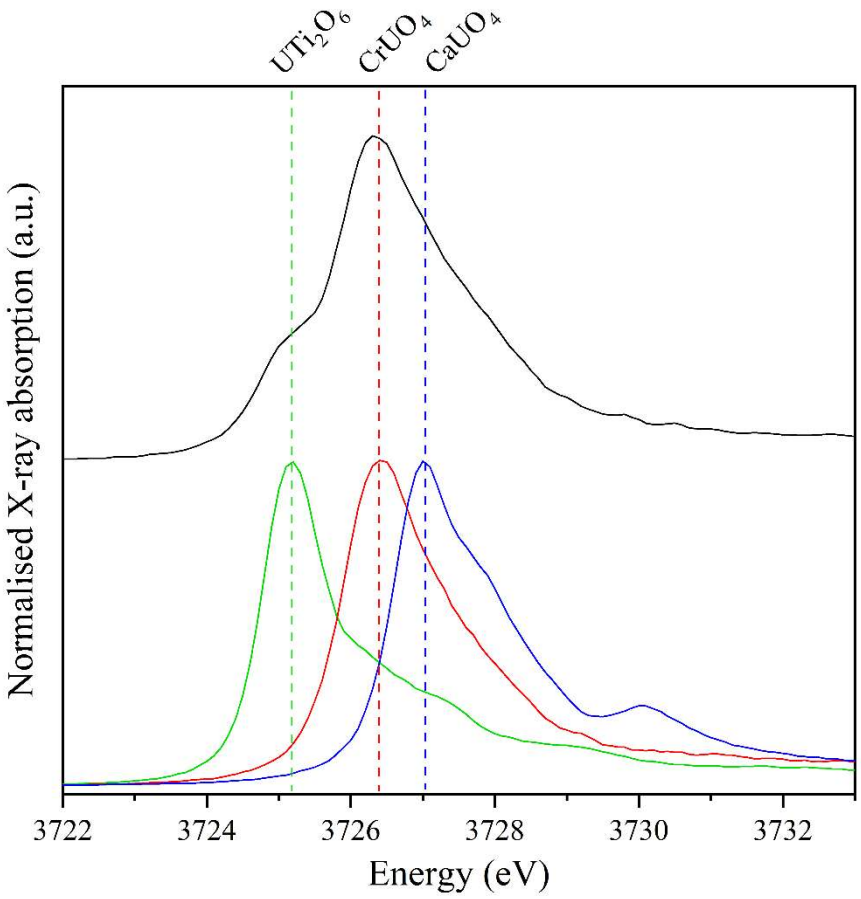

Figure 22: U M_4 edge high energy resolution fluorescence detected (HERFD) X-ray absorption spectra of a U-containing material of unknown oxidation state (black) and three reference materials of known oxidation state: $U^{4+}Ti_2O_6$ (green), $CrU^{5+}O_4$ (red), and $CaU^{6+}O_4$ (blue).

4 The formation of UTi_2O_6 glass-ceramic composites

4.1 Introduction

After reviewing the available literature, it was determined that, although many U^{5+} brannerite glass-ceramic composites had been synthesised, no investigation into the formation of stoichiometric UTi_2O_6 in glass had been reported. This formed the basis of the research examining the compatibility of UTi_2O_6 with a glass system commonly used in glass-ceramic composites, $Na_2AlBSi_6O_{16}$.

An initial investigation on the formation of UTi_2O_6 in this glass system was performed, exploring the reaction temperatures required for brannerite formation, as well as the impact of hyperstoichiometric amounts of TiO_2 on the crystalline phases produced. After the successful production of UTi_2O_6 glass-ceramic composites, the impact of the glass:ceramic ratio was examined, by producing a range of glass-ceramic composites with varying ceramic contents. The compatibility of this system with hot isostatic pressing (HIP) was also examined.

Further to these investigations, it has been reported in the literature that the formation of zirconolite, another titanate ceramic phase relevant to immobilisation of high actinide wastes, in a glass-ceramic composite has been reported to be sensitive to the glass composition.[194] In order to determine whether the glass composition has a similar impact on brannerite formation, a further suite of glass-ceramics was prepared, targeting UTi_2O_6 as the ceramic phase in glasses within the $Na_2Al_{2-x}B_xSi_6O_{16}$ system.

The results of the initial investigation were published in the Journal of Nuclear Materials: "The formation of stoichiometric uranium brannerite (UTi_2O_6) glass-ceramic composites from the component oxides in a one-pot synthesis" (MC Dixon Wilkins, MC Stennett, ER Maddrell, NC Hyatt, *J. Nucl. Mat.,* 2020, **542**, 10.1016/j.jnucmat.2020.152516). The author's contribution was: the production of samples, analysis by X-ray diffraction and SEM/EDX, Rietveld analysis of diffraction data, XAS data analysis, and writing of the manuscript.

The results of the investigation into the impact of the glass:ceramic ratio and material compatibility with HIP were presented by the author at the THERAMIN2020 conference (Manchester, UK, 4-6th February 2020), and the conference proceedings published in a special edition of the IOP Conference Series: Materials Science and Engineering: "Synthesis and characterisation of high ceramic fraction brannerite (UTi_2O_6) glass-ceramic composites" (MC Dixon Wilkins, ER Maddrell, MC Stennett, NC Hyatt, *IOP Conf. Ser.: Mater. Sci. Eng.,* 2020, **818**, 10.1088/1757-899X/818/1/012018). The author's contribution was: production of samples (including HIP operation and sample preparation), analysis by X-ray diffraction and SEM/EDX, and writing of the manuscript.

The results of the final investigation into the effect of glass phase composition on UTi_2O_6 formation have been prepared for submission to a relevant journal. The author's contribution was: production of samples, analysis by X-ray diffraction and SEM/EDX, and writing of the manuscript.

4.2 The formation of stoichiometric uranium brannerite (UTi_2O_6) glass-ceramic composites from the component oxides in a one-pot synthesis

Journal of Nuclear Materials 542 (2020) 152516

Contents lists available at ScienceDirect

Journal of Nuclear Materials

journal homepage: www.elsevier.com/locate/jnucmat

The formation of stoichiometric uranium brannerite (UTi_2O_6) glass-ceramic composites from the component oxides in a one-pot synthesis

Malin C. Dixon Wilkins[a,*], Martin C. Stennett[a], Ewan Maddrell[b], Neil C. Hyatt[a]

[a] Department of Materials Science and Engineering, University of Sheffield, UK
[b] National Nuclear Laboratory, Sellafield, Cumbria, UK

ARTICLE INFO

Article history:
Received 13 July 2020
Revised 1 September 2020
Accepted 6 September 2020
Available online 11 September 2020

Keywords:
Glass-ceramics
Radioactive wasteforms
Brannerite
Uranium compounds

ABSTRACT

Brannerite glass-ceramic composites have been suggested as suitable wasteform materials for high-actinide content wastes, but the formation of glass-ceramic composites containing stoichiometric uranium brannerite (UTi_2O_6) has not been well-studied. Uranium brannerite glass-ceramic composites were synthesised at by a one-pot cold-press and sinter route from the component oxides. As a comparison, two further samples were produced using an alkoxide-nitrate route. A range of compositions with varying molar ratios of uranium and titanium oxides (from 1:2 to 1:3.20) were synthesised, with a range of different heat treatments (1200 °C for 12–48 h, and 1250 °C for 12 h). All compositions were analysed by X-ray diffraction, scanning electron microscopy, energy dispersive X-ray spectroscopy, and X-ray near-edge spectroscopy, and found to contain UTi_2O_6 as the majority crystalline phase forming within a glass matrix of nominal stoichiometry $Na_2AlBSi_6O_{16}$. In compositions with UO_2:TiO_2 ratios of 1:2 and 1:2.28, particles of UO_2 were observed in the glass matrix, likely due to dissolution of TiO_2 in the glass phase; this was prevented by the addition of excess TiO_2. This work demonstrates the suitability of this system to produce highly durable wasteforms with excellent actinide waste loading, even with a simple one-pot process. Some grains of brannerite consist of a UO_2 particle encapsulated in a shell of UTi_2O_6, suggesting that brannerite crystallises around particles of UO_2 until either the UO_2 is fully depleted, or the kinetic barrier becomes too large for further diffusion to occur. We propose that the formation of brannerite within glass-ceramic composites at lower temperatures than that for pure ceramic brannerite is caused by an increase in the rate of diffusion of the reactants within the glass.

1. Introduction

Alongside glass and ceramic materials, glass-ceramic composites are one of the promising candidates for immobilisation of high activity radioactive wastes [1–4]. They have attracted particular attention for use as flexible host matrices for high actinide content wastes that are otherwise unfit for reprocessing [5–7]. A suitable glass-ceramic composite has the benefit of high actinide waste loading due to the ability of ceramics to contain much higher actinide contents than glasses, but still retain the chemical flexibility of glasses, able to contain and immobilise contaminant and/or fission product species [8].

Brannerite (UTi_2O_6) has been proposed as a suitable target ceramic phase in glass-ceramics due to the retention of the brannerite structure even when doped with extremely high proportions of actinide elements (stoichiometric UTi_2O_6 has a uranium content of > 55% by weight) [9,10]. It crystallises in the monoclinic space group *C*2/*m* (No. 12), with a structure consisting of sheets of staggered, edge- and corner-sharing (TiO_6) octahedra (similar to TiO_2 anatase), with adjacent sheets connected by chains of corner-sharing (UO_6) octahedra [11,12]. Examples of natural brannerites (with the oldest being found in host rocks 1.58 billion years old, and the youngest between 5 and 11 million years old) [13,14] are generally found to have been amorphised over time by their high actinide content (metamictisation), but still retain a large proportion of their original uranium inventory, with A-site uranium atoms per formula unit of 0.4 to 0.9 [15,16]. It is also of interest that natural brannerites have been found to contain a wide range of dopant cations (including Ca, Pb, Th, Y, and REE on the

* Corresponding author.
E-mail address: mdixonwilkins1@sheffield.ac.uk (M.C. Dixon Wilkins).

https://doi.org/10.1016/j.jnucmat.2020.152516

U site, and Fe, Al, and Si on the Ti site [15–17]), as the introduction of lower valent cations (commonly Gd^{3+}, Ca^{2+}, or Y^{3+}) has been found to have a strong effect on the formation of the brannerite structure under oxidising conditions by charge balancing higher valent U^{5+} and U^{6+} cations [9, 18–20]. If brannerite is to be considered as a wasteform for disposal of damaged or degraded MOX fuels, then this flexibility with regards to cation content allows for introduction of neutron absorbers such as Hf and/or Gd to address criticality concerns. In this respect, it is notable that Turuani et al., recently reported a comprehensive investigation of lanthanide abundance in brannerites, which was shown to reflect the geological conditions of formation [16].

The direct synthesis of ceramic UTi_2O_6 from the component oxides is hampered by slow diffusion through the solid state. This can be simply remedied by increasing the reaction temperature (*e.g.* reacting at 1400 °C rather than 1300 °C), increasing the reaction time, or by introducing an intermediate re-grinding of the sample to break up reacted material, re-exposing the reactants. Other synthetic routes reported in the literature use wet chemical processes to ensure mixing of the reactants occurs at the nano- or atomic-scale, followed by a reaction at high temperature. The most commonly reported method is an alkoxide-nitrate route, utilising U-nitrate and Ti-isopropoxide (this is discussed in more detail below), but other methods using soluble U and/or Ti precursors have been reported. Mesbah et al. reported a comparison of four different synthetic routes, including a dry oxide-based route, the alkoxide-nitrate route, an acetate-sulphate route, and a hydroxide route starting from U-chloride and Ti-isopropoxide [21].

Although brannerite glass-ceramic composite materials have been reported in the literature, only a single study has attempted the production of end-member U-, Th-, and Ce-brannerite glass-ceramic composites. In that study, we observed that UTi_2O_6 (and to a lesser extent $ThTi_2O_6$) crystallises well in the $Na_2AlBSi_6O_{16}$ glass system, assuming that atmospheric pO_2 is conducive to an average composition with overall 4+ charge on the A-site. Glass-ceramic composites with UTi_2O_6 as the ceramic phase have not yet been extensively studied, but are of interest as a model system for understanding structure – composition – property relationships. The majority of brannerite phases reported as crystallising in glass have been U^{5+} species, with M^{3+} doped onto the U-site to act as a charge balancer (including trivalent Y, Eu, Tb, Dy and mixed tri- and tetravalent Ce) [22–25]. All previous uranium brannerite glass-ceramics introduced the ceramic phase as a ceramic precursor prepared by calcining a stir-dried alkoxide-nitrate reaction mixture at 700 °C under either air or Ar (for Pu-containing samples). The ceramic precursor was then mixed with a glass precursor, pressed into pellets, and heat treated at 1200 °C. For the purpose of industrial application, it would be useful to develop a one-pot synthetic route for brannerite glass-ceramics, from the component oxides and a glass precursor, reducing the number of handling operations necessary to produce the final wasteform. The development of such a synthesis route, applied to stoichiometric UTi_2O_6 brannerite glass-ceramics, is the focus of this contribution. It is envisaged that, in a conceptual industrial process, wasteforms would be produced by hot isostatic pressing (HIP). This means that the wasteform material would ideally form at or below 1300 °C (the maximum service temperature for stainless steel HIP canisters), to avoid necessitating the use of more expensive and exotic alloys. This presents a challenge to the formation of pure or doped ceramic UTi_2O_6 by solid state reaction, which generally requires temperature in excess of 1300 °C (typically in the range of 1320–1350 °C).

2. Experimental

Brannerite glass-ceramic compositions were prepared by a one-pot cold-press and sinter method. The glass phase (composition $Na_2AlBSi_6O_{16}$) was introduced as a batched precursor, prepared by calcining a stoichiometric mixture of H_3BO_3, Na_2CO_3, Al_2O_3 and SiO_2 at 600 °C for 6 h. The ceramic components were added as the oxides, UO_2 and TiO_2 (anatase).

A stoichiometric mixture of UO_2 and TiO_2 (as UO_2 was observed in compositions with required amounts of UO_2 and TiO_2 (excess TiO_2 was added to form some compositions (see Table 1)), were milled together with the precursor mixture in a Fritsch Pulverisette 23 reciprocating ball mill for 5 min at 30 Hz. The resulting slurry was dried in an oven at 85 °C and the powder retrieved and broken up using a mortar and pestle. The milled powders were pressed into 10 mm diameter pellets under 2 t (approx. 250 MPa). The green pellets were placed into crucibles on a bed of coarse ZrO_2 to prevent attachment to the crucible surface, then heat treated in a tube furnace under an inert (Ar) atmosphere. Any ZrO_2 adhered to the outside of the pellets was manually removed.

The heat-treated pellets were broken into pieces for characterisation. Powder X-ray diffraction (XRD) was used to identify the phases present (Bruker D2 Phaser using Ni-filtered Cu Kα radiation), and the relative quantities of the crystalline phases were qualitatively measured using a standard Rietveld refinement method, utilising the software package TOPAS [26,27]. For the purpose of crystalline phase quantification, the amorphous content was neglected, as it contributed little to the overall diffraction pattern in the presence of UTi_2O_6 and UO_2. The background was modelled with a tenth order shifted Chebyshev polynomial and peak shapes were modelled using Pseudo-Voigt functions. The unit cell parameters of each phase (UTi_2O_6 and UO_2, with TiO_2 in some compositions) were allowed to refine, along with the atomic positions of U and Ti. XRD is insensitive to light elements such as O, especially in the presence of heavy elements such as U, so the atomic positions of O were not refined.

Scanning Electron Microscopy with coupled Energy Dispersive X-ray analysis (SEM-EDX) was used to examine the microstructure and microchemical composition of the glass-ceramic products (Hi-

Table 1
As-batched oxide stoichiometries (samples U9 and U10 were produced following an alkoxide-nitrate synthesis) and details of heat treatments for different UTi_2O_6 glass-ceramics. The difference in each composition relative to a parent composition is underlined (*i.e.* U5 to U8 had the same starting composition as U3, but underwent different heat treatments).

ID	Glass	UO_2	TiO_2	U:Ti molar ratio	Heat treatment
U1	50.00%	31.42%	18.58%	1:2	1200 °C, 12 h, Ar
U2	48.75%	30.63%	20.62%	1:2.28	1200 °C, 12 h, Ar
U3	47.50%	29.85%	22.65%	1:2.57	1200 °C, 12 h, Ar
U4	45.00%	28.28%	26.71%	1:3.20	1200 °C, 12 h, Ar
U5	47.50%	29.85%	22.65%	1:2.57	1200 °C, 24 h, Ar
U6	47.50%	29.85%	22.65%	1:2.57	1200 °C, 36 h, Ar
U7	47.50%	29.85%	22.65%	1:2.57	1200 °C, 48 h, Ar
U8	47.50%	29.85%	22.65%	1:2.57	1250 °C, 12 h, Ar
U9	50.00%	31.42%	18.58%	1:2	1200 °C, 12 h, H_2/N_2
U10	47.50%	29.85%	22.65%	1:2.57	1200 °C, 12 h, H_2/N_2

tachi TM3030, operating at 15 kV; Bruker Quantax 70 EDX system). Samples were prepared for SEM-EDX by mounting in a cold set epoxy resin, before polishing to an optical finish using increasingly finer grades of abrasive paper and diamond suspensions (finishing at 1 μm) and coating with a conductive carbon layer.

The alkoxide-nitrate synthesis is described in detail elsewhere [22]. The reaction mixture was calcined for 24 h at 700 °C under a reducing atmosphere (5% H_2 in N_2). The calcine was then used in place of UO_2 and TiO_2 to form a glass-ceramic following the cold-press and sinter method detailed above. Two compositions were made by this route: U9, with a U:Ti ratio of 1:2, and U10, with a U:Ti ratio of 1:2.57, matching other compositions in this study prepared by a one-pot cold press and sinter process, as well as similar titanate ceramics and glass-ceramics in the literature (many contain a small excess of Ti-isopropoxide to encourage full reaction of the mixture and to account for loss of isopropoxide as it readily hydrolyses in air and disperses).

In order to confirm the uranium oxidation state, X-ray absorption spectra were acquired in fluorescence mode at Diamond Light Source beamline B18 [28]. Diamond Light Source operates with an electron energy of 3 GeV and a beam current of 300 mA. Samples were prepared by mixing a small amount of the materials to be examined with polyethylene glycol and pressing into pellets. Spectra were collected at room temperature and pressure in the range 16,940 to 17,970 eV, with a step size of 0.3 eV, and a counting time of 200 ms per step. The energy was selected using a Si (111) monochromator, and aligned using the K-edge of an yttrium metal foil. A 36 element Ge solid state fluorescence detector was used. The data were processed and the resulting spectra analysed using the Demeter suite of programs [29].

The sample composition and heat treatments are summarised in Table 1. Of note is that additional TiO_2 was added by reducing both the targeted amount of UTi_2O_6 and glass (*e.g.* a sample with 10% additional TiO_2 can be described as a ratio of 45:45:10 glass:UTi_2O_6:TiO_2), this means that the overall weight percent of glass varies slightly between samples, from 45% to 50% (see Table 1 for further details). Previous work on glass-ceramic composites in this system has shown that the formation of UTi_2O_6 in the $Na_2AlBSi_6O_{16}$ system is relatively insensitive to the overall glass fraction, so this slight variation in glass fraction will not have a significant effect on the phase assemblages of each product [30].

3. Results

3.1. X-ray diffraction

All samples produced formed brannerite as the majority ceramic phase, with small amounts of UO_2 observed in the XRD patterns of all compositions except U8, and TiO_2 observed in those compositions made from component oxides having a target UO_2:TiO_2 ratio of 2.28 or greater (all compositions, other than U1, U2, and the alkoxide-nitrate samples U9 and U10). The results of qualitative phase abundances, as-derived from Rietveld refinements of XRD data, are shown in Table 2. Due to the presence of high molar fractions of uranium (a very strong scatterer of X-rays), the comparatively weakly scattering glass phase has a very low contribution to the overall diffraction pattern, so cannot be reliably quantified from XRD-based methods; however, qualitative observations can still be made from the trends observed. The values in Table 2 were calculated by using Rietveld refinements to obtain the relative abundances of the different crystalline phases present, then, with the assumption that all ceramic-forming precursors were accounted for in these phase abundances, reduced to the abundance present in the final glass-ceramic product, according to the as-batched weight fractions of glass and ceramic. In reality both UO_2 and TiO_2 were observed in the glass matrix, as well as in the crystalline phases, but for the purpose of identifying the trends observed in these samples, this is not a significant consideration. The as-refined unit cell parameters are in good agreement with reference values, with no significant changes caused by the differing synthetic conditions (see Supplementary Information Table 1). Some variation is seen, most obviously in the unit cell volumes, but, as the measurements did not include an internal standard, and the variation is small, we cannot confidently establish the variation to be attributable to differences in composition or synthesis.

When visually comparing the observed relative intensity of TiO_2 reflections in the series U1 to U4 (where all four samples underwent the same heat treatment, but had differing UO_2:TiO_2 molar ratios, from 1:2 in U1 to 1:3.20 in U4), it is clear that addition of hyperstoichiometric amounts of TiO_2 does not lead to elimination of UO_2; indeed, TiO_2 is observed in samples U3 (approx. 2.22 wt%) and U4 (approx. 9.22 wt%).

Similarly, the phase assemblage of compositions with the same UO_2:TiO_2 ratio heat-treated at 1200 °C, but for differing lengths of time (samples U3, and U5–7), are very similar. As the length of heat treatment was increased from 12 to 48 h, the relative abundance of UO_2 reduces slightly (from approx. 1.10 wt% in U3 to 0.64 wt% in U7), and a corresponding reduction in the relative intensity of the UO_2 (111) reflection is also seen, but does not completely disappear. Similarly, when comparing a sample heat-treated at a higher temperature (U8, fired for 12 h at 1250 °C), to one with the same UO_2:TiO_2 ratio heat-treated at a lower temperature (U3, fired for 12 h at 1200 C), there is a marked reduction in the observed intensity of the UO_2 (111) reflection (however, UO_2 is observed in SEM micrographs, see Section 3.2). These observations

Table 2
Compositional information for samples U1-10. The glass composition was measured using EDX, averaging 10 regions of glass for each composition (B_2O_3 content was assumed to be as-batched), then converted into oxide wt%. The relative amounts of the crystalline phases as-determined from Rietveld refinements of XRD data are also shown.

ID	EDX glass composition (wt%)						Refinement of crystalline phase abundances (wt%)			U:Ti molar ratio
	SiO_2	Na_2O	Al_2O_3	B_2O_3	TiO_2	UO_2	UTi_2O_6	UO_2	TiO_2	
U1	73.3	9.6	6.8	2.5	5.5	2.4	48.41 ±0.09	1.60 ±0.09	–	1:2
U2	73.9	8.9	6.1	2.5	7.3	1.4	49.89 ±0.06	1.36 ±0.06	–	1:2.28
U3	71.8	10.6	6.0	2.5	7.6	1.5	49.18 ±0.30	1.10 ±0.06	2.22 ±0.31	1:2.57
U4	73.1	9.1	5.9	2.5	8.4	1.0	44.71 ±0.43	1.07 ±0.08	9.22 ±0.43	1:3.20
U5	68.4	10.8	6.0	2.5	8.5	3.9	45.68 ±0.34	0.23 ±0.08	6.58 ±0.34	1:2.57
U6	69.3	10.8	6.0	2.5	8.2	3.2	46.71 ±0.34	0.64 ±0.08	5.14 ±0.34	1:2.57
U7	72.2	9.5	5.9	2.5	6.6	3.3	45.83 ±0.56	0.60 ±0.15	6.07 ±0.55	1:2.57
U8	72.5	9.1	6.1	2.5	6.5	3.4	45.22 ±0.53	0.17 ±0.13	7.11 ±0.52	1:2.57
U9	72.3	8.8	6.0	2.5	9.0	1.5	44.93 ±0.10	5.07 ±0.10	–	1:2
U10	70.8	9.8	5.6	2.5	10.1	1.2	51.91 ±0.09	0.59 ±0.09	–	1:2.57

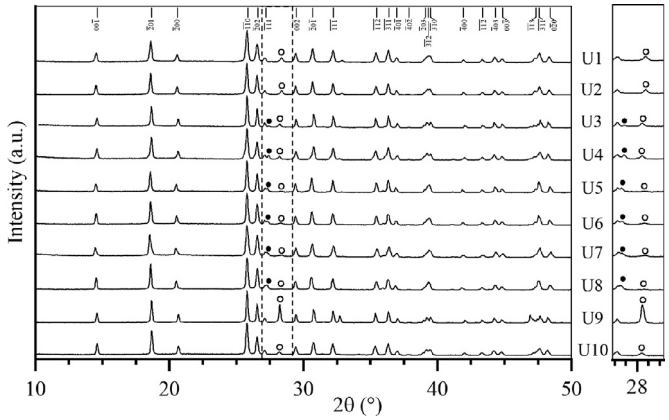

Fig. 1. XRD patterns of samples U1-U10 in the 2θ range 10–75° with a zoomed view (marked by the dashed border) of the 27–29° 2θ range. The reflections of UTi_2O_6 are marked with lines (PDF card 01-084-0496). The peaks associated with the TiO_2 (110) and UO_2 (111) reflections are marked with filled and empty circles respectively.

show that there is a relationship between heat treatment time and temperature, suggesting that diffusion kinetics play an important role in determining the phase assemblage.

The samples prepared by the alkoxide-nitrate route also formed brannerite as the major ceramic phase. U9 contains a relatively high amount of UO_2 (approx. 5.07 wt%, compared to $\leq$ 1.6 wt% for all other compositions) compared to other compositions, as judged from reflection intensity ratios (even sample U1 with the same target UO_2:TiO_2 ratio). The phase assemblage of U10 is very similar to that of U3, consisting of UTi_2O_6 as the majority phase, with a small amount of UO_2 also observed. This was expected from their compositions and similar conditions of heat treatment (the only difference being U10 was fired under a mixed H_2/N_2 atmosphere, whereas U3 was fired under Ar).

3.2. SEM-EDX

The phase assemblages observed by SEM were in good agreement with the XRD data previously discussed, and offer an explanation for the presence of residual UO_2 in all samples. A common feature in the microstructure of all samples was the presence of small regions of UO_2 within the interior of some brannerite ceramic grains; this suggests that brannerite forms around, and from, the original grains of UO_2. A plausible reaction mechanism would involve dissolution of TiO_2 in the glass phase, which then diffuses to, and reacts with, UO_2. The microstructures of all samples exhibited some macroscale porosity and smaller, irregular pores in large regions of glass. However, it was apparent that the ceramic phases did not exhibit any intragranular porosity. Examination of the microstructures of samples U1 and U9, batched with the lowest UO_2:TiO_2 molar ratio of 1:2, showed these compositions to have only partially reacted, with small clusters of UO_2 observed within the glass matrix throughout the samples, not just confined to the interior of brannerite grains. These particles of UO_2 are hereafter referred to as "free UO_2" to distinguish them from UO_2 observed within grains of brannerite. As the relative amount of TiO_2 with respect to UO_2 was increased from 1:2.28 to 1:3.20 in samples U2, U3, and U4 the inclusions of free UO_2 disappear, however, the incidence of UO_2 within the grains of brannerite remained effectively constant. Regions identified as TiO_2 were also observed in samples with other than U1 and U9, showing that at least some of the excess TiO_2 remains undissolved in the glass matrix (it is also possible that this TiO_2 had dissolved, but precipitated out of the glass as the materials cooled). Of note is that very small ($<$ 0.5 μm) regions of UO_2 are observed within grains of brannerite in sample U8 (see Fig. 2 for a comparison between samples U7 and U8), where it was not clearly apparent in the XRD pattern due to the relatively low sensitivity of XRD to phases with a particularly low concentration.

The samples heat treated for longer than 12 h show very similar microstructures, with no obvious differences from those heat treated for only 12 h. The grain sizes are approximately the same across U5, U6, and U7 (in the range 2 to 15 μm), suggesting that no significant growth of the brannerite grains in this glass system occurs on this timescale at the temperature used (1200 °C).

Although EDX is often a useful tool in analysing the elemental composition of materials such as these, the microstructure of these glass-ceramics make quantitative analysis difficult. As the volume of sample that characteristic X-rays are emitted from is larger than that of back-scattered electrons, the EDX spectrum may contain contributions from uranium and titanium dissolved within a region of glass and/or contributions from grain of brannerite located some distance below the surface of the region of glass. This leads to significant uncertainty in quantification of the EDX data, and must be taken into account when drawing conclusions from these analyses. This problem is compounded by the high molar fraction of light elements including oxygen and boron, as EDX is insensitive to such elements.

Quantification of EDX spectra of regions of glass in each sample largely yield the same result (B_2O_3 content was assumed to be equal to the as-batched content, see Table 2) - apparent uranium abundances (calculated assuming UO_2) in the glass are all $<$ 3.9 wt% with absolute errors of the magnitude ±0.3 wt%. It is apparent that the uranium content of the glass phase in all samples is very low, showing excellent partitioning of uranium into the ceramic phases. A spectrum of an area of sample U6 is shown in Fig. 3, and is representative of those seen in all samples. X-ray emission lines showing the presence of uranium and titanium are present but minor in comparison to those of glass-forming species.

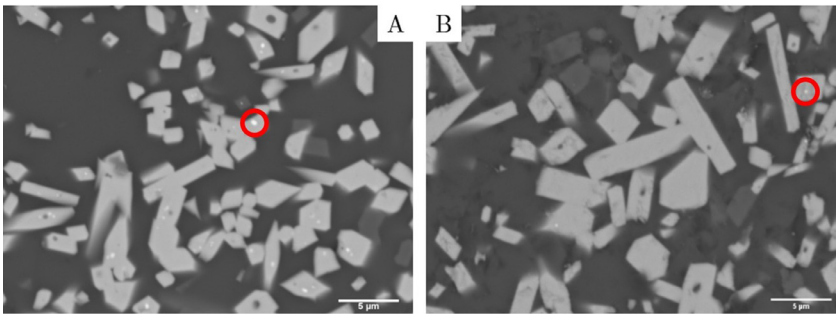

Fig. 2. Representative BSE micrographs of samples U7 and U8 (micrographs A and B respectively). White regions are UO_2, light grey are UTi_2O_6, dark grey are TiO_2, and the dark background is glass. Some regions of UO_2 are circled for clarity.

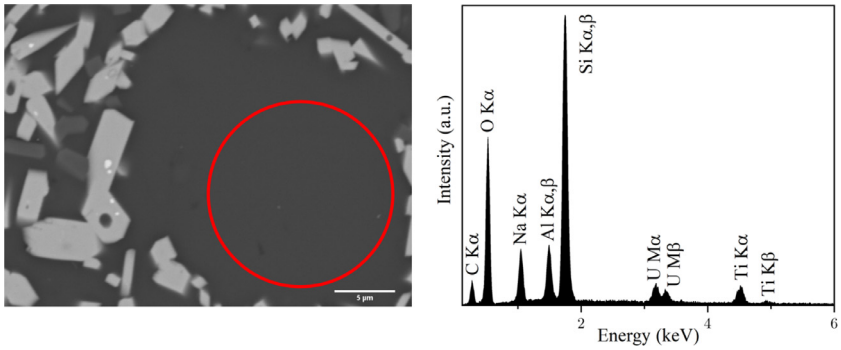

Fig. 3. BSE micrograph and associated EDX spectrum of U6. The region of glass relating to the spectrum is marked. The identities of each X-ray emission line are also marked. The presence of carbon is due to the conductive carbon coat applied during sample preparation.

It should be noted that these measurements will also contain possible systematic errors, and the results have only been used for qualitative analysis.

3.3. Uranium L_3-edge X-ray absorption near-edge spectroscopy

The average uranium oxidation states of all compositions, were examined using U L_3-edge XANES. The spectra of UTi_2O_6 and $U_{0.5}Yb_{0.5}Ti_2O_6$ were also acquired for use as reference compounds with known uranium oxidation state (U^{4+} and U^{5+} respectively). These reference compounds were chosen because they are both brannerite structured, giving them the closest possible match in uranium local structure, and so were the most relevant standards to measure in comparison to our samples. Samples of the ceramic precursors formed by the alkoxide-nitrate route were also analysed in order to confirm that the initial calcination under H_2/N_2 had fully reduced all of the U^{6+} starting material to U^{4+}. This is important, as all other brannerite glass-ceramics formed by an alkoxide-nitrate route were targeting U^{5+}, and so were calcined in either air or argon, with no control needed over the atmospheric pO_2.

The precise energy position of the U-L_3 X-ray absorption edge (the minimum energy necessary to remove a core electron) is dependent on the U oxidation state. Higher U oxidation states require more energy to remove an electron because each electron is more strongly bound to the nucleus, and *vice versa* for lower oxidation states. The E_0 values (as determined by the first maximum of the first derivative of intensity) of all compositions match that of the UTi_2O_6 standard, and the white line positions are also in excellent agreement (see Table 4). This showed that the uranium was present in all compositions as U^{4+}, as expected from the behaviour of ceramic brannerites in inert or reducing processing atmospheres such as those used in this study. It is promising that the precursors of U9 and U10 were fully reduced, even prior to the final heat treatment under a reducing atmosphere at 1200 °C, as it suggests that an inert atmosphere in this final step would be sufficient to retain the desired U^{4+} oxidation state.

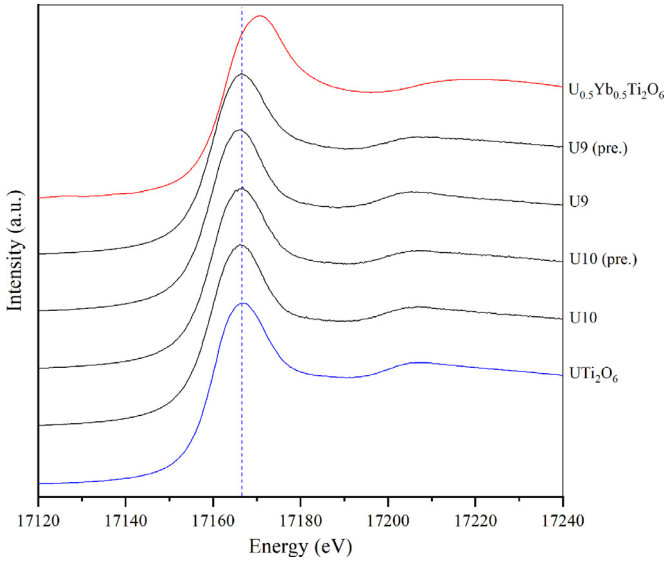

Fig. 4. Representative XANES spectra of samples U9, U10 and their ceramic precursors, along with those for UTi_2O_6 and $U_{0.5}Yb_{0.5}Ti_2O_6$ standards. The blue dashed line shows the white line energy position of the UTi_2O_6 standard.

Table 3
White line energy positions and E_0 (both in eV) values for all compositions U1-10, as well as the precursors to samples U9 and U10, and the standards of known valence UTi_2O_6 (4+) and $U_{0.5}Yb_{0.5}Ti_2O_6$ (5+), as determined from U L_3-edge XANES. E_0 was determined as the maximum in the first derivative of μ(X).

ID	White line position (eV)	E_0 (eV)
U1	17,167.1	17,161.1
U2	17,166.8	17,161.0
U3	17,166.6	17,161.1
U4	17,166.5	17,161.0
U5	17,167.1	17,161.2
U6	17,167.3	17,161.1
U7	17,167.1	17,161.0
U8	17,167.2	17,160.9
U9	17,166.6	17,161.0
U10	17,166.4	17,161.2
U9 (pre.)	17,166.6	17,161.0
U10 (pre.)	17,166.4	17,161.0
UTi_2O_6	17,166.7	17,161.1
$U_{0.5}Yb_{0.5}Ti_2O_6$	17,170.8	17,163.2

4. Discussion

With respect to the final glass-ceramic composite products, all compositions produced had favourable phase assemblages, with stoichiometric UTi_2O_6 being produced in every sample as the majority product, despite the processing temperature of 1200 °C remaining being below the 1300 °C usually necessary for full ceramic samples of UTi_2O_6 to form from their component oxides. It is thought that this increase in reactivity is caused by the presence of the glass phase increasing the ease of diffusion of the reactants, analogous to viscous phase assisted sintering. This is supported by the microstructures observed by SEM: regions of UO_2 held within grains of brannerite, as well as small amounts of both uranium and

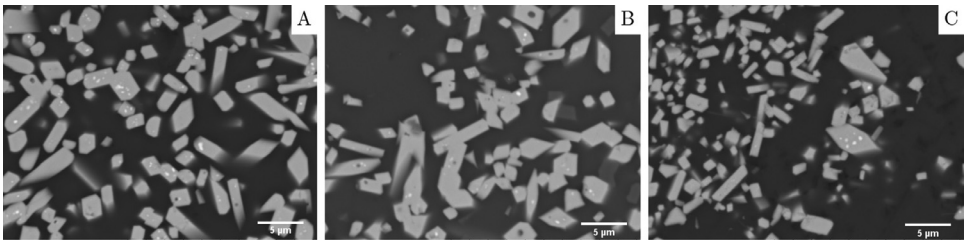

Fig. 5. Representative BSE micrographs of U2 (A), U7 (B), and U10 (C). Small white regions are UO_2, light grey are UTi_2O_6, dark grey are TiO_2, the dark background is glass.

titanium remaining dissolved in the glass matrix. The fact that all compositions formed large amounts of brannerite is important, as this demonstrates the ability of this system to form high-quality, high brannerite-fraction glass-ceramic composites using a simple one-pot cold-press and sinter method.

Sample U1 was the only composition produced from the component oxides where UO_2 particles are seen within the glass matrix (in addition to those regions of UO_2 seen in grains of brannerite), suggesting an incomplete reaction. There are two plausible reasons as to why some apparently unreacted UO_2 remains: either the amount of TiO_2 dissolved in the glass matrix was greater than that of UO_2 (this could be due to differences in solubility at high temperature, and/or solubility at low temperatures, resulting in precipitation), or the brannerite formed was actually U-deficient (resulting in excess UO_2, although synthetic uranium brannerites are not often reported to be non-stoichiometric, compared to cerium brannerites). As mentioned above, it is difficult to analyse how much uranium and titanium are dissolved in the glass using EDX, so this alone cannot distinguish the cause.

To address the presence of free UO_2 samples U2-4 were fabricated, with different amounts of excess TiO_2 added. The UO_2 (111) reflections seen in the diffraction patterns are less intense than that seen in U1, but there was only slight variation in intensity between U2, U3 and U4. This suggests that the addition of 2.5 wt% TiO_2 was sufficient to prevent formation of free UO_2 (and thus decrease the amount of UO_2 observed in the diffraction patterns), but not the UO_2 found within grains of brannerites. The observations from SEM support this interpretation, with no free UO_2 visible in U2, U3 or U4, but small regions of brannerite-encapsulated UO_2 seen in all three. In addition, grains of TiO_2 are also observed in increasing amounts. Further measurement and analysis of the uranium and titanium content in the glass phase will be investigated using more advanced synchrotron techniques; in particular, μ-focus X-ray fluorescence and μ-focus XANES measurements will allow for quantification of the uranium distribution and uranium oxidation states within the different phases of these samples.

The appearance of UO_2 encapsulated within grains of brannerite suggests that the reaction occurs at the surface of particles of UO_2, reaching a point, as the layer of brannerite grows, where diffusion becomes kinetically unfavourable. Samples U5-7 were heat treated for longer periods of time to see if an extended dwell at 1200 °C would be sufficient to allow full reaction of these UO_2 regions, however, the results do not fully bear this out; although there was a reduced amount of UO_2 observed, it was still present (if in trace amounts) in both the XRD and SEM. The same observations are extended to sample U8, where a higher reaction temperature of 1250 °C produced a product that only contained a very trace amount of UO_2. It is possible that this behaviour was caused either by an epitaxial mechanism of brannerite growth on the surface of particles of UO_2 or simply caused by the higher mobility of Ti^{4+} cations and/or particles of TiO_2 within the glass, leading to the reaction occurring closer to the particles of UO_2 (and eventually encapsulating them). It is clear that an important factor preventing a completely single-ceramic-phase product from forming was the kinetic barrier to diffusion caused by this encapsulation of the reactant UO_2.

The samples produced by an alkoxide-nitrate route (samples U9 and U10) display largely the same behaviour as the equivalent oxide stoichiometries. The notable difference being the relatively larger amount of UO_2 observed in the XRD pattern of U9. It is assumed this was caused by the ease at which titanium isopropoxide hydrolyses in air and is lost, leading to non-stoichiometry of the batch during processing. This was corrected for by the addition of excess titanium isopropoxide in sample U10, where the additional titanium precursor accounts for both this effect, and the amount of excess TiO_2 necessary to prevent formation of free UO_2. The phases observed by SEM agree with this interpretation (and match the trend seen in samples U1-4); where in sample U9 UO_2 was observed in the glass matrix and within grains of brannerite, whereas in sample U10 UO_2 was only rarely observed in grains of brannerite, comparable to the microstructure of sample U7. Of note is that the UTi_2O_6 grain sizes are of the same approximate magnitude as the samples made from solid state precursors, but tend to have a slightly wider range of grain sizes (see Fig. 5).

5. Conclusion

Near single-ceramic-phase UTi_2O_6 glass-ceramics were produced at 1200 and 1250 °C. The secondary crystalline phase present in all samples was UO_2, found held within grains of brannerite in all samples, as well as within the glass matrix in composition U1 and U9, both of which had the lowest UO_2:TiO_2 molar ratio of 1:2. The addition of excess TiO_2 prevented generation of UO_2 within the glass matrix, but small regions of UO_2 within grains of brannerite remained, even when samples were subjected to longer or higher temperature heat treatments (Figs. 1 and 4).

This microstructure leads to the observation that, whether caused by different rates of diffusion of the uranium and titanium species or by epitaxial growth of brannerite on the surface of UO_2 particles, the brannerite phase forms around regions of UO_2, until the thickness of the brannerite layer forms a kinetic barrier to diffusion and further reaction (resulting in regions of brannerite-encapsulated UO_2), or the core region of UO_2 is fully depleted (resulting in a grain of brannerite, with no observable UO_2 core).

The use of a ceramic precursor synthesised by an alkoxide-nitrate route did not have an effect on the phases formed. This is notable, as it confirms that a one-pot synthetic route allows or formation of high quality glass-ceramic products, without the additional heat treatment and handling steps necessary for an alkoxide-nitrate synthesis, or other wet chemical processes.

It is assumed that the presence of trace amounts of fully-encapsulated remnant UO_2 would not be an issue, but if materials similar to those produced in this study were to be suggested as a wasteform material for high U-content wastes, then the effect of the presence of this UO_2 would have to be examined to confirm they do not have a deleterious effect on final wasteform performance (Table 3).

Declaration of Competing Interest

The authors declare that they have no known competing financial interests or personal relationships that could have appeared to influence the work reported in this paper.

CRediT authorship contribution statement

Malin C. Dixon Wilkins: Investigation, Visualization, Writing - original draft, Writing - review & editing. **Martin C. Stennett:** Supervision, Writing - review & editing, Investigation. **Ewan Maddrell:** Supervision, Writing - review & editing. **Neil C. Hyatt:** Supervision, Conceptualization, Writing - review & editing, Project administration.

Acknowledgements

MDW is grateful to the UK EPSRC and Nuclear Decommissioning Authority for providing studentship through an EPSRC iCASE award. NCH is grateful to the Royal Academy of Engineering and the Nuclear Decommissioning Authority for funding. This research utilised the HADES/MIDAS facility and Henry Royce Institute at the University of Sheffield established with financial support from UKRI EPSRC and BEIS, under grant EP/T011424/1 and EP/P02470X/1 [31], and was supported in part by grant EP/S01019X/1.

Supplementary materials

Supplementary material associated with this article can be found, in the online version, at doi:10.1016/j.jnucmat.2020.152516.

References

[1] G.J. McCarthy, High-level waste ceramics: materials considerations, process simulation, and product characterization, Nucl. Technol. 32 (1) (Jan. 1977) 92–105, doi:10.13182/NT77-A31741.
[2] W.E. Lee, M.I. Ojovan, M.C. Stennett, N.C. Hyatt, Immobilisation of radioactive waste in glasses, glass composite materials and ceramics, Adv. Appl. Ceram. 105 (1) (Feb. 2006) 3–12, doi:10.1179/174367606X81669.
[3] R.C. Ewing, W.J. Weber, F.W. Clinard, Radiation effects in nuclear waste forms for high-level radioactive waste, Prog. Nucl. Energy 29 (2) (Jan. 1995) 63–127, doi:10.1016/0149-1970(94)00016-Y.
[4] R.C. Ewing, Nuclear waste forms for actinides, Proc. Natl. Acad. Sci. 96 (7) (Mar. 1999) 3432–3439, doi:10.1073/pnas.96.7.3432.
[5] M.L. Carter, H. Li, Y. Zhang, A.L. Gillen, E.R. Vance, HIPed tailored pyrochlore-rich glass-ceramic waste forms for the immobilization of nuclear waste, MRS Online Proc. Libr. Arch. 1124 (Jan. 2008), doi:10.1557/PROC-1124-Q04-01.
[6] E. Maddrell, S. Thornber, N.C. Hyatt, The influence of glass composition on crystalline phase stability in glass-ceramic wasteforms, J. Nucl. Mater. 456 (Jan. 2015) 461–466, doi:10.1016/j.jnucmat.2014.10.010.
[7] Y. Zhang, Z. Zhang, G. Thorogood, E.R. Vance, Pyrochlore based glass-ceramics for the immobilization of actinide-rich nuclear wastes: From concept to reality, J. Nucl. Mater. 432 (1) (Jan. 2013) 545–547, doi:10.1016/j.jnucmat.2012.08.035.
[8] E.R. Vance, M.L. Carter, G.R. Lumpkin, R.A. Day, and B.D. Begg, 'Solid Solubilities of Pu, U, Gd and Hf in Candidate Ceramic Nuclear Wasteforms', Australian Nuclear Science and Technology Organization, Menai, NSW 2234, Australia (US), DOE/ER/45676; Project Number 60387, Apr. 2001. doi: 10.2172/781161.
[9] M. James, M.L. Carter, J.N. Watson, The synthesis, crystal chemistry and structures of Y-doped brannerite (U1−xYxTi2O6) and thorutite (Th1−xYxTi2O6−δ) phases, J. Solid State Chem. 174 (2) (Sep. 2003) 329–333, doi:10.1016/S0022-4596(03)00230-5.
[10] Y. Zhang, D.J. Gregg, G.R. Lumpkin, B.D. Begg, M. Jovanovic, The incorporation of neptunium and plutonium in thorutite (ThTi2O6), J. Alloys Compd. 581 (Dec. 2013) 665–670 no. Supplement C, doi:10.1016/j.jallcom.2013.07.115.
[11] R. Ruh, A.D. Wadsley, The crystal structure of ThTi2O6 (brannerite), Acta Crystallogr. 21 (6) (Dec. 1966) 974–978, doi:10.1107/S0365110X66004274.
[12] J.T. Szymanski, J.D. Scott, A crystal-structure refinement of synthetic brannerite, UTi 2 O 6, and its bearing on rate of alkaline-carbonate leaching of brannerite in ore, Can. Mineral. 20 (2) (May 1982) 271–280.
[13] K.R. Ludwig, J.A. Cooper, Geochronology of Precambrian granites and associated U-Ti-Th mineralization, northern Olary province, South Australia, Contrib. Mineral. Petrol. 86 (3) (Jun. 1984) 298–308, doi:10.1007/BF00373676.
[14] D. Gasquet, et al., Miocene to Messinian deformation and hydrothermal activity in a pre-Alpine basement massif of the French western Alps: new U-Th-Pb and argon ages from the Lauziere massif, Bull. Soc. Geol. Fr. 181 (3) (May 2010) 227–241, doi:10.2113/gssgfbull.181.3.227.
[15] G.R. Lumpkin, S.H.F. Leung, J. Ferenczy, Chemistry, microstructure, and alpha decay damage of natural brannerite, Chem. Geol. 291 (Jan. 2012) 55–68 no. Supplement C, doi:10.1016/j.chemgeo.2011.09.008.
[16] M. Turuani, et al., Geochemical fingerprints of brannerite (UTi2O6): an integrated study, Mineral. Mag. 84 (2) (Apr. 2020) 313–334, doi:10.1180/mgm.2020.7.
[17] F.A. Charalambous, R. Ram, M.I. Pownceby, J. Tardio, S.K. Bhargava, Chemical and microstructural characterisation studies on natural and heat treated brannerite samples, Miner. Eng. 39 (Dec. 2012) 276–288 no. Supplement C, doi:10.1016/j.mineng.2012.08.006.
[18] D.J. Bailey, M.C. Stennett, N.C. Hyatt, Synthesis and characterization of brannerite compositions for MOX residue disposal, MRS Adv. 2 (10) (Jan. 2017) 557–562, doi:10.1557/adv.2016.631.
[19] E.R. Vance, J.N. Watson, M.L. Carter, R.A. Day, B.D. Begg, Crystal chemistry and stabilization in air of brannerite, UTi2O6, J. Am. Ceram. Soc. 84 (1) (Jan. 2001) 141–144, doi:10.1111/j.1151-2916.2001.tb00621.x.
[20] M. James, J.N. Watson, The synthesis and crystal structure of doped uranium brannerite phases U1−xMxTi2O6 (M=Ca2+, La3+, and Gd3+), J. Solid State Chem. 165 (2) (May 2002) 261–265, doi:10.1006/jssc.2002.9519.
[21] A. Mesbah, et al., Direct synthesis of pure brannerite UTi2O6, J. Nucl. Mater. 515 (Mar. 2019) 401–406, doi:10.1016/j.jnucmat.2019.01.003.
[22] Y. Zhang, L. Kong, I. Karatchevtseva, R.D. Aughterson, D.J. Gregg, G. Triani, Development of brannerite glass-ceramics for the immobilization of actinide-rich radioactive wastes, J. Am. Ceram. Soc. 100 (9) (Sep. 2017) 4341–4351, doi:10.1111/jace.14975.
[23] Y. Zhang, I. Karatchevtseva, L. Kong, T. Wei, Z. Zhang, Structural and spectroscopic investigations on the crystallization of uranium brannerite phases in glass, J. Am. Ceram. Soc. 101 (11) (Nov. 2018) 5219–5228, doi:10.1111/jace.15750.
[24] Y. Zhang, L. Kong, R.D. Aughterson, I. Karatchevtseva, R. Zheng, Phase evolution from Ln2Ti2O7 (Ln=Y and Gd) pyrochlores to brannerites in glass with uranium incorporation, J. Am. Ceram. Soc. 100 (11) (Nov. 2017) 5335–5346, doi:10.1111/jace.15051.
[25] Y. Zhang, T. Wei, Z. Zhang, L. Kong, P. Dayal, D.J. Gregg, Uranium brannerite with Tb(III)/Dy(III) ions: phase formation, structures, and crystallizations in glass, J. Am. Ceram. Soc. 102 (12) (2019) 7699–7709, doi:10.1111/jace.16657.
[26] J. Evans, Advanced input files & parametric quantitative analysis using topas, Mater. Sci. Forum 651 (May 2010) 1–9 10.4028/www.scientific.net/MSF.651.1.
[27] A.A. Coelho, TOPAS and TOPAS-Academic: an optimization program integrating computer algebra and crystallographic objects written in C++, J. Appl. Crystallogr. 51 (1) (Feb. 2018) Art. no. 1, doi:10.1107/S1600576718000183.
[28] A.J. Dent, et al., B18: a core XAS spectroscopy beamline for Diamond, J. Phys. Conf. Ser. 190 (Nov. 2009) 012039, doi:10.1088/1742-6596/190/1/012039.
[29] B. Ravel, M. Newville, ATHENA, ARTEMIS, HEPHAESTUS: data analysis for X-ray absorption spectroscopy using IFEFFIT, J. Synchrotron Radiat. 12 (4) (Jul. 2005) 537–541, doi:10.1107/S0909049505012719.
[30] M.C. Dixon Wilkins, E.R. Maddrell, M.C. Stennett, N.C. Hyatt, Synthesis and characterisation of high ceramic fraction brannerite (UTi $_2$ O $_6$) glass-ceramic composites, IOP Conf. Ser. Mater. Sci. Eng. 818 (Apr. 2020) 012018, doi:10.1088/1757-899X/818/1/012018.
[31] N.C. Hyatt, C.L. Corkhill, M.C. Stennett, R.J. Hand, L.J. Gardner, C.L. Thorpe, The HADES facility for high activity decommissioning engineering & science: part of the UK national nuclear user facility, IOP Conf. Ser. Mater. Sci. Eng. 818 (Apr. 2020) 012022, doi:10.1088/1757-899X/818/1/012022.

4.3 Synthesis and characterisation of high ceramic fraction brannerite (UTi_2O_6) glass-ceramic composites

IOP Conf. Series: Materials Science and Engineering **818** (2020) 012018 doi:10.1088/1757-899X/818/1/012018

Synthesis and characterisation of high ceramic fraction brannerite (UTi_2O_6) glass-ceramic composites

M C Dixon Wilkins[1], E R Maddrell[2], M C Stennett[1] and N C Hyatt[1]*

[1] Department of Materials Science & Engineering, The University of Sheffield, Mappin Street, Sheffield, S1 3JD.
[2] National Nuclear Laboratory, Sellafield, Cumbria, UK

*n.c.hyatt@sheffield.ac.uk

Abstract. Brannerite, UTi_2O_6, glass-ceramic composites have been prepared, using UO_2 and TiO_2 as the ceramic phase precursors. A range of cold-press and sinter samples with varying glass:ceramic ratios have been prepared under argon at 1200 °C to investigate the effect of glass content on formation of brannerite. Ceramic brannerite formed well in all compositions, even at low (10% by weight) glass fractions, with UO_2 as a minor product. Three further brannerite glass-ceramics have been prepared by hot isostatic pressing to investigate the compatibility of this system to HIPing. The samples HIPed at 1200 °C form brannerite, with UO_2 as a minor phase with slightly higher abundance than in the cold-press and sinter samples.

1. Introduction

Brannerite (prototypically UTi_2O_6) is a naturally occurring mineral, notable for having a particularly high uranium content (> 55% by weight uranium) and being highly durable. Natural samples of brannerite have been found to retain the majority of their uranium inventory, even when they have been completely amorphised (*i.e.* they are metamict) and altered over time [1]. These properties make brannerite a possible candidate material for immobilisation of high actinide content nuclear wastes, as they are evidence that a brannerite host matrix may have a high waste loading and aqueous durability.

The properties of ceramic wasteforms (such as brannerite) make them excellent hosts for certain waste streams; however, their more limited chemical flexibility (especially compared to vitreous or encapsulating technologies) reduces the possible applications to those waste streams that are already reasonably pure. This lack of chemical flexibility can be remedied by the addition of a secondary vitreous phase, resulting in a glass-ceramic (where the ceramic phase crystallises from the glass during an annealing step) or glass-ceramic composite (where the glass and ceramic phases may either form at the same time, or both be pre-formed, and simply sintered together) depending on the processing route.

Glass-ceramic wasteform materials have many benefits when compared to single-phase ceramic wasteforms. Primarily is the wider range of wastes that the system may feasibly immobilise, where the inclusion of a glass phase with low actinide solubility does not preclude a suitable wasteform, as the actinide will partition into the ceramic phase. An often overlooked factor is the reduction in processing temperature caused by addition of the glass phase during synthesis. For example, uranium brannerite ceramics require temperatures of 1350 °C or higher for an extended duration to form [2–5], but various

brannerite-structured ceramic phases within a glass-ceramic composite system have been shown to form at 1200 °C [6–9].

This is especially important when considering the compatibility of these materials with thermal processing techniques. In this study hot isostatic pressing (HIP or HIPing) has been used to consolidate these materials. The temperature of formation is of particular importance for HIP, as the most common and easily available canister material is stainless steel, with a maximum HIPing temperature of 1300 °C; so it is desirable to reduce the reaction temperature *e.g.* through the addition of a glass phase.

In this study UTi_2O_6 glass-ceramics have been produced by two separate methods to investigate the viability of HIP as a processing route. Starting from the component oxides (UO_2, TiO_2) and a glass precursor, a cold-press and sinter (CPS) method has been used to examine how this lowered temperature of formation may be dependent on the relative abundance of the vitreous phase, and preliminary HIP samples have been prepared as an initial proof-of-concept.

2. Experimental

2.1. Production of glass-ceramics

All samples were prepared using UO_2 and TiO_2 to form the ceramic phase, and a pre-calcined glass precursor to form the vitreous phase. The glass precursor was formed by calcining a homogeneous mixture (targeting a glass composition of $Na_2AlBSi_6O_{16}$) of the glass reagents (Na_2CO_3, H_3BO_3, Al_2O_3, and SiO_2) at 600 °C for 6 hours to remove volatile species. The ceramic components and the glass precursor were then wet milled together in isopropanol to homogenise. The resulting slurry was dried at 90 °C, and the powders retrieved for further processing.

Samples prepared by a CPS route were prepared by pressing into pellets (approximately 250 mg each) and then heat treated on a bed of coarse ZrO_2 (to prevent them from sticking to the crucibles) at 1200 °C for 12 hours, under an Ar atmosphere.

Samples prepared by HIP were prepared by first calcining the as-milled powders at 600 °C to remove any remaining volatiles. The powders were then pressed into stainless steel HIP canisters under approximately 1 ton using a hydraulic press (each canister contained approximately 25 g of material). The can lids were welded on, and the cans evacuated under vacuum at 600 °C to further ensure removal of all volatile materials. The evacuation tube was then crimped off and welded shut. The prepared cans were then HIPed at 100 MPa at the desired temperature and time.

Table 1 contains the as-batched compositions of all samples, as well as the U:Ti molar ratio and details of all heat treatments.

2.2. Characterisation

All samples were characterised using powder X-ray diffraction (XRD, Bruker D2 Phaser, Ni-filtered Cu Kα), and scanning electron microscopy (SEM, Hitachi TM3030 with Bruker Quantax EDX system). Samples were prepared for SEM by mounting and polishing to an optical finish using successive grades of abrasive paper and diamond suspensions.

Table 1. As-batched compositions (% by weight) of brannerite glass-ceramics, along with details of their heat treatment.

Sample ID	Glass	UO_2	TiO_2	U:Ti molar ratio	Heat treatment
CPS50	50%	31.42%	18.58%	1:2	1200 °C, 12 h, Ar
CPS60	40%	37.70%	22.30%	1:2	
CPS70	30%	43.98%	26.02%	1:2	
CPS80	20%	50.27%	29.73%	1:2	
CPS90	10%	56.55%	33.45%	1:2	
HIP1100	50%	31.42%	18.58%	1:2	HIP, 1100 °C, 24 h
HIP1200a	50%	31.42%	18.58%	1:2	HIP, 1200 °C, 4 h
HIP1200b	48.75%	30.63%	20.62%	1:2.277	

3. Results and discussion

3.1. The effect of glass-ceramic ratio on the formation of brannerite

The compositions that were processed by a CPS route show broadly the same phase assemblage. The XRD patterns all confirm that brannerite, UTi_2O_6, was formed as the predominant crystalline product, along with a small amount of unreacted UO_2 (less than 2% by weight). As the ratio of glass to ceramic is changed from 50:50 (by weight) to 10:90 the relative amount of UO_2 increases, but still remains a minor phase (see Figure 2).

The microstructures seen in the SEM micrographs are in good agreement with the XRD phase assemblages. As the glass content decreases from sample CPS50 to sample CPS90, the observed microstructures show increasing amounts of brannerite, with a corresponding increase in the amount of UO_2 also observed. In all samples, the majority of UO_2 is seen as small regions encapsulated within grains of brannerite, with a smaller amount of UO_2 particles held directly within the glass phase. Macroscale pores are visible in all samples; these are most likely due to incomplete calcination of the glass precursor causing some volatiles to only be removed during the final heat treatment at 1200 °C, rather than during the glass precursor forming pre-calcination at 600 °C (see Figure 1).

The presence of excess unreacted UO_2 is unsurprising; previous reports of brannerite glass-ceramics in the literature have noted that addition of superstoichiometric amounts of the titanium starting material is necessary to prevent formation of these regions of UO_2. This may be due to one or more different factors, depending on choice of processing route. Dissolution of TiO_2 in the glass phase during heat treatment may prevent full reaction of the uranium, loss of titanium during processing will also have the same effect (especially relevant for alkoxide/nitrate based routes, where titanium isopropoxide will readily hydrolyse in air during sample preparation), or some level of A-site non-stoichiometry in the final brannerite phase (which has previously been observed in natural and synthetic brannerites alike [1,10]).

As the relative glass content decreases from 50% to 10% by weight, the temperature dependence of brannerite formation appears to be unaffected. This is evidenced by the majority crystalline product in all samples being brannerite, with no remaining crystalline TiO_2 observed in the diffraction patterns or SEM micrographs. This shows that this glass-ceramic composite system forms well at processing temperatures achievable in standard stainless steel HIP canisters, and so three preliminary HIPed samples have also been prepared to confirm this.

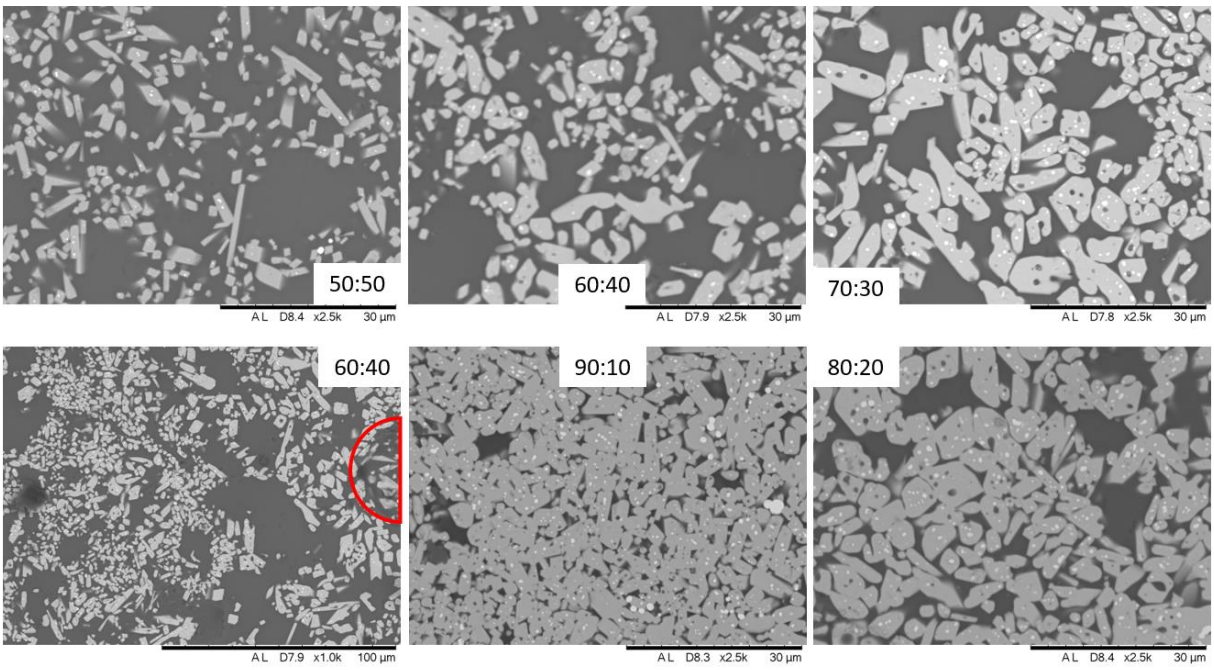

Figure 1. SEM micrographs of UTi_2O_6 glass-ceramics with different ceramic:glass ratios, as indicated. The white phase is UO_2, light grey is UTi_2O_6, and dark grey is glass. Note that the bottom left image is at a different magnification, and has a large region of porosity (as indicated in red).

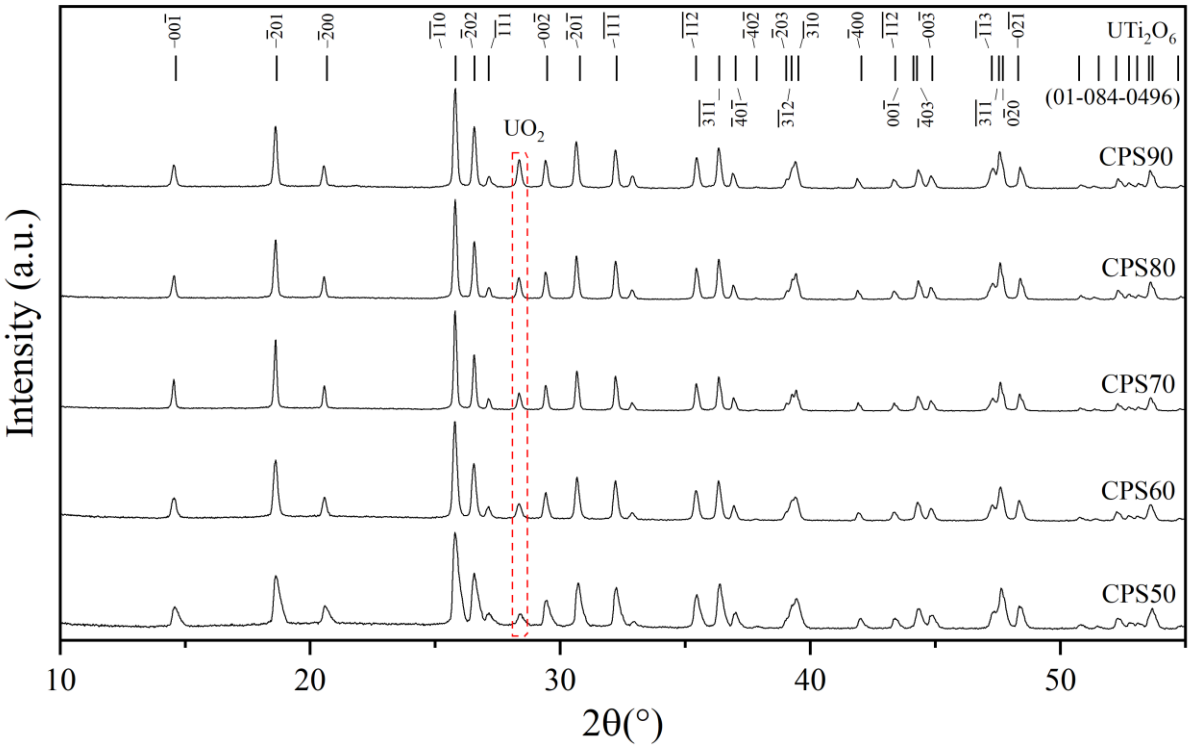

Figure 2. XRD patterns of CPS brannerite glass-ceramics with differing ceramic:glass ratio. The ceramic:glass ratio of each pattern is indicated, and the reflections of UTi_2O_6 are marked at the top.

3.2. HIPed brannerite glass-ceramic composites

Three HIP samples were prepared, one at 1100 °C and two at 1200 °C. The first sample, HIP1200a has the same composition as the sample CPS50, and was also processed at 1200 °C (however it was only heated at 1200 °C for four hours, rather than the 12 hours of the CPS samples). The main phases observed by XRD and SEM are brannerite and UO_2; however, the relative amount of UO_2 is higher (approximately 5% by weight) than that of the sample CPS50 (see Figure 3). As mentioned above, previous reports have shown that hyperstoichiometric amounts of TiO_2 can be necessary to prevent formation of free UO_2, so sample HIP1200b was batched from the same precursors as HIP1200a but with the addition of a further 2.5 wgt% TiO_2 prior to the final homogenisation step. The phases observed by XRD and SEM match those of HIP1200a; however, the addition of excess TiO_2 reduced the relative amount of UO_2 in the phase assemblage. A small peak assignable to TiO_2, rutile, is also observed, suggesting that addition of further TiO_2 would not cause complete reaction of the UO_2.

The sample HIP1100 was made to investigate if the temperature of reaction could be further reduced (with a corresponding increase of the time at temperature to encourage full reaction) whilst still producing a high brannerite fraction glass-ceramic composite. The phase assemblage as observed by XRD and SEM consists of brannerite and UO_2, the same as the samples processed at 1200 °C; however, the relative amount of UO_2 is evidently higher than for all other samples.

It is unclear why more UO_2 is observed in the HIPed samples when compared to CPS samples of the same composition. A possible explanation is offered by a report that the brannerite structure is unstable in reducing conditions

[5], such as those exerted by the stainless steel HIP canister. This is supported by the observation of higher amounts of unreacted UO_2 at the can-sample interface in the HIPed samples. However, samples of pure ceramic UTi_2O_6 have been formed under reducing atmospheres (24 hours at 1350 °C in 5% H_2/95% N_2 atmosphere, unpublished work), so this may not offer a complete explanation of the phenomenon.

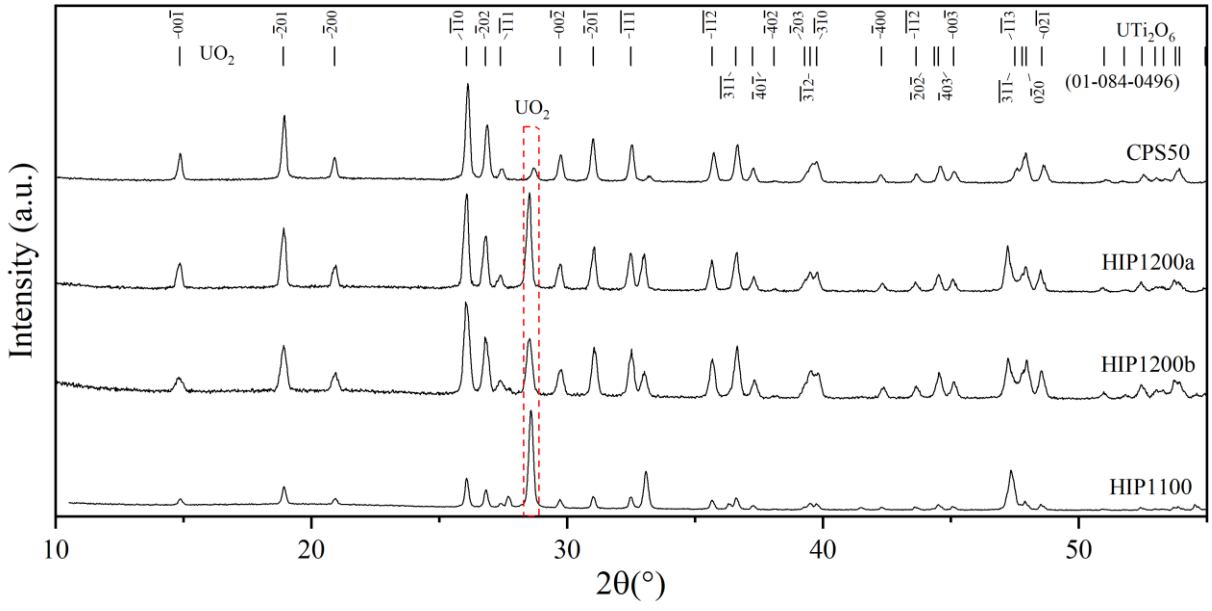

Figure 3. XRD patterns of brannerite glass-ceramics HIPed under different conditions. The conditions of each HIP sample are indicated and the reflections of UTi_2O_6 are marked at the top.

4. Conclusion

A range of UTi_2O_6 glass-ceramic composites have been synthesised, with a focus on investigating the effect of the glass:ceramic ratio on the temperature of formation of brannerite. When processed via a

CPS route at 1200 °C, UTi_2O_6 formed as the major crystalline phase for glass:ceramic ratios from 50:50 to 10:90, with UO_2 as a secondary product. When HIPed at 1200 °C, brannerite is still the majority product; however, the relative amount of UO_2 increases when compared to a CPS sample of the same as-batched composition. The mechanism causing this is not clear. When the temperature of reaction is further reduced to 1100 °C, significantly less brannerite is formed, with a much higher proportion of UO_2 observed in the final product.

As expected from the synthesis of brannerite glass-ceramic composites in the literature, UTi_2O_6 forms well in glass at 1200 °C, below the temperatures required for synthesis of a full ceramic from component oxides. Further work required to fully understand the extent and exact cause (although it is most likely caused by the glass phase lowering the barrier to diffusion of the ceramic phase reactants) of this effect is ongoing, with a focus on in-situ high temperature diffraction techniques.

5. References

[1] Lumpkin G R, Leung S H F and Ferenczy J 2012 *Chem. Geol.* **291** 55.
[2] Bailey D J, Stennett M C and Hyatt N C 2016 *Procedia Chem.* **21** 371.
[3] Bailey D J, Stennett M C and Hyatt N C 2017 *MRS Adv.* **2** 557.
[4] James M, Carter M L and Watson J N 2003 *J. Solid State Chem.* **174** 329.
[5] Vance E R, Watson J N, Carter M L, Day R A and Begg B D 2001 *J. Am. Ceram. Soc.* **84** 141.
[6] Zhang Y, Kong L, Karatchevtseva I, Aughterson R D, Gregg D J and Triani G 2017 *J. Am. Ceram. Soc.* **100** 4341.
[7] Zhang Y, Karatchevtseva I, Kong L, Wei T and Zhang Z 2018 *J. Am. Ceram. Soc.* **101** 5219.
[8] Zhang Y, Wei T, Zhang Z, Kong L, Dayal P and Gregg D J 2019 *J. Am. Ceram. Soc.* **102** 7699.
[9] Dixon Wilkins M C, Stennett M C and Hyatt N C 2019 *MRS Adv.* in press.
[10] Stennett M C, Freeman C L, Gandy A S and Hyatt N C 2012 *J. Solid State Chem.* **192** 172.

Acknowledgment

This research was sponsored in part by EPSRC under grant references EP/N017870/1, EP/S011935/1 and EP/S01019X/1. MCDW is grateful to EPSRC and NDA for provision of a doctoral training award. This research utilised the HADES / MIDAS Facility, established with financial support from the UK Department for Business, Energy and Industrial Strategy and EPSRC under grant reference EP/T011424/1.

4.4 The effect of glass composition ($Na_2Al_{2-x}B_xSi_6O_{16}$) on the formation of brannerite (UTi_2O_6) in glass-ceramic composites

The effect of glass composition ($Na_2Al_{2-x}B_xSi_6O_{16}$) on the formation of brannerite (UTi_2O_6) in glass-ceramic composites

Malin C. Dixon Wilkins[1], Ewan R. Maddrell[2], Martin C. Stennett[1], Neil C. Hyatt[1]*

[1]Department of Materials Science and Engineering, University of Sheffield, Sheffield, UK

[2]National Nuclear Laboratory, Sellafield, Cumbria, UK

*Corresponding author: n.c.hyatt@sheffield.ac.uk

Abstract

Introduction

In the search for suitable materials to immobilise nuclear wastes, it is common to examine synthetic analogues of long-lived minerals[1]. Brannerite (prototypically UTi_2O_6) is a naturally occurring mineral that displays the ability to retain the majority of its U inventory, even when rendered partially or fully metamict by its high U content[2]–[4]. Due to the particularly high waste loading of U and other actinides (*e.g.* UTi_2O_6 contains approx. 55.4% U by weight), it has been suggested as a wasteform material either as a full ceramic or as a ceramic phase within a glass-ceramic composite. A range of brannerite glass-ceramic composites have been reported in the literature, and can be separated into two main groups: those targeting a U^{4+} brannerite, and those targeting a U^{5+} brannerite. All brannerite glass-ceramic composites, including both U^{4+}[5], [6] and U^{5+}[7]–[10] brannerites, reported in the literature have utilised the same glass matrix: a borate-albite glass, $Na_2AlBSi_6O_{16}$.

It has been previously shown that UTi_2O_6 formation occurs in glass over a wide range of glass:ceramic ratios, from 50:50 by weight to 10:90 by weight[6], with the addition of only 10% by weight of glass permitting formation of UTi_2O_6 at 1200 °C (formation of brannerites

from the component oxides often requires temperatures in excess of 1350 °C). Previous investigation demonstrated that a slight excess of TiO_2 improved the final ceramic phase assemblage of UTi_2O_6 glass-ceramic composites by preventing excess UO_2 from remaining as isolated grains within the glass matrix[5].

It has been previously reported that the formation of zirconolite ($CaZrTi_2O_7$, another candidate ceramic wasteform material) as a ceramic phase in similar glasses (the mixed albite-borate system $Na_2Al_{2-x}B_xSi_6O_{16}$) has a strong dependence on the glass composition[11]. Zirconolite only formed as the dominant ceramic phase in those glasses with the highest Al contents. This was ascribed to differences in silica activity, with other silicate phases (notably zircon, $ZrSiO_4$ and sphene, $CaTiSiO_5$) dominating in glasses with higher B contents, and so higher silica activities.

In the context of ceramic phase formation in glass-ceramic composites, the major difference between zirconolite and brannerite is the accessibility of secondary silicate phases. Zirconolite formation in high B content glasses of the family $Na_2Al_{2-x}B_xSi_6O_{16}$ was hindered by the formation of zircon and sphene, with only TiO_2 remaining as an oxide[11]. In comparison, the UTi_2O_6 system does not have easily formed silicate phases, with synthetic coffinite ($USiO_4$) often reported as notably difficult to prepare[12]–[14], so it was expected that UTi_2O_6 formation would not have a strong dependence on glass composition.

In order to examine the impact of the glass composition on the formation of UTi_2O_6 glass-ceramic composites, a suite of samples was produced. The glass:ceramic ratio was fixed to 50:50 by weight, and the glass composition varied according to $Na_2Al_{2-x}B_xSi_6O_{16}$ in increments of x = 0.2. It should be noted that the ceramic compositions in this work following the 1:2 molar ratio of UO_2 and TiO_2, rather than utilising hyperstoichiometric amounts of TiO_2 as mentioned above.

Experimental

Samples were prepared following a simple cold-press and sinter method. The glass phases were introduced as glass precursors, prepared by calcining a stoichiometric mixture of H_3BO_3, Na_2CO_3, Al_2O_3 and SiO_2 at 600 °C for 6 hours. The glass composition was varied according to the stoichiometry $Na_2Al_{2-x}B_xSi_6O_{16}$ (x = 2.0, 1.8, …, 0.2, 0.0). The ceramic components were then added as stoichiometric amounts of the oxides, UO_2 and TiO_2 (anatase). The mixtures were then milled together with the glass precursor (Fritsch Pulverisette reciprocating ball mill) for 5 minutes at 30 Hz. The resulting slurry was dried in an oven at 85 °C and the dry powder retrieved and broken up by hand using a mortar and pestle. The milled powders were pressed into 10 mm diameter pellets under 2 tons (approx. 250 MPa). The green pellets were then heat treated on a bed of coarse ZrO_2 at 1200 °C for 12 hours under flowing Ar. It was noted during sample retrieval that those samples with high B content glasses had partially slumped during

heat treatment, and had adhered to the bed of coarse ZrO_2, which was removed by manual grinding with grit paper.

The heat-treated pellets were broken into pieces for characterisation. Powder XRD (Bruker D2 Phaser using Ni-filtered Cu K_α) was used to identify the phases present, by matching to phases in the PDF database[15]. SEM was used to examine the microstructure and homogeneity within the sample (Hitachi TM3030, operating at 15 kV). Samples were prepared for SEM by polishing with sequentially finer grades of grit paper and diamond paste to an optical finish before coating with a conductive carbon layer to prevent sample charge build-up.

Results

X-ray diffraction

The phase assemblages of each sample were determined by analysis of X-ray diffraction (XRD) patterns. The diffraction patterns of some materials displayed some asymmetry of the reflections; this is due to XRD sample preparation rather than from any contribution from the material itself. All glass compositions studied contained brannerite, UTi_2O_6, as the majority crystalline phase and UO_2 as a minor phase. As the B content of the glass phases increased from x = 1.0 to x = 2.0 (according to $Na_2Al_{2-x}B_xSi_6O_{16}$) the relative amount of UO_2 present decreased.

Samples with glass compositions $0 \leq x \leq 1$ $Na_2Al_{2-x}B_xSi_6O_{16}$, did not contain any other crystalline phases, as expected from previous reports of formation of UTi_2O_6 in the $Na_2AlBSi_6O_{16}$ glass (x = 1.0), see Figure 1[5]. Samples with higher B contents (those with x > 1) contained additional minor crystalline phases, including ZrO_2 (baddeleyite) and TiO_2 (rutile), see Figure 2. The presence of ZrO_2 shows that not all of the ZrO_2 that had adhered to the pellets had been removed, likely due to the lower viscosity of the high B content glasses.

The sample containing the boron end-member glass, $Na_2B_2Si_6O_{16}$, also contained a significant fraction of SiO_2 (cristobalite). The presence of SiO_2 was attributed to volatilisation of Na-borates during heat treatment, which in turn prevented full glass formation at the process temperature of 1200 °C[16], [17].

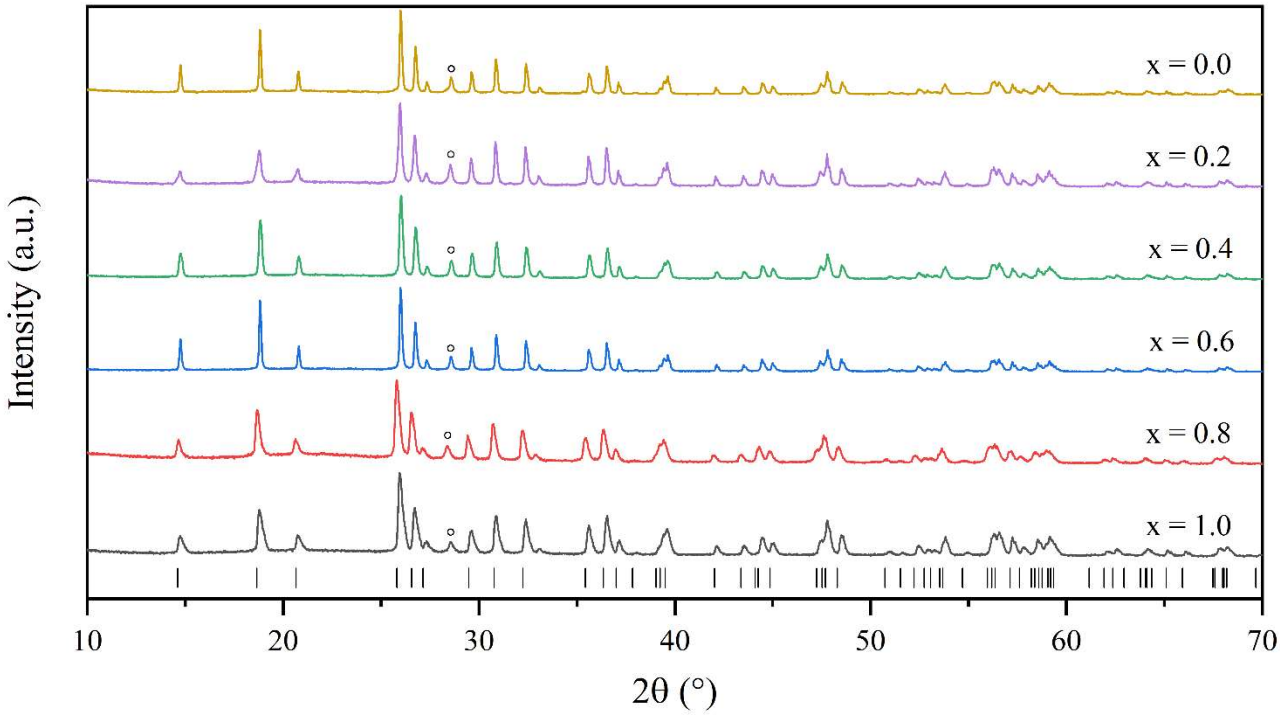

Figure 1: Powder X-ray diffraction patterns of UTi_2O_6 glass-ceramic composites with differing glass compositions according to $Na_2Al_{2-x}B_xSi_6O_{16}$. The major reflections of UTi_2O_6 (PDF #01-084-0496) are marked below. Reflections indexed as UO_2 are marked with empty circles.

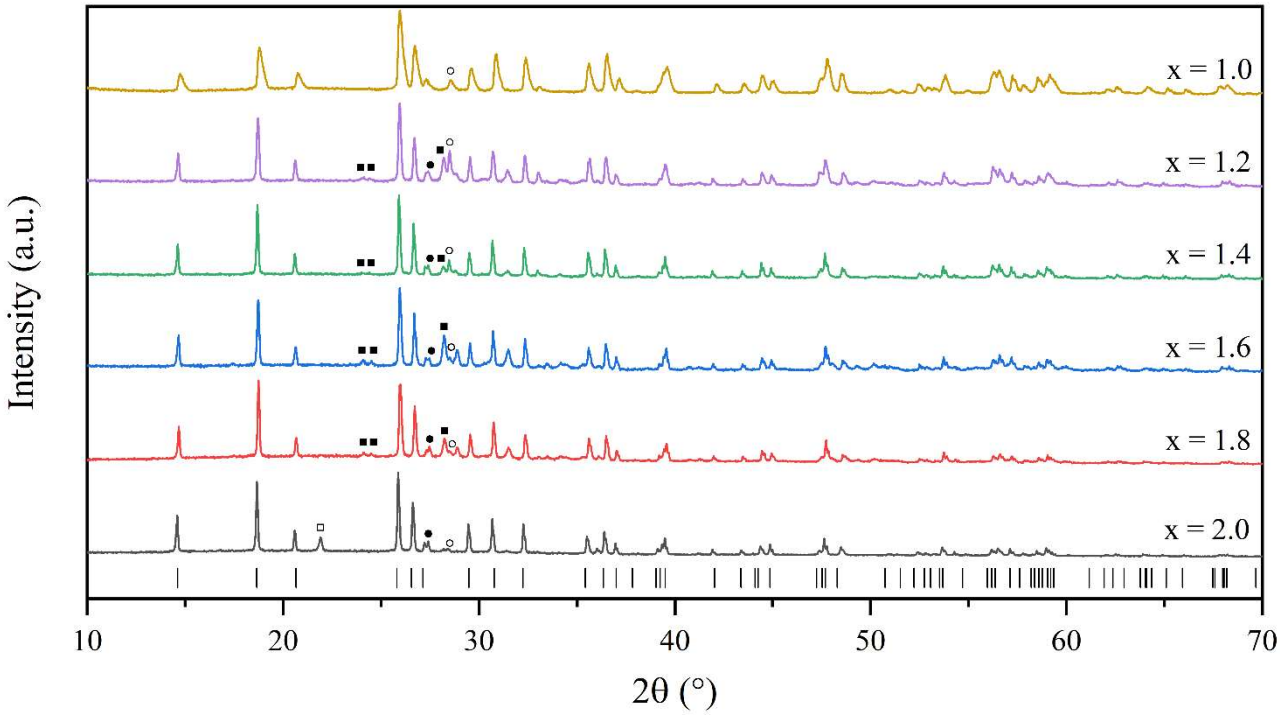

Figure 2: Powder X-ray diffraction patterns of UTi_2O_6 glass-ceramic composites with differing glass compositions according to $Na_2Al_{2-x}B_xSi_6O_{16}$. The major reflections of UTi_2O_6 (PDF #01-084-0496) are marked below. Reflections indexed as UO_2 are marked with empty circles; TiO_2 with filled circles; ZrO_2 with filled squares; SiO_2 cristobalite with empty squares.

Scanning electron microscopy

The microstructures produced were examined by scanning electron microscopy (SEM). As expected from the phases identified by XRD, the two most abundant phases in all materials were the glass phase and brannerite, UTi_2O_6. UO_2 was also observed in all materials examined, in two different environs: small regions of UO_2 encapsulated by UTi_2O_6 and as isolated grains of UO_2 held within the glass. This is in good agreement with the previous report of UTi_2O_6 formation in the $Na_2AlBSi_6O_{16}$ glass, where grains of UO_2 were observed in the glass matrix when the batched molar stoichiometry of UO_2 and TiO_2 was 1:2[5]. In materials with glass compositions $Na_2Al_{2-x}B_xSi_6O_{16}$ with $x \leq 1$, no other phases were observed, as expected from the phases identified by XRD.

As the B content of the glass phase increases (compositions with $x \geq 1.2$), grains of TiO_2 are also observed. This, along with the decrease in the fraction of UO_2 observed by XRD, suggests that more UO_2 has dissolved into the glass at higher B contents, leaving a slight excess of TiO_2.

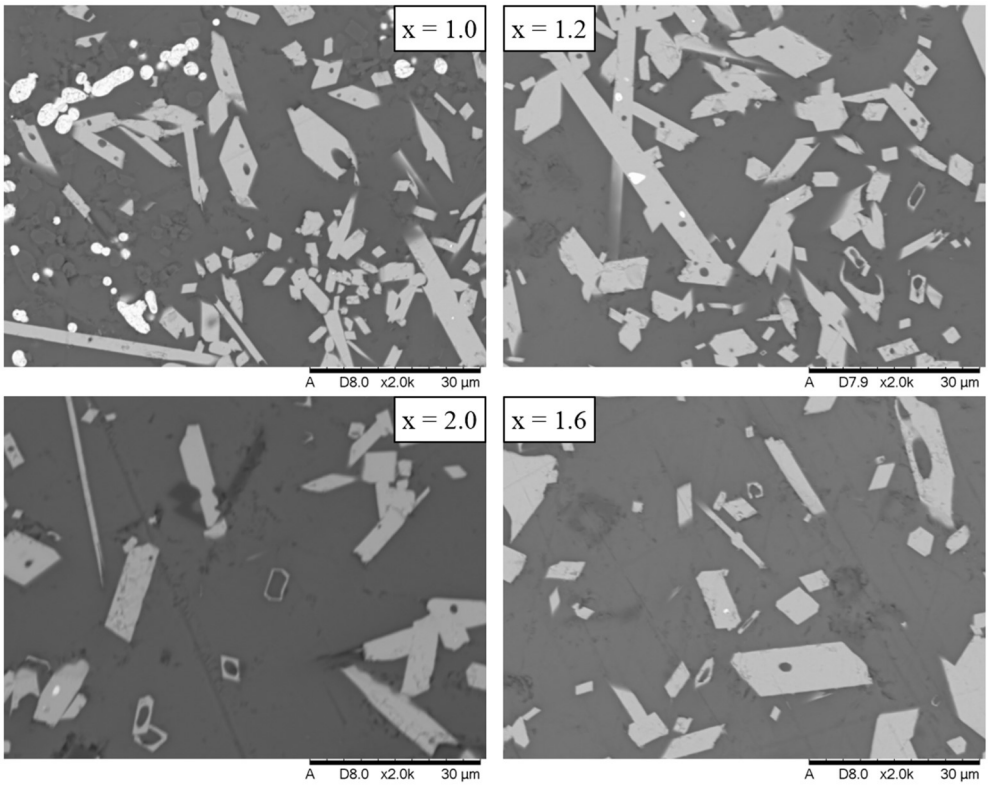

Figure 3: Scanning electron micrographs of select UTi_2O_6 glass-ceramic composites with varying glass compositions according to $Na_2Al_{2-x}B_xSi_6O_{16}$ (clockwise from top left: x = 1.0; 1.2; 1.6; and 2.0). In all compositions regions of UTi_2O_6 are light grey, UO_2 are white, and glass is the dark background. In x = 1.6, 2.0 TiO_2 is seen as dark grey regions.

Discussion

The initial goal of this investigation was to examine the impact of the glass composition on the formation of UTi_2O_6 as the ceramic phase in glass-ceramic composites. In particular, the formation of zirconolite in similar glasses has a strong dependence on the glass composition. In all glass compositions examined here, UTi_2O_6 formed as the major crystalline product, showing that brannerite formation in these systems is not controlled by the glass composition. As briefly mentioned above, this is likely due to the lack of energetically favourable U- and Ti-silicate phases, in contrast to zirconolite glass-ceramic composites systems, where zircon ($ZrSiO_4$) and sphene/titanite ($CaTiSiO_5$) can easily form.

Although all glass compositions examined here allowed for UTi_2O_6 formation, non-ideal products were formed in glasses with high B contents ($x \geq 1.2$). For example, many of the high B glass-ceramic composites had slumped and adhered to the bed of coarse ZrO_2 used to prevent the pellets from sticking to the crucibles, with ZrO_2 observed in the XRD patterns despite the manual removal of any visible grains. This is likely due to the glass phase viscosity at temperature decreasing with increasing B content. The material with the B end-member glass $Na_2B_2Si_6O_{16}$ appears to have lost both Na and B (likely as Na-borate phases) during heat

treatment, leaving an excess of SiO_2 which was observed in the XRD pattern as SiO_2-cristobalite.

Although these are clearly undesirable behaviours for wasteform materials, they may not occur when the materials are produced by hot isostatic pressing (HIP), one of the proposed processing technologies for wasteform materials. During the HIP process the materials must be sealed within HIP canisters (often made of stainless steel) for pressure to apply isostatically across the workpiece. This means that issues related to glass viscosity can be neglected, as the sealed canisters prevent material-equipment contact by design. This also applies to the possible volatilisation of Na-borates in the sample with glass composition $Na_2B_2Si_6O_{16}$, with the additional pressure during HIP often helping to prevent volatilisation and the sealed canisters preventing off-gases from escaping In fact, these are some of the reasons HIP is seen as a desirable processing route for radioactive wastes.

HIPed UTi_2O_6 glass-ceramic composites (with the $Na_2AlBSi_6O_{16}$ glass) have been previously reported, with the formation process of UTi_2O_6 appearing to be unaffected by the HIP pressure or canister material[6]. However, the phase assemblages reported did contain higher fractions of UO_2 than cold-press and sinter samples of the same composition. The mechanism causing this is unclear, and more work is necessary to examine the differences in glass-ceramic composite phase formation in HIP compared to pressureless methods.

Conclusions

A suite of UTi_2O_6 glass-ceramic composites with varying glass compositions ($Na_2Al_{2-x}B_xSi_6O_{16}$, with x = 0.0, 0.2, … , 1.8, 2.0) have been produced at 1200 °C in Ar, following a cold-press and sinter route. The glass composition has little effect on the formation of UTi_2O_6 due to the lack of energetically favourable silicate phases in the UO_2-TiO_2-SiO_2 system. The higher B content glasses had lower viscosities than the higher Al content glasses, resulting in sticking and slight slumping of the pellets, which is particularly undesirable if a cold-press and sinter process is to be used to produce these materials as wasteforms. The use of HIP would avoid these issues, permitting the production of high quality UTi_2O_6

Bibliography

[1] G. R. Lumpkin, “Alpha-decay damage and aqueous durability of actinide host phases in natural systems,” *J. Nucl. Mater.*, vol. 289, no. 1, pp. 136–166, Feb. 2001, doi: 10.1016/S0022-3115(00)00693-0.

[2] M. Turuani *et al.*, “Geochemical fingerprints of brannerite (UTi2O6): an integrated study,” *Mineral. Mag.*, vol. 84, no. 2, pp. 313–334, Apr. 2020, doi: 10.1180/mgm.2020.7.

[3] G. R. Lumpkin, S. H. F. Leung, and J. Ferenczy, “Chemistry, microstructure, and alpha decay damage of natural brannerite,” *Chem. Geol.*, vol. 291, no. Supplement C, pp. 55–68, Jan. 2012, doi: 10.1016/j.chemgeo.2011.09.008.

[4] F. A. Charalambous, R. Ram, M. I. Pownceby, J. Tardio, and S. K. Bhargava, "Chemical and microstructural characterisation studies on natural and heat treated brannerite samples," *Miner. Eng.*, vol. 39, no. Supplement C, pp. 276–288, Dec. 2012, doi: 10.1016/j.mineng.2012.08.006.
[5] M. C. Dixon Wilkins, M. C. Stennett, E. Maddrell, and N. C. Hyatt, "The formation of stoichiometric uranium brannerite (UTi2O6) glass-ceramic composites from the component oxides in a one-pot synthesis," *J. Nucl. Mater.*, vol. 542, p. 152516, Dec. 2020, doi: 10.1016/j.jnucmat.2020.152516.
[6] M. C. Dixon Wilkins, E. R. Maddrell, M. C. Stennett, and N. C. Hyatt, "Synthesis and characterisation of high ceramic fraction brannerite (UTi_2O_6) glass-ceramic composites," *IOP Conf. Ser. Mater. Sci. Eng.*, vol. 818, p. 012018, Apr. 2020, doi: 10.1088/1757-899X/818/1/012018.
[7] Y. Zhang, I. Karatchevtseva, L. Kong, T. Wei, and Z. Zhang, "Structural and spectroscopic investigations on the crystallization of uranium brannerite phases in glass," *J. Am. Ceram. Soc.*, vol. 101, no. 11, pp. 5219–5228, Nov. 2018, doi: 10.1111/jace.15750.
[8] Y. Zhang, L. Kong, R. D. Aughterson, I. Karatchevtseva, and R. Zheng, "Phase evolution from Ln2Ti2O7 (Ln=Y and Gd) pyrochlores to brannerites in glass with uranium incorporation," *J. Am. Ceram. Soc.*, vol. 100, no. 11, pp. 5335–5346, Nov. 2017, doi: 10.1111/jace.15051.
[9] Y. Zhang, L. Kong, I. Karatchevtseva, R. D. Aughterson, D. J. Gregg, and G. Triani, "Development of brannerite glass-ceramics for the immobilization of actinide-rich radioactive wastes," *J. Am. Ceram. Soc.*, vol. 100, no. 9, pp. 4341–4351, Sep. 2017, doi: 10.1111/jace.14975.
[10] M. C. Dixon Wilkins, M. C. Stennett, and N. C. Hyatt, "The Effect of A-Site Cation on the Formation of Brannerite (ATi2O6, A = U, Th, Ce) Ceramic Phases in a Glass-Ceramic Composite System," *MRS Adv.*, vol. 5, no. 1–2, pp. 73–81, ed 2020, doi: 10.1557/adv.2019.470.
[11] E. Maddrell, S. Thornber, and N. C. Hyatt, "The influence of glass composition on crystalline phase stability in glass-ceramic wasteforms," *J. Nucl. Mater.*, vol. 456, pp. 461–466, Jan. 2015, doi: 10.1016/j.jnucmat.2014.10.010.
[12] X. Guo *et al.*, "Thermodynamics of formation of coffinite, USiO4," *Proc. Natl. Acad. Sci.*, vol. 112, no. 21, pp. 6551–6555, May 2015, doi: 10.1073/pnas.1507441112.
[13] S. Labs, C. Hennig, S. Weiss, H. Curtius, H. Zänker, and D. Bosbach, "Synthesis of Coffinite, USiO4, and Structural Investigations of UxTh(1–x)SiO4 Solid Solutions," *Environ. Sci. Technol.*, vol. 48, no. 1, pp. 854–860, Jan. 2014, doi: 10.1021/es403995b.
[14] S. Szenknect *et al.*, "Coffinite formation from UO2+x," *Sci. Rep.*, vol. 10, no. 1, p. 12168, Jul. 2020, doi: 10.1038/s41598-020-69161-1.
[15] S. Gates-Rector and T. Blanton, "The Powder Diffraction File: a quality materials characterization database," *Powder Diffr.*, vol. 34, no. 4, pp. 352–360, Dec. 2019, doi: 10.1017/S0885715619000812.
[16] M. Cable, "Kinetics of Volatilization of Sodium Borate Melts," in *Borate Glasses: Structure, Properties, Applications*, L. D. Pye, V. D. Fréchette, and N. J. Kreidl, Eds. Boston, MA: Springer US, 1978, pp. 399–411. doi: 10.1007/978-1-4684-3357-9_20.
[17] M. Shimbo, "Volatilization at High Temperature from Na2O-K2O-(B2O3+SiO2) and Na2O-Li2O-(B2O3+SiO2) Systems," *J. Ceram. Assoc. Jpn.*, vol. 76, no. 12, 1968.

5 The thermodynamic stability of cerium brannerite in inert and oxidising atmospheres

5.1 Introduction

During the initial investigations in UTi_2O_6 formation in glass-ceramic composites outlined in Chapter 4, the synthesis of analogous Ce brannerite ($CeTi_2O_6$) glass-ceramic composites was also attempted. However, despite $CeTi_2O_6$ being easily produced as a ceramic, it did not form as the ceramic phase in a glass-ceramic composite when heated at the same temperatures as UTi_2O_6 containing composites.

Previous literature reports had suggested that $CeTi_2O_6$ can contain varying Ce oxidation states (*i.e.* mixed Ce^{+} and Ce^{4+})[154,155], O vacancy concentrations[143,195], and Ce vacancy concentrations[143]. The main trend reported in the literature is the temperature dependent reduction of Ce^{4+} to Ce^{3+}, and related behaviours on annealing in air. In order to isolate this process, an investigation into the stability of $CeTi_2O_6$ with respect to temperature and atmosphere (inert and oxidising) was performed, utilising thermogravimetric analysis (TGA) to elucidate the factors impacting the formation and stability of $CeTi_2O_6$.

The results of this investigation were published in Inorganic Chemistry: "The effect of temperature on the stability and cerium oxidation state of $CeTi_2O_6$ in inert and oxidizing atmospheres" (MC Dixon Wilkins, ER Maddrell, MC Stennett, NC Hyatt, *Inorg. Chem.*, 2020, **59**(23), 10.1021/acs.inorgchem.0c02681). The author's contribution was: TGA/MS measurements and analysis, analysis by X-ray diffraction, Le Bail method analysis of diffraction data, XAS data analysis, and writing of the manuscript.

5.2 The effect of temperature on the stability and cerium oxidation state of $CeTi_2O_6$ in inert and oxidizing atmospheres

Inorganic Chemistry

pubs.acs.org/IC

Article

The Effect of Temperature on the Stability and Cerium Oxidation State of $CeTi_2O_6$ in Inert and Oxidizing Atmospheres

Malin C. Dixon Wilkins, Ewan R. Maddrell, Martin C. Stennett, and Neil C. Hyatt*

Cite This: *Inorg. Chem.* 2020, 59, 17364−17373

Read Online

ACCESS | Metrics & More | Article Recommendations

ABSTRACT: Aliquots of well-characterized Ce-brannerite were annealed at different temperatures under N_2 and synthetic air atmospheres. The autoreduction of cerium at temperature was observed using thermogravimetry to monitor the mass lost as O_2 was evolved. It has been shown that the brannerite structure is stable with a small fraction of Ce^{3+}, charge-balanced by O vacancies. The range of stability was determined to be $Ce^{4+}_{0.975}Ti_2O_{5.95}$, the fully oxidized end-member, to $Ce^{3.87+}_{0.975}Ti_2O_{5.886}$, as reduced by annealing under N_2 at 1075 °C. Higher temperatures under N_2 led to further reduction of Ce and collapse of the brannerite structure. Ce-brannerite remained stable on heating to 1300 °C in synthetic air, with multiple steps of oxidation and reduction corresponding to changes in the average Ce oxidation state. We propose that the autoreduction of Ce at temperature is an important factor in the overall thermodynamic stability of Ce-brannerite at temperature and has a large impact on the energetics of formation of Ce-brannerite.

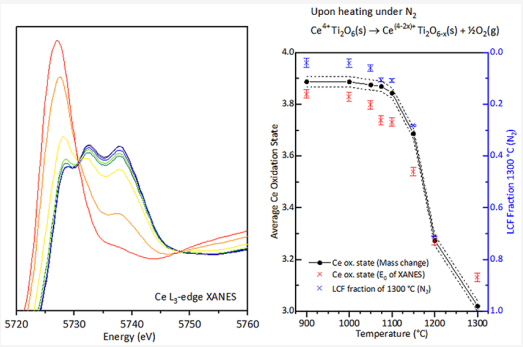

1. INTRODUCTION

Titanate phases observed in nature, incorporating uranium and thorium, (including brannerite, prototypically UTi_2O_6) have shown promise as ceramic[1] and glass−ceramic[2] materials for high actinide content nuclear fuel residues.[3] Natural brannerites are an important U-bearing mineral and have been well-studied with regard to their age and actinide inventories. Microprobe analysis of mineral specimens has shown that they contain significant fractions of other elements including Ca, Pb, Th, Y, and Ln on the U site and Si, Al, and Fe on the Ti site.[4−8] The family of synthetic brannerites includes the (prototypical) end members $CeTi_2O_6$, UTi_2O_6, $ThTi_2O_6$, and $PuTi_2O_6$.[9−12] The nonradioactive Ce-brannerite does not require stringent radioprotection safeguards to handle, and this, combined with the fact that Ce and Pu have very similar crystal chemistry and ionic radii, has led to interest in it as a surrogate material for the Pu-end member (nominally $PuTi_2O_6$).[13−15] However, the temperature-dependent nature of the Ce^{4+}/Ce^{3+} redox couple leads to a difference in chemical behavior when compared to Pu, for example in solubility within glass matrices.[13] The Ce-end member (nominally Ce^{4+}) has been previously reported to support nonstoichiometry of the Ce site and a degree of reduction caused by autoreduction at temperature. The stability of the brannerite structure with respect to high Ce^{3+} and O vacancy content caused by autoreduction is not well understood.

The oxidation state and stoichiometry of Ce in Ce-brannerite has been shown to be dependent on precise thermal history and composition, with a cooling rate of particular importance. Stennett et al. examined a sample that had been produced by a solid-state method and cooled relatively slowly (i.e., that had not been quenched) and used neutron diffraction and quantitative energy dispersive X-ray analysis to show that the stoichiometry is more correctly expressed as $Ce_{0.975}Ti_2O_{5.95}$, with vacancies on the O1 site. The location of the O vacancies and relative stability of different O−Ce−O vacancy clusters were determined by defect energy calculations. Using Ce L_3-edge XANES (X-ray absorption near-edge spectroscopy), all Ce was determined to be Ce^{4+}, with a detection limit of approximately 6%.[16] Samples prepared by a wet chemical route and slow-cooled in air show the same behavior, as reported by Kong et al.[17]

Reports of Ce-brannerite that were quenched at high temperature were shown to incorporate a small amount of Ce^{3+}, charge balanced by oxygen vacancies. Huynh et al. quenched the synthesized material from a reaction temperature of 1350 °C, then annealed aliquots of the as-quenched material at temperatures from 700 to 1100 °C. Using Ce L_3-edge XANES, the as-quenched material was determined to have a small amount of Ce^{3+}, which was not observed in any of the

Received: September 8, 2020
Published: November 11, 2020

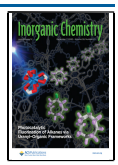

https://dx.doi.org/10.1021/acs.inorgchem.0c02681
Inorg. Chem. 2020, 59, 17364−17373

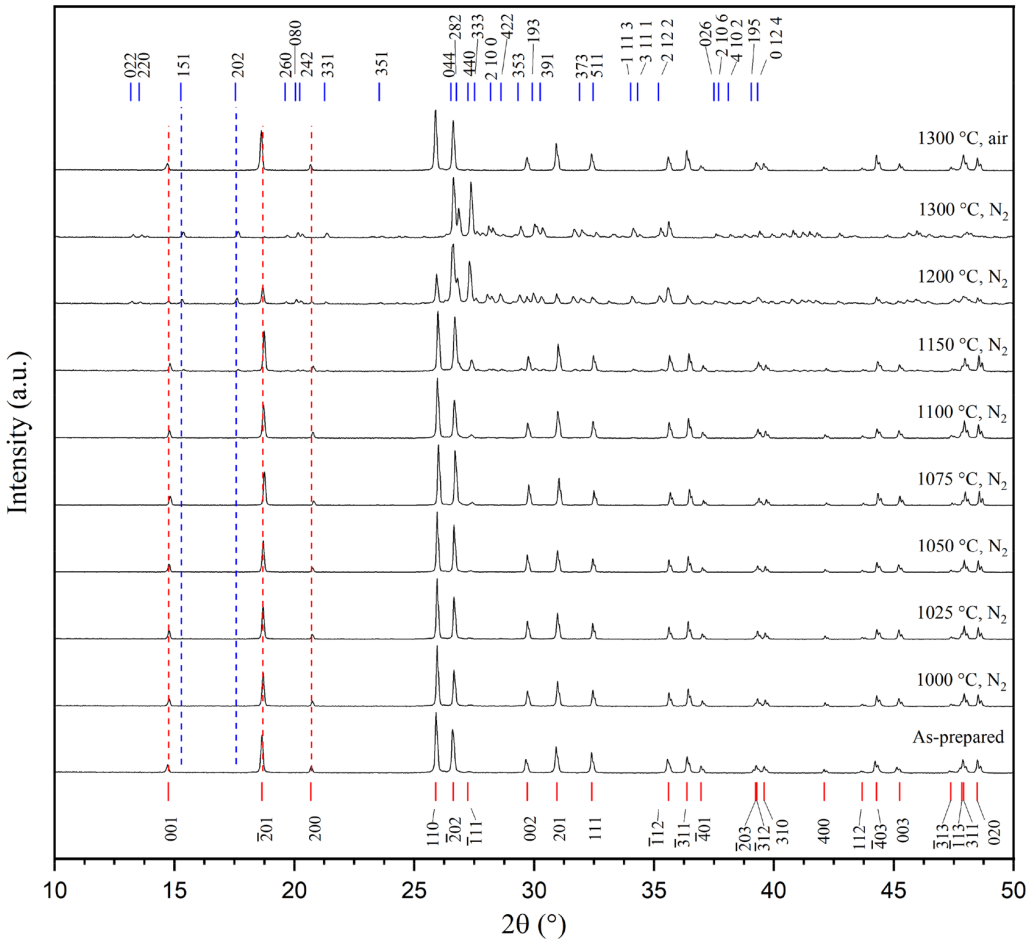

Figure 1. XRD patterns for aliquots of Ce-brannerite heated to a range of temperatures under N_2 or air. The reflections of $CeTi_2O_6$ (red, below) and $Ce_4Ti_9O_{24}$ (blue, above), and the corresponding Miller indices are marked. Three dashed lines show the positions of the first three peaks of $CeTi_2O_6$ (red) and two isolated peaks of $Ce_4Ti_9O_{24}$ (blue) to assist the reader.

annealed samples. The presence of Ce^{3+} in the as-quenched material was confirmed using Ce $M_{4,5}$-edge XANES.[18] Aluri et al. compared the Ce oxidation states of as-quenched material and material that had been annealed at 800 °C or slow-cooled in air using Ce L_3-edge XANES, Ce 3d X-ray photoelectron spectroscopy (XPS), and measurements of the magnetic susceptibility. The differences in the Ce L_3-edge XANES between the as-quenched and slow-cooled brannerite agree with the earlier findings of Huynh et al. The XPS determined that Ce^{3+} contents were significantly greater than was determined in the present work: 41% Ce^{3+} for the material quenched from 1325 °C and 32% Ce^{3+} for the material slow-cooled from 1325 °C, with an estimation of 38% Ce^{3+} for a material annealed at 800 °C determined by magnetic susceptibility measurements.[19]

A recent report[20] of DFT computed oxygen vacancy formation energies (E_{vf}^{O}) suggests that, in comparison to many other Ce^{4+} oxides, $CeTi_2O_6$ has a relatively low E_{vf}^{O} and can support a high fraction of O vacancies when the mechanism of charge balancing is reduction of Ce^{4+} to Ce^{3+}. Defect formation energies for Ce-brannerite have also been reported by Stennett et al., where the mechanism of charge balancing was taken to be the formation of Ce vacancies (e.g., the formation of O−Ce−O vacancy clusters), with no reduction of Ce.[16]

These previous investigations show the difficulty in accurately determining the average oxidation state of Ce in the solid state. Different methods of determining the Ce oxidation state infer the Ce speciation from observations of other phenomena (e.g., measurements of magnetic susceptibility infer the average Ce oxidation state from the magnetic response of the material) and can be strongly influenced by other factors, resulting in varying values of the oxidation state determined. For example, analysis of Ce L_3-edge XANES is often difficult, because, although the spectral envelopes characteristic of Ce^{3+} and Ce^{4+} are very different, the features present are also influenced by the Ce coordination environment.

The use of an in situ method, such as thermogravimetric analysis with coupled mass spectrometry (TGA/MS), to detect the loss of oxygen and reduction of Ce allows for a more direct observation of the change in Ce^{3+}/Ce^{4+} ratio and oxygen content as a function of temperature.

2. EXPERIMENTAL SECTION

The Ce-brannerite used in this investigation was that synthesized and characterized by Stennett et al.[16] Stoichiometric amounts of CeO_2 and TiO_2 were milled for 16 h using yttria-stabilized zirconia media, high density polyethylene pots, and isopropanol as a carrier fluid. The milled slurry was allowed to dry and the resulting powder cake sieved

https://dx.doi.org/10.1021/acs.inorgchem.0c02681
Inorg. Chem. 2020, 59, 17364−17373

Table 1. Crystallographic Information Determined from Le Bail Refinements of XRD Patterns of $Ce_{0.975}Ti_2O_6$, before[16] and after Heat Treatment at 1300 °C in Synthetic Air

ID	*a*	*b*	*c*	*β*	Volume	rR_{wp}	GOF
As-received	9.8351(4) Å	3.7537(1) Å	6.9010(2) Å	119.203(15)°	222.39(6) Å^3	8.544	1.158
1300 °C air	9.8277(2) Å	3.7517(1) Å	6.8837(1) Å	119.216(14)°	221.52(8) Å^3	7.654	1.126

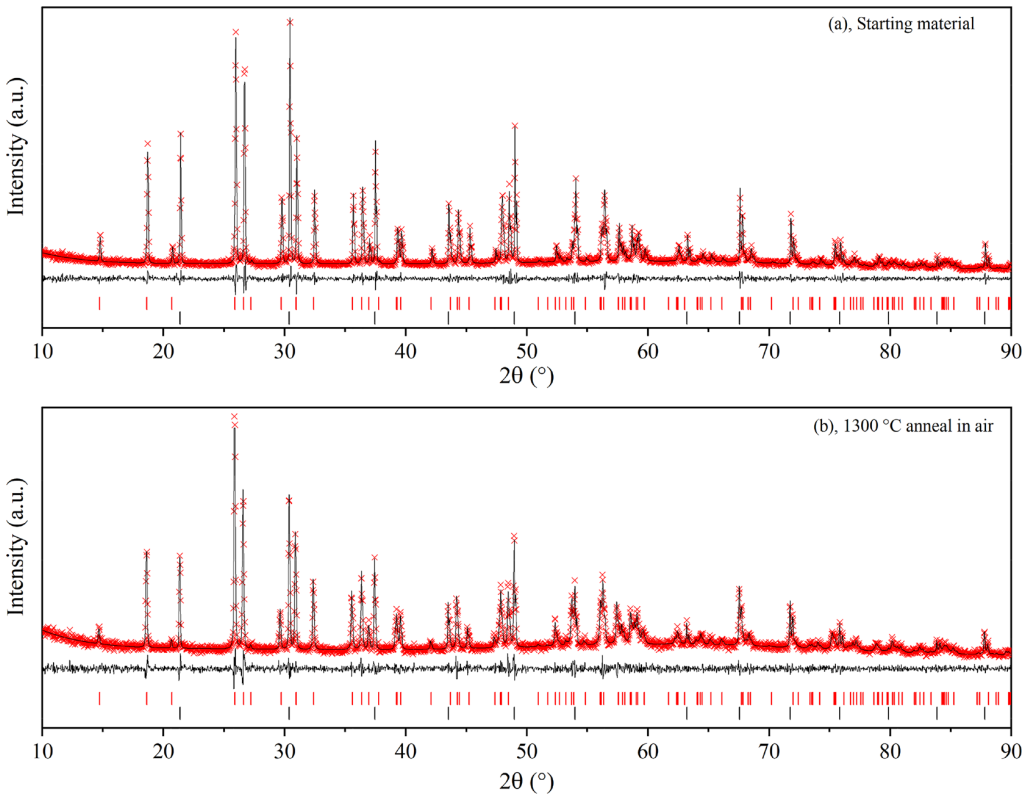

Figure 2. Calculated and observed XRD patterns for the starting material and the material after annealing at 1300 °C under synthetic air. The observed intensities are marked with red crosses, calculated intensities (following a LeBail refinement of the experimental pattern) with black lines, and the difference plot in black lines underneath the diffraction patterns. The peak positions of Ce-brannerite (red lines) and the LaB_6 internal standard (black lines) are marked below.

using a 250 μm mesh. The dry powder was pressed into pellets, fired at 1350 °C for 48 h, reground to rehomogenize the material, and fired for 48 h a second time. Aliquots of the material were heated in a Netzsch Jupiter TG 449 F3 simultaneous thermal analyzer (STA), with an Aëolos QMS 403 D mass spectrometer (MS). The powders were held in Al_2O_3 crucibles and heated in either an inert (N_2) or oxidizing (synthetic air: 79% N_2 and 21% O_2) atmosphere. To account for the effect of adsorbed atmospheric water, once each aliquot of material was loaded into the crucible, it was first heated to 250 °C, then cooled to 100 °C prior to the main heating cycle.

X-ray diffraction (XRD) patterns were collected using a Bruker D2 Phaser diffractometer, with Ni-filtered Cu Kα radiation. The unit cell parameters of the as-received material and material heat-treated at 1300 °C under synthetic air were determined using Le Bail method[21,22] refinements of the diffraction patterns in the Topas software package.[23] LaB_6 was added to act as an internal standard for these samples, to enable determination of accurate and precise unit cell dimensions.

Ce L_3-edge XANES spectra were collected at the NSLS-II beamline 6BM (Brookhaven National Laboratory, USA).[24] Samples of one absorption length were prepared by homogeneously mixing the material with (poly)ethylene glycol and uniaxially pressing it into 13 mm pellets. Measurements were conducted at room temperature in transmission mode, using a Si(111) monochromator, a Rh/Pt-coated paraboloid collimating mirror, and a flat Si stripe harmonic rejection mirror. The beam size was defined using slits to give a beam size of 1 mm (v) by 5 mm (h). Signal intensity of the incident and transmitted X-rays were measured using ionization chambers operating in a stable region of their current vs voltage curve. Spectra were recorded between 5523 and 5965 with energy steps of 10 eV (5523−5693), 2 eV (5693−5713), 0.25 eV (5713−5753), and 0.05k (5753−8k); an accumulation time of 1 s step^{-1} was used for all regions. The optically encoded monochromator was calibrated on the correct absolute energy scale by measuring the angular position of a range of metal foils and comparing them to the energy values tabulated in Kraft et al.[25] Energy stability over the measurement was in the range ±0.05 eV. Data were normalized and analyzed using the program Athena.[26,27] E_0 was set at the energy corresponding to half of the edge step. The spectra of a range of standards (CeO_2, Ce_3NbO_7, $SrCeO_3$, $CeAlO_3$, $CePO_4$, $Ce_2Ti_2O_7$, $SrCe_2Ti_4O_{12}$, confirmed by XRD) of known Ce oxidation state and coordination were also collected to act as a reference, following the same sample preparation.

3. RESULTS

3.1. X-ray Diffraction. Phase analysis was conducted by XRD. The contents of the starting material were checked to confirm it had not degraded over time, and only $Ce_{0.975}Ti_2O_{5.95}$ was observed in the diffraction pattern. Material heated in N_2 to 1075 °C or below consisted only of Ce-brannerite (PDF 01-

https://dx.doi.org/10.1021/acs.inorgchem.0c02681
Inorg. Chem. 2020, 59, 17364−17373

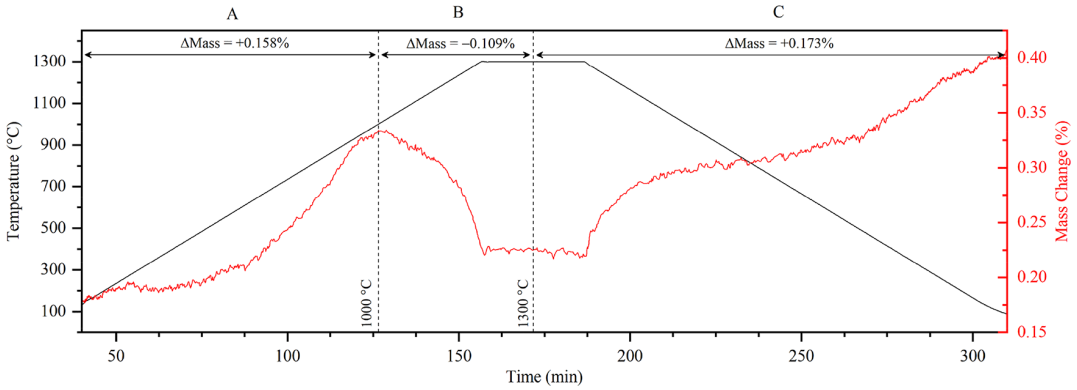

Figure 3. Thermogravimetric data of Ce-brannerite heated under synthetic air to 1300 °C. The data is divided into sections according to the three regions of interest A, B, and C (marked at 1000 and 1300 °C with dashed lines). The mass changes over these regions of interest are marked above.

083-6112), with no decomposition products observed (see eq 1). The diffraction pattern of the material heated to 1100 °C contained some very low intensity reflections corresponding to the presence of trace amounts of $Ce_4Ti_9O_{24}$ (a Ce^{3+} species) (visible in the range $28 < 2\theta < 29°$, see Figure 1). The reflection at $2\theta = 27.5°$ could be attributed to the presence of TiO_2 (rutile), but this could not be reliably confirmed due to overlap with the brannerite $(\bar{1}11)$ and $Ce_4Ti_9O_{24}$ (440) and (333) reflections.

As the annealing temperature was increased, the relative amount of $Ce_4Ti_9O_{24}$ increased compared to Ce-brannerite, evidencing decomposition of the brannerite phase (see eq 2 for the hypothesized decomposition pathway). At 1150 °C, brannerite was still the major phase, with reflection intensities much higher than those attributed to $Ce_4Ti_9O_{24}$. The diffraction patterns of brannerite heated to 1200 °C and higher were complex, consisting mostly of $Ce_4Ti_9O_{14}$ and a smaller amount of Ce-brannerite, but also containing other Ti and Ce^{3+} phases (including $Ce_2Ti_2O_7$ and trace amounts of Ce_2O_3). Brannerite was still present in the material heated to 1200 °C but was noticeably depleted compared to those heated to lower temperatures; the major crystalline phase was $Ce_4Ti_9O_{24}$. By 1300 °C, the phase assemblage comprised $Ce_4Ti_9O_{24}$, with trace amounts of other phases; no brannerite was observed in the diffraction pattern (a small reflection at $2\theta = 18.7°$ was visible, which may correspond to the brannerite $(\bar{2}10)$ reflection, but the more intense (110) was not visible).

$$Ce^{4+}Ti_2O_6(s) \xrightarrow{\leq 1075°C(N_2)} Ce^{(4-2x)+}Ti_2O_{6-x}(s) + \frac{x}{2}O_2(g) \quad (1)$$

$$5(Ce^{4+}_{1-2x}Ce^{3+}_{2x})Ti_2O_{6-x}(s) \xrightarrow{\gg 1100°C(N_2)} Ce^{3+}_4Ti_9O_{24}(s) + \frac{5}{4}O_2(g) + \frac{1}{2}Ce^{3+}_2Ti_2O_7(s) \quad (2)$$

The unit cell parameters of the as-prepared Ce-brannerite and the product from heat treatment at 1300 °C in synthetic air were determined using Le Bail refinements with LaB_6 as an internal standard (see Table 1 and Figure 2). The change from the as-prepared material to the material post-heat-treatment consisted of small contractions in the *a* and *b* parameters (0.0074(4) Å and 0.0020(1) Å respectively), a larger contraction in *c* (0.0173(2) Å), and a decrease in overall unit cell volume (0.873(10) Å^3). Although the changes in unit cell parameters *a* and *b* are small, when they are considered along with the contraction in the *c* parameter and unit cell volume, the overall changes in unit cell dimension suggest a decrease in Ce^{3+} content (six-coordinate ionic radius of 1.01 Å^3), with a corresponding increase in Ce^{4+} content (six-coordinate ionic radius of 0.87 Å^3),[28] as confirmed by XANES and thermogravimetric techniques (see below). This is in good agreement with previous reports of structural changes within the brannerite structure caused by changes in the average A-site ionic radius.[29,30] The unit cell parameters of the as-prepared material were slightly larger than those previously reported by Stennett et al.,[16] likely due to differences in the instrumental contributions to the final diffraction patterns from X-ray diffraction and neutron diffraction.

3.2. Thermogravimetric Analysis. *Material Heated in Air.* The material heated to 1300 °C in synthetic air (79% N_2, 21% O_2) showed complex behavior when heated (see Figure 3). The evolution of a small amount of CO_2 at 375 °C was observed in the MS channel corresponding to masses of 44, but the TGA data during heating from 100 to 1000 °C was dominated by a mass gain (region A, change of +0.158(2)%), suggesting that the as-prepared material was slightly reduced, but was then partially oxidized during the heating cycle. From the maximum at 1000 °C, a mass loss was observed on heating to 1300 °C (region B, change of −0.109(2)%). A corresponding mass gain of similar magnitude was then seen on cooling from 1300 to 100 °C (region C, +0.173(2)% of total sample mass). An overall mass change of +0.222(2)% was observed over the course of the heating cycle. This demonstrates that the initial material was indeed slightly reduced. The average Ce oxidation states and corresponding mass losses are shown in Table 1.

Making the assumption that the final product of this heating cycle was fully oxidized (i.e., only $Ce_{0.975}{}^{4+}Ti_2O_{5.95}$), the overall mass gain of +0.222(2)% corresponds to a starting stoichiometry of $Ce_{0.975}Ti_2O_{5.905}$, with an average Ce oxidation state of +3.906(5). This is in good agreement with the XANES measurements detailed below. This was taken to be the first of the two calculated starting stoichiometries ($Ce_{0.975}{}^{3.91+}Ti_2O_{5.905}$) from which oxygen was lost during annealing under N_2. This is in close agreement with the other calculated starting stoichiometry of $Ce_{0.975}{}^{3.87+}Ti_2O_{5.885}$ (see below).

https://dx.doi.org/10.1021/acs.inorgchem.0c02681
Inorg. Chem. 2020, 59, 17364−17373

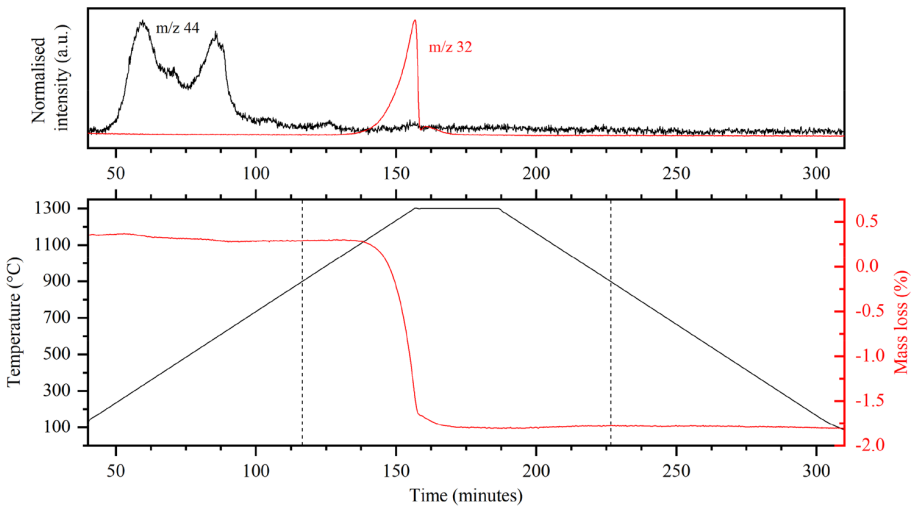

Figure 4. Thermogravimetry and mass spectrometry data of Ce-brannerite heated to 1300 °C under a N_2 atmosphere. A low temperature heating step to 250 °C was performed before the main heating step; this is not shown. The dashed black lines show the temperature region over which the mass losses were normalized (900 to 900 °C). The normalized intensities over time of the mass channels of interest are shown above in black (m/z of 44, corresponding to CO_2) and red (m/z of 32, corresponding to O_2).

Table 2. Details of Mass Losses of Ce-Brannerite Heated to Various Temperatures under Different Atmospheres[a]

Atm.	Sample identifier	Mass change (%)	Average Ce ox. state from mass changes	E_0 from Ce L_3-edge XANES	Est. Ce ox. state from E_0 positions	Major phases in XRD
N/A	As-received	N/A	3.886+ (±0.02)	5724.16 eV	+3.90	Bran
N_2	1000 °C	N/A	3.886+ (±0.02)	5724.12 eV	+3.89	Bran
	1050 °C	−0.028%	3.874+ (±0.02)	5723.99 eV	+3.86	Bran
	1075 °C	−0.042%	3.869+ (±0.02)	5723.75 eV	+3.78	Bran
	1100 °C	−0.104%	3.843+ (±0.02)	5723.72 eV	+3.77	Bran, CTO (trace)
	1150 °C	−0.478%	3.686+ (±0.02)	5722.95 eV	+3.55	CTO, Bran
	1200 °C	−1.465%	3.273+ (±0.02)	5721.87 eV	+3.22	CTO, Bran
	1300 °C	−2.069%	3.020+ (±0.02)	5721.30 eV	+3.05	CTO
Air	1300 °C (total)	+0.222%	3.979+ (±0.02)	5724.55 eV	+4.02	Bran
	1300 °C (region A)	+0.158%	3.953+ (±0.02)	N/A	N/A	Bran
	1300 °C (region B)	−0.109%	3.887+ (±0.02)	N/A	N/A	Bran
	1300 °C (region C)	+0.173%	3.979+ (±0.02)	N/A	N/A	Bran
N/A	Ce_3NbO_7	N/A	N/A	5721.12 eV	+3	N/A
	CeO_2	N/A	N/A	5724.48 eV	+4	N/A

[a]The average Ce oxidation state is calculated as the mid-point of the oxidation states calculated starting from the two stoichiometries of $(Ce^{3.907+})_{0.975}Ti_2O_{5.905}$ and $(Ce^{3.866+})_{0.975}Ti_2O_{5.885}$. Specimens with large amounts of brannerite and $Ce_4Ti_9O_{24}$ identified by XRD are labelled Bran and CTO, respectively.

Our estimated actual oxygen stoichiometry derived from TGA analysis is within the estimated uncertainty of ±0.05 formula units for the determination by neutron diffraction. Note that in the previous neutron diffraction analysis, a compositional constraint was applied to refinement of Ce and O vacancies, ensuring charge neutrality assuming all Ce was present as Ce^{4+}.

Material Heated in N_2. To establish the temperature at which autoreduction of Ce and O_2 loss begins to occur under an inert atmosphere, a specimen of the as-prepared material was heated under a N_2 atmosphere to 1300 °C. Due to the low relative mass losses examined, the sensitivity of thermogravimetric methods causes changes in buoyancy of the crucible containing the material as a function of heating to affect the apparent mass. This effect is significant below 350 °C, with changes on the order of ±0.025%, but becomes negligible at temperatures above 400 °C. A mass loss of 0.062(2)% starting at 375 °C was attributed to the loss of CO_2, with corresponding features also observed at this temperature range in the MS channel of mass 44. After this mass loss, no other changes were observed until above 1000 °C, where a mass loss of −2.070(2)% was observed, beginning at approximately 1050 °C. A clear signal in the MS channel of mass 32 showed that this was a loss of O_2 as the material began to autoreduce (see Figure 4). This shows the near-complete reduction of Ce and collapse of the brannerite structure as the fraction of Ce^{3+} moves out of the domain of stability. This is in agreement with the phases observed by XRD, where the major crystalline phase observed after heating to 1300 °C was $Ce_4Ti_9O_{24}$.

https://dx.doi.org/10.1021/acs.inorgchem.0c02681
Inorg. Chem. 2020, 59, 17364−17373

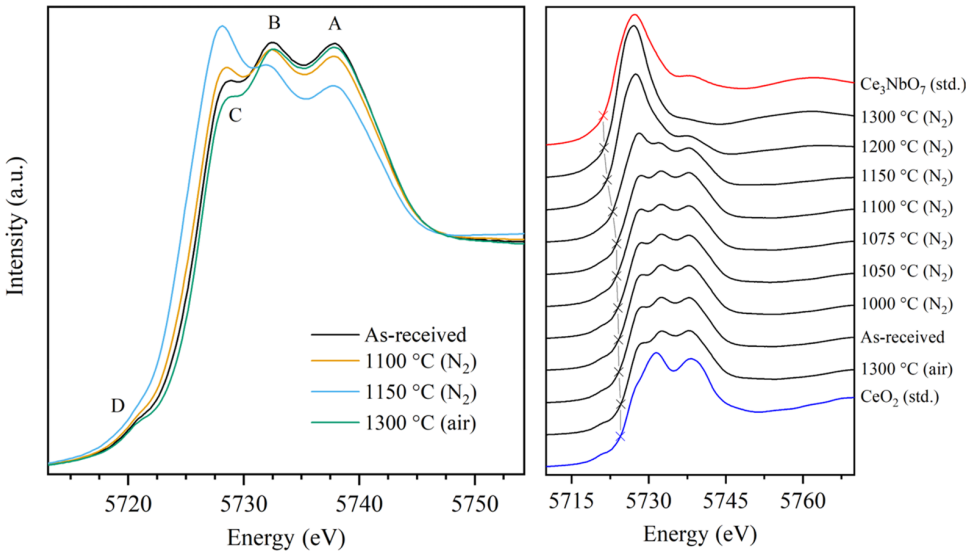

Figure 5. (Left) Normalized XANES spectra of four samples of Ce-brannerite postheat treatment, showing the changes in the four features A–D. (Right) XANES spectra of samples of Ce-brannerite heat treated at different temperatures and in different atmospheres. CeO_2 and Ce_3NbO_7 were used as standards of known Ce oxidation state to examine the E_0 values of the spectra (evaluated as the energy at half of the edge step, marked by crosses).

Aliquots of the material heated to different temperatures under N_2 showed the same behavior, differing only in the overall fractional mass lost. Making the assumption that the phase assemblage produced after heating to 1300 °C in N_2 was fully reduced to Ce^{3+} (in agreement with the phases indexed from the XRD pattern, above, and Ce L_3-edge XANES, below), the mass loss of −2.070(2)% corresponds to a starting stoichiometry of $Ce_{0.975}Ti_2O_{5.885}$, with an average Ce oxidation state of +3.866(5) (*c.f.* the average Ce oxidation state determined from the sample heated under air, +3.906(5)). These initial stoichiometries were then used to estimate the Ce oxidation states of the products of different heating cycles (see Table 1) and, as expected, give close agreement.

The observations made from the material heated to 1300 °C under N_2 informed the temperature range of interest for investigation of further heating cycles. In order to remove the influence of buoyancy effects and surface adsorbed species, observed below 400 °C, the mass lost or gained by the material was taken as the mass change over the range 900 to 900 °C (that is, 900 °C during heating and 900 °C during cooling). For example, assuming no Ce or Ti was lost and no reduction of Ti occurred, the mass loss after heating to 1100 °C was −0.104(2)%. This corresponds to an average Ce oxidation state of 3.863(5)+ if the stoichiometry of the starting material is calculated assuming the material heated at 1300 °C in air (detailed above) was fully oxidized. On the other hand, this corresponds to an average of 3.823(5)+ if the assumption is made that the material heated at 1300 °C under N_2 was fully reduced. As the calculated average Ce oxidation states are similar, differing by a constant 0.040, and within mutual uncertainties of the methods of estimation, the average of these two values was taken to determine a representative oxidation state, with the two calculated values forming the upper and lower bounds of uncertainty (e.g., average Ce oxidation state of 3.84(2)+ for the material heated to 1100 °C in N_2). The errors in the measured masses are small enough to be neglected compared to this uncertainty.

To establish a lower bound of interest for the temperature at which autoreduction of Ce-brannerite begins, material was heated to 1000 °C under N_2. The mass loss over the course of this heating cycle was determined to be −0.0001(20)%, i.e., no significant mass loss. As a result, a range of temperatures between 1000 and 1300 °C were selected for investigation, with a focus on the region around 1050 °C. The 900 to 900 °C mass loss over each dwell temperature is shown in Table 2, along with the major crystalline phases indexed from the XRD diffraction patterns and average Ce oxidation state, calculated from normalized mass losses and Ce L_3-edge XANES.

3.3. Ce L_3-Edge X-ray Absorption Near-Edge Spectroscopy. The Ce L_3-edge XANES spectra showed the same trend as that observed in the mass changes observed by thermogravimetric methods. When heated under N_2, increasing temperature resulted in a higher mass loss and a corresponding increase in Ce^{3+} content, with XANES able to probe the bulk Ce oxidation state and local environment. The trend seen in the mass losses observed by thermogravimetric analysis was also observed in the XANES spectra. As the temperature increased, the features A, B, and D (characteristic of Ce^{4+}, and not present in spectra of Ce^{3+} species) became less intense, and feature C (very weak in Ce^{4+} species, but overlaps with the single intense feature of Ce^{3+} species) predominated (see Figure 5). This is in agreement with the phases indexed in the XRD patterns of each product, as well the average oxidation states calculated from the normalized mass changes. The sample heated under air to 1300 °C showed contrasting behavior, with a reduction in intensity of feature C relative to the as-received starting material, demonstrating that the overall effect of the heat treatment was oxidation, as was also observed by the mass gain apparent in the thermogravimetric measurements.

For confirmation of the Ce oxidation states calculated from the normalized mass losses during heating, the values of E_0 (taken as the energy at half the edge step) were compared to those of the standards of known Ce oxidation state and coordination with the highest and lowest measured values of E_0

https://dx.doi.org/10.1021/acs.inorgchem.0c02681
Inorg. Chem. 2020, 59, 17364−17373

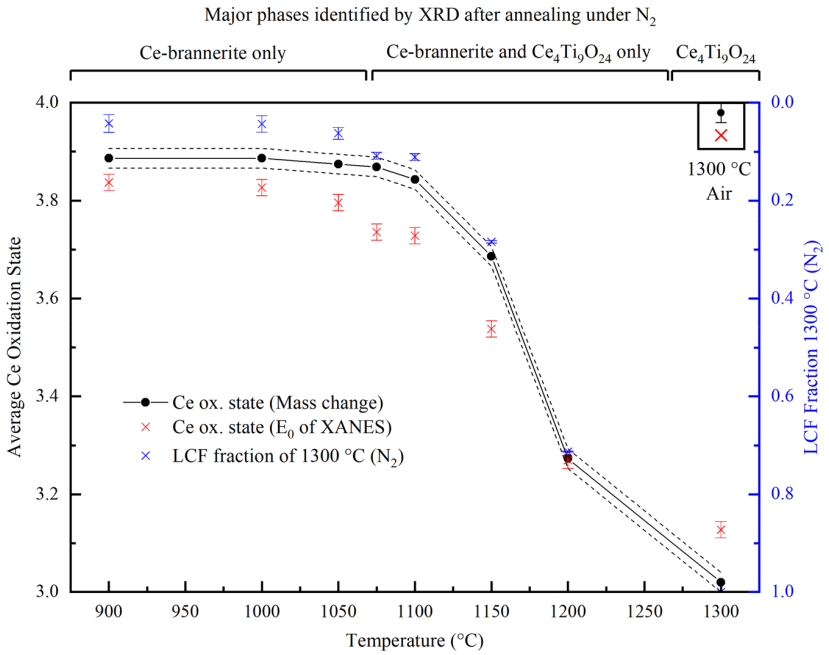

Figure 6. Changes in average cerium oxidation state as calculated from the mass change (black), and estimated from the energy position, E_0, of the Ce L3-edge (red) of aliquots of Ce-brannerite heated at varying temperatures under N_2. The fraction of the sample reduced at 1300 °C under N_2 present in the best linear combination fit is also shown on the same scale (blue). Standard errors are shown as error bars (red and blue) or as dashed lines (black). The phases observed in the XRD patterns of the materials heated under N_2 are annotated above.

(CeO_2 and Ce_3NbO_7, respectively). Under the assumption that E_0 varies linearly with average Ce oxidation state, the Ce oxidation state in the heat treated materials could be estimated (see Table 1 and Figure 5). There are some shortcomings with this method, including the effect of differing Ce local environment on the Ce L_3-edge energy position, and the lack of ideal standards (CeO_2 and Ce_3NbO_7 have coordination numbers of eight, but Ce is six-coordinate in the brannerite structure). In reality, this relationship was not perfectly linear, due to the local environment changing across the temperature range investigated (as established by the phases indexed in XRD patterns), but still allowed for confirmation of the values calculated from normalized sample mass losses with an estimate of the bulk Ce oxidation state. The oxidation states estimated in this way are in agreement with those calculated from the mass changes.

Linear combination fitting (LCF) was also performed on the XANES data, using the two samples heated to 1300 °C as reference standards. This was done using the two samples of highest (that heated in air) and lowest (that heated in N_2) average Ce oxidation state, as this allowed for a better description of the changes in Ce oxidation state that occurred as the temperature of annealing (under N_2) increased, without the need for exact values for the oxidation states of the standards used. As the temperature is increased, the fraction of the reduced Ce standard (that is, the sample heated to 1300 °C in N_2) increased from 4.24(18)% to 71.3(1)%, in excellent agreement with the trends seen in a Ce oxidation state by both mass loss and Ce L_3-edge energy position (see Figure 6). It must be noted that this is a qualitative method of observing the change in spectral peak shape and intensity with respect to temperature of heat treatment and is not strictly a quantitative measure of the Ce oxidation state.

4. DISCUSSION

The aliquots of Ce-brannerite heated to 1300 °C under synthetic air and N_2 allowed identification of the degree of reduction in the initial material. The overall mass change across the heat treatment was +0.222(2)%, with two separate oxidation events resulting in mass gain. The first, beginning at approximately 500 °C, showed the oxidation of the initial material, up to an average Ce oxidation state of +3.95(2). This oxidation event coincided with the onset of autoreduction as the temperature exceeded 1000 °C, preventing it from fully oxidizing during heating. The second oxidation event occurred during cooling of the sample, with a final mass (and therefore average Ce oxidation state) greater than the initial sample mass; this showed that the initial material was not fully oxidized (i.e., not all Ce was present as Ce^{4+}). This is likely due to the sample not reaching equilibrium during cooling from temperature, effectively quenching a small fraction of Ce^{3+} and O vacancies into the structure.

The overall mass change of the material heated to 1300 °C in the air (+0.222(2)%) corresponds to a starting stoichiometry of $Ce_{0.975}^{3.91+}Ti_2O_{5.905}$. In comparison, the overall mass change gained by the material heated to 1300 °C in N_2 (−2.070(5)%) corresponds to a starting stoichiometry of $Ce_{0.975}^{3.87+}Ti_2O_{5.885}$. These calculated stoichiometries formed reasonable upper and lower bounds for the starting stoichiometry and average Ce oxidation state.

A previous study of mixed A-site cation brannerite (A = Ce, U, Th) glass-ceramic composites has shown that the presence of U can stabilize the formation of a Ce-containing brannerite under argon by charge-balancing Ce^{3+} with equimolar fractions of U^{5+} within brannerite.[29] A further report of $U_{1-x}^{5+}REE_x^{3+}Ti_2O_6$ (where REE is Ce, Y, Eu) glass ceramics also observed this behavior.[31] This shows that the autoreduction of Ce at temperature does not preclude the

https://dx.doi.org/10.1021/acs.inorgchem.0c02681
Inorg. Chem. 2020, 59, 17364−17373

stability of the brannerite structure, provided compatible species are available to achieve an overall balance of charge without excessive O vacancies. This can allow for reduction of some or all Ce in the sample, while the brannerite structure is retained.

As expected from previous reports of the autoreduction of Ce-brannerite at high temperatures, the amount of oxygen lost was strongly dependent on the annealing temperature.[17−20] As temperature increases, reduction of Ce^{4+} to Ce^{3+} becomes thermodynamically preferred, with the resulting phase releasing oxygen to maintain overall charge balance. This trend was observed when comparing the relative mass losses of samples heated under N_2. As the temperature of heat treatment was increased, the observed mass losses increased from negligible at 1000 °C, to −2.070(2)% of the total sample mass at 1300 °C. The mass lost at 1300 °C corresponds to a final average Ce oxidation state of +3.02(2), showing near-complete reduction of the material, with no reflections characteristic of Ce-brannerite observed in the XRD pattern. This is in good agreement with the observed Ce L_3-edge XANES spectrum.

When heated to 1075 °C under N_2, Ce-brannerite was reduced but remained single phase, with a mass loss of 0.042(2)%, corresponding to a final stoichiometry $Ce_{0.975}^{3.87+}Ti_2O_{5.886}$. The diffraction pattern of the sample heated to 1100 °C under N_2 was observed to be near-single-phase brannerite (nominally, $Ce_{0.975}^{3.84+}Ti_2O_{5.872}$), with only trace amounts of $Ce_4Ti_9O_{24}$. These observations show that the compositional range of stability of Ce-brannerite is $Ce_{0.975}^{4.00+}Ti_2O_{5.950}$ to $Ce_{0.975}^{3.87+}Ti_2O_{5.886}$ (equivalent to 13.1% Ce^{3+}), when the material is reduced by annealing under an anoxic atmosphere. This is in contrast to literature reports of Ce^{3+} fractions of 30−41%, as measured by XPS and measurements of magnetic susceptibility.[19]

This extent of reduction and the corresponding amount of O vacancies is in good agreement with the recently reported DFT calculations, which predicted a relatively high upper bound of stability in the system $Ce^{(4-2\delta)+}Ti_2O_{6-\delta}$, when compared to other Ce^{4+} oxides.[20] When the reported energies of O vacancy formation are compared to each other, both DFT[20] and Mott-Littleton[16] methods predict that the vacancies formed will be preferentially located at the O sites coordinated with at least one Ce cation.

The sample heated to 1300 °C in the air also gave some insight into the thermodynamic stability of Ce-brannerite. Previous reports of the thermodynamics of Ce-brannerite formation from component oxides showed that it is entropically stabilized at high temperatures and best described at room temperature as metastable due to extremely slow diffusion in the solid state.[32] From the standard enthalpy of formation, the lower limit of the entropy of formation of Ce-brannerite was calculated to be 18.1 (±2.2) J K^{-1} mol^{-1}, assuming $\Delta G_{f\text{-}ox}^{\ 0} \leq 0$ at the temperature of reaction, 1350 °C. The post-heat-treatment phase assemblage of the sample heated in the air to 1300 °C in the present study showed it contained only Ce-brannerite. Diffusion through the solid state at these temperatures is non-negligible, yet decomposition of Ce-brannerite was not observed, suggesting the phase remained stable at this temperature. There are two possible explanations for this: the entropy of formation of Ce-brannerite is higher than that reported by Helean et al., or the thermodynamically favorable autoreduction of some Ce^{4+} at temperature has lowered the enthalpy of formation.

If the true entropy of formation of Ce-brannerite is higher than the lower limit previously reported, for $\Delta G_{f\text{-}ox}^{\ 0} \leq 0$ at 1300 °C, this corresponds to $\Delta S_{f\text{-}ox}^{\ 0}$ of 18.7 J K^{-1} mol^{-1}, which may account for the stability of Ce-brannerite at 1300 °C.[32]

At the common reaction temperature of 1350 °C in the air, a non-negligible amount of Ce^{3+} (initially Ce^{4+}, usually from CeO_2) is present, and we propose the stability at temperature of Ce-brannerite may be dependent on the presence of this small fraction of Ce^{3+} at temperature. A smaller subfraction could then be effectively quenched into the structure during cooling, while the remainder is reoxidized to Ce^{4+} (even at nonquenched cooling rates at a magnitude of 5 °C min^{-1}), with the amount of Ce^{3+} remaining at room temperature controlled by the rate of cooling from 1350 °C to the temperature at which solid-state diffusion of O is negligible. As the drop solution enthalpy measurements in that study were taken for CeO_2 at 700 °C and no terms correcting for the presence of Ce^{3+} were applied, the possible enthalpic effect of the presence of Ce^{3+} was not accounted for in the thermochemical cycles used to calculate the enthalpy of formation of Ce-brannerite. Using the method and data published by Ushakov et al. to determine the enthalpy of formation of $CePO_4$ (which only contains Ce^{3+}) using the measured drop solution enthalpy of CeO_2 (and so accounting for the enthalpic effect of the oxidation of Ce^{3+} to Ce^{4+} upon dissolution),[33] the positive enthalpy of formation of Ce-brannerite is reduced from +29.6 kJ mol^{-1} with an average Ce oxidation state of +4[32] and becomes zero at an average Ce oxidation state of +3.85. Further evidence for the true enthalpy of formation being smaller (and possibly negative) is the observation made from DFT calculations that the presence of O vacancies allows for partial relief of the strain present in the distorted (TiO_6) octahedra.[20] As observed by Stennett et al.,[16] the Shannon polyhedral distortion indices (a measure of the distortion of polyhedral subunits) of (TiO_6) octahedra distortion decrease substantially as the M-site radius increases from U^{4+} (1.03 Å^3) to Th^{4+} (1.08 Å^3). If the charge-balancing mechanism of O vacancy formation is taken to be a reduction of some Ce^{4+} (1.01 Å^3) to Ce^{3+} (1.15 Å^3), both of these effects will be observed, and the resulting relief of strain could well be an important energetic consideration during the formation of Ce-brannerite.

Although the above explanations are only hypotheses made in the absence of adequate data in the literature, they suggest that Ce-brannerite may plausibly be thermodynamically stabilized by the presence of Ce^{3+} at high temperatures. It is unclear to which, if either, of these explanations the observed stability of Ce-brannerite at 1300 °C can be attributed, and it is likely that both have an impact. Further energetic studies are hampered by the highly complex thermodynamics of phase formation of Ce-containing oxides at temperatures where the Ce^{3+}/Ce^{4+} redox couple is active. Previous systematic studies of the autoreduction of Hf-doped CeO_2 have shown that the presence of an additional phase-forming element has a strong effect on the Ce^{3+}/Ce^{4+} equilibrium.[34]

The work presented in this study demonstrates the relative flexibility of Ce-brannerite with respect to oxygen content and Ce oxidation state; however, the same flexibility also raises issues with the use of Ce-brannerite as a simulant material for actinide-containing brannerites. Both UTi_2O_6 and $ThTi_2O_6$ have been suggested as possible materials for the disposal of high-actinide fraction wastes, with and without Pu, but have starkly different thermal behavior than that of the Ce analogue.

https://dx.doi.org/10.1021/acs.inorgchem.0c02681
Inorg. Chem. 2020, 59, 17364−17373

This is partially due to the lack of available oxidation states below +4 for these cations (in solid oxides, U is usually present as +4, +5, or +6, and Th is present as +4), which prevents them from showing the same self-reduction that has been demonstrated here. Although Pu^{3+} does form some oxide materials, the Pu^{3+}/Pu^{4+} redox couple does not show the same temperature dependence as the equivalent Ce^{3+}/Ce^{4+} couple. This shows that, while it may be an acceptable surrogate in some systems, Ce-brannerites should be used with due caution as a surrogate for actual actinide containing materials, as the differences in redox behavior will affect a wide range of properties, including dissolution resistance and behavior, the effect of radiation damage, and compatibility with other phases in the final wasteform.

5. CONCLUSIONS

Coupled thermogravimetric and mass spectroscopy measurements were used to identify the range of stability of the Ce-brannerite structure with respect to the average Ce oxidation state and O vacancies that form to charge balance. Of all samples heated under N_2 that retained the brannerite structure, the samples heated to 1075 and 1100 °C were reduced the most, having lost the highest amount of oxygen. The sample heated to 1100 °C appeared to be just over the stability limit, as trace amounts of the major decomposition product of Ce-brannerite, $Ce_4Ti_9O_{24}$, were identified by XRD. These samples show that the maximum fraction of Ce^{3+} that can be supported in the brannerite structure when introduced by annealing under an inert atmosphere is between 13.1% and 15.7% of the total Ce content, with the corresponding increase in oxygen vacancies being the limiting factor as to the stability of the structure.

When decomposition of the brannerite structure is avoided, the reduction of the material is reversible. This is obvious on examination of the thermogravimetric measurements of the material heated under synthetic air, where different regimes of mass change were observed, corresponding to the changes in the equilibrium position of the Ce^{3+}/Ce^{3+} redox couple as the temperature changed. These changes in oxidation state are also observed in the change of relative intensity of feature C in the Ce L_3-edge XANES, which shows that the material after heat treatment in air has a lower Ce^{3+} content than the starting material, in excellent agreement with the overall increase in mass of the sample (+0.222(2)%, corresponding to a final oxidation state of $Ce^{3.979+}$).

The autoreduction of Ce may have an impact on the overall energetics of Ce-brannerite formation. The exothermic reduction process is likely of a sufficient magnitude to overcome the positive enthalpy of formation of Ce-brannerite.

AUTHOR INFORMATION

Corresponding Author

Neil C. Hyatt − *Department of Materials Science and Engineering, University of Sheffield, Sheffield, United Kingdom*; Email: n.c.hyatt@sheffield.ac.uk

Authors

Malin C. Dixon Wilkins − *Department of Materials Science and Engineering, University of Sheffield, Sheffield, United Kingdom*; orcid.org/0000-0003-1520-7672

Ewan R. Maddrell − *National Nuclear Laboratory, Sellafield, Cumbria, United Kingdom*

Martin C. Stennett − *Department of Materials Science and Engineering, University of Sheffield, Sheffield, United Kingdom*; orcid.org/0000-0002-8363-9103

Complete contact information is available at: https://pubs.acs.org/10.1021/acs.inorgchem.0c02681

Notes

The authors declare no competing financial interest.

ACKNOWLEDGMENTS

The authors would like to thank Dr. Bruce Ravel for his assistance at NSLS-II beamline 6BM and his helpful comments on this manuscript. This research utilized the HADES/MIDAS[35] facility at the University of Sheffield established with financial support from EPSRC and BEIS, under grant EP/T011424/1. This research was partly conducted on beamline 6-BM of the National Synchrotron Light Source II, a U.S. Department of Energy (DOE) Office of Science User Facility operated for the DOE Office of Science by Brookhaven National Laboratory under Contract No. DE-SC0012704. M.D.W. is grateful to the UK EPSRC and Nuclear Decommissioning Authority for providing studentship through an EPSRC iCASE award. This work was also supported and enabled by EPSRC under grant EP/S01019X/1.

REFERENCES

(1) Vance, E. R.; Stewart, M. W. A.; Moricca, S. Advanced Ceramics and Glass-Ceramics for Immobilisation of ILW and HLW. *MRS Online Proc. Libr. Arch.* **2012**, 1475 DOI: 10.1557/opl.2012.571.

(2) Dixon Wilkins, M. C.; Stennett, M. C.; Maddrell, E.; Hyatt, N. C. The Formation of Stoichiometric Uranium Brannerite (UTi_2O_6) Glass-Ceramic Composites from the Component Oxides in a One-Pot Synthesis. *J. Nucl. Mater.* **2020**, *542*, 152516.

(3) Ewing, R. C. Ceramic Matrices for Plutonium Disposition. *Prog. Nucl. Energy* **2007**, *49* (8), 635−643.

(4) Lumpkin, G. R.; Leung, S. H. F.; Ferenczy, J. Chemistry Microstructure, and Alpha Decay Damage of Natural Brannerite. *Chem. Geol.* **2012**, *291*, 55−68.

(5) Charalambous, F. A.; Ram, R.; Pownceby, M. I.; Tardio, J.; Bhargava, S. K. Chemical and Microstructural Characterisation Studies on Natural and Heat Treated Brannerite Samples. *Miner. Eng.* **2012**, *39*, 276−288.

(6) Hess, F. L.; Wells, R. C. Brannerite, a New Uranium Mineral. *J. Franklin Inst.* **1920**, *189* (2), 225−237.

(7) Zhang, Y.; Lumpkin, G. R.; Li, H.; Blackford, M. G.; Colella, M.; Carter, M. L.; Vance, E. R. Recrystallisation of Amorphous Natural Brannerite through Annealing: The Effect of Radiation Damage on the Chemical Durability of Brannerite. *J. Nucl. Mater.* **2006**, *350* (3), 293−300.

(8) Turuani, M.; Choulet, F.; Eglinger, A.; Goncalves, P.; Machault, J.; Mercadier, J.; Seydoux-Guillaume, A.-M.; Reynaud, S.; Baron, F.; Beaufort, D.; Batonneau, Y.; Gouy, S.; Mesbah, A.; Szenknect, S.; Dacheux, N.; Chapon, V.; Pagel, M. Geochemical Fingerprints of Brannerite (UTi_2O_6): An Integrated Study. *Mineral. Mag.* **2020**, *84* (2), 313−334.

(9) Bazuev, G. V.; Makarova, O. V.; Zhilyaev, V. A.; Shveikin, G. P. *Russ. J. Inorg. Chem.* **1976**, *21*, 1447.

(10) Gotman, Y. D.; Khapaev, I. A. Thorutite - A New Mineral of the Group of Titanates of Thorium. *Zap Vses Miner. Obshch* **1958**, *87*, 201−202.

(11) Kaiman, S. Synthesis of Brannerite. *Can. Mineral.* **1959**, *6* (3), 389−390.

(12) Patchett, J. E.; Nuffield, E. W. Studies of Radioactive Compounds. X. The Synthesis and Crystallography of Brannerite. *Can. Mineral.* **1960**, *6* (4), 483−490.

(13) Lopez, C.; Deschanels, X.; Bart, J. M.; Boubals, J. M.; Den Auwer, C.; Simoni, E. Solubility of Actinide Surrogates in Nuclear Glasses. *J. Nucl. Mater.* **2003**, *312* (1), 76−80.
(14) Marra, J. C.; Cozzi, A. D.; Pierce, R. A.; Pareizs, J. M.; Jurgensen, A. R.; Missimer, D. M. Cerium as a Surrogate in the Plutonium Immobilized Form. In *Environmental Issues and Waste Management Technologies in the Ceramic and Nuclear Industries VII*; John Wiley & Sons Ltd, 2012; pp 381−388, DOI: 10.1002/9781118371435.ch36.
(15) Zamoryanskaya, M. V.; Burakov, B. E. Feasibility Limits in Using Cerium as a Surrogate for Plutonium Incorporation in Zircon, Zirconia and Pyrochlore. *MRS Online Proc. Libr. Arch.* **2000**, 663 DOI: 10.1557/PROC-663-301.
(16) Stennett, M. C.; Freeman, C. L.; Gandy, A. S.; Hyatt, N. C. Crystal Structure and Non-Stoichiometry of Cerium Brannerite: $Ce_{0.975}Ti_2O_{5.95}$. *J. Solid State Chem.* **2012**, *192*, 172−178.
(17) Kong, L.; Gregg, D. J.; Karatchevtseva, I.; Zhang, Z.; Blackford, M. G.; Middleburgh, S. C.; Lumpkin, G. R.; Triani, G. Novel Chemical Synthesis and Characterization of $CeTi_2O_6$ Brannerite. *Inorg. Chem.* **2014**, *53* (13), 6761−6768.
(18) Huynh, L. T.; Eger, S. B.; Walker, J. D. S.; Hayes, J. R.; Gaultois, M. W.; Grosvenor, A. P. How Temperature Influences the Stoichiometry of $CeTi_2O_6$. *Solid State Sci.* **2012**, *14* (6), 761−767.
(19) Aluri, E. R.; Grosvenor, A. P.; Forbes, S. H.; Greedan, J. E.; Bachiu, L. M. Assessing the Oxidation States and Structural Stability of the Ce Analogue of Brannerite. *Surf. Interface Anal.* **2017**, *49* (13), 1335−1344.
(20) Naghavi, S. S.; He, J.; Wolverton, C. $CeTi_2O_6$—A Promising Oxide for Solar Thermochemical Hydrogen Production. *ACS Appl. Mater. Interfaces* **2020**, *12* (19), 21521−21527.
(21) Le Bail, A. Whole Powder Pattern Decomposition Methods and Applications: A Retrospection. *Powder Diffr.* **2005**, *20* (4), 316−326.
(22) Le Bail, A.; Duroy, H.; Fourquet, J. L. Ab-Initio Structure Determination of $LiSbWO_6$ by X-Ray Powder Diffraction. *Mater. Res. Bull.* **1988**, *23* (3), 447−452.
(23) Coelho, A. A. TOPAS and TOPAS-Academic: An Optimization Program Integrating Computer Algebra and Crystallographic Objects Written in C++. *J. Appl. Crystallogr.* **2018**, *51* (1), 210−218.
(24) Weiland, C.; Jaye, C.; Quackenbush, N. F.; Gann, E.; Fu, Z.; Kirkland, J. P.; Karlin, B. A.; Ravel, B.; Woicik, J. C.; Fischer, D. A. NIST HAXPES at NSLS and NSLS-II. *Synchrotron Radiat. News* **2018**, *31* (4), 23−28.
(25) Kraft, S.; Stümpel, J.; Becker, P.; Kuetgens, U. High Resolution X-ray Absorption Spectroscopy with Absolute Energy Calibration for the Determination of Absorption Edge Energies. *Rev. Sci. Instrum.* **1996**, *67* (3), 681−687.
(26) Ravel, B.; Newville, M. ATHENA, ARTEMIS, HEPHAESTUS: Data Analysis for X-Ray Absorption Spectroscopy Using IFEFFIT. *J. Synchrotron Radiat.* **2005**, *12* (4), 537−541.
(27) Ravel, B.; Newville, M. ATHENA and ARTEMIS: Interactive Graphical Data Analysis Using IFEFFIT. *Phys. Scr.* **2005**, *2005* (T115), 1007.
(28) Shannon, R. D. Revised Effective Ionic Radii and Systematic Studies of Interatomic Distances in Halides and Chalcogenides. *Acta Crystallogr., Sect. A: Cryst. Phys., Diffr., Theor. Gen. Crystallogr.* **1976**, *32* (5), 751−767.
(29) Dixon Wilkins, M. C.; Stennett, M. C.; Hyatt, N. C. The Effect of A-Site Cation on the Formation of Brannerite (ATi_2O_6, A = U, Th, Ce) Ceramic Phases in a Glass-Ceramic Composite System. *MRS Adv.* **2020**, *5* (1−2), 73−81.
(30) Zhang, Y.; Wei, T.; Zhang, Z.; Kong, L.; Dayal, P.; Gregg, D. J. Uranium Brannerite with Tb(III)/Dy(III) Ions: Phase Formation, Structures, and Crystallizations in Glass. *J. Am. Ceram. Soc.* **2019**, *102* (12), 7699−7709.
(31) Zhang, Y.; Karatchevtseva, I.; Kong, L.; Wei, T.; Zhang, Z. Structural and Spectroscopic Investigations on the Crystallization of Uranium Brannerite Phases in Glass. *J. Am. Ceram. Soc.* **2018**, *101* (11), 5219−5228.
(32) Helean, K. B.; Navrotsky, A.; Lumpkin, G. R.; Colella, M.; Lian, J.; Ewing, R. C.; Ebbinghaus, B.; Catalano, J. G. Enthalpies of Formation of U-, Th-, Ce-Brannerite: Implications for Plutonium Immobilization. *J. Nucl. Mater.* **2003**, *320* (3), 231−244.
(33) Ushakov, S. V.; Helean, K. B.; Navrotsky, A.; Boatner, L. A. Thermochemistry of Rare-Earth Orthophosphates. *J. Mater. Res.* **2001**, *16* (9), 2623−2633.
(34) Rothensteiner, M.; Bonk, A.; Vogt, U. F.; Emerich, H.; van Bokhoven, J. A. Structural Changes in Equimolar Ceria−Hafnia Materials under Solar Thermochemical Looping Conditions: Cation Ordering, Formation and Stability of the Pyrochlore Structure. *RSC Adv.* **2017**, *7* (85), 53797−53809.
(35) Hyatt, N. C.; Corkhill, C. L.; Stennett, M. C.; Hand, R. J.; Gardner, L. J.; Thorpe, C. L. The HADES Facility for High Activity Decommissioning Engineering & Science: Part of the UK National Nuclear User Facility. *IOP Conf. Ser.: Mater. Sci. Eng.* **2020**, *818*, No. 012022.

https://dx.doi.org/10.1021/acs.inorgchem.0c02681
Inorg. Chem. 2020, 59, 17364−17373

6 Crystal chemistry of actinide brannerites

6.1 Introduction

Although much attention has been given to U brannerite (UTi_2O_6) and doped U^{5+} brannerites, little research has been published on the other two stoichiometric titanate brannerites, $CeTi_2O_6$ and $ThTi_2O_6$, and the solid solutions between them. This formed the basis of an investigation into the relative ease of formation of the three end-member titanate brannerites as ceramic phases in glass-ceramic composites, as well as the possible formation of the three mixed actinide cation brannerites $U_{0.5}Th_{0.5}Ti_2O_6$, $U_{0.5}Ce_{0.5}Ti_2O_6$, and $Ce_{0.5}Th_{0.5}Ti_2O_6$. The investigation was focussed on the differences in stability of the brannerite structures caused by the range of A-site oxidation states available (*e.g.* Th is uniformly present as Th^{4+} in oxide materials).

The results of this investigation were presented at the 43rd Symposium on the Scientific Basis for Nuclear Waste Management (Vienna, Austria, 21-24th October 2019) and the conference proceedings published in MRS Advances: "The effect of A-site cation on the formation of brannerite (ATi_2O_6, A = U, Th, Ce) ceramic phases in a glass-ceramic composite system" (MC Dixon Wilkins, MC Stennett, NC Hyatt, *MRS Adv.*, 2019, **5**, 10.1557/adv.2019.470). The author's contribution was: production of samples, analysis by XRD and SEM, Rietveld analysis of diffraction data, XAS data analysis, and writing of the manuscript.

Similarly, although many U-site doped U brannerites have been reported in the literature, little research has been published on Ti-site dopants. Doping of a lower oxidation state species on the Ti-site would allow for retention of the full U content, whilst still allowing for charge balancing of higher oxidation states of U. To examine the possibility of Ti-site doping, the solid solubility of Al in UTi_2O_6 (in the system $UTi_{2-x}Al_xO_6$) was investigated.

The results of this investigation have been submitted to Inorganic Chemistry. The Author's contribution was: production of samples, analysis by X-ray diffraction and SEM/EDX, Rietveld analysis of X-ray and neutron diffraction data, U L_3 and M_4 edge XAS sample preparation and data analysis, and writing of the manuscript.

6.2 The effect of A-site cation on the formation of brannerite (ATi_2O_6, A = U, Th, Ce) ceramic phases in a glass-ceramic system

MRS Advances © 2019 Materials Research Society
DOI: 10.1557/adv.2019.470

The Effect of A-Site Cation on the Formation of Brannerite (ATi_2O_6, A = U, Th, Ce) Ceramic Phases in a Glass-Ceramic Composite System

Malin C. Dixon Wilkins[1], Martin C. Stennett[1], and Neil C. Hyatt[1]

[1]*Immobilisation Science Laboratory, Department of Materials Science and Engineering, The University of Sheffield, Sheffield, UK*

ABSTRACT

A range of stoichiometric and mixed A-site cation brannerite glass-ceramics have been synthesised and characterised. The formation of UTi_2O_6 in glass is reliant on ensuring all uranium remains tetravalent by processing in an inert atmosphere. $ThTi_2O_6$ forms in glass under both inert and oxidising atmospheres due to the lack of other easily available oxidation states. $CeTi_2O_6$ could not be made to form within this glass system. The formation of $A_{0.5}B_{0.5}Ti_2O_6$ phases depends strongly on the oxidation states of the A and B cations available in the process atmosphere, with the most successful compositions having an average final oxidation state of $(A,B)^{4+}$. Mixed cation brannerite compositions that formed in argon include $U_{0.75}Th_{0.25}Ti_2O_6$ and $U_{0.71}Ce_{0.29}Ti_2O_6$. Those forming in air include $U_{0.23}Th_{0.77}Ti_2O_6$, $Th_{0.37}Ce_{0.63}Ti_2O_6$, and $U_{0.41}Ce_{0.59}Ti_2O_6$.

INTRODUCTION

Brannerite (prototypically UTi_2O_6) is a naturally occurring titanate mineral phase containing a particularly high fraction of uranium (> 55% uranium by weight), and has been suggested as a possible candidate host for high actinide content wastes.[1] The analogous phase $ThTi_2O_6$ is relatively rare in nature,[2] but naturally occurring U-brannerites often have a high proportion of Th doped on the U site.[3,4] Natural samples of $CeTi_2O_6$ with the brannerite structure have not been observed.

It was first found that to successfully synthesise UTi_2O_6 the oxygen partial pressure in the sintering atmosphere must be minimised to retain all U as U^{4+}.[5,6] Mixed cation brannerite ceramics have previously been investigated, with the substitution of lower valent cations (Ca^{2+}, Y^{3+}, Gd^{3+}, and La^{3+}) stabilising the presence of higher valent U in the brannerite structure.[7–10] Brannerite ceramics have also been investigated as hosts

for MOX (mixed oxide, *i.e.* mixed UO_2 and PuO_2) fuels, $U_{0.9}Ce_{0.1}Ti_2O_6$ and $U_{0.81}Ce_{0.09}Gd_{0.1}Ti_2O_6$ (Ce as a surrogate for Pu) .[11]

A reasonable range of brannerite glass-ceramics have previously been reported in the literature, with the vast majority focussing on air-fired compositions following a batched ceramic stoichiometry of $U_{0.5}M_{0.5}Ti_2O_6$ (M is Tb^{3+}, Dy^{3+}, Y^{3+}, and Eu^{3+}).[12–14] Pu-containing glass-ceramics have also been synthesised ($Gd_{0.2}Pu_{0.5}U_{0.5}Ti_2O_6$ and $Gd_{0.1}Hf_{0.1}Pu_{0.2}U_{0.6}Ti_2O_6$),[13] which gives some indication that Pu is usefully soluble in UTi_2O_6, and does not interfere with the formation of these glass-ceramics. All of these glass-ceramics except one ($Gd_{0.1}Hf_{0.1}Pu_{0.2}U_{0.6}Ti_2O_6$) contained the same glass phase, $Na_2AlBSi_6O_{16}$, that has previously been demonstrated as a suitable glass for similar titanate-phase glass-ceramics.[15–17] $CeTi_2O_6$ glass-ceramics have also been investigated, however they were formed by simple co-sintering of pre-synthesised glass and ceramic phases.[18,19]

The synthesis of stoichiometric brannerite glass-ceramics has not been reported; this study examines the formation of the three stoichiometric titanate brannerites in $Na_2AlBSi_6O_{16}$ glass. In addition, glass-ceramics targeting the mixed cation phases $U_{0.5}Th_{0.5}Ti_2O_6$, $Th_{0.5}Ce_{0.5}Ti_2O_6$, and $Ce_{0.5}U_{0.5}Ti_2O_6$ were synthesised, to try and further elucidate the different behaviours of the cations studied within the brannerite structure.

In this investigation, brannerite glass-ceramics were synthesised by an all oxide solid-state route, in contrast to previous examples, which first made a ceramic precursor using an alkoxide/nitrate route that was then mixed with a glass precursor and heat-treated.

As noted in the literature, many ceramic brannerites seem to have some degree of non-stoichiometry, and it was expected that a certain amount of the TiO_2 would dissolve in the glass. As a result, samples were batched with a hyperstoichiometric amount of TiO_2. As-batched stoichiometry was $1AO_2 : 2.15TiO_2$. However, it was expected that any brannerite formed would closely follow the nominal ATi_2O_6 stoichiometry.

EXPERIMENTAL

Samples were prepared using a cold-press and sinter method. The targeted glass:ceramic ratio for all samples was 1:1 by weight. A glass precursor was prepared by calcining a homogenised mixture of SiO_2, H_3BO_3, $Na_2(CO_3)$, and Al_2O_3 at 600 °C for 6 hours. The ceramic precursors were then added as the component oxides (UO_2, ThO_2, CeO_2, TiO_2) and the mixture wet milled in isopropanol in a Fritsch Pulverisette 23 reciprocating ball mill for 5 minutes at 30 Hz. The resulting slurry was then dried in an oven at 85 °C, and the powder cakes retrieved and broken up using a mortar and pestle. The homogenised powders were pelletised under 2 t into 10 mm pellets. The pellets were then placed into crucibles lined with coarse ZrO_2 to prevent sticking, then heat treated (1200 °C, 12 hours, ramp rate of 5 °Cmin^{-1}) in a tube furnace under either argon or air. Any ZrO_2 adhered to the outside of the pellets was removed by hand.

The resulting pellets were then characterised. Pieces of the pellets were ground using a mortar and pestle, and powder x-ray diffraction (XRD) was used for phase identification (Bruker D2 Phaser, using Ni-filtered Cu K_α radiation). Diffraction patterns for refinement were collected on the same instrument, with LaB_6 used as a peak position standard.

Samples were prepared for Raman spectroscopy and scanning electron microscopy (SEM) by mounting in cold-set resin, before polishing to an optical finish. Raman spectra were collected from various points on the polished surface (Horiba XploRa PLUS Raman microscopy, 532 nm laser, 100x magnification). The samples were

carbon-coated to reduce sample charge build-up and SEM used to investigate the microstructure and phase assemblage, with energy-dispersive x-ray spectroscopy (EDX) being used to confirm the identities of phases observed (Hitachi TM3030, operating at 15 kV; Bruker Quantax 70 EDX system).

RESULTS AND DISCUSSION

UTi_2O_6 glass-ceramics

When heat-treated under argon, UTi_2O_6 was the majority phase formed, with some UO_2 and trace TiO_2 also observed in the XRD pattern (see Figure 1). The microstructure consists of uneven grains of UTi_2O_6 in the glass matrix. UO_2 is seen encapsulated in some grains of brannerite, as well as a small amount free in the glass. The Raman spectrum of the brannerite phase closely matches that of stoichiometric UTi_2O_6 as in reported in the literature.[20] Lattice parameters obtained from a Le Bail refinement (see Table 1) closely match those reported previously for stoichiometric UTi_2O_6.[21]

As expected from the related ceramic phase, UTi_2O_6 did not form in air[5,6] (see Figure 2). The main ceramic phases observed in the XRD pattern were U_3O_8 and rutile, indicating that all U was oxidised, thus preventing the brannerite structure from forming. The microstructure observed by SEM is in agreement with this, showing U_3O_8 and TiO_2 in a glassy matrix. A significant amount of uranium is dissolved in the glass, most likely as U^{5+} or U^{6+}; this occurs in all U-containing samples heated in air, and will be further discussed in later sections.

Table 1: Crystallographic details of brannerite phases produced in glass-ceramic composites, as determined by Le Bail refinements of XRD data and SEM-EDX.

Target composition		a (Å)	b (Å)	c (Å)	β (°)	V (Å^3)	EDX A-site composition
Ar	UTi_2O_6	9.8142(2)	3.7650(1)	6.9182(2)	118.913(2)	223.77	
	$U_{0.5}Th_{0.5}Ti_2O_6$	9.8174(5)	3.7818(2)	6.9592(3)	118.913(4)	226.17	$U_{0.75(3)}Th_{0.25(3)}$
	$ThTi_2O_6$	9.8125(3)	3.8224(1)	7.0329(2)	118.814(3)	231.12	
	$Ce_{0.5}U_{0.5}Ti_2O_6$	9.8165(3)	3.7615(1)	6.9580(2)	118.659(3)	225.44	$U_{0.71(3)}Ce_{0.29(3)}$
Air	$U_{0.5}Th_{0.5}Ti_2O_6$	9.8150(7)	3.7857(2)	6.9803(5)	118.745(6)	227.40	$U_{0.23(1)}Th_{0.77(1)}$
	$ThTi_2O_6$	9.8123(3)	3.8223(1)	7.0326(2)	118.810(2)	231.11	
	$Th_{0.5}Ce_{0.5}Ti_2O_6$	9.8204(5)	3.7732(2)	6.9393(4)	119.041(4)	224.80	$Th_{0.37(2)}Ce_{0.63(2)}$
	$Ce_{0.5}U_{0.5}Ti_2O_6$	9.8101(3)	3.7496(1)	6.9517(2)	118.564(2)	224.59	$U_{0.41(3)}Ce_{0.59(3)}$

$ThTi_2O_6$ glass-ceramics

The phase assemblage of the produced $ThTi_2O_6$ glass-ceramics was unchanged with respect to processing atmosphere. The XRD patterns of both samples consist of brannerite, $ThTi_2O_6$, and unreacted component oxides, ThO_2 and TiO_2. The microstructures observed by SEM were in good agreement, comprising large regions of ThO_2 encapsulated by brannerite and smaller grains of TiO_2 held within the glassy matrix (see Figure 3). The large amount of unreacted material is likely due to the refractory nature of ThO_2 (ceramic $ThTi_2O_6$ usually requires temperatures of 1400 °C or above to form).[22,23]

Both the observed Raman spectra and the lattice parameters determined from a Le Bail refinement closely match those reported in the literature for stoichiometric $ThTi_2O_6$.

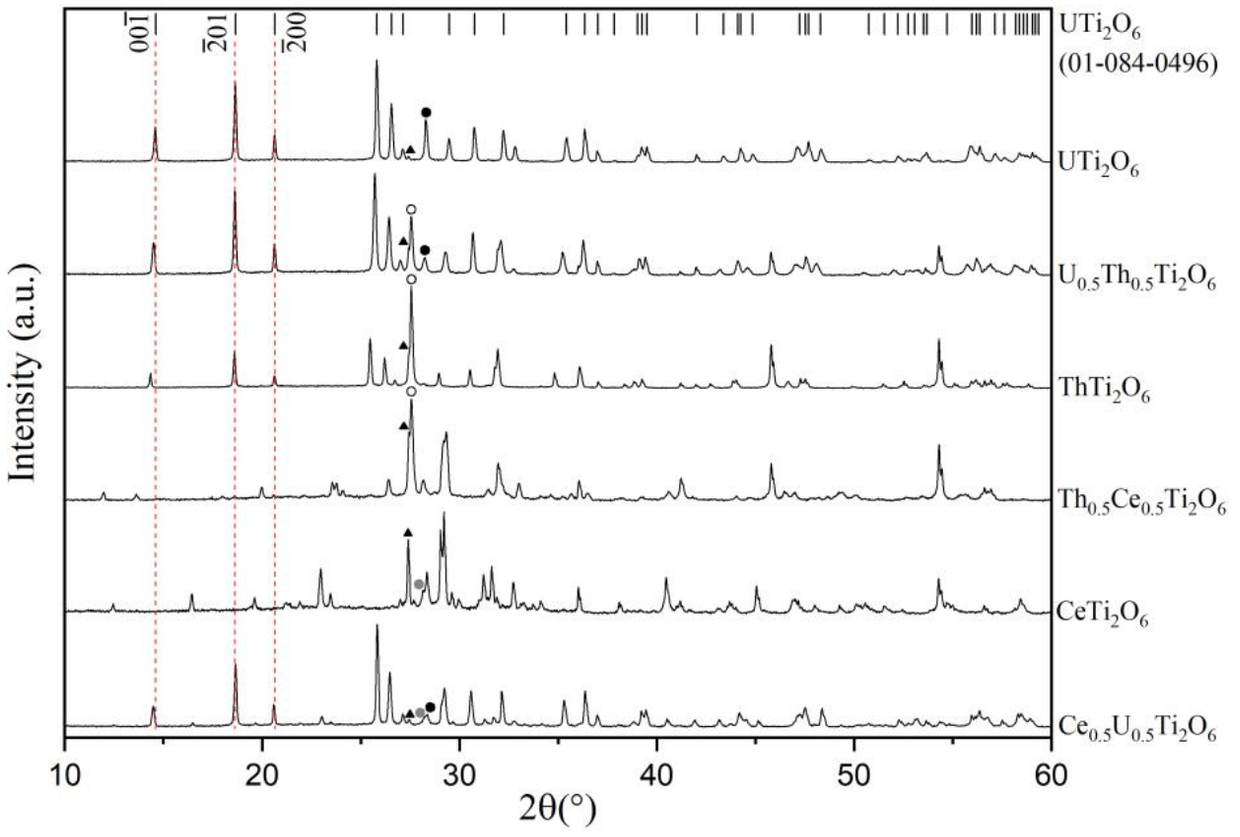

Figure 1: Diffraction patterns of glass-ceramic composites heat-treated under argon. Each pattern is labelled with the as-batched target ceramic composition. The peak positions of stoichiometric UTi_2O_6 are shown by the tick marks above, the positions of the first three peaks are also indicated by dashed red lines. Black circles represent the major peaks of UO_2; white, ThO_2; grey, CeO_2; black triangles, TiO_2.

$CeTi_2O_6$ glass-ceramics

In contrast to the compositions targeting $ThTi_2O_6$, $CeTi_2O_6$ did not form in argon on air. The produced phase assemblages differed depending on the oxidation state of cerium over the course of the reaction. It is well-established that the Ce^{3+}/Ce^{4+} redox couple is strongly temperature dependent, with cerium oxides self-reducing at high temperatures.

When heated under argon, Ce^{3+} forms, releasing O_2 that is then lost in the flowing gas, and the material cannot re-oxidise to Ce^{4+} on cooling as a result. Because of this, the only Ce-containing crystalline phases observed by XRD and SEM are exclusively Ce^{3+} species, including $Ce_2Ti_2SiO_9$ (Ce-trimounsite) and $Ce_2Ti_2O_7$ (a large amount of TiO_2 is also observed).

When heated in air, the phases in the final glass-ceramic product are CeO_2 and TiO_2. There are two possible reasons for the presence of Ce^{4+} but lack of brannerite. The presence of Ce^{3+} at temperature may prevent formation of brannerite, and during cooling the material re-oxidises forming CeO_2. Or, the increased partial pressure of O_2 in the atmosphere may be sufficient to make the auto-reduction to Ce^{3+} unfavourable, and there is a different factor preventing formation of $CeTi_2O_6$. At this point, it is unclear which is the dominant mechanism.

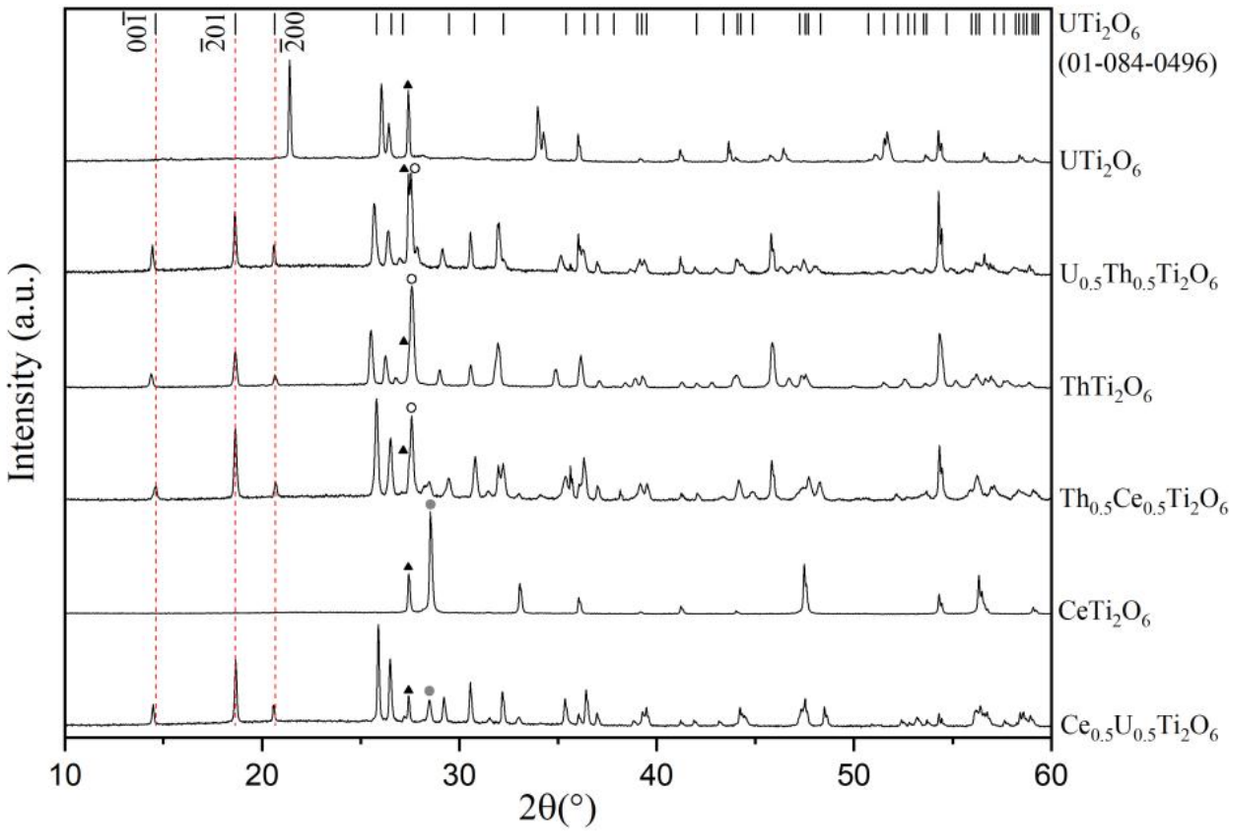

Figure 2: Diffraction patterns of glass-ceramic composites heat-treated in air. Each pattern is labelled with the as-batched target ceramic composition. The peak positions of stoichiometric UTi_2O_6 are shown by the tick marks above, the positions of the first three peaks are also indicated by dashed red lines. Black circles represent the major peaks of UO_2; white, ThO_2; grey, CeO_2; black triangles, TiO_2.

$U_{0.5}Th_{0.5}Ti_2O_6$ glass-ceramics

The sample heated under argon produced phases consistent with the U- and Th-endmembers. The XRD pattern confirms the presence of brannerite as the majority ceramic phase, with ThO_2 and smaller amounts of UO_2 and TiO_2. The microstructure observed by SEM was consistent with the Th- and U-endmembers, with brannerite forming the major phase accompanied by grains of UO_2 (encapsulated in brannerite) and TiO_2 (held in the glass matrix), and larger clusters of ThO_2 (see Figure 3). The relative amount of unreacted AnO_2 (where An = U, Th) was approximately less than that seen in the sample targeting $ThTi_2O_6$, but more than the UTi_2O_6 endmember.

The lattice parameters were determined by a Le Bail fit, with the b and c lattice parameters being slightly larger than those of the UTi_2O_6 endmember, but smaller than those of the $ThTi_2O_6$ endmember. Considering the relative magnitude of the lattice parameters qualitatively, it appears that the average ion size of the $(U,Th)Ti_2O_6$ composition is closer to that of UTi_2O_6 than $ThTi_2O_6$. EDX was used to determine the U:Th ratio in the brannerite phase, giving an overall observed stoichiometry of $U_{0.75}Th_{0.25}Ti_2O_6$ (assuming Ti and O follow the nominal stoichiometry), in good agreement with the observed lattice parameters.

As observed by XRD, the sample heated under air had a similar phase assemblage as the sample heated under argon, with the exception of a larger amount of unreacted ThO_2 and TiO_2. The microstructure observed by SEM was also similar, consisting of grains of brannerite, some of which are encapsulating large grains of ThO_2, and smaller regions of TiO_2. The determined lattice parameters were notably larger, suggesting a higher Th content than for the Ar-fired counterpart. This was confirmed by EDX giving an overall observed stoichiometry of $U_{0.23}Th_{0.77}Ti_2O_6$ (assuming Ti and O follow the nominal stoichiometry). The remainder of the uranium appears to be dissolved

in the glass, with the glass composition as determined by EDX showing approximately ten times the amount of uranium when compared to the sample fired in argon; this suggests that a significant proportion of the uranium was oxidised to U^{5+} and/or U^{6+} during processing (it is well-established that U^{5+} and U^{6+} are more soluble in alumino- and borosilicate glasses).[24,25] It is not clear if the brannerite-forming uranium is U^{4+} or has been oxidised, with either A-site or oxygen vacancies to charge balance.

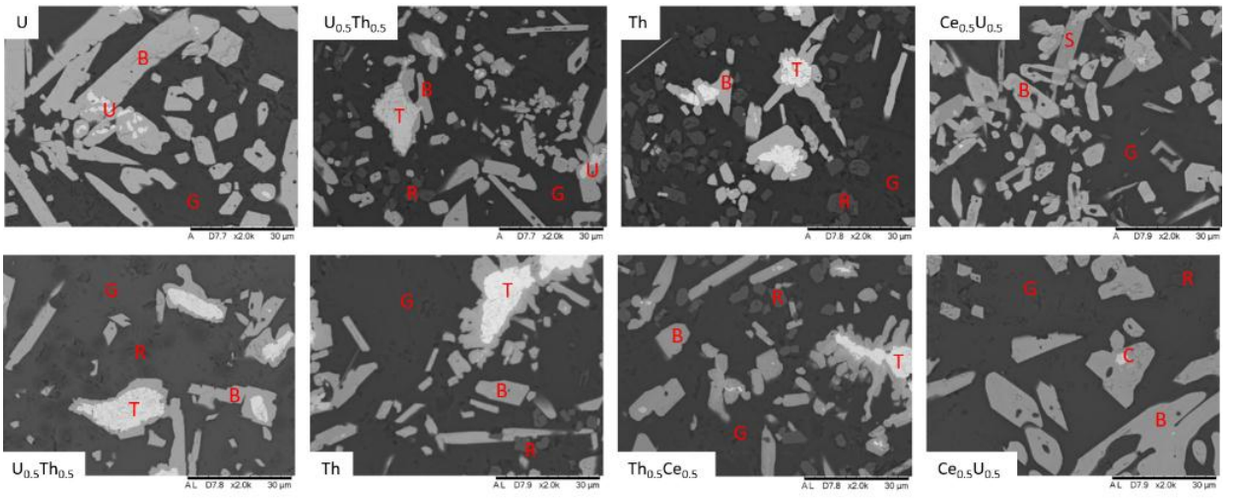

Figure 3: Representative SEM micrographs of the microstructures of all samples that formed brannerite-structured ceramic phases. The top row are those fired under argon, the bottom row are those fired in air. Each micrograph is labelled by the as-batched A-site stoichiometry. B is brannerite, U is UO_2, T is ThO_2, C is CeO_2, R is TiO_2, S is $Ce_2Ti_2SiO_9$, and G is glass.

$Th_{0.5}Ce_{0.5}Ti_2O_6$ glass-ceramics

When processed in argon, no brannerite formed; however, several different phases were observed by XRD, including unreacted ThO_2 and TiO_2, and various Ce^{3+} phases, possibly including $Ce_2Ti_2SiO_9$, as seen in the $CeTi_2O_6$ endmember when heated in argon. Although the lack of cerium-containing brannerite phases was expected, it is unclear why no $ThTi_2O_6$ was observed, when it formed reasonably well in the Th-endmember under both neutral and oxidising atmospheres.

When processed in air, brannerite was the major phase formed, with ThO_2 and TiO_2, and trace amounts of CeO_2. The stoichiometry of the ceramic phase was determined by EDX to be $Th_{0.37}Ce_{0.63}Ti_2O_6$, as expected from the large amount of ThO_2 remaining unreacted. Although Ce^{3+} has been observed in U^{5+} air-fired brannerites before[11,14] due to the lack of higher oxidation states of thorium, it is reasonable to assume that all cerium and thorium is present as Ce^{4+} and Th^{4+} respectively, giving an average A-site ionic radius of 0.89604 Å. With this assumption in mind, the lattice parameters determined from a Le Bail refinement follow the general trend seen in brannerites, where an increase in A-site ion size causes a related increase in the b and c lattice parameters, as well as unit cell volume (see Figure 4).

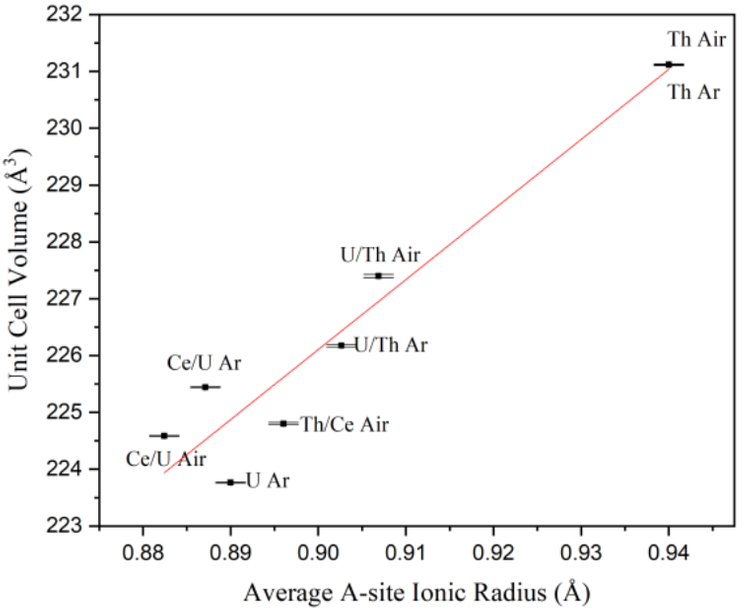

Figure 4: Plot of average A-site ionic radii (as determined from EDX stoichiometries) against unit cell volume as determined by Le Bail refinements. Each point is labelled according to the cations present. The trend line indicated has an R^2 value of 0.9405. The standard errors associated with the refinement models are also indicated.

$Ce_{0.5}U_{0.5}Ti_2O_6$ glass-ceramics

A glass-ceramic targeting a ceramic composition $Ce^{3+}_{0.5}U^{5+}_{0.5}Ti_2O_6$ has previously been reported, using an alkoxide/nitrate route starting from trivalent cerium nitrate and processing in air[14]. It was noted that the final produced ceramic phase $Ce_{0.65}U_{0.35}Ti_2O_6$ was U-deficient compared to the target stoichiometry due to mixed cerium valence, with the remaining uranium being dissolved in the glass phase.

When processed in argon, the major phase observed by XRD was brannerite, with minor amounts of UO_2 and $Ce_2Ti_2SiO_9$, and trace rutile, as expected from the behaviour of the two endmembers in argon. The stoichiometry of the brannerite phase was determined by EDX to be $U_{0.71}Ce_{0.29}Ti_2O_6$.

Preliminary XANES measurements of the Ce and U oxidation states suggest A-site oxidation states of $Ce^{3+}/U^{4,5+}$, where the inclusion of each Ce^{3+} is charge balanced by the oxidation of U^{4+} to U^{5+}. The average A-site ionic radius in this case is 0.887 Å, which closely follows the trend in the effect of ion size on unit cell volume (see Figure 4).

When processed in air, the phase assemblage was broadly similar to that reported in the literature: brannerite as the major phase, with lesser amounts of TiO_2 and a cubic mixed oxide, $(Ce,U)O_2$. The stoichiometry of the brannerite phase was determined by EDX to be $U_{0.41}Ce_{0.59}Ti_2O_6$, slightly enriched in uranium compared to the $U_{0.35}Ce_{0.65}Ti_2O_6$ described in the literature, but likely following the same trend of U^{5+} with mixed Ce^{3+}/Ce^{4+}. As seen in the other uranium bearing samples heated in air, a considerable amount of uranium is dissolved in the glass (approximately nine times the amount of the argon fired sample as determined by EDX), due to the increased solubility of higher valent uranium previously mentioned. This accounts for the excess oxidised uranium that did not form brannerite due to the higher Ce content.

The unit cell parameters as determined by the Le Bail method are within the expected range (and closely match those reported for $Ce_{0.65}U_{0.35}Ti_2O_6$), but cannot be directly compared to a wider range of brannerites without making assumed assignments of the oxidation states of uranium and cerium. The most likely assignment is that of sufficient Ce^{3+} to charge balance all uranium as U^{5+}, with the remainder of the cerium

tetravalent. If this is the case, the average A-site ion size would be 0.882 Å, which is in good agreement with the general trend (see Figure 4).

CONCLUSION

As expected from previous literature reports of uranium-containing brannerites, the most important factor in producing a targeted brannerite phase as the ceramic component in these glass-ceramic systems appears to be retaining an average oxidation state of the A-site cations of 4+. As a result, $ThTi_2O_6$ is insensitive to different atmospheres during processing, but does not form at a high yield over these timescales (this is most likely due to the refractory nature of ThO_2 rather than any thermodynamic effect). UTi_2O_6 only forms in argon, and $CeTi_2O_6$ did not form at all, due to auto-reduction of cerium at temperature.

Of the mixed cation compositions, $U_{0.5}Ce_{0.5}Ti_2O_6$ formed high yields of brannerite both in air, as a $Ce^{3,4+}/U^{5+}$ system, and in argon, presumably as a $Ce^{3+}/U^{4,5+}$ brannerite as determined from the lattice parameters and preliminary XANES measurements. The differences in solubility of cerium appears to depend strongly on what charge balancing mechanisms exist. The solid solubility between UTi_2O_6 and $ThTi_2O_6$ in these glass-ceramic systems seems high; however, the large amount of unreacted oxides suggests longer heat treatments are necessary to reach equilibrium (especially due to the refractory nature of ThO_2).

As reported in the literature, the unit cell parameters (especially b and c, as previously reported for other brannerites), as well as the unit cell volume, have a close correlation to the average A-site ion size. This effect most obvious for the argon fired series UTi_2O_6, $U_{0.75}Th_{0.25}Ti_2O_6$, $ThTi_2O_6$, as no non-tetravalent oxidation states are observed in these samples.

ACKNOWLEDGEMENTS

MDW is thankful to the UK EPSRC and Nuclear Decommissioning Authority for providing studentship through an EPSRC iCASE award. This work was performed in part in the MIDAS facility at The University of Sheffield, which was established with support from the Department for Energy and Climate Change, now incorporated within the Department for Business, Energy and Industrial Strategy. NCH is grateful to the Royal Academy of Engineering and the Nuclear Decommissioning Authority for funding.

Reference

1. E.R. Vance, M.L. Carter, G.R. Lumpkin, R.A. Day, and B.D. Begg, *Solid Solubilities of Pu, U, Gd and Hf in Candidate Ceramic Nuclear Wasteforms* (Australian Nuclear Science and Technology Organization, Menai, NSW 2234, Australia (US), 2001).
2. Y.D. Gotman and I.A. Khapaev, Zap Vses Miner. Obshch **87**, 201 (1958).
3. G.R. Lumpkin, S.H.F. Leung, and J. Ferenczy, Chem. Geol. **291**, 55 (2012).
4. F.A. Charalambous, R. Ram, M.I. Pownceby, J. Tardio, and S.K. Bhargava, Miner. Eng. **39**, 276 (2012).
5. J.E. Patchett and E.W. Nuffield, Can. Minerol. **6**, 483 (1960).
6. S. Kaiman, Can. Mineral. **6**, 389 (1959).
7. E.R. Vance, J.N. Watson, M.L. Carter, R.A. Day, and B.D. Begg, J. Am. Ceram. Soc. **84**, 141 (2001).
8. M. James and J.N. Watson, J. Solid State Chem. **165**, 261 (2002).
9. M. James, M.L. Carter, and J.N. Watson, J. Solid State Chem. **174**, 329 (2003).

10. D.J. Bailey, M.C. Stennett, and N.C. Hyatt, Procedia Chem. **21**, 371 (2016).
11. D.J. Bailey, M.C. Stennett, and N.C. Hyatt, MRS Adv. **2**, 557 (2017).
12. Y. Zhang, T. Wei, Z. Zhang, L. Kong, P. Dayal, and D.J. Gregg, J. Am. Ceram. Soc. **102**, 7699 (2019).
13. Y. Zhang, L. Kong, I. Karatchevtseva, R.D. Aughterson, D.J. Gregg, and G. Triani, J. Am. Ceram. Soc. **100**, 4341 (2017).
14. Y. Zhang, I. Karatchevtseva, L. Kong, T. Wei, and Z. Zhang, J. Am. Ceram. Soc. **101**, 5219 (2018).
15. Y. Zhang, L. Kong, R.D. Aughterson, I. Karatchevtseva, and R. Zheng, J. Am. Ceram. Soc. **100**, 5335 (2017).
16. L. Kong, I. Karatchevtseva, and Y. Zhang, J. Eur. Ceram. Soc. **37**, 4963 (2017).
17. E. Maddrell, S. Thornber, and N.C. Hyatt, J. Nucl. Mater. **456**, 461 (2015).
18. E. Paknahad and A.P. Grosvenor, Solid State Sci. **74**, 109 (2017).
19. E. Paknahad and A.P. Grosvenor, Can. J. Chem. **95**, 1110 (2017).
20. Y. Zhang, I. Karatchevtseva, M. Qin, S.C. Middleburgh, and G.R. Lumpkin, J. Nucl. Mater. **437**, 149 (2013).
21. J.T. Szymanski and J.D. Scott, Can. Mineral. **20**, 271 (1982).
22. K.S. Finnie, Z. Zhang, E.R. Vance, and M.L. Carter, J. Nucl. Mater. **317**, 46 (2003).
23. Y. Zhang, D.J. Gregg, G.R. Lumpkin, B.D. Begg, and M. Jovanovic, J. Alloys Compd. **581**, 665 (2013).
24. H. Schreiber and G. Balazs, Phys. Chem. Glas. **23**, 139 (1982).
25. H. Schreiber, G. Balazs, P. Jamison, and A. Shaffer, Phys. Chem. Glas. **23**, 147 (1982).

6.3 Synthesis, characterisation, and crystal structure of novel uranium (V) dominant brannerites in the $UTi_{2-x}Al_xO_6$ system

Synthesis, characterisation, and crystal structure of novel uranium (V) dominant brannerites in the $UTi_{2-x}Al_xO_6$ system

Malin C. Dixon Wilkins[1], Lucy M. Mottram[1], Ewan R. Maddrell[2], Martin C. Stennett[1], Claire L. Corkhill[1], Kristina O. Kvashnina[3,4], and Neil C. Hyatt[1]*

[1]Department of Materials Science and Engineering, University of Sheffield, Sheffield, UK

[2]National Nuclear Laboratory, Sellafield, Cumbria, UK

[3]The Rossendorf Beamline at ESRF, CS 40220, 38043 Grenoble Cedex 9, France

[4]Helmholtz-Zentrum Dresden-Rossendorf, Institute of Resource Ecology, Bautzner Landstrasse 400, 01328 Dresden, Germany

*Corresponding author: n.c.hyatt@sheffield.ac.uk

Abstract

The synthesis, characterisation and crystal structure of a novel U^{5+} (dominant) brannerite of composition $U_{1.09(6)}Ti_{1.29(3)}Al_{0.71(3)}O_6$ is reported, as determined from Rietveld analysis of high resolution powder neutron diffraction data. Examination of the $UTi_{2-x}Al_xO_6$ system demonstrated the formation of brannerite structured compounds with varying Al^{3+} and U^{5+} content, from $U_{0.93(6)}Ti_{1.64(3)}Al_{0.36(3)}O_6$ to $U_{0.89(6)}Ti_{1.00(3)}Al_{1.00(3)}O_6$. Substitution of Al^{3+} for Ti^{4+}, with U^{5+} charge compensation, resulted in near-linear changes in the *b* and *c* unit cell parameters and the overall unit cell volume, as expected from ionic radii considerations. The presence of U^{5+} as the dominant oxidation state in near single phase brannerite compositions was evidenced by complementary laboratory U L_3 edge and high energy resolution fluorescence detected (HERFD) U M_4 edge X-ray Absorption Near Edge Spectroscopy. No brannerite phase was found for compositions with Al^{3+} / Ti^{4+} > 1, which would require U^{6+} contribution for charge compensation. These data expand the crystal chemistry of uranium brannerites to the stabilisation of dominant U^{5+} brannerites by substitution of trivalent cations, such as Al^{3+}, on the Ti^{4+} site.

1. Introduction

Synthetic analogues of stable titanate mineral phases have been considered for their suitability as durable ceramic wasteforms for high actinide content nuclear wastes. One of the more promising minerals is brannerite (prototypically UTi_2O_6), with natural samples displaying the ability to retain a large fraction of their initial U content despite high degrees of metamictisation and alteration.[1–3] Though the radiation tolerance[4,5] and aqueous durability[6,7] of brannerites are not as high as some other materials (with critical amorphisation doses of 0.8 to 1.5 × 10^{14} ions cm^{-2}, compared with 2 to 6 × 10^{14} ions cm^{-2} for synthetic zirconolites and pyrochlores), UTi_2O_6 remains a particularly attractive host for actinides because of its notably high U content (55.4% U by weight), and so high waste loading.

It has been established that the synthesis of UTi_2O_6 requires heat treatment(s) under a low pO_2 atmosphere in order to retain U^{4+}.[8–11] The substitution of U^{4+} by a lower valent dopant has also been widely applied in the synthesis of U^{5+} brannerites in air atmospheres.[8,12–14] It should be noted that much of the recent work on brannerites has examined the formation of a brannerite ceramic phase within a glass-ceramic composite (commonly within the $Na_2AlBSi_6O_{16}$ glass system), though in most cases the impact of the glass phase on the brannerite phase crystal chemistry is limited (*i.e.* it is expected that the synthesis of a pure ceramic brannerite of the same composition would be facile).[11,15–19]

Common U-site charge-balancing dopants include Ca^{2+}, Y^{3+}, and trivalent lanthanides (notably Ce^{3+} and Gd^{3+}), resulting in U^{5+} brannerites (*e.g.* $U^{5+}_{0.5}Y^{3+}_{0.5}Ti_2O_6$).[8,13,15–17,20] In addition to materials specifically targeting U^{5+}, other doped or mixed U-site brannerites have been reported, including: $(U_{0.9}Ce_{0.1})_{1-x}Gd_xTi_2O_6$, where Ce was utilised as an analogue of Pu[21,22]; $U_{1-x}Ce_xTi_2O_6$, with average Ce oxidation states varying significantly according to process conditions[15,19]; and $Gd_{0.2}Hf_{0.2}U_{0.4}Pu_{0.2}Ti_2O_6$.[17]

In contrast to the significant volume of work on U-site doped brannerites, little attention has been directed to the possibility of charge-balancing U^{5+} *via* dopants on the Ti-site. Materials with stoichiometries of $UTi_{1.8}Fe_{0.2}O_6$ and $UTi_{1.6}Fe_{0.4}O_6$ were reported to form near single phase brannerites when synthesised under Ar, but formed a mixture of brannerite-structured $UTi_{1.60}Fe_{0.49}O_6$, and the binary oxides U_3O_8 and TiO_2 when synthesis was attempted in air.[8,23,24] In the same work, the paired self-charge compensated substitution of Gd+Nb for U+Ti (overall $U_{1-x}Gd_xTi_{2-x}Nb_xO_6$) was examined, with materials synthesised under Ar. For x = 0.1 and 0.2, near single phase brannerites of the nominal compositions were produced, with the material batched with x = 0.5 forming a multiphase mixture containing the brannerite phase $Gd_{0.67}U_{0.29}Ti_{1.29}Nb_{0.72}O_6$.

A previous report of the ion size limits in the brannerite structure found that the Ti-site of Th brannerite ($ThTi_2O_6$, thorutite) could not be significantly expanded (by doping with Sn^{4+} or Zr^{4+}) or contracted (by doping with Ge^{4+}).[25] In this work, materials across the compositional system $UTi_{2-x}Al_xO_6$ have been synthesised in air and characterised to identify the solubility and impact of a high fraction, lower valence Ti-site dopant on the formation of, and U oxidation state in, U brannerite. The use of Ti-site dopants to stabilise U^{5+} brannerites is notable in that, compared to U-site doping, the high U content is retained, where otherwise up to 0.5 f.u. would be substituted for the charge-balancing element.

2. Experimental

Samples were prepared by a standard cold-press and sinter solid state route. Stoichiometric amounts (according to $UTi_{2-x}Al_xO_6$, with x = 0, 0.2, …, 1.8, 2.0) of UO_2 (ABSCO limited), TiO_2 (rutile, Sigma Aldrich), and Al_2O_3 (Sigma Aldrich) were homogenised by planetary milling (500 rpm, 10 minutes, Retsch PM100) utilising yttria-stabilised zirconia mill pots and milling media, with isopropanol as a carrier fluid. The milled slurries were dried at 85 °C, and the resulting powder cakes broken up by hand in a mortar and pestle. The milled powders were then pressed into 10 mm pellets under 2 t (approx. 250 MPa). Pellets were heat treated in alumina crucibles at 1400 °C for 48 hours in air.

X-ray diffraction (XRD) patterns of each sample were collected on powdered material (Bruker D2 Phaser, Ni-filtered Cu K_α radiation). Phase analysis was conducted by matching the reflections observed to phases in the PDF-4+ database.[26] Unit cell parameters of each brannerite phase were derived using LeBail method refinements, utilising the Topas[27] and JEdit[28] software packages. The background of each diffraction pattern was modelled with an eight term shifted Chebyshev polynomial; peak shapes resulting from instrumental and sample-based contributions were modelled using a Pearson VII function. Additional phases including Al_2O_3, Al_2TiO_5, TiO_2-rutile, and U_3O_8 were added according to the phases identified in the diffraction patterns.

The time-of-flight neutron diffraction pattern of a near-single phase sample with nominal composition $UTiAlO_6$ was collected at the High Resolution Powder Diffraction beamline (HRPD) at the ISIS neutron and muon source, Rutherford Appleton Laboratory, UK.[29] Approximately 3.5 g of material was packed into a vanadium metal can which was then sealed with indium wire. Data were collected over three banks, with a data collection time of *ca.* 5 hours; data from the backscattering bank ($158.46° < 2\theta < 176.11°$; $\Delta d/d \sim 6\times10^{-4}$) was utilised for structure refinement. Data normalisation and reduction were performed in the Mantid open source software package.[30] Rietveld method refinements were used to examine the structure, utilising the Topas[27] and JEdit[28] software packages.

The semi-quantitative chemical composition of each brannerite phase was determined by scanning electron microscopy with coupled energy dispersive X-ray spectroscopy (SEM/EDX). Solid samples were prepared for SEM/EDX analysis by mounting in a cold-set epoxy resin, polishing with increasingly fine grades of diamond suspensions, before coating with a conductive carbon layer. Due to the semi-quantitative nature of the EDX measurements and low accuracy of oxygen determination, a stoichiometric oxygen content was assumed.

U L_3 edge XANES were collected using a modified EasyXAFS XES100 extended spectrometer, utilising a 100 W Pd-anode X-ray tube and operating in Rowland circle geometry.[31,32] Samples were prepared by pressing pellets of sufficient material to form one absorption length mixed with a polyethylene glycol binder (approximately 45 mg). Data were acquired by placing samples in front of a Hitatchi Vortex Silicon Drift Detector (SDD), with a 5 mm exit slit to minimise stray scatter. The energy resolution of the SDD is ca. 140 eV, enabling rejection of the harmonic content of the incident beam and background scatter. X-ray energies were selected using the (1266) harmonic of a Si (211) spherically bent crystal analyser. A He flight path (welded steel enclosure with kapton windows) was employed to minimise air scatter and absorption. Data were acquired with ($I_t(E)$) and without the sample ($I_0(E)$), using the same scan parameters. A step size of 0.5 eV and count time of 20s / step were used in the XANES region, in the pre- and post-edge regions the step size was 1.0 eV with a count time of 10s / step. Typically, 10 spectra were acquired for each composition and summed, the total data collection time was around 20 h for each composition. The absolute energy scale was calibrated using a reference of Y_2O_3 (E_0 = 17042.30 eV), with E_0 set as first peak in first derivative (the Y_2O_3 reference was previously calibrated against Y-foil[33]). Spectra were corrected to the absolute energy scale and for leakage effects, as described by Mottram *et al.,*[33,34] and further processed in Athena, part of the Demeter software package.[35,36] Spectra of well-characterised specimens of UTi_2O_6, $U_{0.5}Yb_{0.5}Ti_2O_6$, and $CaUO_4$ were also collected to act as reference compounds of known U oxidation state (U^{4+}, U^{5+}, and U^{6+} respectively).

High Energy Resolution Fluorescence Detected (HERFD) U M_4 edge XANES were collected at ESRF beamline BM20.[37] The incident energy was selected using the (111) reflection from a double Si crystal monochromator. XANES spectra were measured in high energy resolution fluorescence detected (HERFD) mode using an X-ray emission spectrometer.[38] The sample, analyser crystal, and photon detector (Si drift detector) were arranged in a vertical Rowland geometry. U M_4 edge spectra were obtained by recording the maximum intensity of the U M_β emission line (approx. 3337 eV) as a function of the incident energy, The emission energy was selected using the (220) reflection of five spherically bent striped Si crystal analysers (1 m bending radius) aligned at a 75° Bragg angle. The paths of the incident and emitted X-rays through are were minimised in orger to avoid losses in intensity due to absorption. Spectra were processed and

linear combination fitting performed in Athena, part of the Demeter software package.[35,36] Spectra of well-characterised specimens of UTi_2O_6, $CrUO_4$, and $CaUO_4$ were also collected to act as reference compounds of known U oxidation state (U^{4+}, U^{5+}, and U^{6+} respectively).

3. Results

3.1. X-ray diffraction

X-ray diffraction was used to determine the phases present in each composition, which are summarised in Table 1. A phase with the brannerite structure (UTi_2O_6; PDF #01-084-0496) was formed in all compositions examined except the end-member compositions UTi_2O_6 and UAl_2O_6. The brannerite phase was the major crystalline phase identified in materials with nominal stoichiometries of $UTi_{2-x}Al_xO_6$ with $0.4 \leq x \leq 1.6$, inclusive. As the relative Al content increased, the brannerite unit cell volume decreased, as determined by LeBail refinements (further discussed below).

In the end-member composition UTi_2O_6 the only crystalline phases present were TiO_2 (rutile; PDF #01-070-7347) and U_3O_8 (PDF #04-006-7307), in agreement with literature reports of the attempted synthesis of UTi_2O_6 in air.[8] The nominal end-member composition UAl_2O_6 comprised only Al_2O_3 (corundum; PDF #04-006-3495) and U_3O_8.

At low Al incorporation, in nominal composition $UTi_{1.8}Al_{0.2}O_6$, a relatively small amount of brannerite phase was formed, and TiO_2 and U_3O_8 remained the major components. For nominal compositions in the range $UTi_{2-x}Al_xO_6$ $0.4 \leq x \leq 1.0$, U_3O_8 was no longer observed as an accessory phase. Compositions with $x > 1.0$ contained increasing amounts of U_3O_8, Al_2O_3 and Al_2TiO_5. TiO_2 (rutile) was observed in all samples with as-batched Ti / Al > 1, *i.e.* those with nominal compositions from UTi_2O_6 to $UTi_{1.2}Al_{0.8}O_6$; the relative amount of TiO_2 present decreased from a maximum in UTi_2O_6, to only a trace amount in $UTi_{1.2}Al_{0.8}O_6$.

Al_2O_3 and Al_2TiO_5 (PDF #00-041-0258) were also observed as accessory phases in some compositions. Al_2O_3 was observed in increasing amounts in all samples with nominal Al incorporation of $0.8 \leq x \leq 2.0$ (*i.e.* $UTi_{1.2}Al_{0.8}O_6$ to UAl_2O_6). Al_2TiO_5, with a pseudobrookite structure, was observed alongside Al_2O_3 in nominal compositions $UTi_{1.2}Al_{0.8}O_6$ and $UTi_{1.0}Al_{1.0}O_6$.

Table 1: Phases identified in the XRD patterns of materials with nominal compositions in the system $UTi_{2-x}Al_xO_6$ heat treated in air. The compositions of the brannerite phases present in each material as derived from semi-quantitative EDX measurements are also shown.

Nominal x in $UTi_{2-x}Al_xO_6$	Brannerite	U_3O_8	TiO_2	Al_2O_3	Al_2TiO_5	Brannerite composition (EDX)
0	-	Y	Y	-	-	N/A
0.2	Y	Y	Y	-	-	$U_{0.93(6)}Ti_{1.64(3)}Al_{0.36(3)}O_6$
0.4	Y	-	Y	-	-	$U_{1.04(6)}Ti_{1.53(3)}Al_{0.47(3)}O_6$
0.6	Y	-	Y	-	-	$U_{1.05(6)}Ti_{1.46(3)}Al_{0.54(3)}O_6$
0.8	Y	-	Y	Y	Y	$U_{1.06(6)}Ti_{1.40(3)}Al_{0.60(3)}O_6$
1.0	Y	-	-	Y	Y	$U_{1.09(6)}Ti_{1.29(3)}Al_{0.71(3)}O_6$
1.2	Y	Y	-	Y	-	$U_{1.00(6)}Ti_{1.27(3)}Al_{0.73(3)}O_6$
1.4	Y	Y	-	Y	-	$U_{0.98(6)}Ti_{1.22(3)}Al_{0.78(3)}O_6$
1.6	Y	Y	-	Y	-	$U_{0.91(6)}Ti_{1.01(3)}Al_{0.99(3)}O_6$
1.8	Y	Y	-	Y	-	$U_{0.89(6)}Ti_{1.00(3)}Al_{1.00(3)}O_6$
2.0	-	Y	-	Y	-	N/A

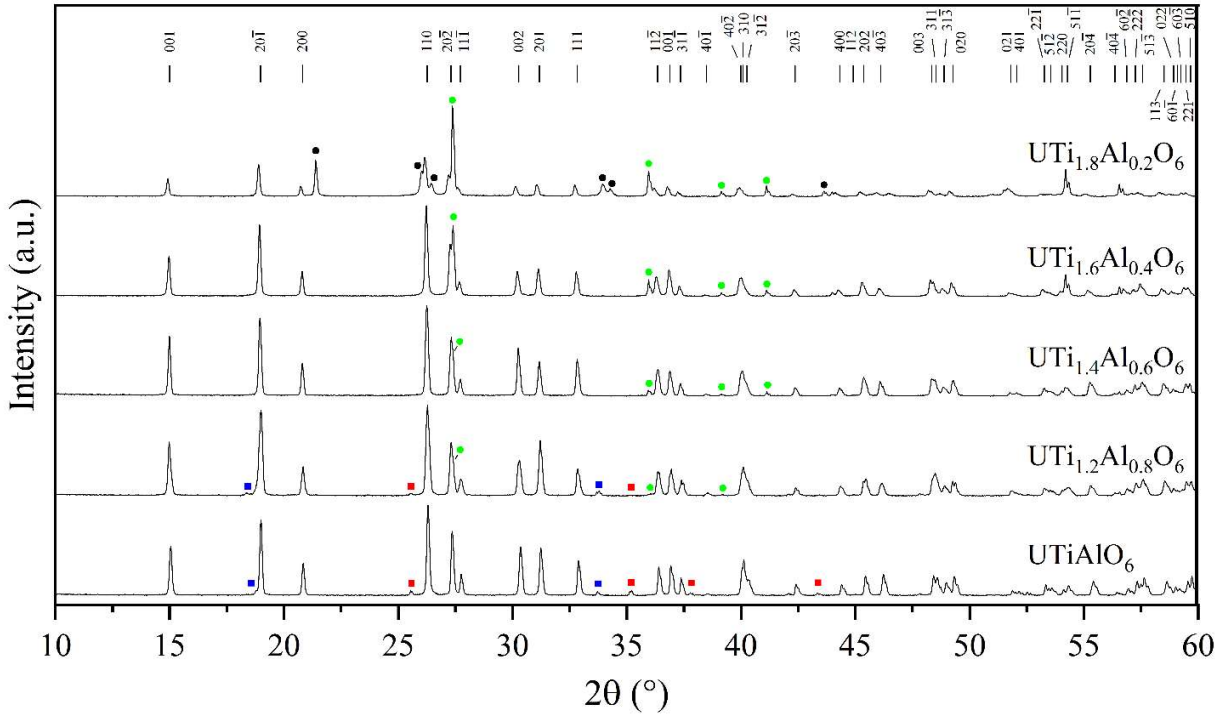

Figure 1: X-ray diffraction patterns of materials with nominal compositions in the system $UTi_{2-x}Al_xO_6$, where $0 \leq x \leq 1$. Only those compositions that formed brannerite are shown. Tick marks below display the positions of reflections of a brannerite structure with unit cell parameters approximating those of $UTiAlO_6$.

Reflections indexed to non-brannerite phases are marked with symbols: black circle, U_3O_8; green circle, TiO_2 (rutile); red square, Al_2O_3 (corundum); blue square, Al_2TiO_5.

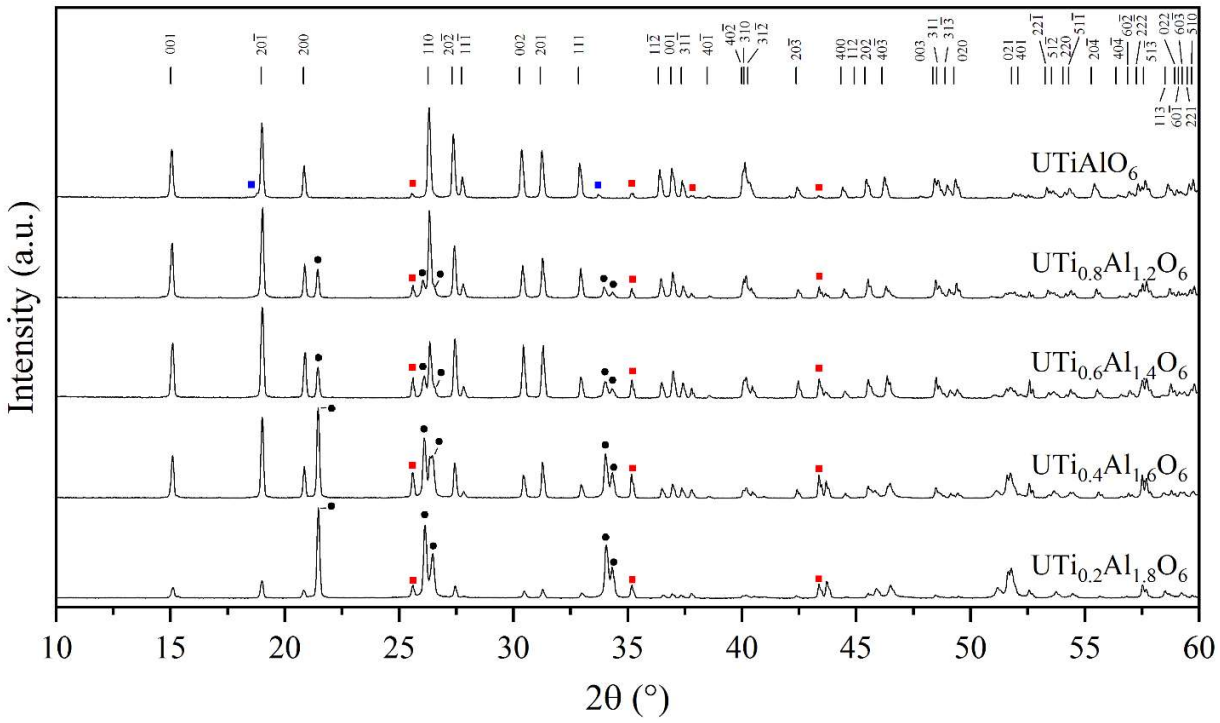

Figure 2: X-ray diffraction patterns of materials with nominal compositions in the system $UTi_{2-x}Al_xO_6$, where $1 \leq x \leq 2$. Only those compositions that formed brannerite are shown. Tick marks below display the positions of reflections of a brannerite structure with unit cell parameters approximating those of $UTiAlO_6$. Reflections indexed to non-brannerite phases are marked with symbols: black circle, U_3O_8; green circle, TiO_2 (rutile); red square, Al_2O_3 (corundum); blue square, Al_2TiO_5.

3.2. Neutron diffraction

Time of flight neutron diffraction data were acquired from the near single phase material with nominal composition $UTi_{1.0}Al_{1.0}O_6$ and were analysed by Rietveld method refinements. The structure of UTi_2O_6 was used as the starting model for the structure refinement,[39] with the unit cell parameters initially set at the values calculated from a LeBail method analysis of X-ray diffraction data (see Section 3.4). The background was fitted using a six term shifted Chebyshev polynomial, followed by systematic refinement of profile and structure parameters until a satisfactory fit was achieved. Two minor impurity phases were identified in the neutron diffraction pattern, Al_2O_3

(corundum; PDF #04-006-3495; 4.8(1) wt.%) and U_3O_8 (PDF #04-006-7307; 8.9(5) wt.%); the structures of both were included in the refinement.

The refinement rapidly converged to an excellent fit (R_{wp} 4.90%, χ^2 2.041) with 57 variables, 33 of which were structural parameters of the brannerite phase. The final structural parameters and fit are shown in Table 2 and Figure 3 respectively. The Ti / Al ratio was allowed to refine under constraint of full site occupancy and the U site occupancy allowed to refine, affording the composition $UTi_{1.23(1)}Al_{0.77(1)}O_6$ (no change in U site occupancy occurred during refinements). This implies an average U oxidation state of 4.8+, in reasonable agreement with the EDX determined composition of $U_{1.09(6)}Ti_{1.29(3)}Al_{0.71(3)}O_6$, and the X-ray absorption spectroscopy determination of average oxidation state discussed below.

In comparison to the UTi_2O_6 structure reported by Szymanski and Scott[39], the unit cell parameters and overall unit cell volume are smaller, as expected from ionic radii considerations arising from substitution of Al^{3+} (0.675 Å) for Ti^{4+}(0.745 Å), and charge compensation by oxidation of U^{4+} (1.03 Å) to U^{5+} (0.90 Å; ionic radii are for 6-fold co-ordination[40]). The UO_6 octahedra are relatively compact in $UTi_{1.23(1)}Al_{0.77(1)}O_6$, with an average U-O bond length of 2.2034(3) Å, compared to 2.2813 Å in UTi_2O_6, and more distorted relative to a regular octahedron (quadratic elongation, 1.052(1) and bond angle variance 169.4(3) $°^2$; compared to 1.047(2) and 156.1(3) $°^2$ for UTi_2O_6).

The BO_6 octahedra in $UTi_{1.23(1)}Al_{0.77(1)}O_6$ also displayed a similar compaction and increase in distortion compared to the TiO_6 octahedra in UTi_2O_6. The average (Ti,Al)-O bond distance in $UTi_{1.23(1)}Al_{0.77(1)}O_6$ was 1.9406(3) Å (compared to 1.9625 Å in UTi_2O_6), with a quadratic elongation of 1.037(1) and bond angle variance of 116.4(3) $°^2$ (1.035(2) and 110.6(3) $°^2$ respectively for UTi_2O_6). These structural changes are linked to the decreases in ionic radii of both U (on partial oxidation from U^{4+} to U^{5+}) and B (as Ti^{4+} is partially substituted by Al^{3+}).

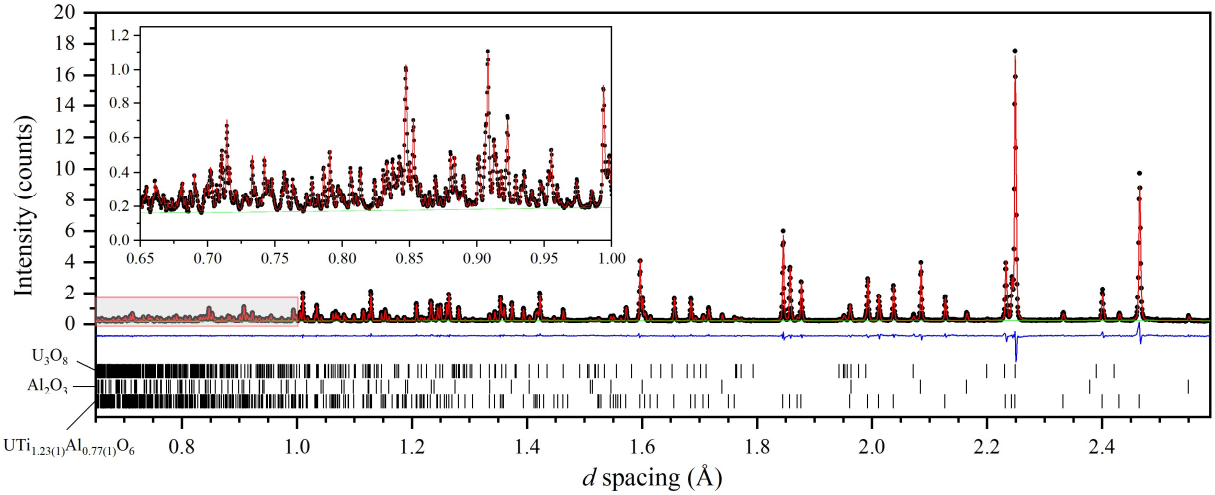

Figure 3: Rietveld refinement fit (y_{calc}; red line) of the neutron time-of-flight diffraction pattern (y_{obs}; black circles) of a material with as-refined composition $U_{1.00(1)}Ti_{1.23(1)}Al_{0.77(1)}O_6$. The allowed reflections for the three phases present ($UTi_{1.23(1)}Al_{0.77(1)}O_6$, U_3O_8, Al_2O_3) are shown as black tick marks.

Table 2: Structural parameters of a material with as-refined composition $UTi_{1.23(1)}Al_{0.77(1)}O_6$, as determined from time-of-flight neutron powder diffraction data.

C2/m (12)		*a*: 9.68255(3) Å	*b*: 3.68910(1) Å	*c*: 6.69628(2) Å	β: 118.548(1)°		V: 210.108(1) Å^3		
Atom	Site	x	y	z	*f*(occ)	U_{11}	U_{22}	U_{33}	U_{13}
U	2a	0	0	0	1	1.22(5)	0.40(4)	0.97(6)	0.53(5)
Ti	4i	0.8255(9)	0	0.3858(12)	0.614(4)	2.18(5)	1.09(4)	1.23(4)	1.05(3)
Al	4i	0.8255(9)	0	0.3858(12)	0.386(4)	2.18(5)	1.09(4)	1.23(4)	1.05(3)
O	4i	0.9779(1)	0	0.3026(2)	1	0.97(5)	1.08(4)	1.08(6)	0.49(5)
O	4i	0.6487(1)	0	0.1008(2)	1	1.03(5)	1.10(4)	1.11(5)	0.32(4)
O	4i	0.2815(1)	0	0.4033(2)	1	1.46(5)	0.42(4)	1.76(5)	1.13(4)
		χ^2: 2.04	R_{wp}: 4.90%	R_p: 4.50%			U_{aniso} × 100 Å^2		

3.3. SEM-EDX

Scanning electron microscopy (SEM) with coupled energy dispersive X-ray spectroscopy (EDX) was primarily used to investigate the compositions of the brannerite phases formed within the multiphase products described above. The microstructures of the produced materials were also examined by backscattered electron imaging.

All samples were porous and poorly sintered, with some pores large enough to have filled with epoxy resin during sample preparation. Compositions that were near single phase brannerite exhibited the lowest porosity, but with evident accessory phases of Ti and Al oxides (*e.g.* the material with nominal composition $UTi_{1.0}Al_{1.0}O_6$, see Figure 4b). Compositions identified as producing grossly multiphase products contained many large pores (*e.g.* the material with nominal composition $UTi_{0.4}Al_{1.6}O_6$, see Figure 4c).

Semi-quantitative energy dispersive X-ray spectroscopy (EDX) was used to examine the Ti:Al ratios of the brannerite phases produced (see Table 1). The Al content of the brannerite phase was found to increase alongside the increase in nominal Al content (*i.e.* as x in $UTi_{2-x}Al_xO_6$ increased from 0.2 to 1.8). The brannerite with the highest Ti content was produced in the material with nominal composition $UTi_{1.8}Al_{0.2}O_6$, and was rich in Al compared to the overall batch stoichiometry, with a determined composition of $U_{0.93(6)}Ti_{1.64(3)}Al_{0.36(3)}O_6$.

The nominal composition $UTi_{1.0}Al_{1.0}O_6$ produced a brannerite phase with determined composition $U_{1.09(6)}Ti_{1.29(3)}Al_{0.71(3)}O_6$. This suggested that some U^{4+} remained after heat treatment, as insufficient Al^{3+} was present to charge-compensate the presence of U^{5+} only. This was in agreement with the average U oxidation state determined by U L_3 ($U^{4.9(1)+}$) and HERFD U M_4 edge ($U^{4.77(2)+}$) XANES, and the evident U^{4+} contribution to the HERFD U M_4 XANES, as discussed below.

The brannerites produced in nominal compositions with the highest Al incorporations, $UTi_{0.4}Al_{1.6}O_6$ and $UTi_{0.2}Al_{1.8}O_6$, had, within error, the same determined compositions $U_{0.91(6)}Ti_{1.01(3)}Al_{0.99(3)}O_6$ and $U_{0.89(6)}Ti_{1.00(3)}Al_{1.00(3)}O_6$ respectively. Following the expected charge compensation of $U^{4+} + Ti^{4+}$ for $U^{5+} + Al^{3+}$, this suggested that all U in these brannerite phases was present as U^{5+}, charge-balanced by 1 f.u. of Al^{3+}. As both compositions produced brannerites of the same stoichiometry, the limit of Al solid solubility in the air-fired system $UTi_{2-x}Al_xO_6$ is at x = 1, where half of the Ti^{4+} is substituted for Al^{3+}.

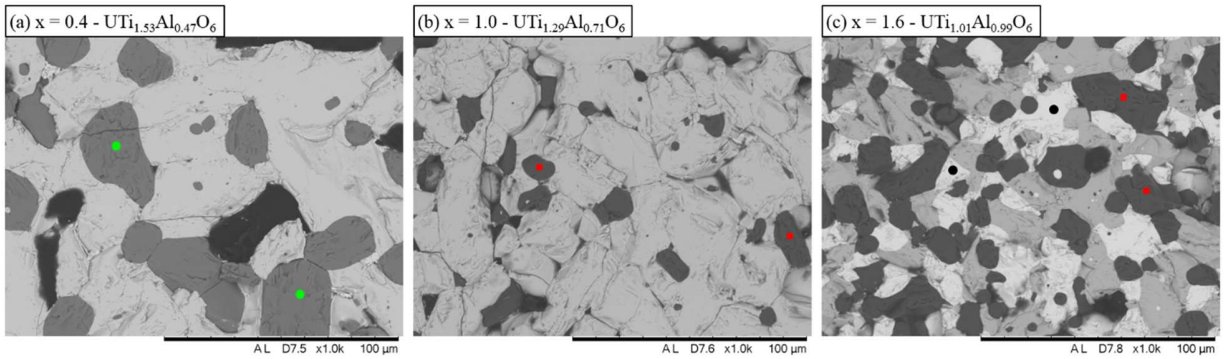

Figure 4: Representative SEM micrographs of materials with nominal compositions in the system $UTi_{2-x}Al_xO_6$: (a) x = 0.4; (b) x = 1.0; and (c) x = 1.6. Brannerite is present in all micrographs as the brightest

phase in (a, b); and second brightest in (c). Some regions of the other phases present are marked with: black circle, U_3O_8 (c, white); green circle, TiO_2 (a, dark grey); red square, Al_2O_3 (b, c, dark grey). The darkest regions of each micrograph are pores.

3.4. U L_3 and HERFD M_4 edge XANES

The charge compensation mechanism in the $UTi_{2-x}Al_xO_6$ solid solution was investigated by X-ray absorption spectroscopy at the U L_3 and HERFD M_4 edges. Initially, conventional U L_3 edge XANES were acquired in transmission mode from all compositions using a laboratory X-ray spectrometer, providing a convenient survey of the average U oxidation state. These data were utilised to guide acquisition of high resolution fluorescence detected (HERFD) U M_4-edge XANES from selected compositions of particular interest, to determine the specific contributions of U^{4+}, U^{5+} and U^{6+} to average U oxidation state.[41]

In U L_3 edge XANES, the energy position of the absorption edge is correlated with the oxidation state of the U absorber species. In this work, the position in energy of the edge, E_0, was taken as the energy at half the edge step. The L_3-edge spectra of two well-characterised brannerite-structured reference compounds, $U^{4+}Ti_2O_6$ and $U^{5+}_{0.5}Yb_{0.5}Ti_2O_6$, were also measured, with E_0 values of 17157.02 eV and 17158.53 eV respectively. The spectra of the $UTi_{2-x}Al_xO_6$ compositions examined here had E_0 values close to that of the U^{5+} brannerite reference (see Figure 5a), suggesting the majority of U was present as U^{5+}. Linear interpolation of the measured E_0 values with respect to U oxidation state was performed, with all compositions having average U oxidation states of 4.7+ or higher (see Table 3).

Further analysis of the U L_3 edge spectra was limited by both the instrumental resolution and the multiphase nature of some compositions. For example, composition $UTi_{0.2}Al_{1.8}O_6$ contained a significant fraction of U in U_3O_8 (average U oxidation state of $5.3\dot{3}$). To further elucidate the trend in U oxidation state in these materials, HERFD (high energy resolution fluorescence detected) U M_4 edge XANES were acquired on selected $UTi_{2-x}Al_xO_6$ compositions containing no (x = 0.6, 1.0) or little (x = 1.2) U_3O_8.

Examination of the HERFD M_4 edge spectra (see Figure 5b) showed that the majority of U in all compositions was present as U^{5+}, with a smaller fraction of U^{4+}, in excellent agreement with the laboratory U L_3 edge XANES. Linear combination fitting (LCF) of the spectra was undertaken to obtain a better qualitative description of the average U oxidation state, utilising the spectra of UTi_2O_6, $CrUO_4$, and $CaUO_4$ as reference compounds of known oxidation state. The best fits obtained for each spectrum are shown in Figure 5c, d, and e (the refined fraction of $CaUO_4$ in each fit was zero). The contribution of UTi_2O_6 to the fit was highest for the nominal composition $UTi_{1.4}Al_{0.6}O_6$ (determined composition $U_{1.05(6)}Ti_{1.46(3)}Al_{0.54(3)}O_6$), suggesting this material had the lowest average U oxidation state. Similarly, the best fit of the spectrum of composition

$UTi_{0.8}Al_{1.2}O_6$ (determined composition $U_{1.00(6)}Ti_{1.27(3)}Al_{0.73(3)}O_6$) had smallest contribution from UTi_2O_6, suggesting this material had the highest average U oxidation state. The fit of the spectrum of composition $UTi_{1.0}Al_{1.0}O_6$ (determined composition $U_{1.09(6)}Ti_{1.29(3)}Al_{0.71(3)}O_6$) had a contribution from UTi_2O_6 approximately halfway between those of (nominal composition) $UTi_{1.4}Al_{0.6}O_6$ and $UTi_{0.8}Al_{1.2}O_6$.

The overall trends observed in the spectra of both U HERFD M_4 and L_3 edge XANES suggest that the U oxidation state in these materials is primarily controlled by the concentration of Al^{3+} substitution on the Ti^{4+} site. This is in agreement with observations of previously reported mixed U site substituted brannerites.[15,19,21] There was no evidence to support the presence of significant U^{6+} in the U HERFD M_4 edge XANES.

Table 3: Tabulated data extracted from U L_3 and HERFD M_4 edge X-ray absorption spectra of materials with nominal compositions in the system $UTi_{2-x}Al_xO_6$. E_0 was defined as the energy position at half the edge step of the L_3-edge spectra; mean oxidation states were calculated from a linear regression of the three materials of known valence: UTi_2O_6, $U_{0.5}Yb_{0.5}Ti_2O_6$, and the material with nominal composition UAl_2O_6 containing U_3O_8 as the only U-bearing phase.

Nominal x in $UTi_{2-x}Al_xO_6$	Brannerite composition (EDX)	E_0 of L_3 edge (eV)	L_3 edge mean U ox. state	LCF $f(UTi_2O_6)$	LCF $f(CrUO_4)$	M_4 edge mean U ox. state
0.2	$U_{0.93(6)}Ti_{1.64(3)}Al_{0.36(3)}O_6$	17158.64	5.0(1)	-	-	-
0.4	$U_{1.04(6)}Ti_{1.53(3)}Al_{0.47(3)}O_6$	17158.60	5.0(1)	-	-	-
0.6	$U_{1.05(6)}Ti_{1.46(3)}Al_{0.54(3)}O_6$	17158.55	4.9(1)	0.901	0.303	4.75(2)
0.8	$U_{1.06(6)}Ti_{1.40(3)}Al_{0.60(3)}O_6$	17158.56	4.9(1)	-	-	-
1.0	$U_{1.09(6)}Ti_{1.29(3)}Al_{0.71(3)}O_6$	17158.37	4.8(1)	0.917	0.281	4.77(2)
1.2	$U_{1.00(6)}Ti_{1.27(3)}Al_{0.73(3)}O_6$	17158.11	4.7(1)	0.934	0.243	4.79(2)
1.4	$U_{0.98(6)}Ti_{1.22(3)}Al_{0.78(3)}O_6$	17158.34	4.8(1)	-	-	-
1.6	$U_{0.91(6)}Ti_{1.01(3)}Al_{0.99(3)}O_6$	17158.63	5.0(1)	-	-	-
1.8	$U_{0.89(6)}Ti_{1.00(3)}Al_{1.00(3)}O_6$	17158.94	5.2(1)	-	-	-
2.0	(U_3O_8 formed)	17159.33	$\underline{5.3\dot{3}}$	-	-	-
-	UTi_2O_6	17157.02	$\underline{4}$	-	-	-
-	$U_{0.5}Yb_{0.5}Ti_2O_6$	17158.53	$\underline{5}$	-	-	-

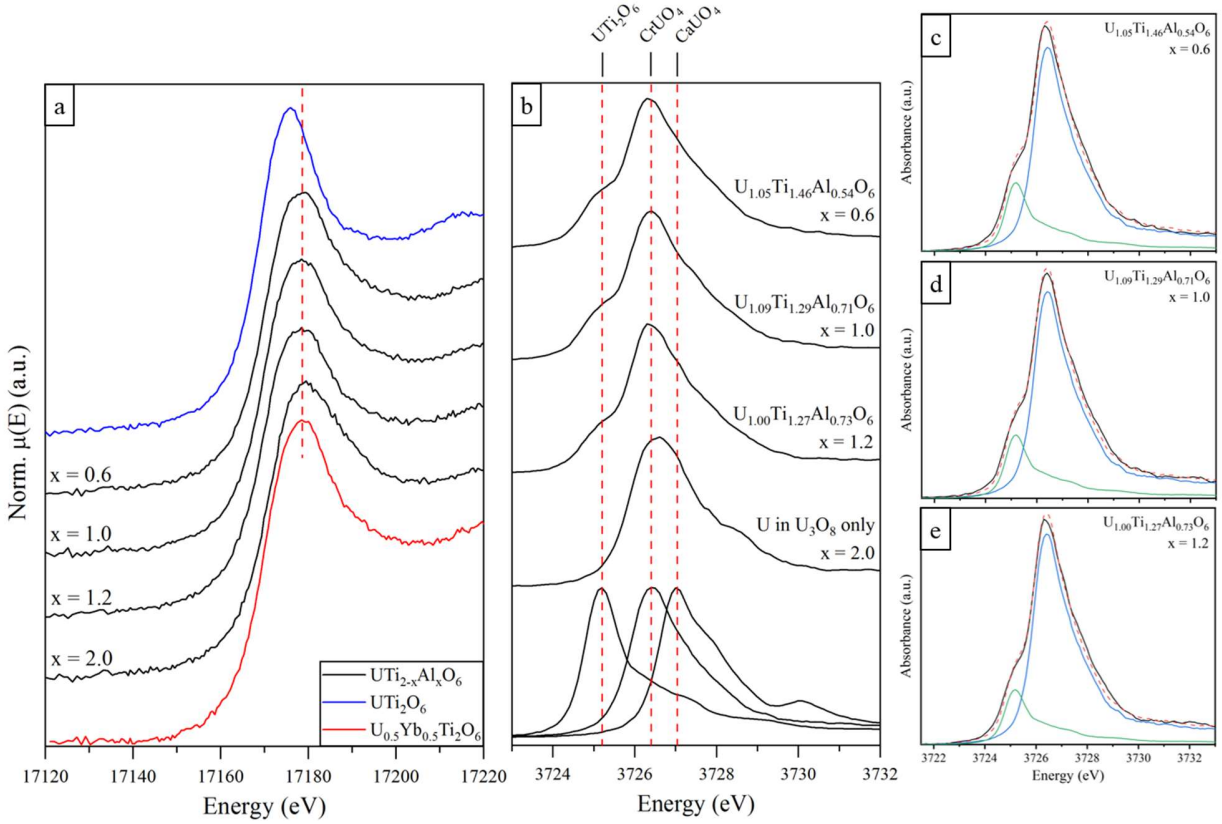

Figure 5: XANES spectra of materials with nominal compositions in the system $UTi_{2-x}Al_xO_6$. (a) Overlaid U L_3 edge XANES spectra of $UTi_{2-x}Al_xO_6$ (x is 0.6, 1.0, 1.2, 2), with UTi_2O_6 and $U_{0.5}Yb_{0.5}Ti_2O_6$ reference compounds (for U^{4+} and U^{5+} respectively). (b) Stacked U HERFD M_4 edge XANES spectra of select compositions, with UTi_2O_6, $CrUO_4$, and $CaUO_4$ reference compounds (for U^{4+}, U^{5+}, and U^{6+} respectively). (c, d, e) linear combination fits (red dashed lines) of $UTi_{2-x}Al_xO_6$ compositions with x = 0.6, 1.0, 1.2, with compositions determined from EDX measurements inset.

3.5. Changes in brannerite phase crystal chemistry

The unit cell parameters of the brannerite compositions were determined using LeBail method refinements of powder XRD patterns. Compositional information was derived from semi-quantitative EDX measurements to aid in determining the actual stoichiometry of the brannerite phases formed. For the purpose of quantifying the trends observed and allowing for comparison between compositions, an average cation radius was calculated, with the assumption that each formula unit of Al^{3+} charge-balanced the equivalent amount of U^{5+}.

As the average ionic radius decreased with increasing Al^{3+} (6-coordinate crystal radius of Al^{3+}, 0.675 Å and Ti^{4+}, 0.745 Å[40]) and U^{5+} contents (6-coordinate crystal radii of U^{4+}, 1.03 Å and U^{5+}, 0.9 Å[40]), the *b* and *c* unit cell parameters and the overall unit cell volume decreased near linearly

(δ/max of 0.62%, 0.94% and 1.80% respectively). The *a* unit cell parameter also decreased, but the observed trend was not directly correlated with the decrease in average ionic radius and was of a lower relative magnitude (δ/max of 0.40% in the brannerites reported here). This is in good agreement with previous reports of the trends observed in U-site doped brannerites, where cation size does not have a strongly correlated effect on the *a* parameter.[17,18] The observed angle β exhibited a small and linear increase as the average ionic radius decreased; this corresponds to a decrease in overall unit cell volume.

The brannerite structure, AB_2O_6, is formed of corrugated sheets of edge-sharing (BO_6) distorted octahedra connected by chains of (AO_6) octahedra parallel to the *b*-axis. The geometry of the (BO_6) sheets is complex, but can be described as two-wide 'zig-zag' chains of edge-sharing (BO_6) octahedra parallel to the *b*-axis connected by edge-sharing with neighbouring (BO_6) chains, with the ensemble overall parallel to the *a*-axis (similar arrangements of octahedra are observed in the TiO_2-anatase structure). See Figure 6 for a representation of the structure.

On consideration of the crystal structure, it is apparent that the decrease in average cation size caused by the substitution of Ti^{4+} with Al^{3+} (and the associated change in average U oxidation state) has differing impacts on the three unit cell length parameters. The strong correlation with the *b* parameter appears to be primarily caused by the edge-sharing (AO_6) chains directly parallel to *b*, with the 'zig-zag' (BO_6) chains having an additional, but lesser contribution. Changes in the *c* parameter are primarily controlled by the (AO_6) octahedra, as the O1-A-O1 bonds are parallel to the *c*-axis, with changes in bond length causing corresponding changes in the spacing of the (BO_6) sheets. The lack of strong correlation between average cationic radius and the *a* parameter is likely due to the tilting of the 'zig-zag' (BO_6) chains relative to the *a* axis: these rigid chains are parallel to *b*, but, though the overall sheets are parallel to *a*, the individual chains are out of plane. This suggests, in agreement with the trends observed here and in the literature, that the changes in the *a* parameter are the result of subtle structural changes.

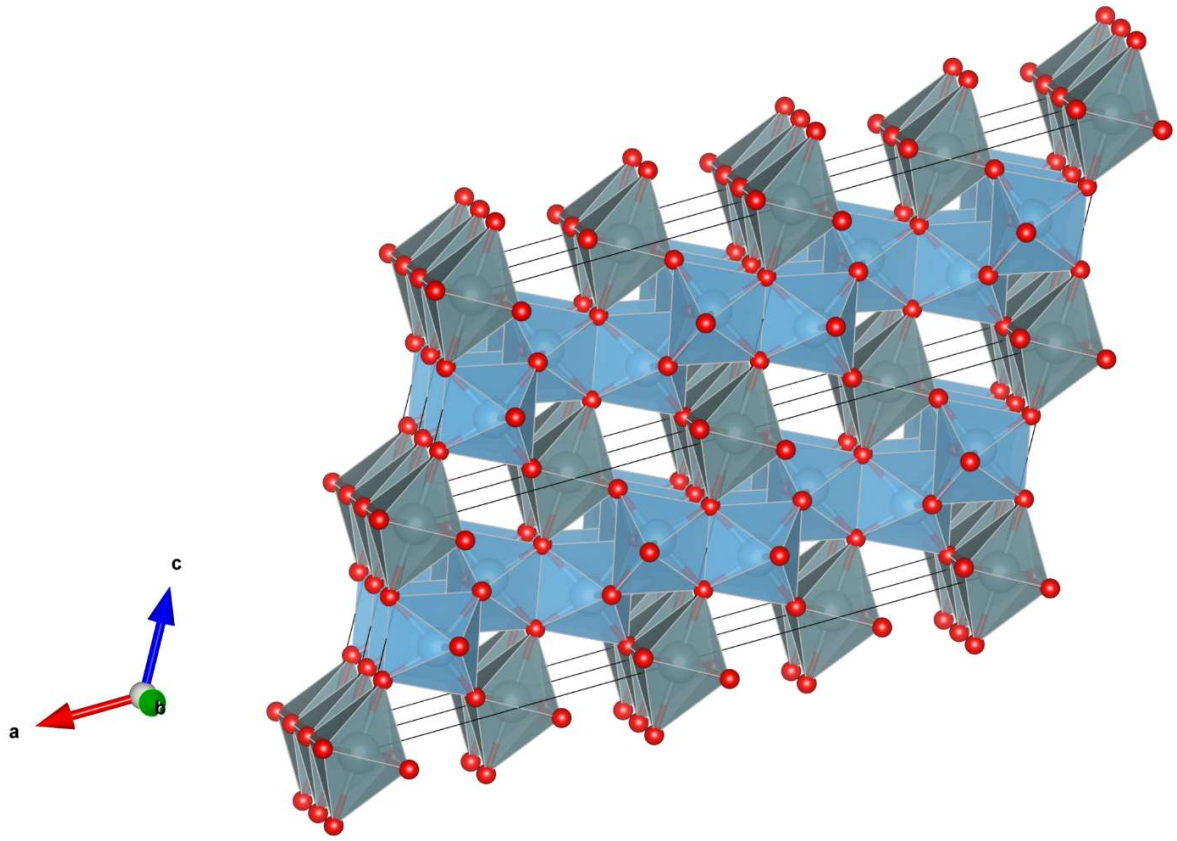

Figure 6: A polyhedral representation of the UTi_2O_6 brannerite structure, as reported by Szymanski and Scott[39], with (AO_6) octahedra in grey, (BO_6) octahedra in light blue, and O atoms in red. The diagram shows a 2×2×2 unit cell ensemble. Produced in the VESTA software package[42].

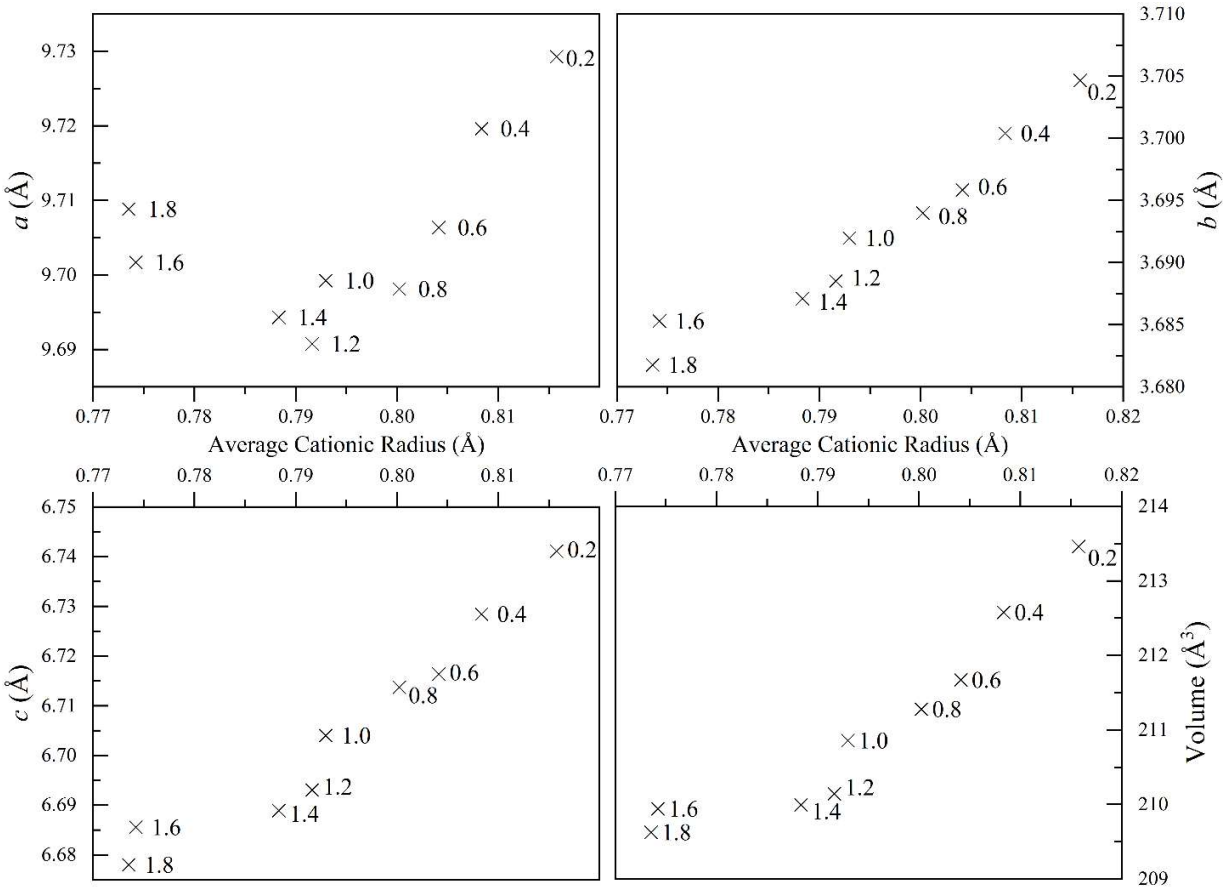

Figure 7: Plots of *a*, *b*, and *c* unit cell parameters and overall unit cell volumes for the brannerite structured phases present in materials with nominal compositions of $UTi_2Al_xO_6$ with $0.2 \leq x \leq 1.8$ (labelled). The overall average cationic radius for each brannerite was calculated as a weighted average of the cation radii, with relative cationic abundances from EDX measurements (U^{5+} content presumed equal to Al^{3+} content).

Table 4: Unit cell parameters and EDX derived approximate compositions for the brannerite structured phases present in materials with nominal compositions $UTi_{2-x}Al_xO_6$. Unit cell parameters were calculated using LeBail method refinements of XRD patterns. The unit cell parameters of $U^{4+}Ti_2O_6$, as previously reported in the literature[39], are included for comparison.

Nominal x in $UTi_{2-x}Al_xO_6$	Brannerite composition	*a* (Å)	*b* (Å)	*c* (Å)	β (º)	Volume (Å^3)	R_{wp}	χ^2
0.2	$U_{0.93(6)}Ti_{1.64(3)}Al_{0.36(3)}O_6$	9.7293(3)	3.7047(1)	6.7411(2)	118.53(1)	213.46(2)	7.10	1.426
0.4	$U_{1.04(6)}Ti_{1.53(3)}Al_{0.47(3)}O_6$	9.7196(2)	3.7004(1)	6.7284(2)	118.55(1)	212.58(1)	7.62	1.509
0.6	$U_{1.05(6)}Ti_{1.46(3)}Al_{0.54(3)}O_6$	9.7064(2)	3.6958(1)	6.7164(2)	118.54(1)	211.67(1)	8.12	1.667
0.8	$U_{1.06(6)}Ti_{1.40(3)}Al_{0.60(3)}O_6$	9.6981(3)	3.6940(1)	6.7137(2)	118.55(1)	211.28(1)	9.75	2.141
1.0	$U_{1.09(6)}Ti_{1.29(3)}Al_{0.71(3)}O_6$	9.6993(2)	3.6920(1)	6.7040(1)	118.56(1)	210.86(1)	7.85	1.621
1.2	$U_{1.00(6)}Ti_{1.27(3)}Al_{0.73(3)}O_6$	9.6908(2)	3.6885(1)	6.6931(1)	118.55(1)	210.15(1)	6.79	1.587
1.4	$U_{0.98(6)}Ti_{1.22(3)}Al_{0.78(3)}O_6$	9.6943(2)	3.6871(1)	6.6889(1)	118.56(1)	210.00(1)	8.08	1.820
1.6	$U_{0.91(6)}Ti_{1.01(3)}Al_{0.99(3)}O_6$	9.7017(2)	3.6853(1)	6.6856(2)	118.56(1)	209.94(1)	7.90	1.858
1.8	$U_{0.89(6)}Ti_{1.00(3)}Al_{1.00(3)}O_6$	9.7088(5)	3.6818(2)	6.6780(3)	118.58(1)	209.63(2)	8.96	2.073
-	UTi_2O_6[39]	9.8123	3.7697	6.9253	118.96	224.14	-	-

4. Discussion

In agreement with the previously reported solid solubility of Fe in air-fired brannerites[23], Al^{3+} is highly soluble in the brannerite structure. From the phase assemblages produced in this work it is apparent that, whilst the solubility of Al^{3+} is closely related to the average U oxidation state, when synthesised in an air atmosphere the structure is chemically flexible, supporting varied Al^{3+} content and mixed $U^{4/5+}$ oxidation state. Initially it was expected that the addition of greater than 1 f.u. of Al^{3+} would allow for charge compensation of a fraction of U^{6+}, supported by both sufficient charge-balancing species and the decrease in unit cell size; however, there was no evidence of brannerite U oxidation states greater than 5+ from either the U L_3 or HERFD M_4-edge XANES, and no evidence of any U^{6+} contribution to HERFD M_4-edge XANES.

The use of a lower valence Ti-site dopant has allowed for close examination of changes in the crystal chemistry of the brannerite structure. The observed changes in the unit cell parameters are similar to those reported for U-site doping, with *b*, *c*, and the overall unit cell volume being strongly correlated to the average cationic radius, with the *a* parameter having a secondary response only. Due to ionic size considerations, it is expected that Al^{3+} was present on the Ti^{4+} site only, though further characterisation of the cationic coordination environments is necessary. The addition of up to 1 f.u. of Al^{3+} and U^{5+} into the brannerite structure results in an increase in relative B-site cationic radius, as evidenced by an increase in the ratio r(B)/r(A) from 0.723 in stoichiometric UTi_2O_6, to

0.789 in the sample with nominal composition $UTi_{0.2}Al_{1.8}O_6$ (brannerite composition approx. $U_{0.89(6)}Ti_{1.00(3)}Al_{1.00(3)}O_6$).

5. Conclusions

This investigation has synthesised and characterised a novel U^{5+} brannerite with composition $U_{1.00(1)}Ti_{1.23(1)}Al_{0.77(1)}O_6$. The structure of this material was examined using TOF powder neutron diffraction, with Al^{3+} substitution on the Ti-site leading to shrinkage of the unit cell and increased distortion of the UO_6 and $(Ti,Al)O_6$ octahedra compared to UTi_2O_6.

The compositional system $UTi_{2-x}Al_xO_6$ was synthesised at 1400 °C under an air atmosphere, producing multiphase samples containing Al-doped brannerites as the major phase. The crystal chemistry of the brannerite phases produced has been examined, utilising LeBail method refinements of XRD data and U L_3 and HERFD M_4 edge XANES. The trends observed are in excellent agreement with those previously observed in U-site doped brannerites, with cationic sizes having a strong, linear effect on the *b* and *c* unit cell parameters, as well as the overall unit cell volume.

The brannerites produced display a relatively wide compositional range, with EDX-derived compositions from $U_{0.93(6)}Ti_{1.64(3)}Al_{0.36(3)}O_6$ to $U_{0.89(6)}Ti_{1.00(3)}Al_{1.00(3)}O_6$, demonstrating an unexpected degree of chemical flexibility with respect to Al^{3+} content and U oxidation state, despite the oxidising process atmosphere. The average U oxidation state in the brannerite phases increased towards U^{5+} as the relative amount of Al^{3+} increased.

The use of a high fraction, lower valence Ti-site dopant to charge balance U^{5+} has been successfully demonstrated, with additions of Al^{3+} stabilising the brannerite structure when fired in air, whilst allowing for retention of the full U content. The limit of solid solubility of Al^{3+} in the air-fired system $UTi_{2-x}Al_xO_6$ has been inferred to be when x = 1. No evidence for the possibility of Al content higher than 1 f.u., charge-balancing U^{6+}, in the brannerite structure was found.

6. Acknowledgments

MDW is grateful to the UK EPSRC and Nuclear Decommissioning Authority for providing studentship through an EPSRC iCASE award, and CLC acknowledges the UK EPSRC for funding through an Early Career Research Fellowship (EP/N017374/1). This research utilised the HADES/MIDAS[43] facility at the University of Sheffield established with financial support from EPSRC and BEIS, under grant EP/T011424/1. The experiment at HRPD, ISIS Neutron and Muon Source was supported by beamtime allocation RB2000257[29] and the authors would like to thank Dr. A. D. Fortes for assistance with data acquisition. We acknowledge the European Synchrotron Radiation Facility for provision of synchrotron radiation facilities and would like to thank Tatiana

Polyakova, Anastasiia Smirnova, and Jurij Galanzaw for assistance in using beamline BM20 for U M_4 edge HERFD XAS data collection. KOK acknowledges support from the European Research Council (ERC) under grant number 759696.

7. References

(1) Charalambous, F. A.; Ram, R.; Pownceby, M. I.; Tardio, J.; Bhargava, S. K. Chemical and Microstructural Characterisation Studies on Natural and Heat Treated Brannerite Samples. *Miner. Eng.* **2012**, *39* (Supplement C), 276–288. https://doi.org/10.1016/j.mineng.2012.08.006.

(2) Turuani, M.; Choulet, F.; Eglinger, A.; Goncalves, P.; Machault, J.; Mercadier, J.; Seydoux-Guillaume, A.-M.; Reynaud, S.; Baron, F.; Beaufort, D.; Batonneau, Y.; Gouy, S.; Mesbah, A.; Szenknect, S.; Dacheux, N.; Chapon, V.; Pagel, M. Geochemical Fingerprints of Brannerite (UTi2O6): An Integrated Study. *Mineral. Mag.* **2020**, *84* (2), 313–334. https://doi.org/10.1180/mgm.2020.7.

(3) Lumpkin, G. R.; Leung, S. H. F.; Ferenczy, J. Chemistry, Microstructure, and Alpha Decay Damage of Natural Brannerite. *Chem. Geol.* **2012**, *291*, 55–68. https://doi.org/10.1016/j.chemgeo.2011.09.008.

(4) Lian, J.; Wang, L. M.; Lumpkin, G. R.; Ewing, R. C. Heavy Ion Irradiation Effects of Brannerite-Type Ceramics. *Nucl. Instrum. Methods Phys. Res. Sect. B Beam Interact. Mater. At.* **2002**, *191* (1), 565–570. https://doi.org/10.1016/S0168-583X(02)00611-0.

(5) Lumpkin, G. R.; Smith, K. L.; Blackford, M. G. Heavy Ion Irradiation Studies of Columbite, Brannerite, and Pyrochlore Structure Types. *J. Nucl. Mater.* **2001**, *289* (1), 177–187. https://doi.org/10.1016/S0022-3115(00)00695-4.

(6) Lin, H.; Szenknect, S.; Mesbah, A.; Baron, F.; Beaufort, D.; Batonneau, Y.; Mercadier, J.; Eglinger, A.; Turuani, M.; Seydoux-Guillaume, A.-M.; Goncalves, P.; Choulet, F.; Chapon, V.; Pagel, M.; Dacheux, N. A Multiparametric Study on the Dissolution of Synthetic Brannerite. *Npj Mater. Degrad.* **2021**, *5* (1), 1–9. https://doi.org/10.1038/s41529-021-00173-6.

(7) Charalambous, F. A.; Ram, R.; McMaster, S.; Tardio, J.; Bhargava, S. K. An Investigation on the Dissolution of Synthetic Brannerite (UTi2O6). *Hydrometallurgy* **2013**, *139* (Supplement C), 1–8. https://doi.org/10.1016/j.hydromet.2013.06.017.

(8) Vance, E. R.; Watson, J. N.; Carter, M. L.; Day, R. A.; Begg, B. D. Crystal Chemistry and Stabilization in Air of Brannerite, UTi2O6. *J. Am. Ceram. Soc.* **2001**, *84* (1), 141–144. https://doi.org/10.1111/j.1151-2916.2001.tb00621.x.

(9) Kaiman, S. Synthesis of Brannerite. *Can. Mineral.* **1959**, *6* (3), 389–390.

(10) Patchett, J. E.; Nuffield, E. W. Studies of Radioactive Compounds. X. The Synthesis and Crystallography of Brannerite. *Can. Mineral.* **1960**, *6* (4), 483–490.

(11) Mesbah, A.; Szenknect, S.; Clavier, N.; Lin, H.; Baron, F.; Beaufort, D.; Batonneau, Y.; Mercadier, J.; Eglinger, A.; Turuani, M.; Goncalves, P.; Choulet, F.; Chapon, V.; Seydoux-Guillaume, A.-M.; Pagel, M.; Dacheux, N. Direct Synthesis of Pure Brannerite UTi2O6. *J. Nucl. Mater.* **2019**, *515*, 401–406. https://doi.org/10.1016/j.jnucmat.2019.01.003.

(12) Bailey, D. J.; Stennett, M. C.; Hyatt, N. C. Synthesis and Characterization of Brannerite Wasteforms for the Immobilization of Mixed Oxide Fuel Residues. *Procedia Chem.* **2016**, *21*, 371–377. https://doi.org/10.1016/j.proche.2016.10.052.

(13) James, M.; Carter, M. L.; Watson, J. N. The Synthesis, Crystal Chemistry and Structures of Y-Doped Brannerite (U1−xYxTi2O6) and Thorutite (Th1−xYxTi2O6−δ) Phases. *J. Solid State Chem.* **2003**, *174* (2), 329–333. https://doi.org/10.1016/S0022-4596(03)00230-5.

(14) Stefanovsky, S. V.; Yudintsev, S. V.; Shiryaev, A. A.; Murzin, V. Y.; Trigub, A. L. Phase Partitioning and Uranium Speciation in Brannerite-Based Ceramics. *J. Eur. Ceram. Soc.* **2017**, *37* (2), 771–777. https://doi.org/10.1016/j.jeurceramsoc.2016.08.028.

(15) Zhang, Y.; Karatchevtseva, I.; Kong, L.; Wei, T.; Zhang, Z. Structural and Spectroscopic Investigations on the Crystallization of Uranium Brannerite Phases in Glass. *J. Am. Ceram. Soc.* **2018**, *101* (11), 5219–5228. https://doi.org/10.1111/jace.15750.

(16) Zhang, Y.; Kong, L.; Aughterson, R. D.; Karatchevtseva, I.; Zheng, R. Phase Evolution from Ln2Ti2O7 (Ln=Y and Gd) Pyrochlores to Brannerites in Glass with Uranium Incorporation. *J. Am. Ceram. Soc.* **2017**, *100* (11), 5335–5346. https://doi.org/10.1111/jace.15051.

(17) Zhang, Y.; Kong, L.; Karatchevtseva, I.; Aughterson, R. D.; Gregg, D. J.; Triani, G. Development of Brannerite Glass-Ceramics for the Immobilization of Actinide-Rich Radioactive Wastes. *J. Am. Ceram. Soc.* **2017**, *100* (9), 4341–4351. https://doi.org/10.1111/jace.14975.

(18) Zhang, Y.; Wei, T.; Zhang, Z.; Kong, L.; Dayal, P.; Gregg, D. J. Uranium Brannerite with Tb(III)/Dy(III) Ions: Phase Formation, Structures, and Crystallizations in Glass. *J. Am. Ceram. Soc.* **2019**, *102* (12), 7699–7709. https://doi.org/10.1111/jace.16657.

(19) Dixon Wilkins, M. C.; Stennett, M. C.; Hyatt, N. C. The Effect of A-Site Cation on the Formation of Brannerite (ATi2O6, A = U, Th, Ce) Ceramic Phases in a Glass-Ceramic Composite System. *MRS Adv.* **2020**, *5* (1–2), 73–81. https://doi.org/10.1557/adv.2019.470.

(20) James, M.; Watson, J. N. The Synthesis and Crystal Structure of Doped Uranium Brannerite Phases U1−xMxTi2O6 (M=Ca2+, La3+, and Gd3+). *J. Solid State Chem.* **2002**, *165* (2), 261–265. https://doi.org/10.1006/jssc.2002.9519.

(21) Bailey, D. J.; Stennett, M. C.; Ravel, B.; Grolimund, D.; Hyatt, N. C. Synthesis and Characterisation of Brannerite Compositions (U0.9Ce0.1)1−xMxTi2O6 (M = Gd3+, Ca2+) for the Immobilisation of MOX Residues. *RSC Adv.* **2018**, *8* (4), 2092–2099. https://doi.org/10.1039/C7RA11742F.

(22) Bailey, D. J.; Stennett, M. C.; Hyatt, N. C. Synthesis and Characterization of Brannerite Compositions for MOX Residue Disposal. *MRS Adv.* **2017**, *2* (10), 557–562. https://doi.org/10.1557/adv.2016.631.

(23) Vance, E. R.; Watson, J. N.; Carter, M. L.; Day, R. Crystal Chemistry, Radiation Effects and Aqueous Leaching of Brannerite, UTi2O6. *Ceram. Trans.* **1999**, *107*, 561–568.

(24) Vance, E. R.; Carter, M. L.; Lumpkin, G. R.; Day, R. A.; Begg, B. D. *Solid Solubilities of Pu, U, Gd and Hf in Candidate Ceramic Nuclear Wasteforms*; DOE/ER/45676, Project Number 60387, 781161; 2001. https://doi.org/10.2172/781161.

(25) Vance, E. R.; Carter, M. L.; Stewart, M. W. A.; Day, R. A.; Begg, B. D.; Ball, C. J. Ionic Size Limits for A Ions in Brannerite (ATi2O6) and Pyrochlore (CaATi2O7) Titanate Structures (A = Tetravalent Rare Earths and Actinides). *MRS Online Proc. Libr. Arch.* **2002**, *713*. https://doi.org/10.1557/PROC-713-JJ2.6.

(26) Gates-Rector, S.; Blanton, T. The Powder Diffraction File: A Quality Materials Characterization Database. *Powder Diffr.* **2019**, *34* (4), 352–360. https://doi.org/10.1017/S0885715619000812.

(27) Coelho, A. A. TOPAS and TOPAS-Academic: An Optimization Program Integrating Computer Algebra and Crystallographic Objects Written in C++. *J. Appl. Crystallogr.* **2018**, *51* (1), 210–218. https://doi.org/10.1107/S1600576718000183.

(28) Evans, J. Advanced Input Files & Parametric Quantitative Analysis Using Topas. *Mater. Sci. Forum* **2010**, *651*, 1–9. https://doi.org/10.4028/www.scientific.net/MSF.651.1.

(29) Hyatt, N. C. Investigation into the Structural Relations of Actinide Brannerites. *STFC ISIS Neutron Muon Source* **2021**. https://doi.org/10.5286/ISIS.E.RB2000257.

(30) Arnold, O.; Bilheux, J. C.; Borreguero, J. M.; Buts, A.; Campbell, S. I.; Chapon, L.; Doucet, M.; Draper, N.; Ferraz Leal, R.; Gigg, M. A.; Lynch, V. E.; Markvardsen, A.; Mikkelson, D. J.; Mikkelson, R. L.; Miller, R.; Palmen, K.; Parker, P.; Passos, G.; Perring, T. G.; Peterson, P. F.; Ren, S.; Reuter, M. A.; Savici, A. T.; Taylor, J. W.; Taylor, R. J.; Tolchenov, R.; Zhou, W.; Zikovsky, J. Mantid—Data Analysis and Visualization Package for Neutron Scattering and μ SR Experiments. *Nucl. Instrum. Methods Phys. Res. Sect. Accel. Spectrometers Detect. Assoc. Equip.* **2014**, *764*, 156–166. https://doi.org/10.1016/j.nima.2014.07.029.

(31) Seidler, G. T.; Mortensen, D. R.; Remesnik, A. J.; Pacold, J. I.; Ball, N. A.; Barry, N.; Styczinski, M.; Hoidn, O. R. A Laboratory-Based Hard x-Ray Monochromator for High-Resolution x-Ray Emission Spectroscopy and x-Ray Absorption near Edge Structure Measurements. *Rev. Sci. Instrum.* **2014**, *85* (11), 113906. https://doi.org/10.1063/1.4901599.

(32) Jahrman, E. P.; Holden, W. M.; Ditter, A. S.; Mortensen, D. R.; Seidler, G. T.; Fister, T. T.; Kozimor, S. A.; Piper, L. F. J.; Rana, J.; Hyatt, N. C.; Stennett, M. C. An Improved Laboratory-Based x-Ray Absorption Fine Structure and x-Ray Emission Spectrometer for

Analytical Applications in Materials Chemistry Research. *Rev. Sci. Instrum.* **2019**, *90* (2), 024106. https://doi.org/10.1063/1.5049383.

(33) Mottram, L. M.; Dixon Wilkins, M. C.; Blackburn, L. R.; Oulton, T.; Stennett, M. C.; Sun, S. K.; Corkhill, C. L.; Hyatt, N. C. A Feasibility Investigation of Laboratory Based X-Ray Absorption Spectroscopy in Support of Nuclear Waste Management. *MRS Adv.* **2020**, *5* (1–2), 27–35. https://doi.org/10.1557/adv.2020.44.

(34) Mottram, L. M.; Cafferkey, S.; Mason, A. R.; Oulton, T.; Sun, S. K.; Bailey, D. J.; Stennett, M. C.; Hyatt, N. C. A Feasibility Investigation of Speciation by Fe K-Edge XANES Using a Laboratory X-Ray Absorption Spectrometer. *J. Geosci.* **2020**, *65* (1), 27–35. https://doi.org/10.3190/jgeosci.299.

(35) Ravel, B.; Newville, M. ATHENA and ARTEMIS: Interactive Graphical Data Analysis Using IFEFFIT. *Phys. Scr.* **2005**, *2005* (T115), 1007. https://doi.org/10.1238/Physica.Topical.115a01007.

(36) Ravel, B.; Newville, M. ATHENA, ARTEMIS, HEPHAESTUS: Data Analysis for X-Ray Absorption Spectroscopy Using IFEFFIT. *J. Synchrotron Radiat.* **2005**, *12* (4), 537–541. https://doi.org/10.1107/S0909049505012719.

(37) Scheinost, A. C.; Claussner, J.; Exner, J.; Feig, M.; Findeisen, S.; Hennig, C.; Kvashnina, K. O.; Naudet, D.; Prieur, D.; Rossberg, A.; Schmidt, M.; Qiu, C.; Colomp, P.; Cohen, C.; Dettona, E.; Dyadkin, V.; Stumpf, T. ROBL-II at ESRF: A Synchrotron Toolbox for Actinide Research. *J. Synchrotron Radiat.* **2021**, *28* (1), 333–349. https://doi.org/10.1107/S1600577520014265.

(38) Kvashnina, K.; Scheinost, A. A Johann-Type X-Ray Emission Spectrometer at the Rossendorf Beamline. *J. Synchrotron Radiat.* **2016**, *23*. https://doi.org/10.1107/S1600577516004483.

(39) Szymanski, J. T.; Scott, J. D. A Crystal-Structure Refinement of Synthetic Brannerite, UTi 2 O 6 , and Its Bearing on Rate of Alkaline-Carbonate Leaching of Brannerite in Ore. *Can. Mineral.* **1982**, *20* (2), 271–280.

(40) Shannon, R. D. Revised Effective Ionic Radii and Systematic Studies of Interatomic Distances in Halides and Chalcogenides. *Acta Crystallogr. A* **1976**, *32* (5), 751–767. https://doi.org/10.1107/S0567739476001551.

(41) Kvashnina, K. O.; Butorin, S. M.; Martin, P.; Glatzel, P. Chemical State of Complex Uranium Oxides. *Phys. Rev. Lett.* **2013**, *111* (25), 253002. https://doi.org/10.1103/PhysRevLett.111.253002.

(42) Momma, K.; Izumi, F. VESTA 3 for Three-Dimensional Visualization of Crystal, Volumetric and Morphology Data. *J. Appl. Crystallogr.* **2011**, *44* (6), 1272–1276. https://doi.org/10.1107/S0021889811038970.

(43) Hyatt, N. C.; Corkhill, C. L.; Stennett, M. C.; Hand, R. J.; Gardner, L. J.; Thorpe, C. L. The HADES Facility for High Activity Decommissioning Engineering & Science: Part of the

UK National Nuclear User Facility. *IOP Conf. Ser. Mater. Sci. Eng.* **2020**, *818*, 012022. https://doi.org/10.1088/1757-899X/818/1/012022.

7 Summary and conclusions

7.1 The formation of UTi_2O_6 glass-ceramic composites

7.1.1 The formation of stoichiometric uranium brannerite (UTi_2O_6) glass-ceramic composites from the component oxides in a one-pot synthesis

This investigation examined the formation of UTi_2O_6 in glass, forming UTi_2O_6 glass-ceramic composites. Although UTi_2O_6 was the majority crystalline phase formed in all materials, during initial investigations UO_2 particles in the glass matrix were also observed when the UO_2:TiO_2 molar ratio was stoichiometric, *i.e.* 1:2. This prompted further investigation into the addition of excess TiO_2, in order to remove the remaining UO_2.

On examination of the microstructures of the produced materials, it was apparent that UO_2 was present in two distinct environments: as isolated particles within the glass matrix, and as regions encapsulated by the brannerite phase. The former was not observed in materials with hyperstoichiometric amounts of TiO_2 (*i.e.* a molar ratio of UO_2:TiO_2 greater than 1:2), but the latter was observed in all compositions examined. This was attributed to the mechanism of formation of UTi_2O_6 within a glass phase; whether caused by a difference in the rates of diffusion of UO_2 of TiO_2 or by an epitaxial growth mechanism of brannerite, UTi_2O_6 formed around grains of UO_2, with the barrier to diffusion increasing as the UTi_2O_6 crystallites grew, resulting in the isolation of these encapsulated regions of UO_2.

In the literature, many of the actinide brannerites reported (and all reported to form in glass-ceramic composites) were formed using an alkoxide/nitrate route. This investigation was the first systematic investigation into the formation of a brannerite glass-ceramic composite from the component oxides, with no significant differences observed between samples made from oxides and those made following an alkoxide/nitrate route.

It is expected that the presence of UO_2 encapsulated within grains of UTi_2O_6 would not have a negative effect on the aqueous durability of these materials; particularly as brannerite is being examined as a potential wasteform material because of its high resistance to dissolution. If these or similar materials are to be proposed for immobilisation of actual wastes, then the impact of these regions of UO_2 on wasteform performance would have to be examined.

7.1.2 Synthesis and characterisation of high ceramic fraction brannerite (UTi_2O_6) glass-ceramic composites

The materials investigated in this report formed an extension to the previous article by examining the impact of the glass:ceramic ratio on the formation of UTi_2O_6 in a glass-ceramic composite, as well as establishing the compatibility of this system with hot isostatic pressing (HIP).

Due to the limitation imposed by the viscous nature of the glass phase at the temperature of reaction, the glass:ceramic ratio was examined from 50:50 by weight up to 10:90 by weight, with higher weight fractions of glass resulting in slumping of the pellets. It was shown that UTi_2O_6 forms as a ceramic phase at all glass:ceramic ratios in this range. The amount of UO_2 present in the

final products was the same as those with the same UO_2:TiO_2 molar ratio in the previous publication.

As the ceramic fraction increased, the abundance of UO_2 also increased, to a maximum in the sample with glass:ceramic ratio of 10:90 by weight, though UO_2 remained a minor phase in all compositions. In comparison, the amount of UO_2 observed as grains in the glass matrix in the HIP samples was much greater than the equivalent cold-press and sinter sample, likely due to reduction and dissolution of TiO_2 by the reducing atmosphere exerted by the canister material at temperature. In the cold-press and sinter glass-ceramic composites reported in the previous publication, the addition of hyperstoichiometric amounts of TiO_2 prevented the formation of grains of UO_2 in the glass matrix; however, in a HIP sample with the same UO_2:TiO_2 molar ratio (1:2.277) UO_2 was still observed as isolated grains in the glass matrix.

The successful formation of high ceramic fraction products is particularly important as it demonstrates the flexibility of the UTi_2O_6 glass-ceramic composite system, one of the main benefits of a glass-ceramic rather than pure ceramic wasteform system. From another point of view, it has been successfully demonstrated that the addition of a low fraction of glass (10% by weight) can reduce the necessary temperature of formation of UTi_2O_6 from ≥ 1300 °C to 1200 °C. This is of particular importance when considering HIP as the processing route for these materials, as temperatures lower than 1300 °C remove the need for more exotic canister materials.

7.1.3 The effect of glass composition ($Na_2Al_{2-x}B_xSi_6O_{16}$) on the formation of brannerite (UTi_2O_6) in glass-ceramic composites

In this work the impact of the glass composition (in the system $Na_2Al_{2-x}B_xSi_6O_{16}$) on the formation of UTi_2O_6 was examined. It has been previously reported that the formation of zirconolite ($CaZrTi_2O_7$) in the same glass system has a strong dependence on the Al:B ratio, only forming in high Al content glasses. It was suggested that this is due to the existence of easily formed Ca/Zr/Ti silicate phases such as sphene/titanite ($CaTiSiO_5$) and zircon ($ZrSiO_4$) that dominated the crystalline phase assemblages in those glasses with higher silica activities (*i.e.* the high B glasses).

The formation of brannerite did not have a strong dependence on the glass composition in this system, with all glasses permitting formation of a high fraction of brannerite. This difference in behaviour compared to zirconolite was ascribed to the lack of easily formed silicate phases when only TiO_2 and UO_2 are present. Coffinite ($USiO_4$) has been frequently reported as difficult to form, in contrast to the isostructural zircon.[196–198]

Though no major differences in crystalline phase assemblages were seen, those glass-ceramic composites where the glass phase had the highest B content did display other undesirable behaviours. In particular, the viscosity of these glasses was lower than the high Al content glasses, leading the pellets to slump and stick to the process crucibles over the course of the heat treatment. This resulted in the inclusion of ZrO_2 that had adhered to the bottom surface of the pellets. Although this is certainly undesirable in the context of a nuclear wasteform produced by a cold-press and

sinter route, it is expected that these materials would be produced by hot isostatic pressing, meaning no material-equipment contact would occur.

7.2 The thermodynamic stability of cerium brannerite in inert and oxidising atmospheres

Thermogravimetric measurements (in air and N_2) and ex-situ Ce L_3 edge XANES were used to isolate and characterise the impact of temperature on the Ce^{3+}/Ce^{4+} redox couple, and so on the stability of Ce brannerite, $CeTi_2O_6$. On heating in N_2, the reduction of Ce^{4+} in the brannerite structure was monitored by TGA-MS, with O_2 released by $CeTi_2O_6$ in increasing amounts at temperatures above 1000 °C. The stability limit of $CeTi_2O_6$ with respect to Ce^{3+} was found to be in the range 13.1% and 15.7% Ce^{3+}, with stability appearing to be limited by the fraction of O vacancies necessary to support Ce^{3+}. The most reduced sample containing only brannerite was that heated under N_2 to 1075 °C, whilst the sample heated under N_2 to 1100 °C contained a trace amount of the decomposition product $Ce_4Ti_9O_{24}$, showing that the stability limit had been reached.

In order to establish whether the temperature dependent Ce^{3+}/Ce^{4+} redox couple is active during formation of $CeTi_2O_6$ (which only forms in oxidising atmospheres), an aliquot was heated to 1300 °C under synthetic air (20% O_2 in 80% N_2). The TGA of this material was complex, with a sequence of mass change events. It was apparent that the initial material was slightly reduced, and then oxidised during heating to a maximum at 1100 °C. As the temperature further increased to 1300 °C, Ce within the brannerite was then reduced, with the resulting minimum in mass relating to a maximum in O_2 loss. During final cooling from 1300 °C the mass (and so Ce oxidation state and brannerite O content) increased to a new maximum. This showed that the initial material was partially reduced, with the Ce^{3+}/Ce^{4+} redox couple able to change reversibly when heated in air.

The impact of this partial Ce reduction at temperature on the thermodynamics of $CeTi_2O_6$ formation were also discussed, with the evidence suggesting that reduction of Ce^{4+} may play an important role in stabilising $CeTi_2O_6$ at the temperature necessary for formation.

7.3 Crystal chemistry of actinide brannerites

7.3.1 The effect of A-site cation on the formation of brannerite (ATi_2O_6, A = U, Th, Ce) ceramic phases in a glass-ceramic system

This work investigated the formation of ATi_2O_6 and $A_{0.5}B_{0.5}Ti_2O_6$ (A and B = U, Th, Ce) brannerite phases within a glass-ceramic composite, with heat treatments occurring under both air and Ar. As expected from previous literature reports of $U_{0.5}M^{3+}{}_{0.5}Ti_2O_6$ brannerites[140,161,162], the factor controlling brannerite formation was the availability of an overall A-site charge of 4+. For example, UTi_2O_6 only formed as a ceramic phase when the material was heated under an inert atmosphere, in this case Ar. The formation of $ThTi_2O_6$ within glass was not limited by process atmosphere (Th^{4+} dominates in solid oxides), but appeared to be slow, likely due to the particularly refractory nature of ThO_2.

The mixed cation compositions produced similar observations, with $(U,Ce)Ti_2O_6$ phases forming well in both air, as a $Ce^{3,4+}/U^{5+}$ brannerite, and Ar, as a $Ce^{3+}/U^{4,5+}$ brannerite. The $U_{0.5}Th_{0.5}Ti_2O_6$ compositions showed high solid solubility between $ThTi_2O_6$ and UTi_2O_6, but the formation of the brannerite phases was also affected by the refractory nature of ThO_2.

7.3.2 Synthesis and characterisation of the brannerite system $UTi_{2-x}Al_xO_6$

This investigation was, to the author's knowledge, the first reported comprehensive study of the solubility of a Ti-site dopant in UTi_2O_6. Materials in compositional system $UTi_{2-x}Al_xO_6$ ($0 \leq x \leq 2.0$, in increments of 0.2) were produced by reaction at 1400 °C in air. The materials formed were multiphase, with differing amounts of brannerite, U_3O_8, TiO_2 (rutile), Al_2O_3 and Al_2TiO_5 depending on the batched stoichiometry. The sample with batched composition $UTi_{1.0}Al_{1.0}O_6$ was near single phase, and so was further examined using time-of-flight neutron diffraction techniques. The structure of this phase displayed increased distortions of the UO_6 and $(Ti,Al)O_6$ octahedra and a smaller unit cell compared to UTi_2O_6, as expected from addition of the smaller Al^{3+} cation and oxidation of U^{4+} to U^{5+}.

The trends in unit cell volume and U oxidation state were examined using Le Bail method refinements of XRD data, and U L_3 and M_4 edge XAS. As the nominal Al incorporation increased, the substitution of Al^{3+} within the produced brannerites also increased, with a similar, but smaller, increase in U oxidation state. As previously reported in the literature[162] and in the above study into ATi_2O_6 and $A_{0.5}B_{0.5}Ti_2O_6$ (A and B = U, Th, Ce) glass-ceramic composites, the average cationic radius has a strong, linear effect on the *b* and *c* unit cell parameters and the overall unit cell volume, with a secondary effect on the *a* parameter.

The brannerites produced in the $UTi_{2-x}Al_xO_6$ system displayed surprising compositional flexibility, with wide variation in Al^{3+} content from $U_{0.93(6)}Ti_{1.64(3)}Al_{0.36(3)}O_6$ to $U_{0.89(6)}Ti_{1.00(3)}Al_{1.00(3)}O_6$. The solid solubility limit of Al^{3+} in the system $UTi_{2-x}Al_xO_6$ was shown to be where x = 1.0, with no evidence for Al^{3+} substitution of greater than one formula unit or U oxidation states of greater than U^{5+}. The use of a high fraction, Ti-site dopant to stabilise a U^{5+} brannerite was successfully demonstrated for the first time, showing the possibility of charge-balancing U^{5+} without reducing the overall U content as would be necessary for a U-site dopant (*e.g.* $U_{0.5}Y_{0.5}Ti_2O_6$).

8 Bibliography

1 E. Rutherford, *Lond. Edinb. Dublin Philos. Mag. J. Sci.*, 1899, **47**, 109–163.
2 F. Soddy, *Nature*, 1913, **92**, 399–400.
3 J. Chadwick, *Proc. R. Soc. Lond. Ser. Contain. Pap. Math. Phys. Character*, 1932, **136**, 692–708.
4 J. Chadwick, *Nature*, 1932, **129**, 312–312.
5 O. R. Frisch, *Nature*, 1939, **143**, 276–276.
6 L. Meitner and O. R. Frisch, *Nature*, 1939, **143**, 239–240.
7 JWB, *Thermal fission yield mass for neutron fission (neutron energy 1,5 MeV) of U-235, U-238, and Pu-239.*, 2008.
8 J. K. Shultis and R. E. Faw, *Fundamentals of Nuclear Science and Engineering*, Taylor & Francis, 2002.
9 2019 UK Radioactive Waste Inventory, https://ukinventory.nda.gov.uk/, (accessed 28 July 2021).
10 G. Choppin, J.-O. Liljenzin and J. Rydberg, *Radiochemistry and Nuclear Chemistry*, Butterworth-Heinemann, 2002.
11 H. a. C. McKay, *The PUREX process*, CRC Press, Boca Raton, FL, 1990.
12 J. E. Birkett, M. J. Carrott, O. D. Fox, C. J. Jones, C. J. Maher, C. V. Roube, R. J. Taylor and D. A. Woodhead, *Chim. Int. J. Chem.*, 2005, **59**, 898–904.
13 A. R. Mason, F. Y. Tocino, M. C. Stennett and N. C. Hyatt, *Ceram. Int.*, 2020, **46**, 29080–29089.
14 T. Nishimura, T. Koyama, M. Iizuka and H. Tanaka, *Prog. Nucl. Energy*, 1998, **32**, 381–387.
15 *Separated plutonium: progress on approaches to management*, Nuclear Decommissioning Authority, 2014.
16 B. E. Burakov, M. I. Ojovan and W. E. Lee, *Crystalline Materials for Actinide Immobilisation*, World Scientific, 2011.
17 2018 annual figures for holdings of civil unirradiated plutonium, http://www.onr.org.uk/safeguards/civilplut18.htm, (accessed 1 March 2021).
18 kallerna, *Capsule for nuclear waste.*, 2009.
19 W. Miller, R. Alexander, N. Chapman, J. C. McKinley and J. A. T. Smellie, *Geological Disposal of Radioactive Wastes and Natural Analogues*, Elsevier, 2000.
20 R. F. Haaker and R. C. Ewing, in *Scientific Basis for Nuclear Waste Management*, Springer, 1980, pp. 281–288.
21 A. Costine, A. N. Nikoloski, M. D. Costa, K. F. Chong and R. Hackl, *Miner. Eng.*, 2013, **53**, 84–90.
22 R. Gilligan and A. N. Nikoloski, *Miner. Eng.*, 2015, **71**, 34–48.
23 S. Graeser and R. Guggenheim, *Schweiz. Mineral. Petrogr. Mitteilungen*, 1990, **70**, 325–331.
24 F. L. Hess and R. C. Wells, *J. Frankl. Inst.*, 1920, **189**, 225–237.
25 G. R. Lumpkin, S. H. F. Leung and J. Ferenczy, *Chem. Geol.*, 2012, **291**, 55–68.
26 J. E. Patchett and E. W. Nuffield, *Can. Mineral.*, 1960, **6**, 483–490.
27 Y. Zhang, G. R. Lumpkin, H. Li, M. G. Blackford, M. Colella, M. L. Carter and E. R. Vance, *J. Nucl. Mater.*, 2006, **350**, 293–300.
28 F. A. Charalambous, R. Ram, S. McMaster, M. I. Pownceby, J. Tardio and S. K. Bhargava, *Miner. Eng.*, 2014, **57**, 25–35.
29 M. Turuani, F. Choulet, A. Eglinger, P. Goncalves, J. Machault, J. Mercadier, A.-M. Seydoux-Guillaume, S. Reynaud, F. Baron, D. Beaufort, Y. Batonneau, S. Gouy, A. Mesbah, S. Szenknect, N. Dacheux, V. Chapon and M. Pagel, *Mineral. Mag.*, 2020, **84**, 313–334.
30 C. Lopez, X. Deschanels, J. M. Bart, J. M. Boubals, C. Den Auwer and E. Simoni, *J. Nucl. Mater.*, 2003, **312**, 76–80.
31 B. Luckscheiter and M. Nesovic, *Waste Manag.*, 1996, **16**, 571–578.

32 H. J. Matzke and J. van Geel, in *Disposal of Weapon Plutonium: Approaches and Prospects*, eds. E. R. Merz and C. E. Walter, Springer, 1995.
33 H. D. Schreiber, G. B. Balazs, P. L. Jamison and A. P. Shaffer, *Phys. Chem. Glas.*, 1982, **23**, 147–153.
34 W. Baehr, *Int. At. Energy Agency Bull.*, 1989, **31**, 43–46.
35 R. Bonniaud, *Nucl. Technol.*, 1977, **34**, 449–460.
36 I. W. Donald, *The Science and Technology of Inorganic Glasses and Glass-Ceramics: From the Past to the Present to the Future*, Society of Glass Technology, 2015.
37 A. V. Demine, N. V. Krylova, P. P. Polyektov, I. N. Shestoperov, T. V. Smelova, V. F. Gorn and G. M. Medvedev, *MRS Online Proc. Libr. Arch.*
38 X. Mao, X. Yuan, C. T. Brigden, J. Tao, N. C. Hyatt and M. Miekina, *AIP Conf. Proc.*, 2017, **1890**, 020001.
39 T. C. Kaspar, J. V. Ryan, C. G. Pantano, J. Rice, C. Trivelpiece, N. C. Hyatt, C. L. Corkhill, C. Mann, R. J. Hand, M. A. Kirkham, C. L. Crawford, C. M. Jantzen, J. Du, X. Lu, M. T. Harrison, C. Cushman, M. R. Linford and N. J. Smith, *Npj Mater. Degrad.*, 2019, **3**, 1–15.
40 M. Guerette and L. Huang, *J. Non-Cryst. Solids*, 2015, **411**, 101–105.
41 M. Collin, M. Fournier, P. Frugier, T. Charpentier, M. Moskura, L. Deng, M. Ren, J. Du and S. Gin, *Npj Mater. Degrad.*, 2018, **2**, 1–12.
42 O. Bouty, S. Cammelli and P. L. Solari, *J. Non-Cryst. Solids*, 2018, **499**, 434–440.
43 J. Hopf and E. M. Pierce, *Procedia Mater. Sci.*, 2014, **7**, 216–222.
44 D. Ngo, H. Liu, N. Sheth, R. Lopez-Hallman, N. J. Podraza, M. Collin, S. Gin and S. H. Kim, *Npj Mater. Degrad.*, 2018, **2**, 1–9.
45 A. Abdelouas, Y. E. Mendili, A. A. Chaou, G. Karakurt, C. Hartnack, J.-F. Bardeau, T. Saito and H. Matsuzaki, *Int. J. Appl. Glass Sci.*, 2013, **4**, 307–316.
46 M. Fournier, A. Ull, E. Nicoleau, Y. Inagaki, M. Odorico, P. Frugier and S. Gin, *J. Nucl. Mater.*, 2016, **476**, 140–154.
47 J. Schofield, S. Swanton, B. Farahani, B. Myatt, T. Heath, S. Burrows, D. Holland, A. Moule, C. Brigden and I. Farnan, *Experimental studies of the chemical durability of UK HLW and ILW glasses – interim progress report*, Radioactive Waste Management Ltd, 2016.
48 P. K. Abraitis, F. R. Livens, J. E. Monteith, J. S. Small, D. P. Trivedi, D. J. Vaughan and R. A. Wogelius, *Appl. Geochem.*, 2000, **15**, 1399–1416.
49 P. K. Abraitis, B. P. McGrail, D. P. Trivedi, F. R. Livens and D. J. Vaughan, *J. Nucl. Mater.*, 2000, **280**, 196–205.
50 C. Utton, R. J. Hand, N. C. Hyatt and S. Swanton, *Glass durability in high pH environments: A review of the literature*, Nuclear Decommissioning Authority.
51 J.-H. Hsu, J. W. Newkirk, C.-W. Kim, C. S. Ray, R. K. Brow, M. E. Schlesinger and D. E. Day, *Corros. Sci.*, 2013, **75**, 148–157.
52 D. Zhu, C.-W. Kim and D. E. Day, *J. Nucl. Mater.*, 2005, **336**, 47–53.
53 M. I. Ojovan and W. E. Lee, in *An Introduction to Nuclear Waste Immobilisation*, 2005, pp. 213–249.
54 S. S. Danilov, S. E. Vinokurov, S. V. Stefanovsky and B. F. Myasoedov, *Radiochemistry*, 2017, **59**, 259–263.
55 S. V. Stefanovsky, O. I. Stefanovskaya, V. Yu. Murzin, A. A. Shiryaev and B. F. Myasoedov, *Dokl. Phys. Chem.*, 2016, **468**, 76–79.
56 K. I. Maslakov, Y. A. Teterin, S. V. Stefanovsky, S. N. Kalmykov, A. Y. Teterin and K. E. Ivanov, *J. Alloys Compd.*, 2017, **712**, 36–43.
57 Y.-P. Sun, X.-B. Xia, Y.-B. Qiao, Z.-Q. Zhao, H.-J. Ma, X.-Y. Liu and Z.-H. Qian, *Nucl. Sci. Tech.*, 2016, **27**, 63.
58 Y. Qiao, Y. Sun, X. Liu, Z. Qian, S. Wang and H. Ma, in *Proceedings of The 20th Pacific Basin Nuclear Conference*, ed. H. Jiang, Springer, Singapore, 2017, pp. 623–633.

59 Y. Sun, X. Xia, Y. Qiao, L. Bao, H. Ma, X. Liu and Z. Qian, *Sci. China Mater.*, 2016, **59**, 279–286.
60 B. L. Metcalfe and I. W. Donald, *J. Non-Cryst. Solids*, 2004, **348**, 225–229.
61 S. V. Yudintsev and A. A. Shiryaev, *Dokl. Phys.*, 2018, **63**, 513–516.
62 C. Erdogan, M. Bengisu and S. A. Erenturk, *J. Nucl. Mater.*, 2014, **445**, 154–164.
63 W. G. Ramsey, N. E. Bibler and T. F. Meaker, *Compositions and Durabilities of Glasses for Immobilization of Plutonium and Uranium*, Westinghouse Savannah River Co., SC, USA, 1995.
64 T. F. Meaker, *Compositional Development of a Plutonium Surrogate Glass Without Listed Rcra Elements (lead and Barium)*, Westinghouse Savannah River Co., SC, USA, 1996.
65 T. F. Meaker, *Homogeneous Glass Processing Region Defined for a Lanthanide Borosilicate Glass Composition for the Mobilization of Plutonium Using Thorium as a Surrogate*, Westinghouse Savannah River Co., SC, USA, 1996.
66 E. M. Pierce, B. P. McGrail, P. F. Martin, J. Marra, B. W. Arey and K. N. Geiszler, *Appl. Geochem.*, 2007, **22**, 1841–1859.
67 J. Marra, *Development of an Alternative Glass Formulation for Vitrification of Excess Plutonium*, Westinghouse Savannah River Co., SC, USA, 2006.
68 C. J. Mertz, A. J. Bakel, J. K. Bates, D. B. Chamberlain, J. A. Fortner, J. M. Hanchar and S. F. Wolf, *Comparison of the corrosion behavior of plutonium glasses*, Argonne National Laboratory, 1997.
69 N. E. Bibler, W. G. Ramsey, T. F. Meaker and J. M. Pareizs, *Durabilities and microstructures of radioactive glasses to immobilize excess actinides and reprocessing wastes at SRS*, Westinghouse Savannah River Co., SC, USA.
70 A. G. Solomah, T. S. Sridhar and S. C. Jones, in *Nuclear waste management II*, American Ceramic Society, OK, USA, 1986.
71 A. G. Solomah, P. G. Richardson and A. K. McIlwain, *J. Nucl. Mater.*, 1987, **148**, 157–165.
72 Y. Zhang, K. P. Hart, W. L. Bourcier, R. A. Day, M. Colella, B. Thomas, Z. Aly and A. Jostsons, *J. Nucl. Mater.*, 2001, **289**, 254–262.
73 J. W. Yang, B. L. Tang and S. G. Luo, in *Scientific Basis for Nuclear Waste Management XXIV*, eds. K. P. Hart and G. R. Lumpkin, Materials Research Society, PA, USA, 2000, pp. 333–339.
74 H. Xu, Y. Wang, P. Zhao, W. L. Bourcier, R. Van Konynenburg and H. F. Shaw, *Environ. Sci. Technol.*, 2004, **38**, 1480–1486.
75 J. P. Icenhower, B. P. McGrail, D. M. Strachan, R. D. Scheele, V. L. Legore, E. A. Rodriguez, J. L. Steele, C. F. Brown and M. J. O'Hara, in *Scientific Basis for Nuclear Waste Management XXV*, eds. B. P. McGrail and G. A. Cragnolino, Materials Research Society, PA, USA, 2002, pp. 433–440.
76 J. P. Icenhower, B. P. McGrail, W. J. Weber, B. D. Begg, N. J. Hess, E. A. Rodriguez, J. L. Steele, C. F. Brown and M. J. O'Hara, in *Scientific Basis for Nuclear Waste Management XXV*, eds. B. P. McGrail and G. A. Cragnolino, Materials Research Society, PA, USA, 2002, pp. 397–403.
77 A. Ringwood, S. Kesson, K. Reeve, D. Levins and E. Ramm, in *Radioactive waste forms for the future*, eds. W. Lutze and R. Ewing, North-Holland, N.Y., U.S.A, 1988, pp. 233–334.
78 S. S. Shoup, C. E. Bamberger, T. J. Haverlock and J. R. Peterson, *J. Nucl. Mater.*, 1997, **240**, 112–117.
79 G. R. Lumpkin, *J. Nucl. Mater.*, 2001, **289**, 136–166.
80 G. R. Lumpkin, E. M. Foltyn and R. C. Ewing, *J. Nucl. Mater.*, 1986, **139**, 113–120.
81 H. F. Xu and Y. F. Wang, *J. Nucl. Mater.*, 1999, **265**, 117–123.

82 G. R. Lumpkin, R. C. Ewing, C. T. Williams and A. N. Mariano, in *Scientific Basis for Nuclear Waste Management XXIV*, eds. K. P. Hart and G. R. Lumpkin, Materials Research Society, PA, USA, 2000, pp. 921–934.
83 R. V. Bogdanov, Y. F. Batrakov, E. V. Puchkova, A. S. Sergeev and B. E. Burakov, in *Scientific Basis for Nuclear Waste Management XXV*, eds. B. P. McGrail and G. A. Cragnolino, Materials Research Society, PA, USA, 2002, pp. 295–302.
84 G. R. Lumpkin and R. C. Ewing, *Am. Mineral.*, 1996, **81**, 1237–1248.
85 G. R. Lumpkin and R. C. Ewing, *Am. Mineral.*, 1995, **80**, 732–743.
86 G. R. Lumpkin and R. C. Ewing, *Am. Mineral.*, 1992, **77**, 179–188.
87 W. J. Weber, J. W. Wald and Hi. Matzke, *MRS Proc.*, , DOI:10.1557/PROC-44-679.
88 R. Turcotte, J. Wald, F. Roberts, J. Rusin and W. Lutze, *J. Am. Ceram. Soc.*, 1982, **65**, 589–593.
89 W. Weber and F. Roberts, *Nucl. Technol.*, 1983, **60**, 178–198.
90 J. W. Wald and P. Offemann, *MRS Online Proc. Libr. Arch.*, , DOI:10.1557/PROC-11-369.
91 W. Weber, J. Wald and H. Matzke, *Mater. Lett.*, 1985, **3**, 173–180.
92 W. Weber, J. Wald and H. Matzke, *J. Nucl. Mater.*, 1986, **138**, 196–209.
93 D. M. Strachan, R. D. Scheele, W. C. Buchmiller, J. D. Vienna, R. L. Sell and R. J. Elovich, *Preparation and Characterization of 238Pu-Ceramics for Radiation Damage Experiments*, Pacific Northwest National Laboratory, Richland, WA, 2000.
94 D. M. Strachan, R. D. Scheele, J. P. Icenhower, A. E. Kozelisky, R. L. Sell, V. L. Legore, H. T. Schaef, M. J. O'Hara, C. F. Brown and W. C. Buchmiller, *The Status of Radiation Damage Experiments*, Pacific Northwest National Laboratory, Richland, WA, 2001.
95 J. P. Icenhower, D. M. Strachan, M. J. Lindberg, E. A. Rodriguez and J. L. Steele, *Dissolution Kinetics of Titanate-Based Ceramic Waste Forms: Results from Single-Pass Flow Tests on Radiation Damaged Specimens*, Pacific Northwest National Laboratory, Richland, WA, 2003.
96 B. Burakov, E. Anderson, M. Yagovkina, M. Zamdryanskaya and E. Nikolaeva, *J. Nucl. Sci. Technol.*, 2002, **39**, 733–736.
97 S. V. Yudintsev, A. A. Lizin, T. S. Livshits, S. V. Stefanovsky, S. V. Tomilin and R. C. Ewing, *J. Mater. Res.*, 2015, **30**, 1516–1528.
98 R. E. Sykora, P. E. Raison and R. G. Haire, *J. Solid State Chem.*, 2005, **178**, 578–583.
99 J. Wen, C. Sun, P. P. Dholabhai, Y. Xia, M. Tang, D. Chen, D. Y. Yang, Y. H. Li, B. P. Uberuaga and Y. Q. Wang, *Acta Mater.*, 2016, **110**, 175–184.
100 S. Moll, G. Sattonnay, L. Thome, J. Jagielski, C. Decorse, P. Simon, I. Monnet and W. J. Weber, *Phys. Rev. B*, 2011, **84**, 064115.
101 X. Lu, Y. Ding, X. Shu, X. Mao and X. Wang, *RSC Adv.*, 2015, **5**, 64247–64253.
102 M. Lang, J. Lian, J. Zhang, F. Zhang, W. J. Weber, C. Trautmann and R. C. Ewing, *Phys. Rev. B*, 2009, **79**, 224105.
103 C. A. Taylor, M. K. Patel, J. A. Aguiar, Y. Zhang, M. L. Crespillo, J. Wen, H. Xue, Y. Wang and W. J. Weber, *Acta Mater.*, 2016, **115**, 115–122.
104 W. Jiang, W. J. Weber, S. Thevuthasan and L. A. Boatner, *Nucl. Instrum. Methods Phys. Res. Sect. B-Beam Interact. Mater. At.*, 2003, **207**, 85–91.
105 A. Chartier, C. Meis, J. P. Crocombette, W. J. Weber and L. R. Corrales, *Phys. Rev. Lett.*, 2005, **94**, 025505.
106 R. E. Williford and W. J. Weber, *J. Nucl. Mater.*, 2001, **299**, 140–147.
107 W. Sinclair and A. Ringwood, *Geochem. J.*, 1981, **15**, 229–243.
108 J. Lian, L. M. Wang, J. Chen, R. C. Ewing and K. V. G. Kutty, in *Scientific Basis for Nuclear Waste Management XXV*, eds. B. P. McGrail and G. A. Cragnolino, Materials Research Society, PA, USA, 2002, vol. 713, pp. 507–512.
109 S. X. Wang, B. D. Begg, L. M. Wang, R. C. Ewing, W. J. Weber and K. V. G. Kutty, *J. Mater. Res.*, 1999, **14**, 4470–4473.

110 S. X. Wang, L. M. Wang, R. C. Ewing and K. V. G. Kutty, in *Microstructural Processes in Irradiated Materials*, eds. S. J. Zinkle, G. E. Lucas, R. C. Ewing and J. S. Williams, Materials Research Society, PA, USA, 1999, vol. 540, pp. 355–360.
111 H. Kamizono, I. Hayakawa and S. Muraoka, *J. Am. Ceram. Soc.*, 1991, **74**, 863–864.
112 I. Hayakawa and H. Kamizono, *J. Mater. Sci.*, 1993, **28**, 513–517.
113 J. P. Icenhower, W. J. Weber, N. J. Hess, S. Thevuthasen, B. D. Begg, B. P. McGrail, E. A. Rodriguez, J. L. Steele and K. N. Geiszler, in *Scientific Basis for Nuclear Waste Management XXVI*, eds. R. J. Finch and D. B. Bullen, Materials Research Society, PA, USA, 2003, pp. 227–234.
114 K. E. Sickafus, L. Minervini, R. W. Grimes, J. A. Valdez, M. Ishimaru, F. Li, K. J. McClellan and T. Hartmann, *Science*, 2000, **289**, 748–751.
115 B. D. Begg, N. J. Hess, D. E. McCready, S. Thevuthasan and W. J. Weber, *J. Nucl. Mater.*, 2001, **289**, 188–193.
116 J. Lian, J. Chen, L. M. Wang, R. C. Ewing, J. M. Farmer, L. A. Boatner and K. B. Helean, *Phys. Rev. B*, 2003, **68**, 134107.
117 J. Lian, X. T. Zu, K. V. G. Kutty, J. Chen, L. M. Wang and R. C. Ewing, *Phys. Rev. B*, 2002, **66**, 054108.
118 F. W. Clinard, L. W. Hobbs, C. C. Land, D. E. Peterson, D. L. Rohr and R. B. Roof, *J. Nucl. Mater.*, 1982, **105**, 248–256.
119 B. D. Begg, R. A. Day and A. Brownscombe, in *Scientific Basis for Nuclear Waste Management XXIV*, eds. K. P. Hart and G. R. Lumpkin, Materials Research Society, Warrendale, 2000, vol. 663, pp. 259–266.
120 E. R. Vance, G. R. Lumpkin, M. L. Carter, D. J. Cassidy, C. J. Ball, R. A. Day and B. D. Begg, *J. Am. Ceram. Soc.*, **85**, 1853–1859.
121 M. R. Gilbert, C. Selfslag, M. Walter, M. C. Stennett, J. Somers, N. C. Hyatt and F. R. Livens, *IOP Conf. Ser. Mater. Sci. Eng.*, 2010, **9**, 012007.
122 X. Deschanels, V. Picot, B. Glorieux, F. Jorion, S. Peuget, D. Roudil, C. Jégou, V. Broudic, J. N. Cachia, T. Advocat, C. Den Auwer, C. Fillet, J. P. Coutures, C. Hennig and A. Scheinost, *J. Nucl. Mater.*, 2006, **352**, 233–240.
123 F. W. Clinard, R. J. Livak, L. W. Hobbs and D. L. Rohr, *MRS Proc.*
124 F. W. Clinard, D. L. Rohr and R. B. Roof, *Nucl. Instrum. Methods Phys. Res. Sect. B Beam Interact. Mater. At.*, 1984, **1**, 581–586.
125 S. X. Wang, L. M. Wang, R. C. Ewing, G. S. Was and G. R. Lumpkin, *Nucl. Instrum. Methods Phys. Res. Sect. B Beam Interact. Mater. At.*, 1999, **148**, 704–709.
126 S. X. Wang, G. R. Lumpkin, L. M. Wang and R. C. Ewing, *Nucl. Instrum. Methods Phys. Res. Sect. B Beam Interact. Mater. At.*, 2000, **166–167**, 293–298.
127 D. P. Reid, M. C. Stennett, B. Ravel, J. C. Woicik, N. Peng, E. R. Maddrell and N. C. Hyatt, *Nucl. Instrum. Methods Phys. Res. Sect. B Beam Interact. Mater. At.*, 2010, **268**, 1847–1852.
128 M. Gilbert, C. Davoisne, M. Stennett, N. Hyatt, N. Peng, C. Jeynes and W. E. Lee, *J. Nucl. Mater.*, 2011, **416**, 221–224.
129 J. T. Szymanski and J. D. Scott, *Can. Mineral.*, 1982, **20**, 271–280.
130 K. Momma and F. Izumi, *J. Appl. Crystallogr.*, 2011, **44**, 1272–1276.
131 S. Kaiman, *Can. Mineral.*, 1959, **6**, 389–390.
132 K. B. Helean, A. Navrotsky, G. R. Lumpkin, M. Colella, J. Lian, R. C. Ewing, B. Ebbinghaus and J. G. Catalano, *J. Nucl. Mater.*, 2003, **320**, 231–244.
133 G. R. Lumpkin, K. L. Smith and M. G. Blackford, *J. Nucl. Mater.*, 2001, **289**, 177–187.
134 J. Lian, L. M. Wang, G. R. Lumpkin and R. C. Ewing, *Nucl. Instrum. Methods Phys. Res. Sect. B Beam Interact. Mater. At.*, 2002, **191**, 565–570.

135 E. R. Vance, J. N. Watson, M. L. Carter, R. A. Day and B. D. Begg, *J. Am. Ceram. Soc.*, 2001, **84**, 141–144.
136 A. Mesbah, S. Szenknect, N. Clavier, H. Lin, F. Baron, D. Beaufort, Y. Batonneau, J. Mercadier, A. Eglinger, M. Turuani, P. Goncalves, F. Choulet, V. Chapon, A.-M. Seydoux-Guillaume, M. Pagel and N. Dacheux, *J. Nucl. Mater.*, 2019, **515**, 401–406.
137 A. Hussein, J. Tardio and S. Bhargava, in *Chemeca 2008: Towards a Sustainable Australasia*, Barton, Australia, 2008.
138 F. A. Charalambous, R. Ram, S. McMaster, J. Tardio and S. K. Bhargava, *Hydrometallurgy*, 2013, **139**, 1–8.
139 V. Balek, Y. Zhang, V. Zelenak, J. Subrt and I. N. Beckman, *J. Therm. Anal. Calorim.*, 2008, **92**, 155–160.
140 Y. Zhang, L. Kong, I. Karatchevtseva, R. D. Aughterson, D. J. Gregg and G. Triani, *J. Am. Ceram. Soc.*, 2017, **100**, 4341–4351.
141 Y. Zhang, I. Karatchevtseva, M. Qin, S. C. Middleburgh and G. R. Lumpkin, *J. Nucl. Mater.*, 2013, **437**, 149–153.
142 K. S. Finnie, Z. Zhang, E. R. Vance and M. L. Carter, *J. Nucl. Mater.*, 2003, **317**, 46–53.
143 M. C. Stennett, C. L. Freeman, A. S. Gandy and N. C. Hyatt, *J. Solid State Chem.*, 2012, **192**, 172–178.
144 T. Kidchob, L. Malfatti, D. Marongiu, S. Enzo and P. Innocenzi, *J. Sol-Gel Sci. Technol.*, 2009, **52**, 356.
145 T. Kidchob, L. Malfatti, D. Marongiu, S. Enzo and P. Innocenzi, *Thin Solid Films*, 2010, **518**, 1653–1657.
146 A. Verma, A. K. Srivastava and K. N. Sood, *Solid State Ion.*, 2007, **178**, 1288–1296.
147 A. Verma, A. Goyal and R. K. Sharma, *Thin Solid Films*, 2008, **516**, 4925–4933.
148 M. James, M. L. Carter and J. N. Watson, *J. Solid State Chem.*, 2003, **174**, 329–333.
149 M. Yoshida, N. Koyama, T. Ashizawa, Y. Sakata and H. Imamura, *Jpn. J. Appl. Phys.*, 2007, **46**, 977.
150 V. Valeš, L. Matějová, Z. Matěj, T. Brunátová and V. Holý, *J. Phys. Chem. Solids*, 2014, **75**, 265–270.
151 L. Kong, D. J. Gregg, I. Karatchevtseva, Z. Zhang, M. G. Blackford, S. C. Middleburgh, G. R. Lumpkin and G. Triani, *Inorg. Chem.*, 2014, **53**, 6761–6768.
152 L. Kong, D. J. Gregg, E. R. Vance, I. Karatchevtseva, G. R. Lumpkin, M. G. Blackford, R. Holmes, M. Jovanovic and G. Triani, *J. Eur. Ceram. Soc.*, 2017, **37**, 2179–2187.
153 M. Colella, G. R. Lumpkin, Z. Zhang, E. C. Buck and K. L. Smith, *Phys. Chem. Miner.*, 2005, **32**, 52–64.
154 L. T. Huynh, S. B. Eger, J. D. S. Walker, J. R. Hayes, M. W. Gaultois and A. P. Grosvenor, *Solid State Sci.*, 2012, **14**, 761–767.
155 E. R. Aluri, A. P. Grosvenor, S. H. Forbes, J. E. Greedan and L. M. Bachiu, *Surf. Interface Anal.*, 2017, **49**, 1335–1344.
156 B. Ebbinghaus, R. Van Konynenburg, F. Ryerson, E. R. Vance, M. W. A. Stewart, A. Jostsons, J. S. Allender, T. Rankin and J. Congdon, in *Waste Management '98*, WM Symposia Inc., Tucson, AZ, USA, 1998.
157 E. R. Vance, M. W. A. Stewart, R. A. Day, K. P. Hart, M. J. Hambley and A. Brownscombe, *Pyrochlore-rich titanate ceramics for incorporation of plutonium, uranium and process chemicals*, ANSTO, Sydney, Australia, 1997.
158 M. James and J. N. Watson, *J. Solid State Chem.*, 2002, **165**, 261–265.
159 D. J. Bailey, M. C. Stennett and N. C. Hyatt, *Procedia Chem.*, 2016, **21**, 371–377.
160 D. J. Bailey, M. C. Stennett and N. C. Hyatt, *MRS Adv.*, 2017, **2**, 557–562.
161 Y. Zhang, I. Karatchevtseva, L. Kong, T. Wei and Z. Zhang, *J. Am. Ceram. Soc.*

162 Y. Zhang, T. Wei, Z. Zhang, L. Kong, P. Dayal and D. J. Gregg, *J. Am. Ceram. Soc.*, 2019, **102**, 7699–7709.
163 Y. Zhang, L. Kong, R. D. Aughterson, I. Karatchevtseva and R. Zheng, *J. Am. Ceram. Soc.*, 2017, **100**, 5335–5346.
164 C. A. Born, P. B. Queneau and R. A. Ronzio, *Trans. Soc. Min. Eng. AIME Am. Inst. Min. Metall. Pet. Eng.*, 1975, **258**, 218–221.
165 G. Smits, Thesis, Potchefstroom University for Christian Higher Education, 1990.
166 M. J. Lottering, L. Lorenzen, N. S. Phala, J. T. Smit and G. A. C. Schalkwyk, *Miner. Eng.*, 2008, **21**, 16–22.
167 E. M. Gogoleva, *J. Radioanal. Nucl. Chem.*, 2012, **293**, 185–191.
168 F. Habashi, *Precipitation in Hydrometallurgy*, Australasian Inst. Mining & Metallurgy, Victoria, AUS, 1993, vol. 93.
169 Y. Zhang, B. S. Thomas, G. R. Lumpkin, M. Blackford, Z. Zhang, M. Colella and Z. Aly, *J. Nucl. Mater.*, 2003, **321**, 1–7.
170 B. S. Thomas and Y. Zhang, *Radiochim. Acta*, 2003, **91**, 463–472.
171 H. Lin, S. Szenknect, A. Mesbah, F. Baron, D. Beaufort, Y. Batonneau, J. Mercadier, A. Eglinger, M. Turuani, A.-M. Seydoux-Guillaume, P. Goncalves, F. Choulet, V. Chapon, M. Pagel and N. Dacheux, *Npj Mater. Degrad.*, 2021, **5**, 1–9.
172 World Intellectual Property Organization, WO2018009782A1, 2018.
173 D. J. S. Findlay, in *2007 IEEE Particle Accelerator Conference (PAC)*, 2007, pp. 695–699.
174 J. W. G. Thomason, *Nucl. Instrum. Methods Phys. Res. Sect. Accel. Spectrometers Detect. Assoc. Equip.*, 2019, **917**, 61–67.
175 A. K. Cheetham, B. E. F. Fender and M. J. Cooper, *J. Phys. C Solid State Phys.*, 1971, **4**, 3107–3121.
176 H. M. Rietveld, *J. Appl. Crystallogr.*, 1969, **2**, 65–71.
177 H. M. Rietveld, *Acta Crystallogr.*, 1967, **22**, 151–152.
178 A. C. Larson and R. B. Von Dreele, *GSAS General Structure Analysis System*, Los Alomos National Laboratory, 1994.
179 B. H. Toby, *J. Appl. Crystallogr.*, 2001, **34**, 210–213.
180 A. A. Coelho, *J. Appl. Crystallogr.*, 2018, **51**, 210–218.
181 J. Evans, *Mater. Sci. Forum*, 2010, **651**, 1–9.
182 T. Degen, M. Sadki, E. Bron, U. König and G. Nénert, *Powder Diffr.*, 2014, **29**, S13–S18.
183 N. Doebelin and R. Kleeberg, *J. Appl. Crystallogr.*, 2015, **48**, 1573–1580.
184 T. Taut, R. Kleeberg and J. Bergmann, *Mater. Struct.*, 1998, **5**, 57–66.
185 J. Rodríguez-Carvajal, *Phys. B Condens. Matter*, 1993, **192**, 55–69.
186 R. W. Cheary and A. Coelho, *J. Appl. Crystallogr.*, 1992, **25**, 109–121.
187 L. W. Finger, D. E. Cox and A. P. Jephcoat, *J. Appl. Crystallogr.*, 1994, **27**, 892–900.
188 B. H. Toby, *Powder Diffr.*, 2006, **21**, 67–70.
189 G. S. Pawley, *J. Appl. Crystallogr.*, 1981, **14**, 357–361.
190 A. Le Bail, H. Duroy and J. L. Fourquet, *Mater. Res. Bull.*, 1988, **23**, 447–452.
191 A. Le Bail, *Powder Diffr.*, 2005, **20**, 316–326.
192 C. V. Raman and K. S. Krishnan, *Nature*, 1928, **121**, 501–502.
193 B. Ravel and M. Newville, *J. Synchrotron Radiat.*, 2005, **12**, 537–541.
194 E. Maddrell, S. Thornber and N. C. Hyatt, *J. Nucl. Mater.*, 2015, **456**, 461–466.
195 S. S. Naghavi, J. He and C. Wolverton, *ACS Appl. Mater. Interfaces*, 2020, **12**, 21521–21527.
196 X. Guo, S. Szenknect, A. Mesbah, S. Labs, N. Clavier, C. Poinssot, S. V. Ushakov, H. Curtius, D. Bosbach, R. C. Ewing, P. C. Burns, N. Dacheux and A. Navrotsky, *Proc. Natl. Acad. Sci.*, 2015, **112**, 6551–6555.

197 S. Szenknect, D. Alby, M. López García, C. Wang, R. Podor, F. Miserque, A. Mesbah, L. Duro, L. Zetterström Evins, N. Dacheux, J. Bruno and R. C. Ewing, *Sci. Rep.*, 2020, **10**, 12168.
198 S. Labs, C. Hennig, S. Weiss, H. Curtius, H. Zänker and D. Bosbach, *Environ. Sci. Technol.*, 2014, **48**, 854–860.

9 Appendices

9.1 List of figures

9.2 List of tables